CHARACTERISTICS OF AIRFOILS IN AN OSCILLATING EXTERNAL FLOW AT LOW REYNOLDS NUMBERS

by

ANDREW MAN-CHUNG WO

B.S., University of Virginia (1982)
S.M., Massachusetts Institute of Technology (1986)

Submitted to the
Department of Aeronautics and Astronautics
in partial fulfillment of the requirements
for the degree of

DOCTOR OF PHILOSOPHY

at the

MASSACHUSETTS INSTITUTE OF TECHNOLOGY

January 1990

© Andrew Man-Chung Wo 1990
The author grants to M.I.T. permission to reproduce and to distribute copies of this thesis document in whole or in part.

Signature of Author_____
Department of Aeronautics and Astronautics, January 1990

Certified by_____
Dr. Eugene E. Covert
Thesis Supervisor and Department Head
Professor of Aeronautics and Astronautics

Certified by_____
Dr. Marten T. Landahl
Professor of Aeronautics and Astronautics

Certified by_____
Dr. Edward M. Greitzer
H. Nelson Slater Professor of Aeronautics and Astronautics

Certified by_____
Dr. Michael B. Giles
Assistant Professor of Aeronautics and Astronautics

Accepted by_____
Dr. Harold Y. Wachman
Professor of Aeronautics and Astronautics
Chairman, Department Graduate Committee

MASSACHUSETTS INSTITUTE OF TECHNOLOGY
FEB 26 1990
LIBRARIES
Aero

Characteristics of Airfoils in an Oscillating External Flow at Low Reynolds Numbers

by

Andrew M. Wo

Submitted to the Department of Aeronautics and Astronautics on January 1990 in partial fulfillment of the requirements for the Degree of *Doctor of Philosophy* in *Fluid Mechanics*

Abstract

An experimental study is conducted on airfoils in an oscillating external flow at reduced frequencies of $0 \leq k \equiv \frac{\omega C}{2U_\infty} \leq 6.4$ and chord Reynolds numbers of 125000 and 400000. Both Wortmann FX63-137 and NACA 0012 airfoils are tested in free-stream turbulence levels of 0.05% and 0.8%.

Results show that the thin airfoil theory is a good design tool to account for unsteady forces at Reynolds numbers as low as 125000; the difference in C_l between the measurement and Theodorsen's theory is within 10% in amplitude and 10 degrees in phase. Higher harmonics in the lift and moment data are present due to the response of the transition region to imposed excitation.

The transition from laminar to turbulent flow is shown to dominate the behavior and geometry of a laminar separation bubble. The process of transition is sensitive to Reynolds number, unsteadiness, and pressure gradient. In general, an increase in the free-stream turbulence level causes earlier transition, analogous to an increase in Reynolds number.

The unsteady Kutta-Joukowski condition is studied by computing the ensemble averaged streamlines leaving the trailing edge of a NACA 0012 at $Re = 125000$ and $k = 2.0$. The variation of streamlines, over one unsteady cycle, is within the trailing edge angle and in-phase with the unsteady excitation; this qualitatively agrees with the triple-deck analysis of Brown and Daniels. The unsteady Kutta-Joukowski condition appears to hold for the parameters investigated.

Boundary layer profiles near the laminar separation point are obtained in steady and unsteady external flow. For steady flow, the terms in the Navier-Stokes equations are calculated. Results show that $\frac{1}{Re}\frac{\partial^2 u^*}{\partial x^{*2}}$ is less than 0.2% of $v^*\frac{\partial u^*}{\partial y^*}$. The convection terms in the y-momentum equation are 14% to 22% of the corresponding x equation terms. The transverse pressure gradient has the same order of magnitude as the convection terms. Above the boundary layer displacement thickness the viscous terms can be neglected.

Secondary vorticity, having opposite sign to that of the unseparated boundary layer, is found at the intermediate frequency range ($k = 0.15$). This is not observed at the high frequency ($k = 2.0$). The origin of the secondary vortices is likely from the balance of forces near the unsteady laminar separation region.

Thesis Supervisor : Dr. Eugene Edzards Covert
Title : Professor & Chairman, Dept. of Aeronautics and Astronautics

Acknowledgements

I would like to sincerely thank Professor Eugene Edzards Covert for his guidance, patience, and encouragement over the years. His words of perspective are often timely during the course of my study. Among many ways that Prof. Covert has an influence on me, two particularly stand out: i) his eager quest for physical truth, demonstrated by prudent interpretation of data and 'on the spot' order of magnitude calculations and ii) the broadness of his knowledge in all aspects of fluid mechanics. Indeed, he has been a superb teacher. Thank you Prof. Covert.

Thanks are also due to other members of my thesis committee: Professors M. Landahl, E.M. Greitzer, M.B. Giles. Prof. Greitzer, a man of high standard, deserves credit for teaching me the importance of asking the right questions in research. Prof. Giles influences me through his sincerity and honesty in research and in helping others in general. Thanks Professors.

The Office of Naval Research has kindly provided financial support for portion of this work (ONR grant N00014-85-K-0513). Dr. S.G. Lekoudis is the technical monitor.

Five years ago the Lord Jesus Christ opened the way for me to pursue graduate studies. Many lessons, spiritual and otherwise, have been learned and re-learned. Perhaps one most frequent lesson is: *to trust in the lord in all circumstances as an act of the will* (interpreted from Proverbs 3:5,6). Indeed, graduate studies at M.I.T. provides a natural environment to take this lesson to heart. I expect hard times ahead. So, I thank the Lord for the past five years of preparation.

Academically, the Lord has also guided me in search of the truth in the fascinating world of fluid mechanics. Sir Sydney Goldstein said it well.

> "There be three things which are which are too wonderful for me, yea four which I know not," of which two were "The way of an eagle in the air" and "The way of a ship in the midst of the sea," which I take to be questions of aerodynamics and naval architecture, questions that concern us still.
> *Annual Review of Fluid Mechanics, Vol.1, p.4* (quotations from Proverbs 30:19)

Many others have also played a part during my course of study here. Dr. Xiao-Liu Liu deserves special acknowledgement in getting me started on the LDA system, which I came to love. Thanks are also due to my friends and office-mates – Patrick

Hanley, Fei Li, Stephane Mondoloni, Bor-Chyuan Lin, Kevin Huh, Peter Grooth, Jorgen Olsson, Sean Tavares, Sasi Digavalli, and Douglas Ling. Also, I appreciate Roger Biasca's help on keeping Werner working as smooth as silk. Thanks everybody.

It is impossible to know, much less to mention, all those who have prayed for us in the last five years. A brief list includes Mrs. Ruth Bohnert, Ms. Clara Chyen, Rev. & Mrs. Tom Eynon, Mr. & Mrs. Tom Hess, Mrs. Mary Murdoch, Rev. & Mrs. Ronnie Stevens, and Rev. & Mrs. John Tan. Only the Lord knows the full impact of their prayers.

Mom and Dad have been a constant source of encouragement. Thanks. I love you two. May the Lord richly bless you and guide you.

In the Lord's wonderful provision, I met my dear wife Chi-Fang Chen in graduate school. Indeed, He knows best. Without her constant help, words of exortation, and wisdom in speaking the truth in love, the load of life would be twice as heavy. Chi-Fang, I love you dearly. Let's us keep pressing on to know the Lord.

I hereby dedicate this thesis to the task of making known the love of Jesus Christ in the hearts and minds of Chinese all over the world, especially to those from and in Mainland China in this hour when Darkness seems to reign.

Contents

Acknowledgments 3

Table of Contents 6

List of Figures 9

1 Introduction 21

1.1 Motivation 21

1.2 Fundamentals of low Reynolds number flow 22

1.3 Previous research at low chord Reynolds numbers 24

1.3.1 Steady Flow 24

1.3.2 Unsteady Flow 26

1.4 Objectives and scope of investigation 27

2 Experimental Apparatus and Procedures 31

2.1 Wind tunnels 32

2.2 Airfoils 33

2.3 The unsteady flow generator 34

2.4 Pressure apparatus 34

2.5 Pressure data acquisition 35

2.6 Laser Doppler anemometer system 36

2.7 Uncertainty analyses 38

3 The Unsteady Flow Field 47

3.1 Time mean upwash 48
3.2 Unsteady upwash 48
3.3 A model of flow induced by rotating ellipse 49
3.3.1 Time mean upwash model 50
3.3.2 Wind tunnel wall effect 53
3.3.3 Unsteady upwash model 54
3.4 Time mean airfoil/upwash interference effect 56
3.4.1 NACA 0012/ellipse interference 59
3.4.2 Wortmann FX63-137/ellipse interference 60

4 Measured Airfoil Steady and Unsteady Surface Pressure 70
4.1 Steady external flow results 70
4.1.1 Reynolds number effects 71
4.1.2 Free-stream turbulence effects 71
4.1.3 Pressure gradient effects 72
4.2 Definition of time mean and unsteady pressure coefficient 72
4.3 Time mean results 74
4.4 Unsteady results 76

5 Unsteady Flow aft of the Trailing Edge 87
5.1 The unsteady potential flow aft of the trailing edge position 89
5.1.1 Formulation 89
5.1.2 Unsteady potential streamlines 90
5.2 Experimental setup for study of unsteady Kutta condition 91
5.3 The ensemble averaged streamlines aft of the trailing edge 92
5.4 Discussions 93

6 Dynamics of Laminar Separation Bubbles in *Steady* External Flow 98
6.1 Laminar boundary layers near separation – present status 98
6.2 Velocity profiles near laminar separation 99
6.3 Values of terms in the Navier-Stokes equation near separation 100

7 Dynamics of Bubbles in *Unsteady* External Flow **110**

7.1 Unsteady laminar boundary layer near separation – present status . 112

7.2 Measurement and discussions of unsteady velocity profiles near separation 113

7.2.1 Time mean velocity profiles 113

7.2.2 Velocity amplitude and phase 114

7.2.3 Ensemble averaged velocity profiles 115

7.2.4 Ensemble averaged vorticity contours 115

8 Summary and Conclusions **136**

8.1 Steady pressure results 136

8.2 Unsteady pressure results 137

8.3 Unsteady flow aft of the trailing edge 139

8.4 Balance of forces near laminar separation in steady flow 139

8.5 Unsteady laminar separation 141

8.6 Conclusions 142

8.7 Recommendations 143

Bibliography **145**

A Uncertainties in Laser Doppler Anemometer measurements **153**

B Uncertainties in pressure data **157**

C Formulation for the chordwise distribution of angle attack **164**

D Theorectical time mean and unsteady airfoil pressure **169**

D.1 Time mean difference pressure 169

D.2 Unsteady pressure–Theodorsen's unsteady airfoil theory 170

E Unsteady pressure data **179**

List of Figures

1.1 Schematic of a laminar separation bubble (Brendel [7]) 30
1.2 Illustration of airfoil performance over a large range of Reynolds numbers (Lissaman [38]) 30

2.1 A sketch of the general experimental setup 40
2.2 The M.I.T. Wright Brothers Wind Tunnel (WBWT), free-stream turbulence level of 0.8% 41
2.3 The M.I.T. Low Turbulence Wind Tunnel (LTWT), free-stream turbulence level of 0.05% 42
2.4 Spectrum of the free-stream in WBWT at 12 ft/s 43
2.5 Sketch of Laser Doppler anemometer optics layout (TSI 9100-7) . . . 43
2.6 Schematic of pressure data acquisition system 44
2.7 The pressure taps locations 45
2.8 Amplitude response of the pressure tubings (Wortmann airfoil) . . . 46
2.9 Phase response of the pressure tubings (Wortmann airfoil) 46

3.1 Sketch of time mean upwash model 51
3.2 Model for calculating the time mean interference effect 56
3.3 Comparison of time mean upwash data with calculation (LTWT, $Re = 125{,}000$) 62
3.4 Comparison of time mean upwash data with calculation (LTWT, $Re = 400{,}000$) 62
3.5 Amplitude of upwash at fundamental frequency 63
3.6 Phase of upwash at fundamental frequency 63

3.7 Amplitude of upwash at 2^{nd} harmonic 63
3.8 Amplitude of upwash at 3^{nd} harmonic 63
3.9 Amplitude of upwash at fundamental frequency 64
3.10 Phase of upwash at fundamental frequency 64
3.11 Amplitude of upwash at 2^{nd} harmonic 64
3.12 Amplitude of upwash at 3^{nd} harmonic 64
3.13 Amplitude of upwash at fundamental frequency 65
3.14 Phase of upwash at fundamental frequency 65
3.15 Amplitude of upwash at 2^{nd} harmonic 65
3.16 Amplitude of upwash at 3^{nd} harmonic 65
3.17 Amplitude of upwash at fundamental frequency 66
3.18 Phase of upwash at fundamental frequency 66
3.19 Amplitude of upwash at 2^{nd} harmonic 66
3.20 Amplitude of upwash at 3^{nd} harmonic 66
3.21 Tunnel wall effect with stationary cylinder 67
3.22 Calculation of time mean upwash at $k = 6.4$ 67
3.23 0012/upwash interference effect (LTWT, $k = 6.4$) 68
3.24 Bound vorticity/upwash interference (0012, LTWT, Re =125K, k =6.4) 68
3.25 Bound vorticity/upwahs interference (0012, LTWT, Re =400K, k =6.4) 68
3.26 Upwash/Wortmann interference effect (LTWT, $k = 6.4$) 69
3.27 Bound vorticity/upwash interference (Wort., LTWT, Re =125K, k =6.4) 69
3.28 Bound vorticity/upwash interference (Wort., LTWT, Re =400K, k =6.4) 69

4.1 Wortmann pressure distribution in steady flow (LTWT, $\alpha = 0°$) . . . 78
4.2 Wortmann pressure distribution in steady flow (WBWT, $\alpha = 0°$) . . 78
4.3 Wortmann pressure distribution in steady flow (LTWT, $\alpha = 10°$) . . 79
4.4 Wortmann pressure distribution in steady flow (WBWT, $\alpha = 10°$) . 79
4.5 Time mean C_p (0012, Re = 125000, $\alpha = 10°$, $k = 2.0$) 80
4.6 Time mean C_p (0012, Re = 125000, $\alpha = 10°$, $k = 6.4$) 80
4.7 Time mean C_p (0012, Re = 400000, $\alpha = 10°$, $k = 2.0$) 81

4.8 Time mean C_p (0012, $Re = 400000$, $\alpha = 10^o$, $k = 6.4$) 81
4.9 $\overline{C_l}/\overline{C_{l\,theory}}$ for both wind tunnels and Reynolds numbers (0012, $\alpha = 0^o$) 82
4.10 Unsteady lift and moment coefficients (ensemble averaged) 83
4.11 Unsteady lift and moment coefficients (ensemble averaged) 84
4.12 Ensemble averaged C_p over an unsteady period (Wortmann, LTWT, $Re = 400000$, $\alpha = 0^o$, $k = 0.15$) 85
4.13 Ratio of measured amplitude of lift coefficient at fundamental frequency to the prediction of Theodorsen's theory (0012, $\alpha = 0^o$) . . . 86

5.1 Upwash ensemble averaged streamlines without airfoil (WBWT, $Re =$ 125,000, $k = 2.0$) 94
5.2 LDA measurement locations 94
5.3 Ensemble averaged velocity vectors at ellipse of 0^o (LTWT, $Re =$ 125,000, $k = 2.0$) 95
5.4 Ensemble averaged velocity vectors at ellipse of 60^o (LTWT, $Re =$ 125,000, $k = 2.0$) 95
5.5 Ensemble averaged streamlines aft of 0012 trailing edge, enlarged for clearity (LTWT, $Re = 125{,}000$, $k = 2.0$) 96
5.6 Ensemble averaged streamlines aft of 0012 trailing edge (LTWT, $Re = 125{,}000$, $k = 2.0$) 96
5.7 Maskell's model for streamlines leaving the trailing edge tangentially. (See Basu and Hancock) 97

6.1 Steady boundary layer U-profile near laminar separation (Wortmann upper surface, LTWT, $Re = 125000$, $\alpha = 0^o$) 104
6.2 Steady boundary layer V-profile near laminar separation (Wortmann upper surface, LTWT, $Re = 125000$, $\alpha = 0^o$) 104
6.3 Skin friction of steady boundary layer near laminar separation (Wortmann upper surface, LTWT, $Re = 125000$, $\alpha = 0^o$) 105
6.4 Steady boundary layer parameters near laminar separation (Wortmann upper surface, LTWT, $Re = 125000$, $\alpha = 0^o$) 105

6.5 Values of terms in the X-momentun eq. (X/C= 48%) (Wortmann upper surface, LTWT, $Re = 125000$, $\alpha = 0^o$) 106
6.6 Values of terms in the X-momentun eq. (X/C= 50%) (Wortmann upper surface, LTWT, $Re = 125000$, $\alpha = 0^o$) 106
6.7 Values of terms in the X-momentun eq. (X/C= 52%) (Wortmann upper surface, LTWT, $Re = 125000$, $\alpha = 0^o$) 107
6.8 Values of terms in the X-momentun eq. (X/C= 54%) (Wortmann upper surface, LTWT, $Re = 125000$, $\alpha = 0^o$) 107
6.9 Values of terms in the Y-momentun eq. (X/C= 48%) (Wortmann upper surface, LTWT, $Re = 125000$, $\alpha = 0^o$) 108
6.10 Values of terms in the Y-momentun eq. (X/C= 50%) (Wortmann upper surface, LTWT, $Re = 125000$, $\alpha = 0^o$) 108
6.11 Values of terms in the Y-momentun eq. (X/C= 52%) (Wortmann upper surface, LTWT, $Re = 125000$, $\alpha = 0^o$) 109
6.12 Values of terms in the Y-momentun eq. (X/C= 54%) (Wortmann upper surface, LTWT, $Re = 125000$, $\alpha = 0^o$) 109

7.1 Low and High Frequency Approximations for an unsteady flat plate boundary layer Lighthill (1954) (LFA: $\omega x/U_\infty \leq 0.02$, HFA: $\omega x/U_\infty \geq 0.6$) 117
7.2 Time mean profile (Wortmann upper surface, LTWT, $Re = 125000$, $\alpha = 0^o$, $k = 0.15$) 118
7.3 Time mean profile (Wortmann upper surface, LTWT, $Re = 125000$, $\alpha = 0^o$, $k = 2.0$) 118
7.4 Contour of fundamental U-velocity amplitude near laminar separation normalized by local free-stream fundamental amplitude (Wortmann upper surface, LTWT, $Re = 125000$, $\alpha = 0^o$, $k = 0.15$) 119
7.5 Contour of fundamental U-velocity amplitude near laminar separation normalized by local free-stream fundamental amplitude (Wortmann upper surface, LTWT, $Re = 125000$, $\alpha = 0^o$, $k = 2.0$) 120

7.6 Curves of constant amplitude of oscillation in the neighborhood of separation for $f = 0.2Hz.$ obtained experimentally by Mezaris and Telionis (1980). The numbers in the figure denote the ratio of the velocity amplitude over the corresponding amplitude at the edge of the viscous region. 121
7.7 Phase Lag of U-velocity at fundamental freq. near laminar separation (Wortmann upper surface, LTWT, $Re = 125000$, $\alpha = 0^o$, $k = 0.15$) . 122
7.8 Phase Lag of U-velocity at fundamental freq. near laminar separation (Wortmann upper surface, LTWT, $Re = 125000$, $\alpha = 0^o$, $k = 2.0$) . 122
7.9 Excursion of laminar separation location (Wortmann upper surface, LTWT, $Re = 125000$, $\alpha = 0^o$, $k = 0.15$) 123
7.10 Ensemble Averaged U-velocity at $t/T = 0.00$ (Wortmann upper surface, LTWT, $Re = 125000$, $\alpha = 0^o$, $k = 0.15$) 124
7.11 Ensemble Averaged U-velocity at $t/T = 0.11$ (Wortmann upper surface, LTWT, $Re = 125000$, $\alpha = 0^o$, $k = 0.15$) 124
7.12 Ensemble Averaged U-velocity at $t/T = 0.22$ (Wortmann upper surface, LTWT, $Re = 125000$, $\alpha = 0^o$, $k = 0.15$) 125
7.13 Ensemble Averaged U-velocity at $t/T = 0.33$ (Wortmann upper surface, LTWT, $Re = 125000$, $\alpha = 0^o$, $k = 0.15$) 125
7.14 Ensemble Averaged U-velocity at $t/T = 0.44$ (Wortmann upper surface, LTWT, $Re = 125000$, $\alpha = 0^o$, $k = 0.15$) 126
7.15 Ensemble Averaged U-velocity at $t/T = 0.55$ (Wortmann upper surface, LTWT, $Re = 125000$, $\alpha = 0^o$, $k = 0.15$) 126
7.16 Ensemble Averaged U-velocity at $t/T = 0.66$ (Wortmann upper surface, LTWT, $Re = 125000$, $\alpha = 0^o$, $k = 0.15$) 127
7.17 Ensemble Averaged U-velocity at $t/T = 0.77$ (Wortmann upper surface, LTWT, $Re = 125000$, $\alpha = 0^o$, $k = 0.15$) 127
7.18 Ensemble averaged velocity vectors near $x/c = 0.5$ and at $t/T = 0$ in moving frame. (Wortmann upper surface, LTWT, $Re = 125000$, $\alpha = 0^o$, $k = 0.15$) 128

7.19 Ensemble averaged velocity vectors near x/c= 0.5 and at t/T = 11% in moving frame. (Wortmann upper surface, LTWT, Re = 125000, $\alpha = 0^o$, k = 0.15) 128
7.20 Ensemble averaged velocity vectors near x/c= 0.5 and at t/T = 22% in moving frame. (Wortmann upper surface, LTWT, Re = 125000, $\alpha = 0^o$, k = 0.15) 129
7.21 Ensemble averaged velocity vectors near x/c= 0.5 and at t/T = 33% in moving frame. (Wortmann upper surface, LTWT, Re = 125000, $\alpha = 0^o$, k = 0.15) 129
7.22 Ensemble averaged velocity vectors near x/c= 0.5 and at t/T = 44% in moving frame. (Wortmann upper surface, LTWT, Re = 125000, $\alpha = 0^o$, k = 0.15) 130
7.23 Ensemble averaged velocity vectors near x/c= 0.5 and at t/T = 55% in moving frame. (Wortmann upper surface, LTWT, Re = 125000, $\alpha = 0^o$, k = 0.15) 130
7.24 Ensemble averaged velocity vectors near x/c= 0.5 and at t/T = 66% in moving frame. (Wortmann upper surface, LTWT, Re = 125000, $\alpha = 0^o$, k = 0.15) 131
7.25 Ensemble averaged velocity vectors near x/c= 0.5 and at t/T = 77% in moving frame. (Wortmann upper surface, LTWT, Re = 125000, $\alpha = 0^o$, k = 0.15) 131
7.26 Ensemble averaged vorticity contour at t/T = 0 (Wortmann upper surface, LTWT, Re = 125000, $\alpha = 0^o$, k = 0.15) 132
7.27 Ensemble averaged vorticity contour at t/T = 3.5% (Wortmann upper surface, LTWT, Re = 125000, $\alpha = 0^o$, k = 0.15) 132
7.28 Ensemble averaged vorticity contour at t/T = 7% (Wortmann upper surface, LTWT, Re = 125000, $\alpha = 0^o$, k = 0.15) 133
7.29 Ensemble averaged vorticity contour at t/T = 10.5% (Wortmann upper surface, LTWT, Re = 125000, $\alpha = 0^o$, k = 0.15) 133

7.30 Ensemble averaged vorticity contour at $t/T = 14\%$ (Wortmann upper surface, LTWT, $Re = 125000$, $\alpha = 0^o$, $k = 0.15$) 134
7.31 Ensemble averaged vorticity contour at $t/T = 17.5\%$ (Wortmann upper surface, LTWT, $Re = 125000$, $\alpha = 0^o$, $k = 0.15$) 134
7.32 Ensemble averaged vorticity contour at $t/T = 22\%$ (Wortmann upper surface, LTWT, $Re = 125000$, $\alpha = 0^o$, $k = 0.15$) 135
7.33 Moore's postulated velocity profiles for unsteady separation on a fixed wall. Moore (1958) 135

C.1 Chordwise time mean U-velocity ($Re = 125000$, LTWT) 167
C.2 Chordwise amplitude of U-velocity at fundamental freq. ($Re = 125000$, LTWT) 167
C.3 Chordwise amplitude of U-velocity at 2^{nd} harmonic ($Re = 125000$, LTWT) 168
C.4 Chordwise amplitude of U-velocity at 3^{rd} harmonic ($Re = 125000$, LTWT) 168

D.1 Calculated time mean loading (0012 in LTWT, $Re = 125{,}000$) 173
D.2 Calculated time mean loading (0012 in LTWT, $Re = 400{,}000$) 173
D.3 Calculated time mean loading (0012 in WBWT, $Re = 125{,}000$) . . . 174
D.4 Calculated time mean loading (0012 in WBWT, $Re = 400{,}000$) . . . 174
D.5 Calculated time mean loading (Wort. in LTWT, $Re = 125{,}000$) . . . 175
D.6 Calculated time mean loading (Wort. in LTWT, $Re = 400{,}000$) . . . 175
D.7 Calculated time mean loading (Wort. in WBWT, $Re = 125{,}000$) . . 176
D.8 Calculated time mean loading (Wort. in WBWT, $Re = 400{,}000$) . . 176
D.9 Calculated loading amplitude at fund. frequency (LTWT, $Re = 125{,}000$) 177
D.10 Calculated loading amplitude at fund. frequency (LTWT, $Re = 400{,}000$) 177
D.11 Calculated loading amplitude at fund. frequency (WBWT, $Re = 125{,}000$) 178

D.12 Calculated loading amplitude at fund. frequency (WBWT, Re = 400,000) 178

E.1 Amplitude of C_p at fundamental frequency (Wortmann, LTWT, Re = 125000, $\alpha = 0^o$, $k = 0.15$) 181

E.2 Phase of C_p at fundamental frequency (Wortmann, LTWT, Re = 125000, $\alpha = 0^o$, $k = 0.15$) 181

E.3 Amplitude of C_p at 2^{nd} harmonic (Wortmann, LTWT, Re = 125000, $\alpha = 0^o$, $k = 0.15$) 181

E.4 Amplitude of C_p at fundamental frequency (Wortmann, LTWT, Re = 125000, $\alpha = 0^o$, $k = 0.5$) 182

E.5 Phase of C_p at fundamental frequency (Wortmann, LTWT, Re = 125000, $\alpha = 0^o$, $k = 0.5$) 182

E.6 Amplitude of C_p at 2^{nd} harmonic (Wortmann, LTWT, Re = 125000, $\alpha = 0^o$, $k = 0.5$) 182

E.7 Amplitude of C_p at fundamental frequency (Wortmann, LTWT, Re = 125000, $\alpha = 0^o$, $k = 0.75$) 183

E.8 Phase of C_p at fundamental frequency (Wortmann, LTWT, Re = 125000, $\alpha = 0^o$, $k = 0.75$) 183

E.9 Amplitude of C_p at 2^{nd} harmonic (Wortmann, LTWT, Re = 125000, $\alpha = 0^o$, $k = 0.75$) 183

E.10 Amplitude of C_p at fundamental frequency (Wortmann, LTWT, Re = 125000, $\alpha = 0^o$, $k = 1.0$) 184

E.11 Phase of C_p at fundamental frequency (Wortmann, LTWT, Re = 125000, $\alpha = 0^o$, $k = 1.0$) 184

E.12 Amplitude of C_p at 2^{nd} harmonic (Wortmann, LTWT, Re = 125000, $\alpha = 0^o$, $k = 1.0$) 184

E.13 Amplitude of C_p at fundamental frequency (Wortmann, LTWT, Re = 125000, $\alpha = 0^o$, $k = 2.0$) 185

E.14 Phase of C_p at fundamental frequency (Wortmann, LTWT, Re = 125000, $\alpha = 0^o$, $k = 2.0$) 185
E.15 Amplitude of C_p at 2^{nd} harmonic (Wortmann, LTWT, $Re = 125000$, $\alpha = 0^o$, $k = 2.0$) 185
E.16 Amplitude of C_p at fundamental frequency (Wortmann, LTWT, Re = 125000, $\alpha = 0^o$, $k = 6.4$) 186
E.17 Phase of C_p at fundamental frequency (Wortmann, LTWT, Re = 125000, $\alpha = 0^o$, $k = 6.4$) 186
E.18 Amplitude of C_p at 2^{nd} harmonic (Wortmann, LTWT, $Re = 125000$, $\alpha = 0^o$, $k = 6.4$) 186
E.19 Amplitude of C_p at fundamental frequency (Wortmann, LTWT, Re = 400000, $\alpha = 0^o$, $k = 0.15$) 187
E.20 Phase of C_p at fundamental frequency (Wortmann, LTWT, Re = 400000, $\alpha = 0^o$, $k = 0.15$) 187
E.21 Amplitude of C_p at 2^{nd} harmonic (Wortmann, LTWT, $Re = 400000$, $\alpha = 0^o$, $k = 0.15$) 187
E.22 Amplitude of C_p at fundamental frequency (Wortmann, LTWT, Re = 400000, $\alpha = 0^o$, $k = 0.5$) 188
E.23 Phase of C_p at fundamental frequency (Wortmann, LTWT, Re = 400000, $\alpha = 0^o$, $k = 0.5$) 188
E.24 Amplitude of C_p at 2^{nd} harmonic (Wortmann, LTWT, $Re = 400000$, $\alpha = 0^o$, $k = 0.5$) 188
E.25 Amplitude of C_p at fundamental frequency (Wortmann, LTWT, Re = 400000, $\alpha = 0^o$, $k = 0.75$) 189
E.26 Phase of C_p at fundamental frequency (Wortmann, LTWT, Re = 400000, $\alpha = 0^o$, $k = 0.75$) 189
E.27 Amplitude of C_p at 2^{nd} harmonic (Wortmann, LTWT, $Re = 400000$, $\alpha = 0^o$, $k = 0.75$) 189
E.28 Amplitude of C_p at fundamental frequency (Wortmann, LTWT, Re = 400000, $\alpha = 0^o$, $k = 1.0$) 190

E.29 Phase of C_p at fundamental frequency (Wortmann, LTWT, Re = 400000, $\alpha = 0^o$, $k = 1.0$) 190
E.30 Amplitude of C_p at 2^{nd} harmonic (Wortmann, LTWT, $Re = 400000$, $\alpha = 0^o$, $k = 1.0$) 190
E.31 Amplitude of C_p at fundamental frequency (Wortmann, LTWT, Re = 400000, $\alpha = 0^o$, $k = 2.0$) 191
E.32 Phase of C_p at fundamental frequency (Wortmann, LTWT, Re = 400000, $\alpha = 0^o$, $k = 2.0$) 191
E.33 Amplitude of C_p at 2^{nd} harmonic (Wortmann, LTWT, $Re = 400000$, $\alpha = 0^o$, $k = 2.0$) 191
E.34 Amplitude of C_p at fundamental frequency (Wortmann, LTWT, Re = 400000, $\alpha = 0^o$, $k = 6.4$) 192
E.35 Phase of C_p at fundamental frequency (Wortmann, LTWT, Re = 400000, $\alpha = 0^o$, $k = 6.4$) 192
E.36 Amplitude of C_p at 2^{nd} harmonic (Wortmann, LTWT, $Re = 400000$, $\alpha = 0^o$, $k = 6.4$) 192
E.37 Amplitude of C_p at fundamental frequency (0012, LTWT, Re = 125000, $\alpha = 0^o$, $k = 0.15$) 193
E.38 Phase of C_p at fundamental frequency (0012, LTWT, $Re = 125000$, $\alpha = 0^o$, $k = 0.15$) 193
E.39 Amplitude of C_p at 2^{nd} harmonic (0012, LTWT, $Re = 125000$, $\alpha = 0^o$, $k = 0.15$) 193
E.40 Amplitude of C_p at fundamental frequency (0012, LTWT, Re = 125000, $\alpha = 0^o$, $k = 0.5$) 194
E.41 Phase of C_p at fundamental frequency (0012, LTWT, $Re = 125000$, $\alpha = 0^o$, $k = 0.5$) 194
E.42 Amplitude of C_p at 2^{nd} harmonic (0012, LTWT, $Re = 125000$, $\alpha = 0^o$, $k = 0.5$) 194
E.43 Amplitude of C_p at fundamental frequency (0012, LTWT, Re = 125000, $\alpha = 0^o$, $k = 0.75$) 195

E.44 Phase of C_p at fundamental frequency (0012, LTWT, Re = 125000, $\alpha = 0^o$, $k = 0.75$) 195
E.45 Amplitude of C_p at 2^{nd} harmonic (0012, LTWT, $Re = 125000$, $\alpha = 0^o$, $k = 0.75$) 195
E.46 Amplitude of C_p at fundamental frequency (0012, LTWT, Re = 125000, $\alpha = 0^o$, $k = 1.0$) 196
E.47 Phase of C_p at fundamental frequency (0012, LTWT, Re = 125000, $\alpha = 0^o$, $k = 1.0$) 196
E.48 Amplitude of C_p at 2^{nd} harmonic (0012, LTWT, $Re = 125000$, $\alpha = 0^o$, $k = 1.0$) 196
E.49 Amplitude of C_p at fundamental frequency (0012, LTWT, Re = 125000, $\alpha = 0^o$, $k = 2.0$) 197
E.50 Phase of C_p at fundamental frequency (0012, LTWT, Re = 125000, $\alpha = 0^o$, $k = 2.0$) 197
E.51 Amplitude of C_p at 2^{nd} harmonic (0012, LTWT, $Re = 125000$, $\alpha = 0^o$, $k = 2.0$) 197
E.52 Amplitude of C_p at fundamental frequency (0012, LTWT, Re = 125000, $\alpha = 0^o$, $k = 6.4$) 198
E.53 Phase of C_p at fundamental frequency (0012, LTWT, Re = 125000, $\alpha = 0^o$, $k = 6.4$) 198
E.54 Amplitude of C_p at 2^{nd} harmonic (0012, LTWT, $Re = 125000$, $\alpha = 0^o$, $k = 6.4$) 198
E.55 Amplitude of C_p at fundamental frequency (0012, LTWT, Re = 400000, $\alpha = 0^o$, $k = 0.15$) 199
E.56 Phase of C_p at fundamental frequency (0012, LTWT, Re = 400000, $\alpha = 0^o$, $k = 0.15$) 199
E.57 Amplitude of C_p at 2^{nd} harmonic (0012, LTWT, $Re = 400000$, $\alpha = 0^o$, $k = 0.15$) 199
E.58 Amplitude of C_p at fundamental frequency (0012, LTWT, Re = 400000, $\alpha = 0^o$, $k = 0.5$) 200

E.59 Phase of C_p at fundamental frequency (0012, LTWT, $Re = 400000$, $\alpha = 0^o$, $k = 0.5$) 200
E.60 Amplitude of C_p at 2^{nd} harmonic (0012, LTWT, $Re = 400000$, $\alpha = 0^o$, $k = 0.5$) 200
E.61 Amplitude of C_p at fundamental frequency (0012, LTWT, $Re = 400000$, $\alpha = 0^o$, $k = 0.75$) 201
E.62 Phase of C_p at fundamental frequency (0012, LTWT, $Re = 400000$, $\alpha = 0^o$, $k = 0.75$) 201
E.63 Amplitude of C_p at 2^{nd} harmonic (0012, LTWT, $Re = 400000$, $\alpha = 0^o$, $k = 0.75$) 201
E.64 Amplitude of C_p at fundamental frequency (0012, LTWT, $Re = 400000$, $\alpha = 0^o$, $k = 1.0$) 202
E.65 Phase of C_p at fundamental frequency (0012, LTWT, $Re = 400000$, $\alpha = 0^o$, $k = 1.0$) 202
E.66 Amplitude of C_p at 2^{nd} harmonic (0012, LTWT, $Re = 400000$, $\alpha = 0^o$, $k = 1.0$) 202
E.67 Amplitude of C_p at fundamental frequency (0012, LTWT, $Re = 400000$, $\alpha = 0^o$, $k = 2.0$) 203
E.68 Phase of C_p at fundamental frequency (0012, LTWT, $Re = 400000$, $\alpha = 0^o$, $k = 2.0$) 203
E.69 Amplitude of C_p at 2^{nd} harmonic (0012, LTWT, $Re = 400000$, $\alpha = 0^o$, $k = 2.0$) 203
E.70 Amplitude of C_p at fundamental frequency (0012, LTWT, $Re = 400000$, $\alpha = 0^o$, $k = 6.4$) 204
E.71 Phase of C_p at fundamental frequency (0012, LTWT, $Re = 400000$, $\alpha = 0^o$, $k = 6.4$) 204
E.72 Amplitude of C_p at 2^{nd} harmonic (0012, LTWT, $Re = 400000$, $\alpha = 0^o$, $k = 6.4$) 204

Chapter 1

Introduction

1.1 Motivation

In the past decade, there has been renewed interest in improving the performance of remotely piloted vehicles (RPV), sailplanes, human powered machines, wind turbines, propellers, leading-edge devices and high altitude vehicles. This has been a period of exploring new design limits for virtually the whole spectrum of low chord Reynolds number ($10^5 < Re < 10^6$) flight applications – military, commercial, and recreational. It is evident, however, that our overall knowledge of aerodynamics for these applications is far from complete, especially phenomena associated with boundary layer behavior. This has prompted extensive experimental and computational research in all aspects of low Reynolds number flight – wind tunnel testings of airfoils, developing more efficient computational schemes, numerical and analytical modeling of the laminar separation bubble, etc. Carmichael [13] and Mueller [52] present excellent reviews on the development of low Reynolds number research.

Almost all design of low Reynolds number airfoils has been based on experimental and computational results for *steady* free-stream flow. However, real life aerodynamics is unsteady by nature. For example, helicopter and gas turbine blades operate in the wakes of the previous blades, vortices shedding off the leading edge of a delta wing induce velocities on the entire wing, and aerodynamic bodies may

flutter causing very unsteady loading and unsteady shed vortex fields downstream. Vehicle dynamics, such as phugoid or short period motions, and aerodynamics, such as wing-stabilizer interference, also contribute to flow unsteadiness. RPVs operate in the atmospheric boundary layer where the local wind fluctuations may be comparable to the vehicle speed. Predicting the stability of a vehicle operating in an unsteady environment requires incorporating the unsteady response. Hence, there is a need to include unsteadiness which an airfoil or vehicle experiences during operation into the design process.

To illustrate the range of reduced frequencies encountered in low Reynolds number flight, consider wind turbines of chords 0.25 to 0.5 meters rotating at 0.5 to 1.0 Hz. in a 10 m/s wind. The reduced frequencies, based on half chord, range from 0.04 to 0.16. The corresponding Theodorsen's function [72] at these two reduced frequencies are $C(k = 0.04) = 0.927 - i0.116$ and $C(k = 0.16) = 0.763 - i0.188$; the absolute values of the imaginary part to the real part are 0.125 and 0.246 respectively. The magnitude of the imaginary parts implies that the contribution to the lift due to the unsteady wake is not negligible [72].

1.2 Fundamentals of low Reynolds number flow

The fundamental physics of low Reynolds number ($10^5 < Re < 10^6$) aerodynamics lies with the state of the boundary layer which can be divided into three Reynolds number regimes for the sake of discussion. Above chord Reynolds number of about a million, the boundary layer usually will transition upstream of the minimum pressure location. The resultant turbulent boundary layer, with greater mixing of momentum across the layer than in a laminar boundary layer, can better negotiate the adverse pressure gradient and if the pressure gradient is not too severe, the turbulent boundary layer will stay attached until very close to the trailing edge.

When the Reynolds number is between about 70,000 and one million, a laminar

boundary layer persists past the point of minimum pressure, refer to figure 1.1. Since mixing across a laminar boundary layer is much less than that of a turbulent layer, the adverse pressure gradient separates the laminar boundary layer from the surface and a region of reverse flow follows downstream. The instability associated with this shear layer induces flow transition to a turbulent state. If the adverse pressure gradient is not too large, the boundary layer reattaches as a turbulent layer. The so-called *laminar separation bubble* extends from laminar separation to turbulent reattachment.

For Reynolds number less than about 70,000, the boundary will stay laminar past the point of minimum pressure but then the Tollmien and Schlichting waves are so weakly amplified that even with a laminar separation transition usually does not occur until flow is passed the trailing edge; global separation results downstream of the laminar separation point. The physics of boundary layer phenomena in the low Reynolds number regime is very rich and much research has been devoted to understand its behavior especially in the region of the laminar separation bubble. Covert and Drela [16] and Lissaman [38] offer excellent discussions on this subject.

The performance of an airfoil is degraded with the presence of a laminar separation bubble. Figure 1.2 sketches the range of C_l/C_d over a span of Reynolds numbers. As Reynolds number decreases near 10^5, C_l/C_d reduces drastically. In general, the increase in drag, mostly pressure drag, is much greater than the decrease in lift. For example, computational results of Drela[22] show that for a Wortmann FX63-137 at $\alpha = 2^o$, C_l= 1.117, C_d= 0.0082, hence C_l/C_d= 136.2 at Re= 10^6. At Re= 10^5, C_l= 0.858, C_d= 0.0281, hence C_l/C_d= 30.5. Surface pressure distributions show the laminar separation bubble extends about 10% chord at $Re = 10^6$ but lengthens to near 30% chord at $Re = 10^5$.

The boundary layer at low chord Reynolds numbers is sensitive to flow disturbances due to free-stream turbulence (velocity fluctuation), acoustic phenomena (pressure fluctuation), and mechanical vibrations [51]. Free-stream velocity fluctu-

ations depend, at least, on screens or flow straighteners upstream of the test section and separation of flow due to struts and turning vanes. Acoustic disturbances are associated with noise emitted from the tunnel fan drive system, turbulent boundary layers, and any phenomenon resulting in shedding of vortices. Mechanical vibrations are primarily due to rigidity of both the airfoil mounting fixture and the airfoil itself. Surface roughness and pressure tabs can also contribute to disturbance in the boundary layer. With numerous sources of flow disturbances, it is not surprising that definitive experiments at low Reynolds numbers are lacking.

1.3 Previous research at low chord Reynolds numbers

1.3.1 Steady Flow

The phenomena associated with boundary layer separation, transition, and turbulence have been a continuous research topic for the past eighty years beginning with the eight-page paper of Prandtl in 1904 setting forth the idea of a thin layer of rotational flow near the wall. In this short review, I only hope to highlight some of the major contributions related to boundary layer research in the low Reynolds number range ($Re \leq 10^6$). Mueller [52] has already presented an excellent review on the subject matter, on which much of the material here is based. For an overall review on the development of boundary layer research in the first half on the century, see Goldstein [31].

Separation bubbles were first studied by Jones [32] in 1933. He recorded that flow can separate and then reattach on thin slightly cambered airfoils. Schmitz [65] in 1940's tested model airplanes in the low Reynolds number regime. Schmitz was one of the first pioneers to use boundary layer tripping devices in achieving attached flow with a separation bubble upstream. Gault [29] conducted experiments, between 1949 and 1955, investigating the regions of separated laminar flow and categorized the types of boundary layer behavior. Owen and Klanfer [54] in 1953 studied

boundary layer bursting and attempted to develop a criterion for the phenomenon. Pfenninger [56] in 1956 tested gas turbine blades in Reynolds number range of 30,000 to 100,000 and concluded that devices which disturbed the boundary layer can shorten the laminar separation region. Moore [50] in 1960 found that the Reynolds number based on the displacement thickness was less than 500 at laminar separation for the formation of a long separation bubble, on the order of the chord. Gaster [28] also studied separation bubbles extensively and determined criteria for bursting of short bubbles to form long bubbles. In 1965, van Ingen [75] conducted theoretical and experimental studies of boundary layers focusing on the process of transition.

Topics which require further research are the process of transition in the separated shear layer and the unsteady behavior of the laminar separation bubble. (The latter topic will be discussed as an objective for the present work in Section 1.4.) Computationally, the e^n model ($8 \leq n \leq 14$ depending on free-stream turbulence level) is used to signal completion of transition from laminar to turbulent flow. The justification of this model is lacking, except that it produces a reasonable match with experimental data. The e^n model has been used successfully to predict flow transition on flat plate boundary layers; its application to flow transition within a separated shear layer is not clear. Due to lack of a better tool, Mack's [43] formula is widely accepted [22] [14] to relate the n factor to free-stream turbulence level. That is

$$n = -8.43 - 2.4\, ln\, T \tag{1.1}$$

where T is the free-stream turbulence level. Using T as a single parameter for n is certainly not completely correct since spectral content plays a role in flow transition. For example, Gedney [30] showed that some Tollmien-Schlichting waves can be attenuated with vibration of a flat plate at certain frequencies in an otherwise steady flow. Blevins [6] demonstrated experimentally that vortex shedding on a circular cylinder can be excited by external sound waves near the Strouhal frequency. So the question remains: how does the amplitude and spectral content of the free-stream

affect flow transition in the separated shear layer of a laminar separation bubble?

Until recent years, much of the efforts in low Reynolds number research had been concentrated above Reynolds numbers of 500,000. However, one of the conclusions of the *Conference on Low Reynolds Number Aerodynamics*, June 1989, was that airfoils can now be reliably designed for Reynolds number as low as 200,000. Computational efforts had been greatly advanced by the viscous/inviscid interactive code of Drela [22]. (The traditional Eppler and Somers code [24] treats separation bubble as a point; Drela solves the Orr-Sommerfeld equation to determine flow transition.)

1.3.2 Unsteady Flow

Research on externally imposed unsteady flow on a stationary airfoil or airfoil in motion in an otherwise steady free-stream at low Reynolds numbers is scarce. Some examples follow. Krause et al. [35] studied vortex shedding of two relatively thick airfoils, NACA 4409 and 4424, at Reynolds numbers between 1500 and 21000, and Strouhal numbers between 0.07 and 0.29. Unsteadiness was imposed by opening and closing a gate in the water tunnel. Flow visualization results indicate that the separated region was decreased when the flow is accelerated and increased during deceleration. Hence, the extent of the separated region is in phase with the free-stream flow.

Saxena [64] has studied an airfoil boundary layer in an oscillating free-stream experimentally for a NACA 0012 at $Re = 250000$ near the critical angle of attack. This is probably the first hot-wire survey of an unsteady boundary layer with a laminar separation bubble. Saxena shows that, in general, the global flow field behaves quasi-steadily for reduced frequency of 0.06 and angles of attack below the stall angle. Steady and unsteady pressure distributions also reveal large $r.m.s.$ fluctuations near the point where the separated shear layer reattaches as a turbulent boundary layer.

Brendel and Mueller [7] have studied unsteady boundary layers on a Wortmann

FX63-137 in periodic free-stream at Re = 105,000 and k = 0.35. They conclude that for all angles of attack tested, $-3^o \leq \alpha \leq 7^o$, the mean unsteady displacement and momentum thicknesses in the region of the separation bubble is found to be 15% to 25% lower than for the corresponding steady flow cases. Also, the overall length of the separation bubble is 5% to 10% shorter in unsteady flow. Hence, this suggests that unsteadiness may be used to improve airfoil performance.

1.4 Objectives and scope of investigation

The objectives of the present investigation are focused on answering five questions for flow at low chord Reynolds number ($Re \sim 10^5$).

1. How good is the unsteady thin airfoil theory as a design tool at these Reynolds numbers?

2. How does tunnel free-stream turbulence affect the measured unsteady lift and moment?

3. Does the flow leave the trailing edge smoothly at high reduced frequency?

4. What are the magnitude of terms in the Navier-Stokes equations near laminar separation in steady flow?

5. How does imposed unsteadiness affect the motion of a laminar separation bubble?

Question 1 addresses the design of low Reynolds number airfoils in an unsteady environment. If thin airfoil theory, *e.g.* Theodorsen (1935)[72], is indeed 'acceptable', the definition of which depends on the design and application, it offers a well understood and straight forward approach to incorporate unsteadiness in the design process. In steady flow, thin airfoil theory prediction of C_l for a Wortmann FX63-137 airfoil at $\alpha = 0^o$ and 5^o are 21% and 18%, respectively, higher than that calculated by the viscous/inviscid interactive code of Drela [22] at Re = 125000.

In this case, classical theory overpredicts C_l by about 20% in steady flow; hence the applicability of unsteady thin airfoil theory at low Reynolds number is not clear. Chapter 4 discusses inviscid limits of time mean and unsteady airfoil loading based on measurements of the upwash. Unsteady loading is calculated based on Theodorsen's unsteady airfoil theory [72]. Chapter 4 compares the classical results with experimental data.

Question 2 is raised because in steady flow free-stream turbulence has a pronounced effect on the location of transition, and hence the pressure field. Similar effects are expected in unsteady flow. This question is also important in applying the present results to the actual flight environment. To answer this question, see Chapter 4, the airfoils are tested in two turbulence levels: 0.05% (LTWT) and 0.8% (WBWT).

The applicability of the unsteady Kutta condition at high reduced frequency is investigated under Question 3. If the flow does not exit the trailing edge smoothly, loss of circulation, hence lift, will result. This question has broad applications, especially for analytical and numerical modeling of flow at high reduced frequency. The unsteady wake downstream of the NACA 0012 trailing edge is measured using a LDA system at a reduced frequency of $k = 2.0$ and $Re = 125000$. Time mean and ensemble averaged streamlines are calculated and presented in Chapter 5.

The answer to Question 4 will address the following questions. For a 2-D incompressible flow, how bad is the assumption of pressure in the potential region penetrating across the boundary layer near laminar separation? How small are the terms in the y-momentum equation compared to the corresponding terms in the x-momentum equation? How large is the $\partial^2 u/\partial x^2$ term compare to others? The answers to the questions just stated are relevant for modeling of flow with laminar separation. Its relevance depends on the model used; for a Navier-Stokes code, Question 4 can probably be ignored. But for most viscous/inviscid codes, it has implications for algorithm and computational efforts. Chapter 6 presents the results of the analyses.

With the presence of a laminar separation bubble as a dominant feature for most untripped airfoils at $Re \leq 10^6$, Question 5 focuses on the effects of unsteadiness on the forward portion of the bubble. (This problem also falls under the research topic of *unsteady boundary layer separation.*) It is not clear whether the bubble will simply oscillate at the excitation frequency, at its own frequency, or even burst during part of the cycle. If the last case occurs, drastic alteration of the flow field is expected. Chapter 7 presents results of the unsteady boundary layer near laminar separation on the upper surface of a Wortmann FX63-137 at $Re = 125000$ and $k = 0.15$ and 2.0. Data analysis shows secondary vorticity, having opposite sign to that of the unseparated boundary layer, at the intermediate frequency range ($k = 0.15$). This is not observed at high frequency ($k = 2.0$). The origin of the secondary vortices is likely from the balance of forces near the unsteady laminar separation region.

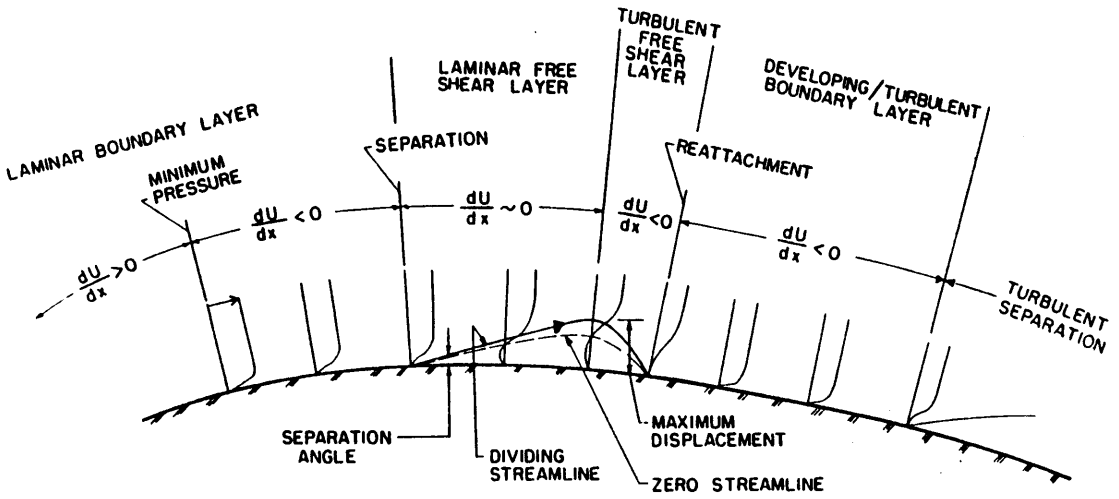


Figure 1.1: Schematic of a laminar separation bubble (Brendel [7])

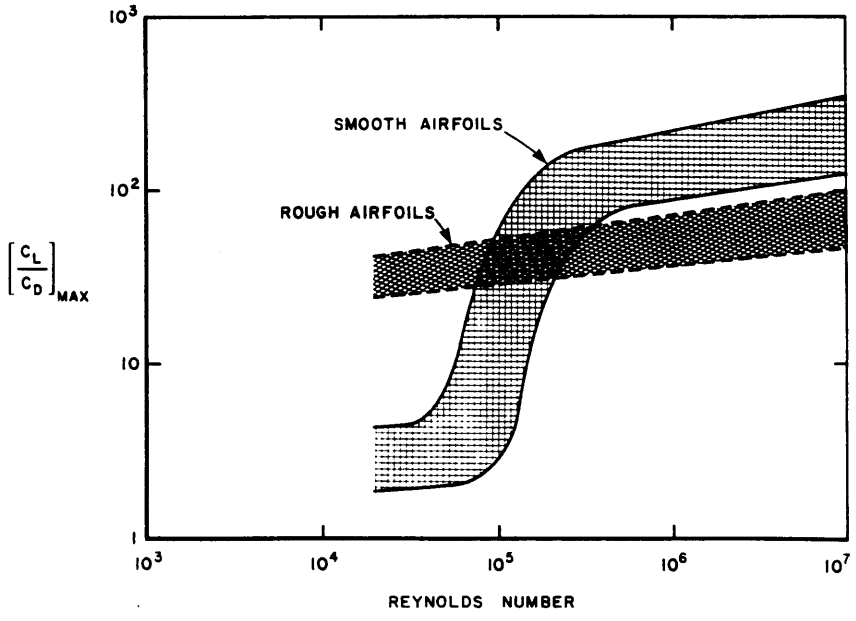


Figure 1.2: Illustration of airfoil performance over a large range of Reynolds numbers (Lissaman [38])

Chapter 2

Experimental Apparatus and Procedures

The experimental setup consist of an oscillating flow about a stationary airfoil, as illustrated in figure 2.1. An airfoil is mounted between two end-planes to encourage two-dimensionality in the external flow. The end-planes diverge downstream by a total angle of 0.4 degrees to account for pressure loss due to the boundary layers. The oscillating flow is generated by an ellipse rotating behind and below the airfoil trailing edge so that the airfoil experiences a constant phase unsteady upwash. Measurements include the upwash induced by rotating ellipse without airfoil, the airfoil surface pressure, boundary layer profiles near laminar separation, and wake profiles.

The design of the experiment is a compromise between several factors. To maximize the measured unsteady pressure amplitude, the distance between the measurement point and transducer has to be minimized. For example, pressure amplitude attenuates 50% with a 800mm long by 0.8mm diameter tubing [7]. Hence transducers, and Scannivalves, has to be placed as close to the airfoil surfaces as possible. For our experiment, they are located inside the airfoil. This increases the airfoil thickness hence the chord as well. A larger chord is beneficial for boundary layer measurement, since spatial resolution is increased. However, for a fixed Reynolds

number larger chord means proportionally smaller free-stream velocity. It is desirable to attain as high a free-stream speed as possible to decrease the uncertainty in pressure measurement; this is especially important for low Reynolds number studies. Hence a compromise is involved between higher amplitude response and lower uncertainty in the pressure data. A trade-off is also made in selecting a rotating ellipse to generate the unsteady flow. High reduced frequencies are easily attainable at the cost of higher flow harmonics due to vortex shedding in the wake of the ellipse. Hence several compromises are involved in the design of the experiment.

The following sections describe each portion of the experimental setup and testing procedures in detail. Similar descriptions are also documented in Lorber [42] and Fletcher [27].

2.1 Wind tunnels

Two wind tunnels are used throughout the course of this investigation: the M.I.T. Wright Brothers Wind Tunnel (WBWT) and the M.I.T. Low Turbulence Wind Tunnel (LTWT). Figures 2.2 and 2.3 show a sketch of the WBWT and LTWT, respectively.

The Wright Brother Wind Tunnel has a free-stream turbulence level of about 0.8% at the U_∞ range of 12 to $40 ft/s$. Figure 2.4 shows the free-stream spectral content at of 12 ft/s, corresponding to $Re = 125000$. Dominant peaks are located at the tunnel fan blade passing freqency and its harmonics.

The Low Turbulence Wind Tunnel is a modern tunnel having a maximum turbulence level of 0.05% in the free stream velocity range of 15 to 150 ft/s [44]. This level of turbulence has almost no effect on the critical Reynolds number of a sphere, as measured by Dryden et al. [23], so we assumed that results obtained in the LTWT resemble that of real flight conditions.

2.2 Airfoils

In this work, two airfoils – a Wortmann FX63-137 and a NACA 0012 – are tested, which exhibit different aerodynamic characteristics. First, the Wortmann airfoil is aft-loaded, with a maximum camber of 6% near the mid-chord, whereas the NACA 0012 is forward loaded. Secondly, the trailing edge is a cusped for the Wortmann but a blunted 5.5 degrees wedge for the NACA 0012. Thirdly, the two airfoils both demonstrate trailing edge separation behavior but different transient stalling characteristics as the critical angle of attack is approached. Below the critical angle of attack, the NACA 0012 tends to separate near the trailing edge because of its finite trailing edge angle. The position of this separation point is almost independent of the angle of attack. As the critical angle of attack is approached, about 10 to 12 degrees, the rear separation point moves rapidly forward to meet the separation bubble near the leading edge; the formation of the separation bubble is due to rapid pressure recovery in this region. However, the pressure gradient of the Wortmann airfoil is not as adverse as the 0012 at the same angle of attack, except near the trailing edge. As the angle of attack is increased, the flow separation location on the Wortmann airfoil moves gradually upstream from the trailing edge.

Both airfoils were manufactured from stock metal. The Wortmann airfoil was numerically machined from an aluminum stock with extra thickness of 0.001 inch beyond that of airfoil coordinates. Then a curvature gauge was used to find the curvature of the airfoil surface beginnng from the trailing edge towards the leading edge. The surface was finished to about 100 micro-inches. The coordinate of the Wortmann airfoil was also modified in two ways. First, the cusped trailing edge was too thin to manufacture so the last 1.1% of the airfoil was truncated. The actual chord is 19.78 inches rather than the designed 20.00 inches. Secondly, near the trailing edge of the upper surface a bump was found in the coordinates. This could not be machined accurately, so the bump was smoothed. The NACA 0012 airfoil was manufactured from a steel stock. The orginal polish was 35 micro-inches; the actual surface finish now is probably about 100 micro-inches.

2.3 The unsteady flow generator

The unsteady external flow is generated by a rotating ellipse. The axis of rotation is located at 0.200 chord downstream and 0.263 chord below the trailing edge; the separation distance is 0.330 chord. The ellipse has a major axis of 5.250 inches and minor axis of 2.375 inches. The surface of the ellipse is treated to #120 grit to encourage flow transition to turbulent boundary layer. The direction of rotation is such that induces an *upwash* over the airfoil. A two horsepower D.C. motor, with a feedback circuit, drives the ellipse through a 2:1 reduction flywheel connected by a belt. A photo cell is placed about 0.1 inch from the rotating shaft, which is covered circumferentially by black tapes except for a slit of 0.1 inch width. This allows light to be reflected from the shaft surface and to be detected by the photo cell; hence phase-locked information is obtained.

2.4 Pressure apparatus

Each airfoil is instrumented with 77 pressure taps. Figure 2.7 shows the tap locations. Two Setra model 237 (+/- 0.1 *psid*) capacitance type pressure transducers are mounted inside the airfoil to minimize the length of tubing needed hence maximizing the frequency response. The reference pressure for both transducers is the static pressure from a pitot-static probe. The probe is mounted between the end-planes, since flow in the actual test section might be different. All pressure taps on the upper surface of the airfoil are connected to the Scanivalve unit, which houses the transducer. Identical set of instrumentation is used for the pressure taps on the lower surface.

Sections of plastic tubings with different diameters are used to connect the pressure taps to the Scanivalve inside the Wortmann airfoil. This method is chosen in order to damp the resonance within the tubing. The total length of the sum of the sections are 10 and 12 inches depending on the distance of the pressure tap from the scannivalve. Each tubing consists of three sections. The 10 inch long

tubing is composed of: 4 inches of 0.05 inch I.D., 2 inches of 0.03 I.D., and 4 inches of 0.05 inch I.D. The 12 inch long tubing is composed of: 0.5 inch of 0.05 inch I.D., 1.5 inch of 0.03 inch I.D., and 10 inch of 0.05 inch I.D. The amplitude and phase response of each tube combination is calibrated by comparing the output of a transducer connected by the test tubing to a known acoustic source with the output of a transducer connected to the acoustic source directly. Figures 2.8 and 2.9 present the amplitude and phase of the tubing response, respectively.

For the NACA 0012 airfoil, a fixed length of tubing is used, that is 10 inches of 0.05 inch I.D. Inside each tube, a 0.5 inch long yarn is inserted to reduce the effect of resonance in the frequency band of interest. The advantage of this method is that only one section of tubing is needed for each pressure tape. However, the position and compactness of the yarn has to be adjusted individually to achieve the same response for all tubes. The procedure in calibrating the tubing dynamics in the NACA 0012 airfoil is identical to that of the Wortmann airfoil. The tubing amplitude and phase response are documented by Lorber [42].

2.5 Pressure data acquisition

All pressure data are acquired using a digital computer through an analog to digital interface. Figure 2.6 sketches the pressure acquisition system. Pressure data are taken by a PDP 11/23 in WBWT and a PDP 11/55 in LTWT. The A/D interface can digitize 8 channels simultaneously with 17kHz maximum sampling rate. A pulse generated by the photo cell is sensed by a Schmidt trigger on a real time clock and data acquisition is started. This method ensures all ensemble averages begin at the same point. For a complete ellipse revolution, 256 samples are taken at equal time interval. Data are acquired until the convergence criteria is reached (see next paragraph). Then the Scannivalve steps to the next pressure tap and the entire procedure is repeated.

The convergence criterion in taking unsteady pressure data is defined as follows.

Let $< p(x,t) >^{i}_{t/T=0.33}$ be the ensemble averaged pressure at $t/T=$ 0.33[1] of the i^{th} unsteady cycle. Data acquisition, on a particular pressure tap, is considered complete if the percentage difference between the current and the last ensemble average pressure at $t/T=$ 0.33 is thrice consecutively less than or equal to 0.5%, i.e.

$$\begin{aligned}
\frac{< p(x,t) >^{i+1}_{t/T=0.33} - < p(x,t) >^{i}_{t/T=0.33}}{< p(x,t) >^{i}_{t/T=0.33}} &\leq 0.005 \\
\frac{< p(x,t) >^{i+2}_{t/T=0.33} - < p(x,t) >^{i+1}_{t/T=0.33}}{< p(x,t) >^{i+1}_{t/T=0.33}} &\leq 0.005 \\
\frac{< p(x,t) >^{i+3}_{t/T=0.33} - < p(x,t) >^{i+2}_{t/T=0.33}}{< p(x,t) >^{i+2}_{t/T=0.33}} &\leq 0.005 \qquad (2.1)
\end{aligned}$$

Equation 2.1 is based on the following. The reasons for choosing the ensemble average at $t/T=$ 0.33 as a convergence criterion are twofold. First, the unsteady pressure is largest which means for an uniform variation in pressure the fractional change is smallest compared to other ensembles. Secondly, the average is calculated at only one instant in time, $t/T=$ 0.33, in an ensemble to minimize real time analysis. Thrice consecutive satisfaction of the fractional difference in ensemble averaged pressure within the convergence limit is to ensure that a converging trend, and not an isolated case, is established. The convergence value of 0.5% is chosen based on experiences; value of 0.2% requires excessive tunnel time, or may be even non-convergent, and 1% increases the uncertainty of the ensemble averaged data.

2.6 Laser Doppler anemometer system

As light is reflected from a moving object a frequency shift, or Doppler frequency, with respect to the incident light occurs. This Doppler frequency is directly proportional to the velocity of the moving object. When a particle passes through the LDA measurement point, the scattered Doppler frequency is detected by the LDA and converted to velocity.

[1]The point $t/T=$ 0.33 in a cycle corresponds to 60° angle of attack of the ellipse, which is the minimum distance between the trailing edge and the ellipse surface hence maximum unsteady excitation. Note that ellipse rotation of 180° is one complete unsteady cycle due to symmetry.

The advantages of this method are: i) it is non-intrusive and ii) the Doppler frequency measured varies linearly with velocity; hence no calibration is required. The disadvantages are: i) the velocity of a particle, not of a fluid, is actually measured and ii) it is difficult to seed some portions of the flow field, e.g. in the boundary layers. Seeding difficulties can also occur in open-circuit type wind tunnels since seeding density cannot accumulate over time.

In the present work, a two color LDA backscattering system (TSI Model 9100-7) is used. A schematic of the optics is shown in figure 2.5. The laser is a four watt Argon-Ion type (Lexel Model 95-4) which has two strong emissions at 514.5nm (green) and 488.0nm (blue). The basic optics components consist of a beam collimator, polarization rotator, beam splitter, frequency shifter, beam steerer, photomultiplier, receiving optics, beam expander, traverse mechanism, and focal lens. Two signal counters (TSI Model 1990C), one for each color, process the signal and send to an IBM AT for data acqusition. The beam width at the measurement point is calculated to be 0.2mm and the half angle of beam crossing is 5.1 degrees. The technique of frequency shifting, using a Bragg cell, allows measurement of reversed flow, e.g. within a laminar separation bubble.

Vaporized ethelene glycol is used to seed the flow field. A smoke probe apparatus with a 20 ampere current vaporizes the 50-50 ethelene glycol and water solution. The probe is located at about 3 chords upstream and 1.5 chords below the airfoil leading edge in the LTWT. In the WBWT, the probe is placed at about 3 chords upstream and 2 chords above the leading edge. The probe body diameter is about 1% chord and the ejection nozzle is 0.3% chord. The ejection rate during data taking is adjusted so that the exit velocity is roughly the same as that of the free-stream. This method of seeding is considered safe by the M.I.T. Safety Office. With the seeding and tunnel fan off, small condensed droplets on the wind tunnel wall will evaporate completely after several hours.

The overall data acquisition rate produced by vaporized ethelene glycol is sufficient for our purpose. For tunnel speed of about 3.5 m/s, only 5 minutes are needed

	Reduced Frequency					
	6.4	2.0	1.0	.75	0.5	.15
Re = 125,000	.48%	.37%	.36%	.36%	.36%	.36%
Re = 400,000	1.06%	.48%	.39%	.38%	.37%	.36%

Table 2.1: Total percentage *r.m.s.* error of LDA measured velocity

for the free-stream data rate to accumulate to 10 times the unsteady frequency. In the boundary layer, the maximum data rate for the streamwise velocity is about 5 times the unsteady frequency. This is sufficient in capturing the first few harmonics of interest. However, data rate in the transverse direction to the wall is less than the reduced frequency due to the v-velocity is very small. Hence, only streamwise velocity is measured in the boundary layer.

2.7 Uncertainty analyses

In this work, two types of data are acquired: LDA velocity data and pressure data. The major contributions to the LDA velocity uncertainties are due to i) the alignment of optics, ii) the positioning of the measurement point, and iii) the vapor particles not following unsteady flow field perfectly. Uncertainties in the pressure data consist of numerous sources and mainly due to low velocities involved at low Reynolds numbers. Details of the uncertainty analyses are presented in appendices A and B. Summary of the analyses are given below.

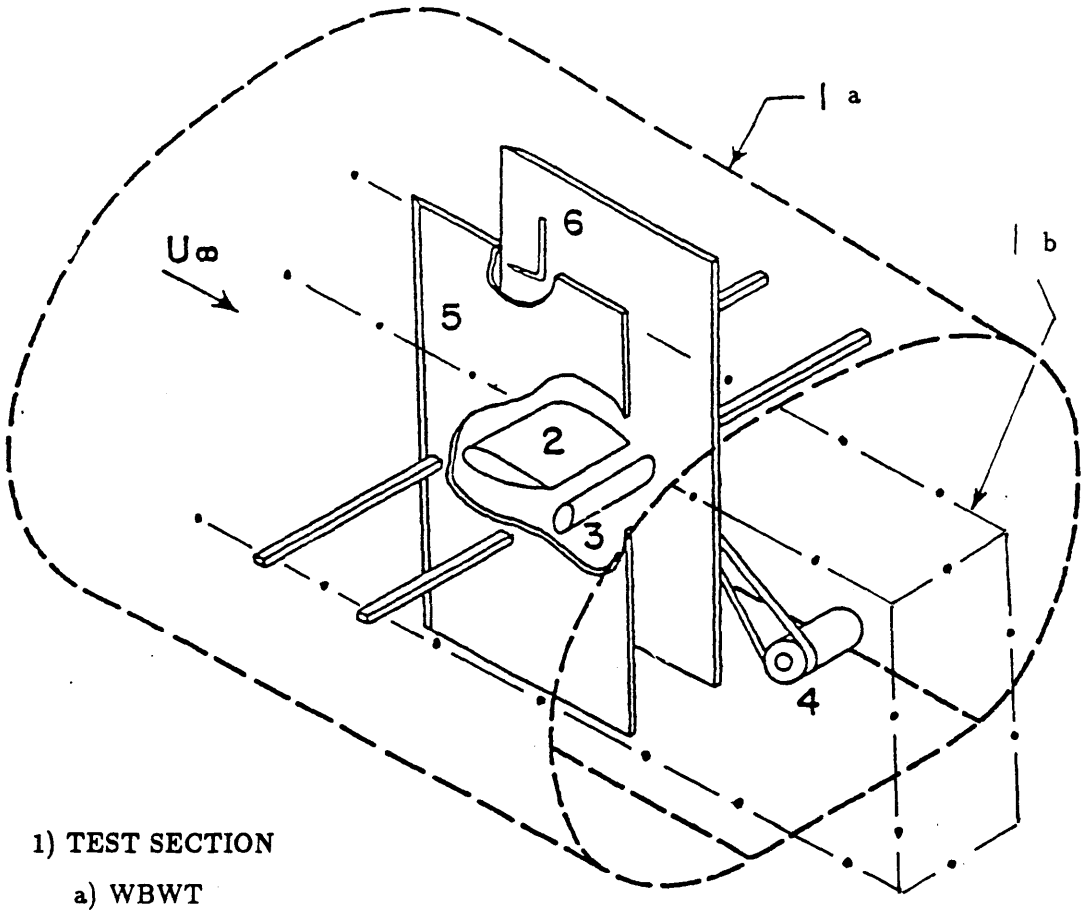
The uncertainties in LDA measurement is summarized in table (2.1). Note that the *r.m.s.* error in the LDA velocity data has a minimum of 0.36% and a maximum of about 1%. At low reduced frequencies, $k \leq 2$, the largest contribution to the *r.m.s.* error is due to positioning of the measurement point. For $k \geq 2$, the main error is due to the vapor particles not following the unsteady flow field faithfully.

The percentage uncertainties in the pressure data are shown in table (2.2). Uncertainties of about 2% in C_p for the results in 0.05% free-stream turbulence level

	LTWT	WBWT
Re = 125,000	2.3%	5.1%
Re = 400,000	1.3%	4.1%

Table 2.2: Fractional uncertainties in C_p, $\frac{W_{C_p}}{C_p}$, in both tunnels and Reynolds numbers

(LTWT) is certainly acceptable. The larger uncertainties in the WBWT is primarily due to temperature variation over a test period (the tests were conducted over the summer) causing uncertainties in the free-stream velocity, for a fixed Reynolds number, which give rise to uncertainties in the pressure data.



1) TEST SECTION
   a) WBWT
   b) LTWT
2) AIRFOIL (NACA 0012 or WORTMANN FX63-137)
3) ROTATING ELLIPTIC CYLINDER
4) DRIVE MOTOR
5) 2-D END PLANES
6) PITOT-STATIC PROBE

Figure 2.1: A sketch of the general experimental setup

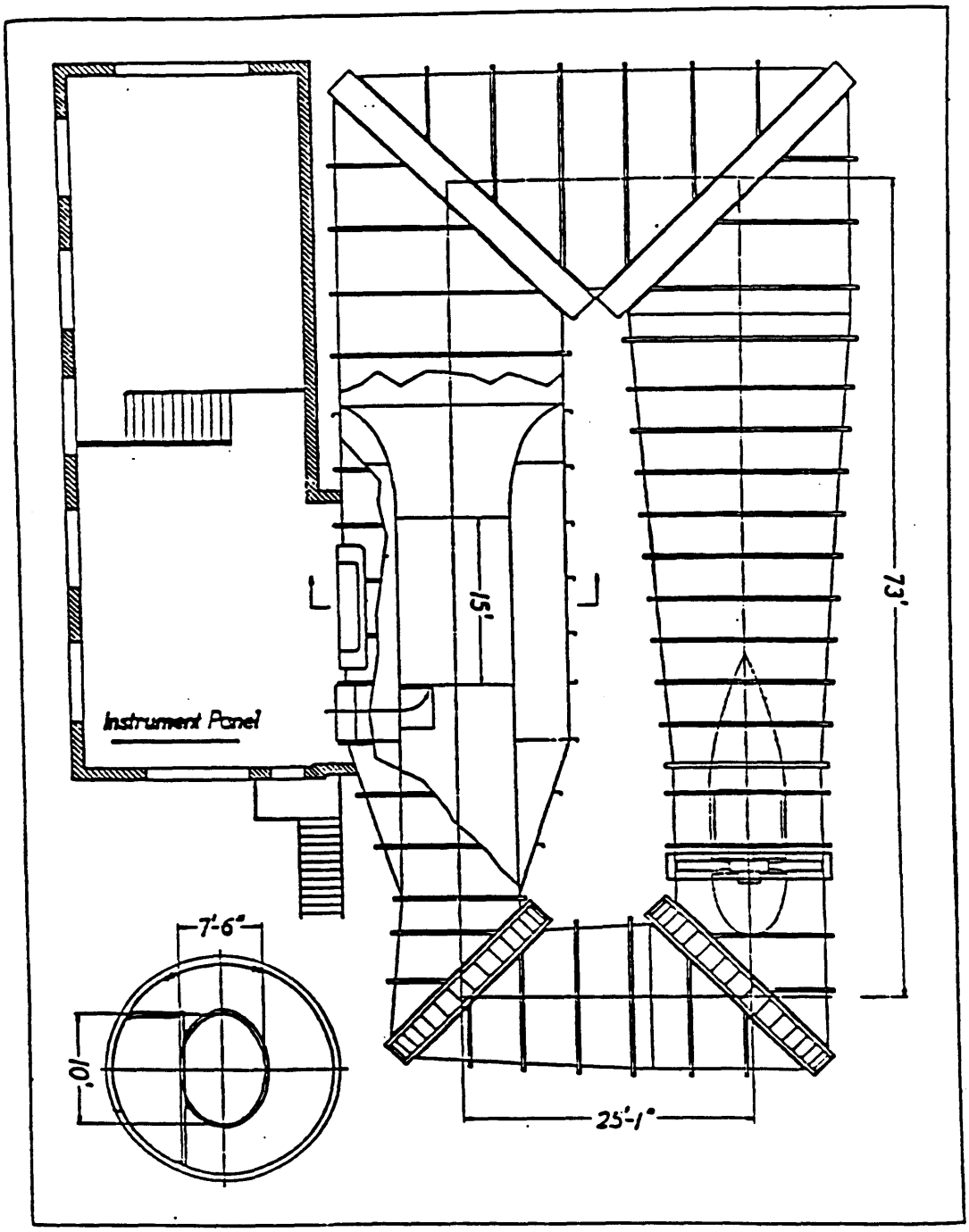


Figure 2.2: The M.I.T. Wright Brothers Wind Tunnel (WBWT), free-stream turbulence level of 0.8%

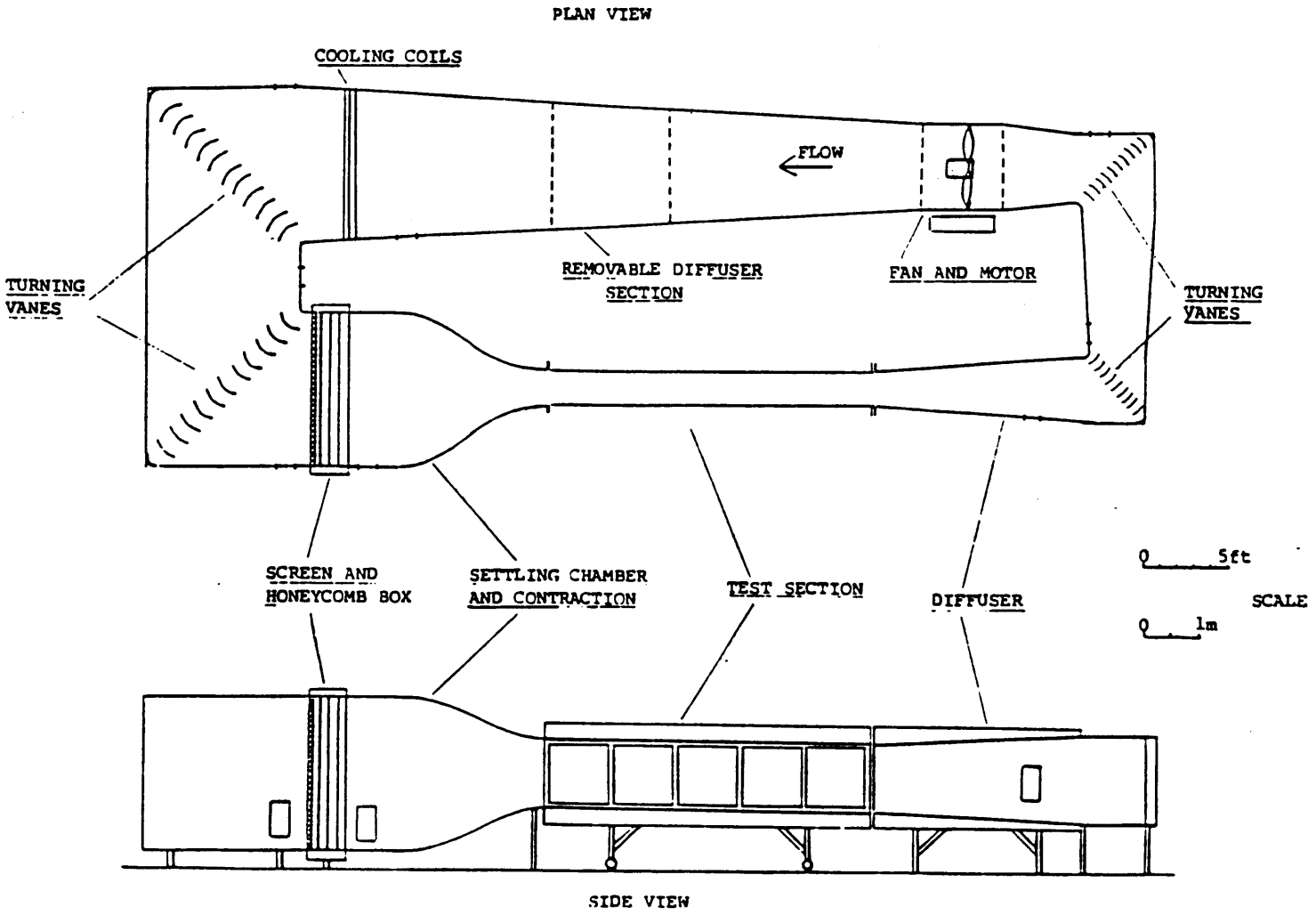


Figure 2.3: The M.I.T. Low Turbulence Wind Tunnel (LTWT), free-stream turbulence level of 0.05%

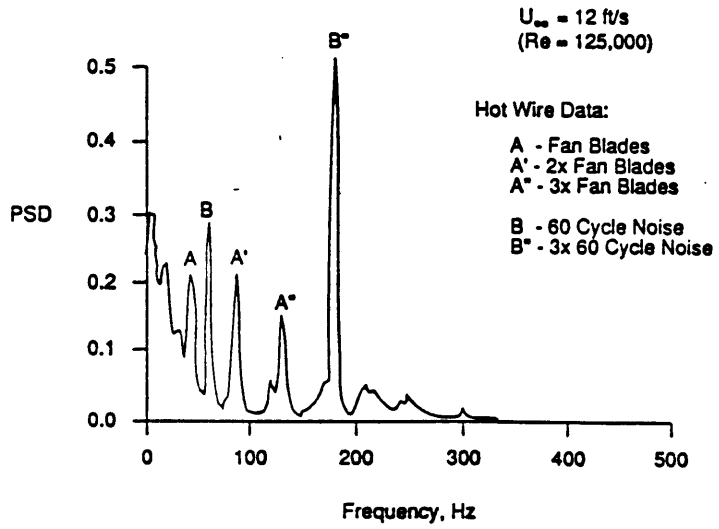


Figure 2.4: Spectrum of free-stream in WBWT at 12 ft/s

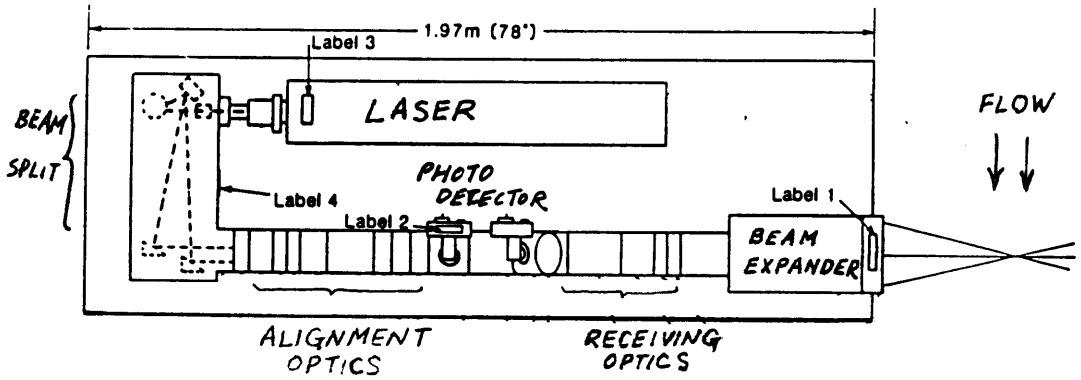


Figure 2.5: Sketch of Laser Doppler Anemometer optics layout (TSI 9100-7)

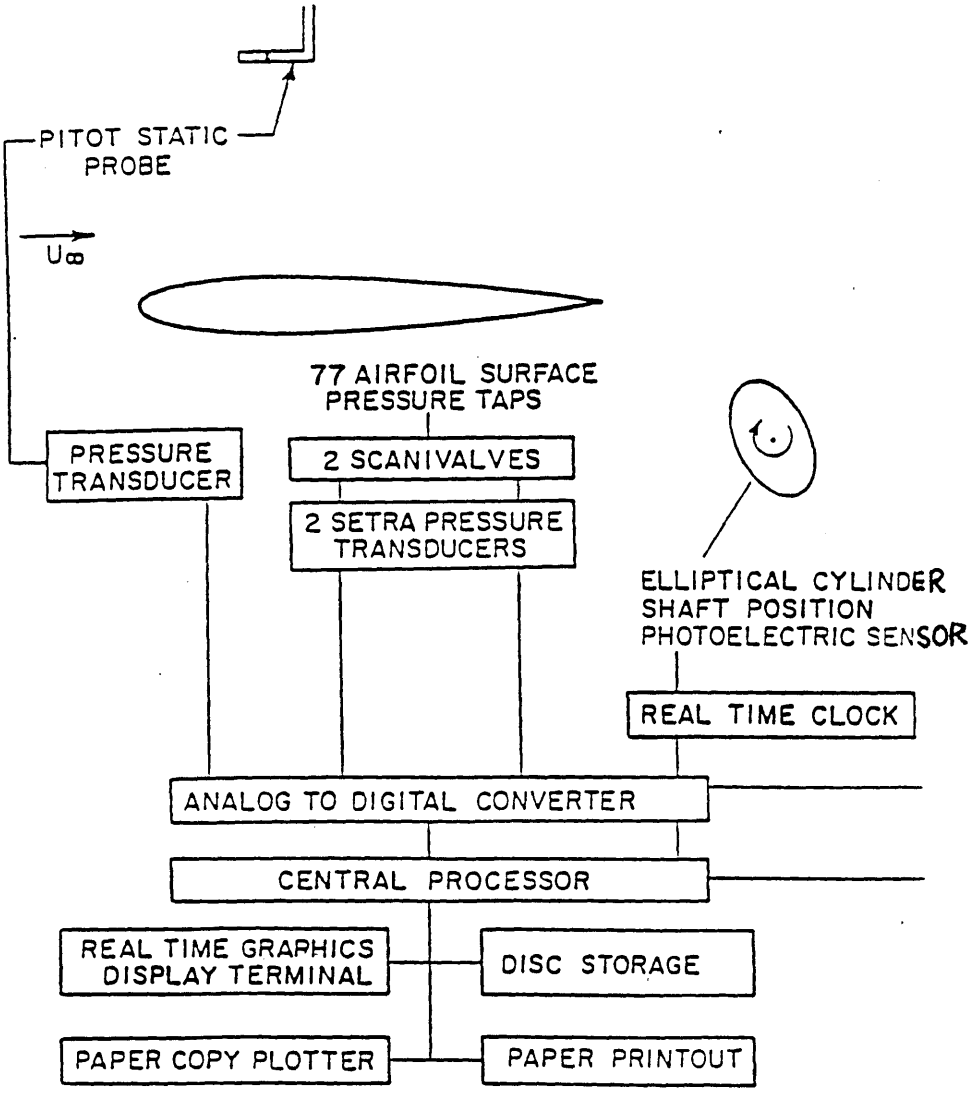
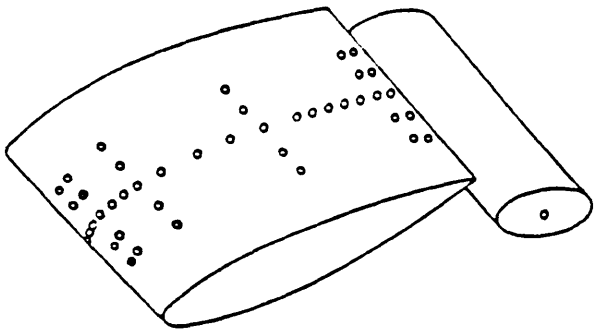


Figure 2.6: Schmetic of pressure data acquisition system



Pressure Tap Locations

X/C	Z/C				
	-.250	-.125	.00	.125	.250
.000			X		
.005			X		
.010			X		
.025	X	X	X	X	X
.050	U	U	X	U	U
.100			X		
.150			X		
.200	X	X	X	X	X
.300			X		
.400			X		
.500			X		
.600	X	X	X	X	X
.700			X		
.750			X		
.800			X		
.850			X		
.900			X		
.950	U	U	X	U	U
.980	X	X	X	X	X

X- Both surfaces U-Upper only

Figure 2.7: The pressure taps locations

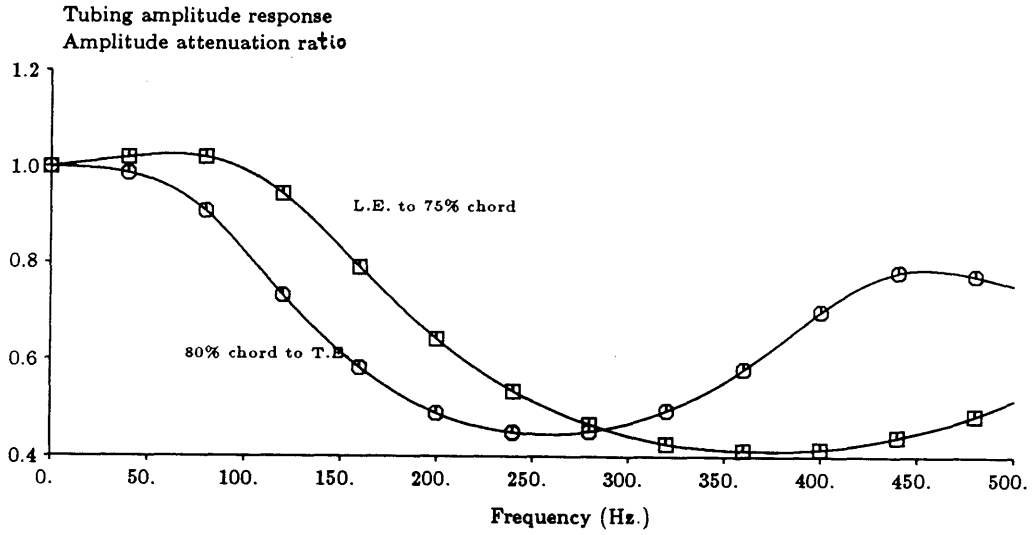


Figure 2.8: Pressure tubing amplitude response

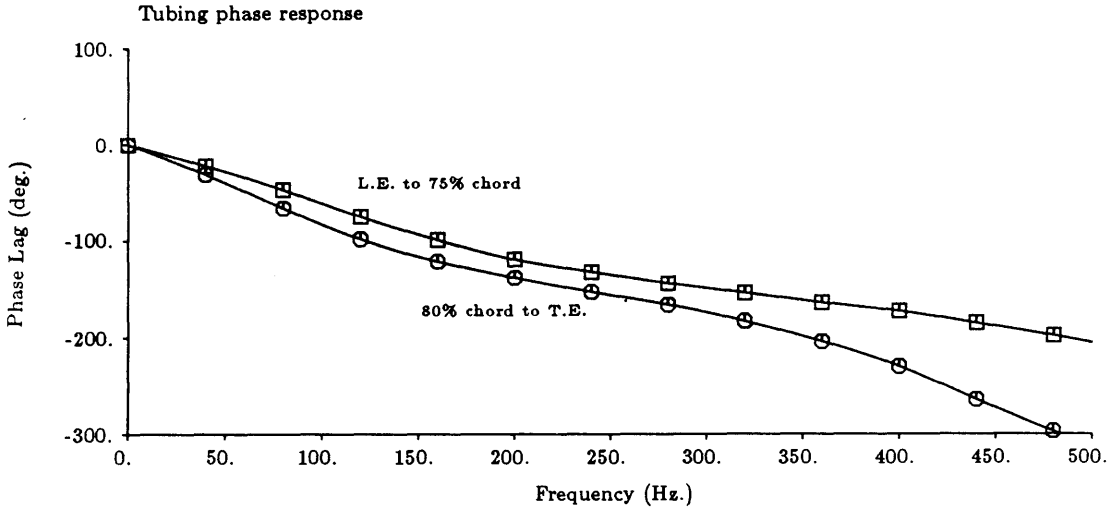


Figure 2.9: Pressure tubing phase response

Chapter 3

The Unsteady Flow Field

The unsteady flow field is generated by a rotating ellipse with its axis located behind and below the airfoil trailing edge position. The axis of rotation is located at 0.200 chord downstream and 0.263 chord below the trailing edge; the separation distance is 0.330 chord (see previous chapter for details on geometry). The direction of rotation is one that induces an *upwash* over the airfoil. Although not common, this type of unsteady excitation has several advantages. With the airfoil surface fixed, the unsteady boundary layer can be measured with conventional methods. A range of excitation frequencies can be achieved with ease by simply varying the rotation speed of the ellipse. The main disadvantage is flow interference between the airfoil and upwash which will be studied in the next chapter.

This chapter discusses the characteristics of the unsteady flow field *without the airfoil.* First, data are presented in the form of time mean upwash and amplitudes at first three harmonics, that is

$$\begin{aligned} v(x,t) = \quad & \overline{v}(x) + \tilde{v}(x)\, cos(\omega t - \varphi) + \\ & \tilde{v}_2(x)\, cos(2\omega t - \varphi_2) + \tilde{v}_3(x)\, cos(3\omega t - \varphi_3) + H.O.T. \end{aligned} \tag{3.1}$$

Standard Fast Fourier Transform algorithm is used for this purpose. The upwash is measured in both wind tunnels due to differences in blockage and possible effect of free-stream turbulence in alternating the structure of the wake behind the ellipse. Secondly, a model is used to study the time mean upwash, unsteady upwash, and

wind tunnel wall effects. Finally, the interference between the upwash flow field and the airfoil is studied based on thin airfoil theory.

3.1 Time mean upwash

Figures 3.3 and 3.4 present the measured time mean upwash in the LTWT induced by the rotating ellipse along the chordline without the airfoil mounted. The calculation shown is based on the time mean flow model (see the section on time mean flow model). The time mean upwash exhibit several characteristics. First, data show chordwise variation of upwash. This is expected since the time mean flow field can be modeled by flow around a rotating circular cylinder plus its wake. Secondly, the time mean upwash generally increases with reduced frequency. This effect is analogous to increase in circulation of the cylinder which induces proportionaly larger velocity and not due to blockage since the time mean streamwise velocity is near constant along the chord. Thirdly, the time mean upwash is a weak function of Reynolds number; the difference in upwash due to Reynolds number at X/C= 1.0 and k= 6.4, the largest upwash measured, is about 2%.

3.2 Unsteady upwash

Figures 3.5 to 3.20 present the unsteady amplitude and phase of upwash for all the combinations of parameters tested. Each page consists of a set of figures – the amplitude of vertical velocity at fundamental frequency, the corresponding phase *lag*, the amplitude of 2^{nd} harmonic, and the amplitude of 3^{rd} harmonic. The phase lag is defined in equation (3.1). Note that variation of 360 degrees in φ corresponds to 180 degrees physical rotation of ellipse due to its symmetry.

Figures 3.5, 3.9, 3.13, and 3.17 present the amplitude of upwash at fundamental excitation frequency for both turbulence levels and Reynolds numbers. Two trends are worth noting. First, for a fixed reduced frequency, the upwash amplitude increases along the chord. This trend is similar to the time mean upwash, *e.g.* figure

3.3. Secondly, the amplitude is essentially independent of reduced frequency for $k \leq 1.0$ and decreases with increasing reduced frequency for larger values of k. The independence of reduced frequency at low k is due to the flow responding to the variation in blockage as the ellipse rotates. This will be justfied by the model in the next section. At higher k, the potential flow can no longer response to the rapidly oscillating boundary layer, analogous to the boundary layer behavior of Rayleigh's unsteady flat plate problem.

The phase of the upwash, *e.g.* figure 3.6, is essentially constant along the chord. Hence, this work concerns body oscillating in its own plane – plunge or pitch; classical thin airfoil theory of Theodorsen [72] and vonKarman and Sears [77] apply.

Data show that the upwash exhibit higher harmonics, *e.g.* figures 3.7 and 3.8. The amplitude of the 2^{nd} harmonic is about a quarter of that of the fundamental frequency. This is a somewhat undesirable but inherent (see equation 3.11) feature of the excitation. The amplitude of the 3^{rd} harmonic, however, is about an order of magnitude less than that at the fundamental frequency.

3.3 A model of flow induced by rotating ellipse

Sears [67] proposed that the unsteady flow around a two-dimensional blunt body in general, can be modeled in two steps. First, a boundary layer calculation is performed over the body to determine the unsteady vorticity fluxes. This gives the time rate of change of bound circulation. Secondly, a bound and free vortex sheet model to determine the perturbed potential flow field needed for the boundary layer calculation. Hence, this procedure couples the viscous and inviscid flow and solves for the flow field in detail. For the purpose of the present work, we are interested in the flow field only in the vicinity of the airfoil location not on the ellipse itself. Hence another, much simpler, model is proposed.

The flow upstream of a rotating ellipse can be modeled using complex potentials.

The time mean flow field is modeled by a rotating cylinder , with two images to account for the wind tunnel wall effect, plus a free-stream. The unsteady upwash is modeled by a cylinder with time varying radius. The effect of the wake is not considered for simplicity. These models are used to study the time mean and unsteady upwash data.

3.3.1 Time mean upwash model

Conceptually, the time mean flow field induced by the rotating ellipse is similar to that induced by a rotating circular cylinder with a radius between the semi-minor and semi-major ellipse axes. Of course, this model flow field is only valid beyond the radius of semi-major axis. Also, one expects that the accuracy of the calculated steady flow field increases with reduced frequency. The first reason is that the flow with its inertia cannot respond instanteously to the rapid imposed fluctuation by the ellipse hence in the high limit of reduced frequency the outer flow can be considered quasi-steady. Secondly, the size of the wake behind a rotating cylinder decreases with increasing reduced frequency, see Prandtl and Tietjens [59], hence the potential flow approximation is more appropriate.

Figure 3.3.1 shows a sketch of the time mean model proposed. The exact complex potential for the model proposed is complicated since there are infinite images involved. Only first order approximation of images is taken into account. The complex potential associated with the circular cylinder t is

$$\overline{W}_t(z) = \overline{W}_{t,t}(z) + \overline{W}_{t,e}(z) + \overline{W}_{t,b}(z) \tag{3.2}$$

where the notation $\overline{W}_{t,e}(z)$ denotes contribution to the complex potential of cylinder t from images due to cylinder e. Hence, the above equation says the total complex potential of cylinder t is the sum of the complex potential of itself plus images due to cylinders e and b. Explicitly,

$$\begin{aligned} \overline{W}_{t,t}(z) &= \frac{U_\infty \overline{a}^2}{z - z_t} + \frac{i\Gamma}{2\pi} ln(z - z_t) \\ \overline{W}_{t,e}(z) &= -\frac{U_\infty \overline{a}^2}{z - z_t} + \frac{U_\infty \overline{a}^2}{z - (z_t - \frac{\overline{a}^2}{z_t^* - z_e^*})} + \frac{i\Gamma}{2\pi} ln(z - z_t) \end{aligned} \tag{3.3}$$

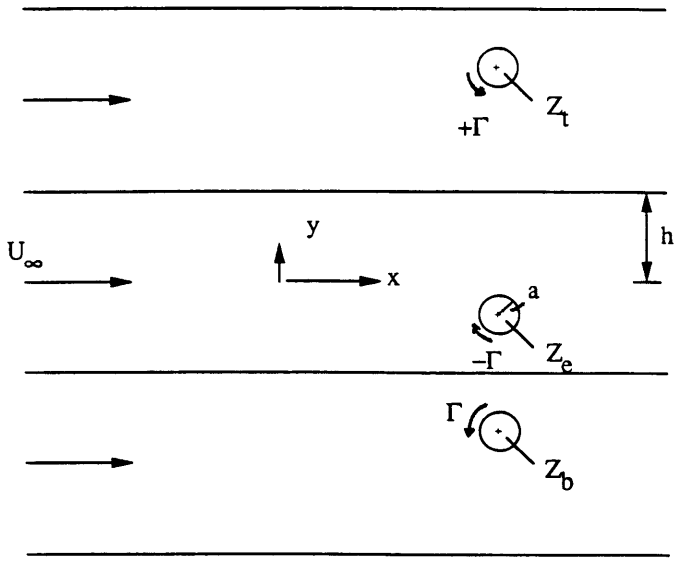


Figure 3.1: Sketch of time mean upwash model

$$-\frac{i\Gamma}{2\pi}ln\left[z-(z_t-\frac{\overline{a}^2}{z_t^*-z_e^*})\right] \tag{3.4}$$

$$\overline{W}_{t,b}(z) = -\frac{U_\infty\overline{a}^2}{z-z_t}+\frac{U_\infty\overline{a}^2}{z-(z_t-\frac{\overline{a}^2}{z_t^*-z_b^*})}-\frac{i\Gamma}{2\pi}ln(z-z_t)$$

$$+\frac{i\Gamma}{2\pi}ln\left[z-(z_t-\frac{\overline{a}^2}{z_t^*-z_e^*})\right] \tag{3.5}$$

where * denotes complex conjugate and $\overline{a}$ is the mean of the semi-minor and semi-major ellipse axes times a multiplicative constant $\overline{C}_a$ (see equation 3.9 and tables 3.1 and 3.2) to account for the upwash induced at lower reduced frequencies. The circulation is defined as

$$\frac{\Gamma}{U_\infty c}=2\pi k\left(\frac{\overline{a}}{c}\right)^2 \tag{3.6}$$

$\overline{W}_{t,t}(z)$ simply defines a dipole with strength $U_\infty\overline{a}^2$ and bound circulation. Dipole images in cylinder t from cylinder e, first two terms in $\overline{W}_{t,e}(z)$, are due to i)equal and opposite strength at z_t and ii)equal strength at inverse point $z_t-\frac{\overline{a}^2}{z_t^*-z_e^*}$. Circulation images, last two terms in $\overline{W}_{t,e}(z)$, are due to i)equal strength at z_t and ii)equal and

opposite strength at $z_t - \frac{\overline{a}^2}{z_t^* - z_e^*}$. The interpretation for $\overline{W}_{t,b}(z)$ is similar to $\overline{W}_{t,e}(z)$ except for the sign of circulation. Analogus expressions can be written for $\overline{W}_e(z)$ and $\overline{W}_b(z)$.

After some simplifications, the first order approximation for the complex potential of the entire flow field is

$$\overline{W}(z) = U_\infty z + \overline{W}_t(z) + \overline{W}_e(z) + \overline{W}_b(z) \tag{3.7}$$

$$\begin{aligned}
\overline{W}(z) = U_\infty \{ z &- \frac{\overline{a}^2}{z - z_t} - \frac{\overline{a}^2}{z - z_e} - \frac{\overline{a}^2}{z - z_b} \\
&+ \frac{\overline{a}^2}{z - (z_t - \frac{\overline{a}^2}{z_t^* - z_e^*})} + \frac{\overline{a}^2}{z - (z_t - \frac{\overline{a}^2}{z_t^* - z_b^*})} \\
&+ \frac{\overline{a}^2}{z - (z_e - \frac{\overline{a}^2}{z_e^* - z_t^*})} + \frac{\overline{a}^2}{z - (z_e - \frac{\overline{a}^2}{z_e^* - z_b^*})} \\
&+ \frac{\overline{a}^2}{z - (z_b - \frac{\overline{a}^2}{z_b^* - z_t^*})} + \frac{\overline{a}^2}{z - (z_b - \frac{\overline{a}^2}{z_b^* - z_e^*})} \\
&- \frac{i\Gamma}{2\pi} ln(z - z_t) - \frac{i\Gamma}{2\pi} ln(z - z_e) - \frac{i\Gamma}{2\pi} ln(z - z_b) \\
&- \frac{i\Gamma}{2\pi} ln[z - (z_t - \frac{\overline{a}^2}{z_t^* - z_e^*})] + \frac{i\Gamma}{2\pi} ln[z - (z_t - \frac{\overline{a}^2}{z_t^* - z_b^*})] \\
&+ \frac{i\Gamma}{2\pi} ln[z - (z_e - \frac{\overline{a}^2}{z_e^* - z_t^*})] + \frac{i\Gamma}{2\pi} ln[z - (z_e - \frac{\overline{a}^2}{z_e^* - z_b^*})] \\
&+ \frac{i\Gamma}{2\pi} ln[z - (z_b - \frac{\overline{a}^2}{z_b^* - z_t^*})] - \frac{i\Gamma}{2\pi} ln[z - (z_b - \frac{\overline{a}^2}{z_b^* - z_e^*})] \}
\end{aligned} \tag{3.8}$$

With this formulation, computation of the time mean flow field is straight forward. All length variables are nomalized by the chord and velocities by the free-stream. A multiplicative constant, $\overline{C}_a$, for the radius of the cylinder is introduced since, as described, the time mean model most accurately approximately the data at high reduced frequency. Explicitly,

$$\overline{a} = \overline{C}_a \frac{a_{semi-minor} + a_{semi-major}}{2} \tag{3.9}$$

where $a_{semi-minor} = 0.0625$ and $a_{semi-major} = 0.138$. The values for $\overline{C}_a$ is found using least square fit with data. Tables 3.1 and 3.2 give the values for $\overline{C}_a$ needed

Reduced Frequency

	6.4	2.0	1.0	.75	0.5	.15
Re = 125,000	1.00	1.21	1.25	1.30	1.31	1.33
Re = 400,000	0.97	1.18	1.21	1.25	1.27	1.29

Table 3.1: $\overline{C}_a$ as function of Reynolds number and reduced frequency (LTWT)

Reduced Frequency

	6.4	2.0	1.0	.75	0.5	.15
Re = 125,000	1.04	1.31	1.43	1.45	1.50	-
Re = 400,000	1.05	1.29	1.38	1.39	1.45	1.51

Table 3.2: $\overline{C}_a$ as function of Reynolds number and reduced frequency (WBWT)

to curve fit the data in the two tunnels, also see figures 3.3 and 3.4. Note that the values for $\overline{C}_a$ is closest to unity at $k = 6.4$. This is indicative that the rotating cycle is indeed behaving like a circular cylinder at high reduced frequencies.

3.3.2 Wind tunnel wall effect

Since the upwash data are obtained in two wind tunnels with different test section geometries, blockage related effect on the upwash is expected. The geometric blockage due to the present of the ellipse is 8.3% in LTWT and 4.4% in WBWT. The proposed model is used to study the magnitude of this effect by varying the distances between cylinders.

In steady flow, figure 3.21 shows little variation for all three curves – with LTWT section, WBWT section, and top and bottom walls being very far away. At the trailing edge position, the maximum velocity variation is only 0.8%. However, differences in upwash increase as circulation increases as shown by comparing figure 3.21 with figure 3.22. At $k = 6.4$, figure 3.22 shows velocity variation between

LTWT and WBWT of 36% at the leading edge position and 2% at the trailing edge. This chordwise variation is largest at the leading edge position since at this point upwash contribution from the rotating cylinder is smallest and contributions from the images, both with opposite sign of bound circulation, are not negligible. This brief study illustrates that the differences in blockage due to the ellipse do not affect the time mean upwash significantly. However, circulation of the ellipse is coupled to the differences in blockage and result in differences in time mean upwash.

3.3.3 Unsteady upwash model

The unsteady upwash induced by the rotating ellipse is modeled by a circular cylinder of periodically varying radius. In this model, the unsteadiness arises from a dipole which accounts for the time dependent radius and a monopole which satisfies the boundary condition on the pulsating cylinder surface. The complex potential for the time mean and the unsteady flow with the cylinder centered at z_e is

$$W(z) = U_\infty(z + \frac{a^2}{z - z_e}) + \frac{i\Gamma}{2\pi} ln(z - z_e) + a\frac{da}{dt} ln(z - z_e) \quad (3.10)$$

$$= \overline{W} + \tilde{W}_0 + \tilde{W}_1 + \tilde{W}_2 \quad (3.11)$$

Explicitly, the dipole term is $U_\infty \frac{a^2}{z - z_e}$ and the monopole term is $a\frac{da}{dt} ln(z - z_e)$.

Let the radius of the cylinder be

$$a(t) = \overline{a} + \tilde{a}\, cos\, \omega t \quad (3.12)$$

where $\overline{a}$ and $\tilde{a}$ are the time mean and the unsteady amplitude of the cylinder radius, respectively. Substituting equation (3.12) into (3.10) and equating the result with (3.11) gives

$$\overline{W} = U_\infty(z + \frac{\overline{a}^2}{z - z_e}) + \frac{i\Gamma}{2\pi} \quad (3.13)$$

$$\tilde{W}_0 = \frac{U_\infty}{2} \frac{\tilde{a}^2}{z - z_e} \quad (3.14)$$

$$\tilde{W}_1 = 2U_\infty \frac{\overline{a}\tilde{a}}{z - z_e} cos\, \omega t - \tilde{a}\overline{a}\, \omega\, ln(z - z_e)\, sin\, \omega t \quad (3.15)$$

$$\tilde{W}_2 = \frac{U_\infty}{2} \frac{\tilde{a}^2}{z - z_e} cos\, 2\omega t - \frac{\tilde{a}^2}{2}\, \omega\, ln(z - z_e)\, sin\, 2\omega t \quad (3.16)$$

where $\overline{W}$ and $\tilde{W}$ are the time mean complex potential, $\tilde{W}_1$ is the first harmonic, and $\tilde{W}_2$ is the second harmonic. For both $\tilde{W}_1$ and $\tilde{W}_2$, the first term represents the unsteadiness due to the pulsating dipole and the second term due to the monopole. The dipole term is important at quasi-steady frequencies and the monopole term dominates at high frequencies. Note that the present of the second harmonic is a natural consequence of the flow due to a pulsating cylinder. This model ignores the source effect of the unsteady wake and the contributions from the top and bottom images.

A correction factor, $\tilde{C}_a$, is used to account for idealizations in the model. That is

$$\tilde{a} = \tilde{C}_a(a_{semi-major} - a_{semi-minor})/2 \tag{3.17}$$

where $a_{semi-major}$ and $a_{semi-minor}$ are the semi-major and the semi-minor axes of the ellipse, respectively. The values for $\tilde{C}_a$ are found from curve fitting the results of the model to the unsteady upwash data. Value of unity in $\tilde{C}_a$ means the calculated amplitude of upwash from the model matches that due to the geometric variation of radius as the ellipse rotates. Tables 3.3 and 3.4 give the values for $\tilde{C}_a$ in 0.05%(LTWT) and 0.8%(WBWT) free-stream turbulence levels, respectively. The values for $\tilde{C}_a$ is closer to unity near $k = 1.0$ and much less at high reduced frequencies. The latter fact suggests that the flow around the rotating ellipse is not responding to the rapidly fluctuating boundary conditions, analogous to Stoke's problem of oscillating plate.

Reduced Frequency

	6.4	2.0	1.0	.75	0.5	.15
$Re = 125{,}000$	0.23	0.63	0.95	0.92	0.89	0.84
$Re = 400{,}000$	.093	0.57	0.97	0.97	0.95	0.89

Table 3.3: $\tilde{C}_a$ as function of Reynolds number and reduced frequency (LTWT)

Figures 3.5, 3.9, 3.13, and 3.17 present the comparison the results from the model with the amplitude of upwash data at the fundamental frequency. Data suggest that the amplitude decay is not as fast as computed. The model can probably be improved by including the unsteady contributions from the top and bottom images; results from the time mean upwash model (last section) show that the presence of the images can alter the distribution of upwash (refer to figures 3.21 and 3.22).

3.4 Time mean airfoil/upwash interference effect

With the airfoil mounted some airfoil/upwash interference effects are expected since no flow can penetrate through the airfoil. This interference effect will then modify the undisturbed upwash.

Let the first order approximation of the upwash induced by the ellipse be represented by the rotating cylinder with its two associated images (see last chapter for detail) and the airfoil by either a flat plate for the NACA 0012 or a cambered plate for the Wortmann airfoil. A sketch is shown in figure 3.2.

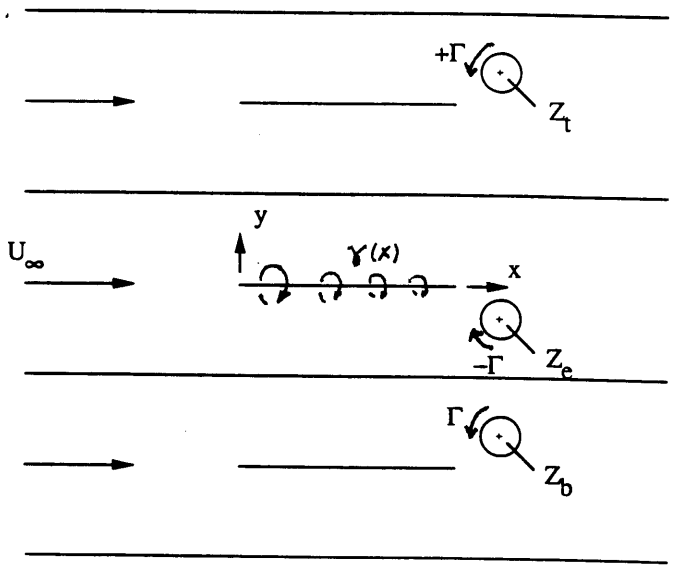


Figure 3.2: Model for calculating the time mean interference effect

The undisturbed upwash acting on the airfoil sets up a chordwise distribution of bound vortices to cancel the upwash, causing the airfoil to be a streamline. This

distribution of vorticity interfere with the flow of the cylinder and result in images inside the cylinder modifying the undisturbed upwash. This modified upwash then acts on the airfoil to alter the vorticity distribution which feeds back to change the strength of the images. The final upwash distribution is established when the strength of the images reaches a steady state.

Equation (3.8) gives the complex potential of the unpertubated upwash, without the airfoil present. This complex potential sets up an upwash $v(x) = -Im[W(z)]$ on the airfoil resulted in bound vortices with strengths given by

$$v(x) = \frac{1}{2\pi}\int_{-1}^{1}\frac{\gamma(\xi)}{\xi - x}d\xi \tag{3.18}$$

Söhngen in [5] proves that for any two functions f and g that the unique solution to the integral equation

$$g(x) = \frac{1}{2\pi}\int_{-1}^{1}\frac{f(\xi)}{x - \xi}d\xi$$

for which $f(1)$ is finite or zero, is

$$f(x) = -\frac{2}{\pi}\sqrt{\frac{1-x}{1+x}}\int_{-1}^{1}\sqrt{\frac{1+\xi}{1-\xi}}\frac{g(\xi)}{x-\xi}d\xi$$

Note that f can be identified with γ and g with $-v$, hence using Söhngen's equation,

$$\gamma(x) = \frac{2}{\pi}\sqrt{\frac{1-x}{1+x}}\int_{-1}^{1}\sqrt{\frac{1+\xi}{1-\xi}}\frac{v(\xi)}{x-\xi}d\xi \tag{3.19}$$

For an infinitesimal section of chord with length 2ϵ and vorticity strenth $\gamma_n(x)$, can be considered constant over 2ϵ, the associated circulation is

$$\Gamma_n(x) = \int_{x-\epsilon}^{x+\epsilon}\gamma_n(\xi)d\xi \tag{3.20}$$

If Γ_n is located at z_n, the images inside the cylinder consist of two vortices: one with strength Γ_n at z_e and another with strength -Γ_n at $z_e - \frac{a^2}{z_e^* - z_n^*}$, where $*$ denotes complex conjugate. Hence the airfoil bound vortices resulted in images inside the cylinder at z_e and an arc of counter vortices at the inverse points. With the airfoil

divided into N infinitesimal segments, the modified complex potential of the rotating cylinder with all the images is

$$\begin{aligned}
\overline{W}(z) = U_\infty\{z &- \frac{\overline{a}^2}{z-z_t} - \frac{\overline{a}^2}{z-z_e} - \frac{\overline{a}^2}{z-z_b} \\
&+ \frac{\overline{a}^2}{z-(z_t - \frac{\overline{a}^2}{z_t^*-z_e^*})} + \frac{\overline{a}^2}{z-(z_t - \frac{\overline{a}^2}{z_t^*-z_b^*})} \\
&+ \frac{\overline{a}^2}{z-(z_e - \frac{\overline{a}^2}{z_e^*-z_t^*})} + \frac{\overline{a}^2}{z-(z_e - \frac{\overline{a}^2}{z_e^*-z_b^*})} \\
&+ \frac{\overline{a}^2}{z-(z_b - \frac{\overline{a}^2}{z_b^*-z_t^*})} + \frac{\overline{a}^2}{z-(z_b - \frac{\overline{a}^2}{z_b^*-z_e^*})} \\
&- \frac{i\Gamma}{2\pi} ln(z-z_t) - \frac{i\Gamma}{2\pi} ln(z-z_e) - \frac{i\Gamma}{2\pi} ln(z-z_b) \\
&- \frac{i\Gamma}{2\pi} ln[z-(z_t - \frac{\overline{a}^2}{z_t^*-z_e^*})] + \frac{i\Gamma}{2\pi} ln[z-(z_t - \frac{\overline{a}^2}{z_t^*-z_b^*})] \\
&+ \frac{i\Gamma}{2\pi} ln[z-(z_e - \frac{\overline{a}^2}{z_e^*-z_t^*})] + \frac{i\Gamma}{2\pi} ln[z-(z_e - \frac{\overline{a}^2}{z_e^*-z_b^*})] \\
&+ \frac{i\Gamma}{2\pi} ln[z-(z_b - \frac{\overline{a}^2}{z_b^*-z_t^*})] - \frac{i\Gamma}{2\pi} ln[z-(z_b - \frac{\overline{a}^2}{z_b^*-z_e^*})] \\
&+ \frac{i}{2\pi} ln(z-z_t) \sum_{n=1}^{N} \Gamma_n - \frac{i}{2\pi} \sum_{n=1}^{N} \Gamma_n ln[z-(z_t - \frac{\overline{a}^2}{z_t^*-z_n^*})] \\
&+ \frac{i}{2\pi} ln(z-z_e) \sum_{n=1}^{N} \Gamma_n - \frac{i}{2\pi} \sum_{n=1}^{N} \Gamma_n ln[z-(z_e - \frac{\overline{a}^2}{z_e^*-z_n^*})] \\
&+ \frac{i}{2\pi} ln(z-z_b) \sum_{n=1}^{N} \Gamma_n - \frac{i}{2\pi} \sum_{n=1}^{N} \Gamma_n ln[z-(z_b - \frac{\overline{a}^2}{z_b^*-z_n^*})]\} \quad (3.21)
\end{aligned}$$

Note that the contributions to the interference effects come from the last six summation terms.

The associated upwash of this complex potential results in $\gamma(x)$ is given by (3.19) and hence the bound circulation is given by (3.20) which modifies (3.21). Therefore the actual upwash that the airfoil sees is found by iteration. The following two subsections presents results of this calculation for NACA 0012 and Wortmann airfoils.

Some comments concerning this approach are in order. Ideas based on thin airfoil theory are used to study the interference effect, rather than panel method say, simply due to convenience. With the complex potential of upwash from the model

(equation 3.8) little extra effort is need to account for the airfoil bound vortices and its images (equation 3.21). Although the interference of airfoil thickness with the upwash is ignored, the velocity due to a dipole decays like $1/r^2$ which is faster than that of a bound vortex. Since I am only interested in the first order interference approximation, this approach is deemed sufficient.

3.4.1 NACA 0012/ellipse interference

Using the iteration process outlined in the previous section, the time mean airfoil/upwash interference effect is calculated on a flat plate, representing a NACA 0012, at zero angle of attack in LTWT and $k = 6.4$. The largest frequency tested is used as a test case since the interference effect is expected to increase with upwash.

Figure 3.23 shows the results for time mean upwash based on measurement, without interference, at Re = 125,000 and 400,000 and results with interference effect. The upwash with interference effect is slightly less than that of the undisturbed upwash since the images at the inverse points, closer to the airfoil than images at the center of cylinder, induce a downwash on the airfoil. The maximum difference between the undisturbed upwash (model) and the final upwash (w/ interference) is located at 80% chord. These differences in upwash are 1.9% for Re = 125,000 and 1.8% for Re = 400,000.

Figure 3.24 and figure 3.25 show the resultant bound vortices on the flat plate. Vorticity distribution on a flat plate in steady flow with equivalent lift coefficient is used for comparison. The bound vortices associated with undisturbed upwash are almost identical with that including the interference effect. For Re = 125000 data, the difference in $\overline{C_l}$ between the two is only is 0.1%, and it is 0.05% for Re = 400000. Hence the interference effect for the NACA 0012 is indeed negligible.

3.4.2 Wortmann FX63-137/ellipse interference

The same interference analysis is performed on the Wortmann airfoil using the camber in place of the flat plate for 0012. Figure 3.26 presents the undisturbed and interferred upwash for both Reynolds numbers. The interferred upwash is generally less than that of the pure upwash, the same trend as that of the 0012. However, the maximum difference between the pure and interferred upwash is larger than that of 0012 - 4.4% for Re = 125,000 and 4.2% for Re = 400,000. This is because the Wortmann is an aft-loaded airfoil and bound vortices of greater strength are present near the trailing edge hence images vortices of equal and opposite strength are induced inside the cylinder.

Figures 3.27 and 3.28 show the bound vorticity distributions for the two Reynolds numbers. The calculated difference in $\overline{C}_l$ is 6.1% for Re = 125,000 and 6.4% for Re = 400,000, which are much larger than that for the 0012.

Reduced Frequency

	6.4	2.0	1.0	.75	0.5	.15
$Re = 125{,}000$	0.28	0.57	0.89	0.84	0.76	-
$Re = 400{,}000$	0.17	0.47	0.92	0.87	0.84	0.65

Table 3.4: $\tilde{C}_a$ as function of Reynolds number and reduced frequency (WBWT)

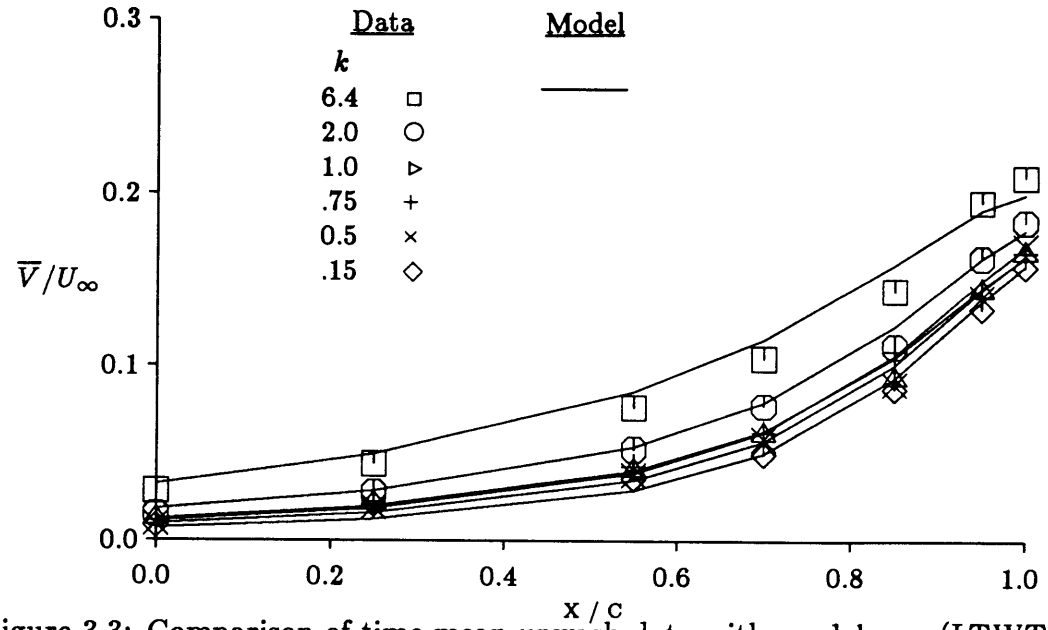


Figure 3.3: Comparison of time mean upwash data with model (LTWT, Re = 125,000)

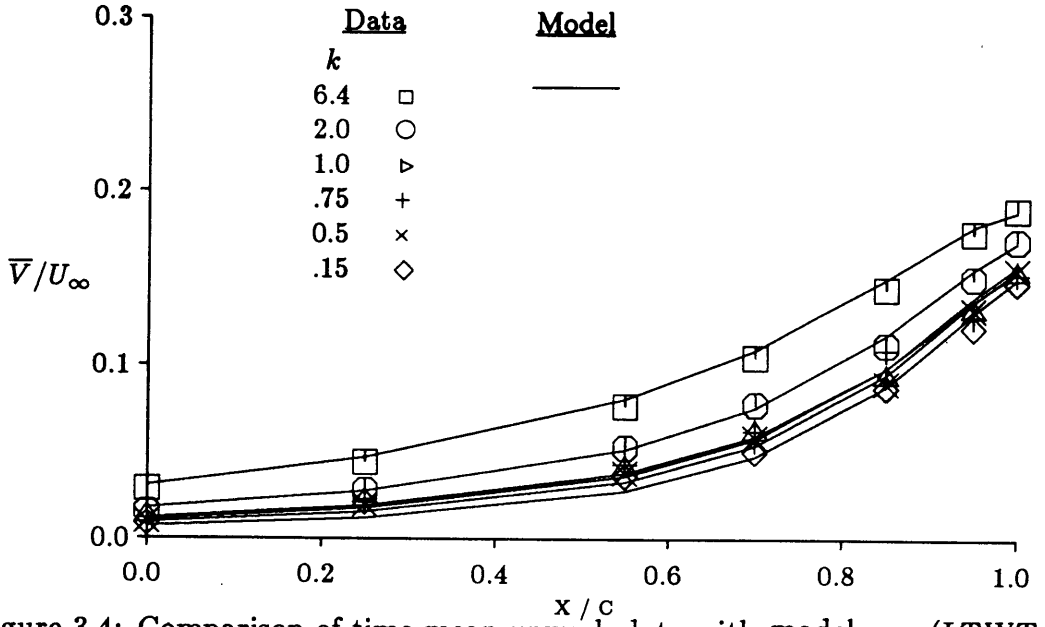


Figure 3.4: Comparison of time mean upwash data with model (LTWT, Re = 400,000)

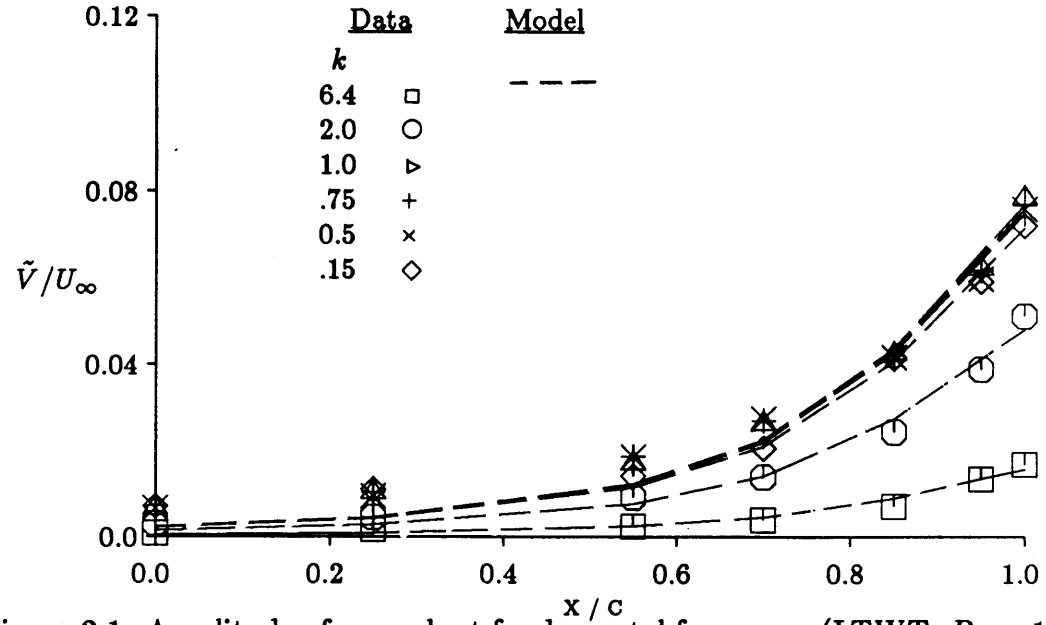


Figure 2.1: Amplitude of upwash at fundamental frequency (LTWT, $Re = 125000$)

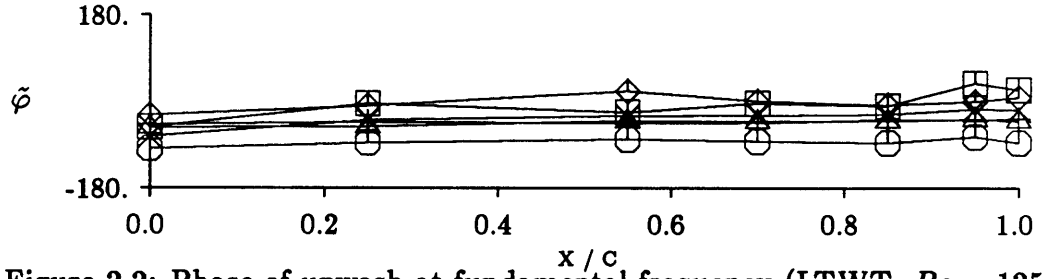


Figure 2.2: Phase of upwash at fundamental frequency (LTWT, $Re = 125000$)

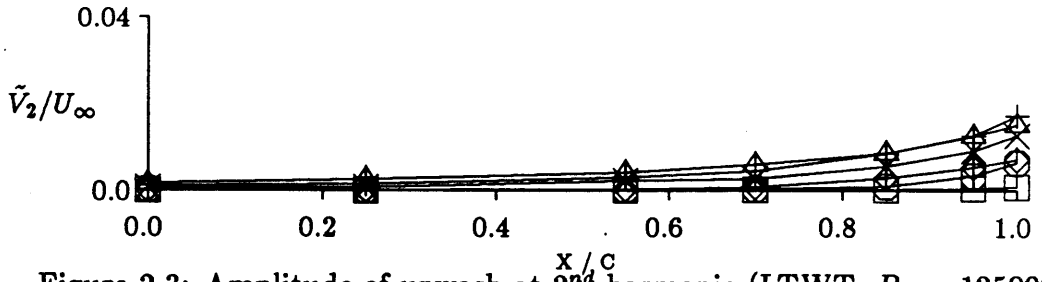


Figure 2.3: Amplitude of upwash at 2^{nd} harmonic (LTWT, $Re = 125000$)

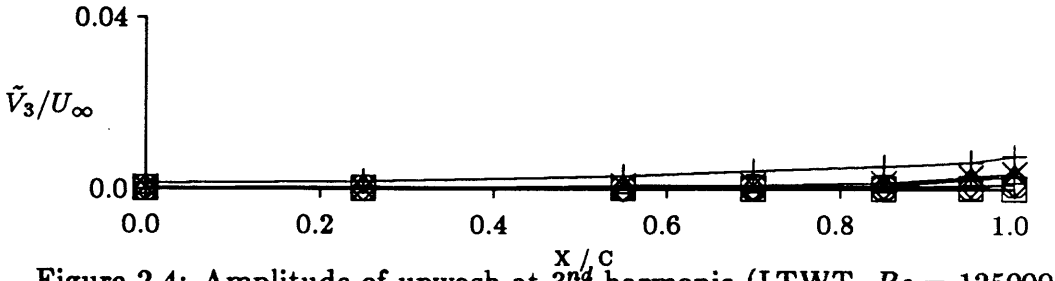


Figure 2.4: Amplitude of upwash at 3^{nd} harmonic (LTWT, $Re = 125000$)

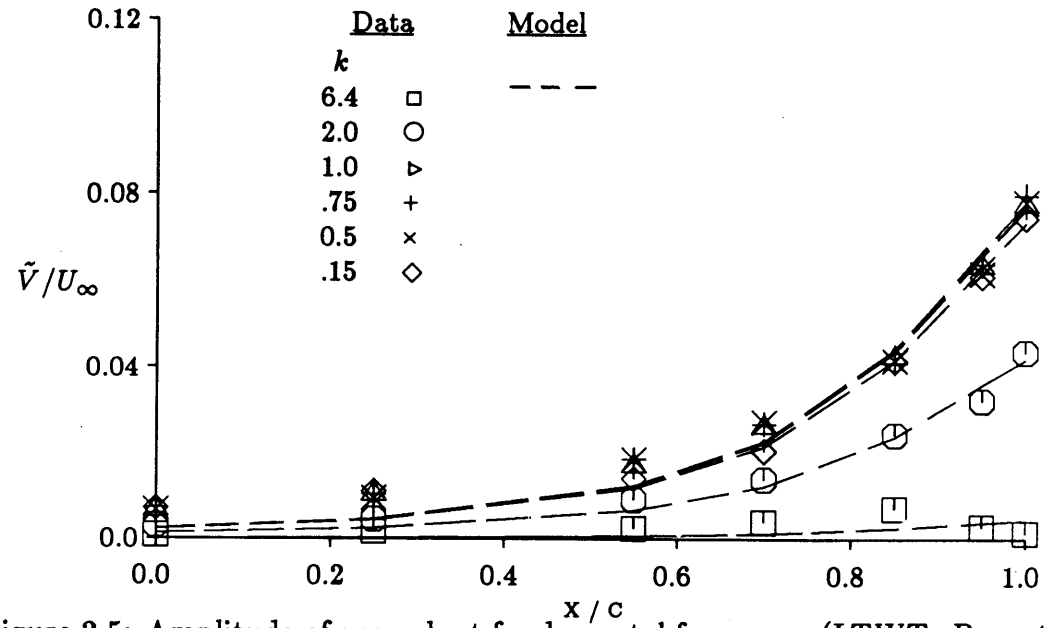


Figure 2.5: Amplitude of upwash at fundamental frequency (LTWT, $Re = 400000$)

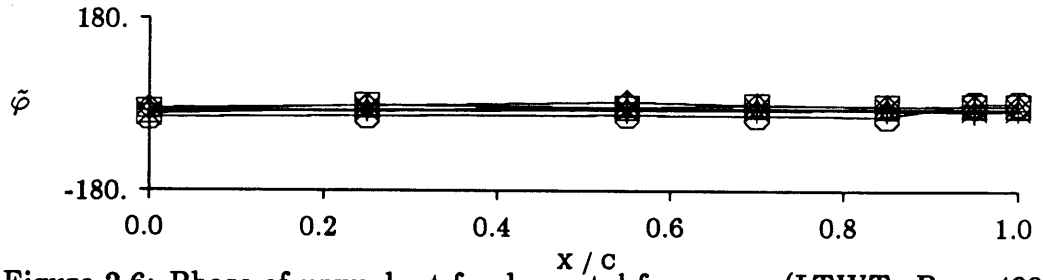


Figure 2.6: Phase of upwash at fundamental frequency (LTWT, $Re = 400000$)

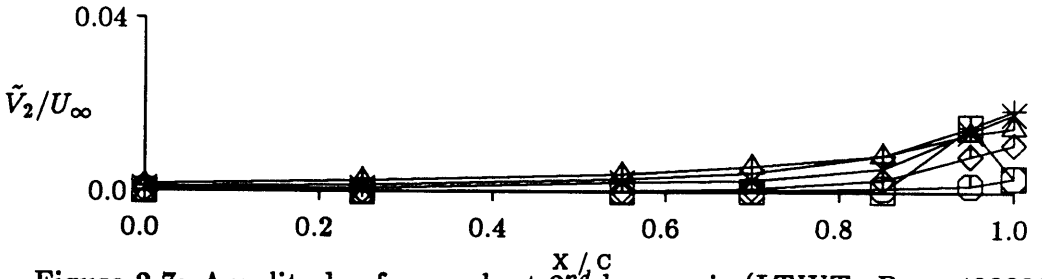


Figure 2.7: Amplitude of upwash at 2^{nd} harmonic (LTWT, $Re = 400000$)

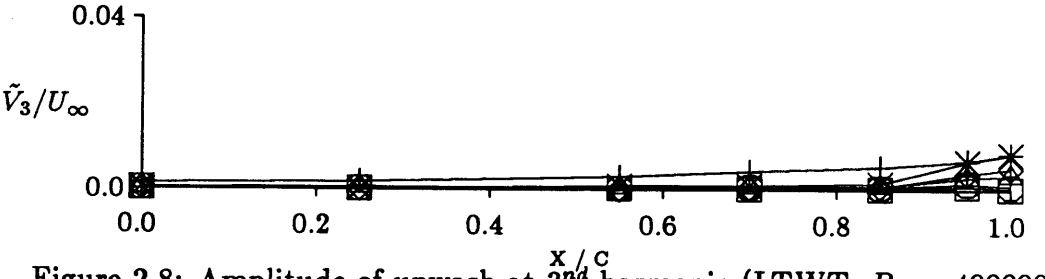


Figure 2.8: Amplitude of upwash at 3^{nd} harmonic (LTWT, $Re = 400000$)

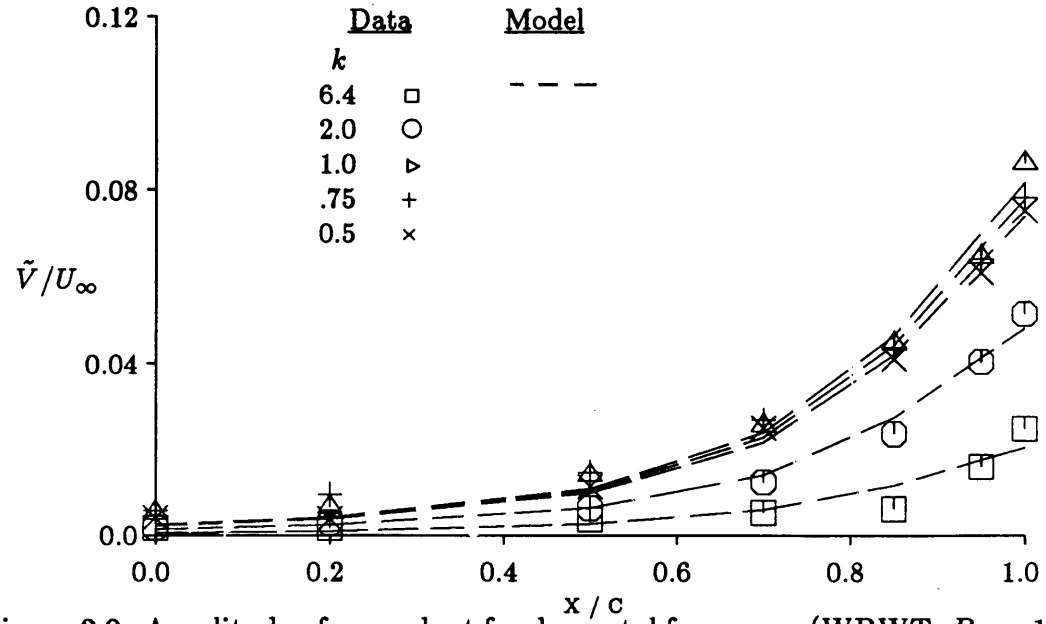


Figure 2.9: Amplitude of upwash at fundamental frequency (WBWT, $Re = 125000$)

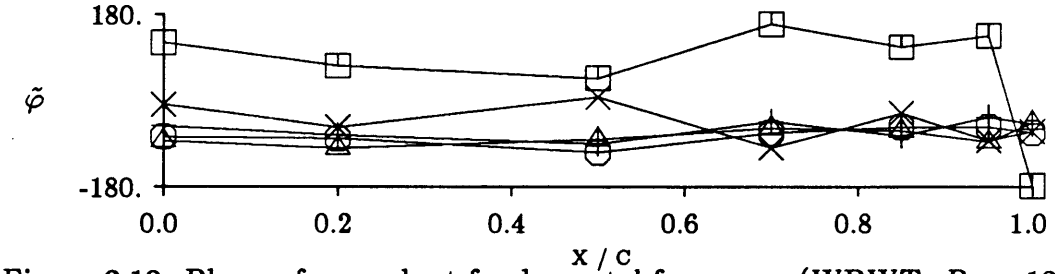


Figure 2.10: Phase of upwash at fundamental frequency (WBWT, $Re = 125000$)

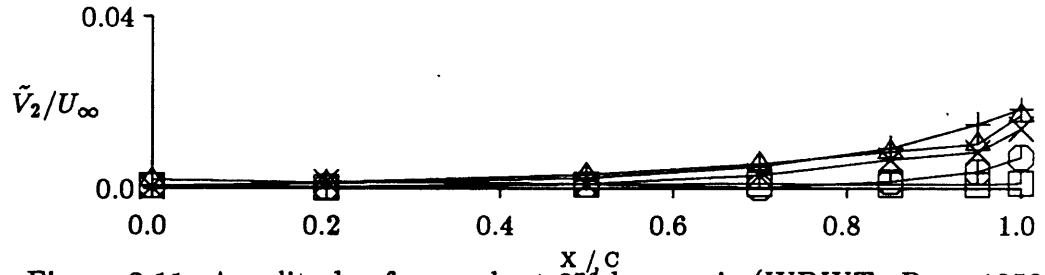


Figure 2.11: Amplitude of upwash at 2^{nd} harmonic (WBWT, $Re = 125000$)

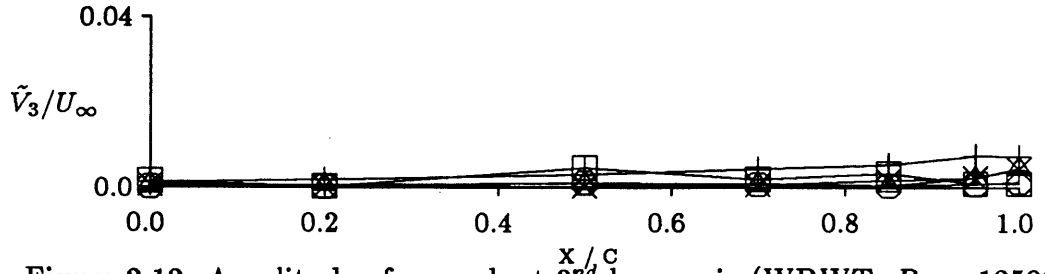


Figure 2.12: Amplitude of upwash at 3^{nd} harmonic (WBWT, $Re = 125000$)

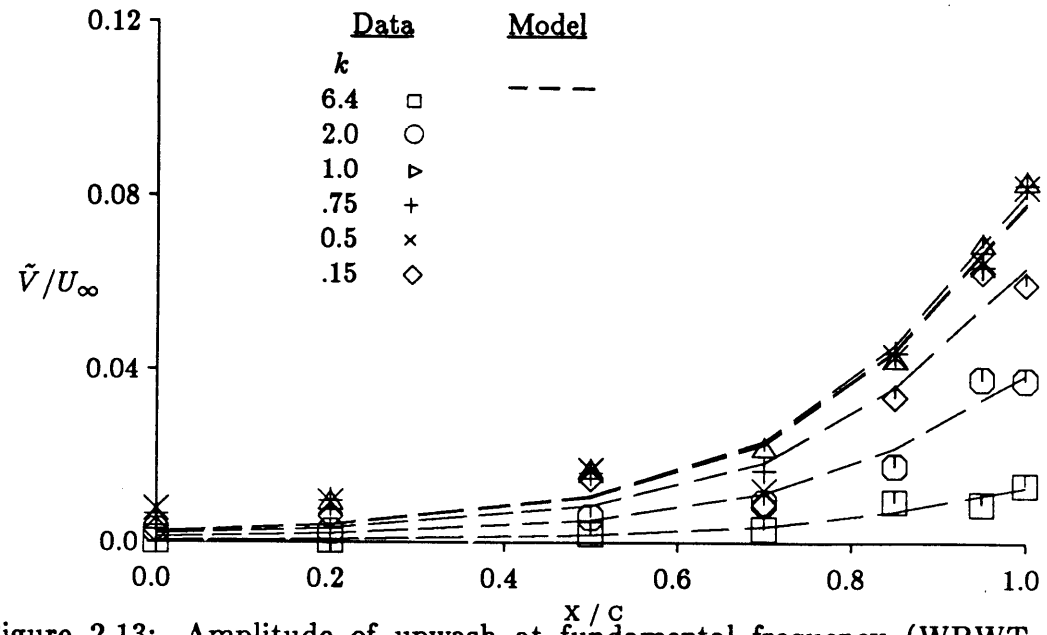


Figure 2.13: Amplitude of upwash at fundamental frequency (WBWT, Re = 400000)

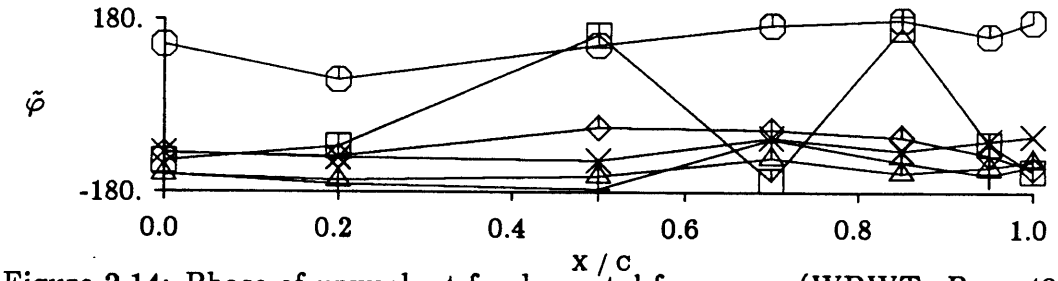


Figure 2.14: Phase of upwash at fundamental frequency (WBWT, Re = 400000)

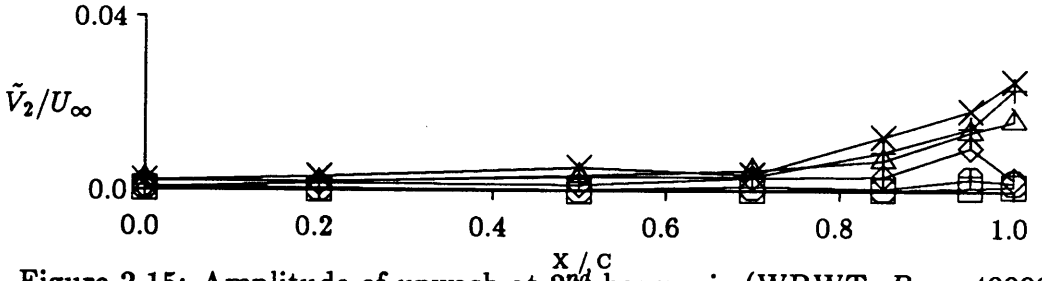


Figure 2.15: Amplitude of upwash at 2^{nd} harmonic (WBWT, Re = 400000)

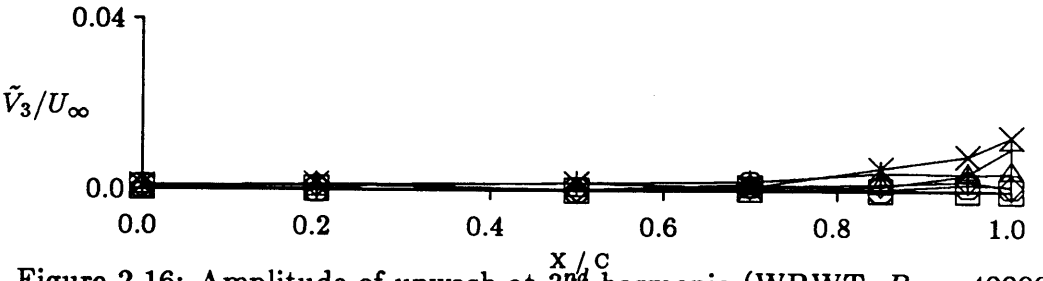


Figure 2.16: Amplitude of upwash at 3^{nd} harmonic (WBWT, Re = 400000)

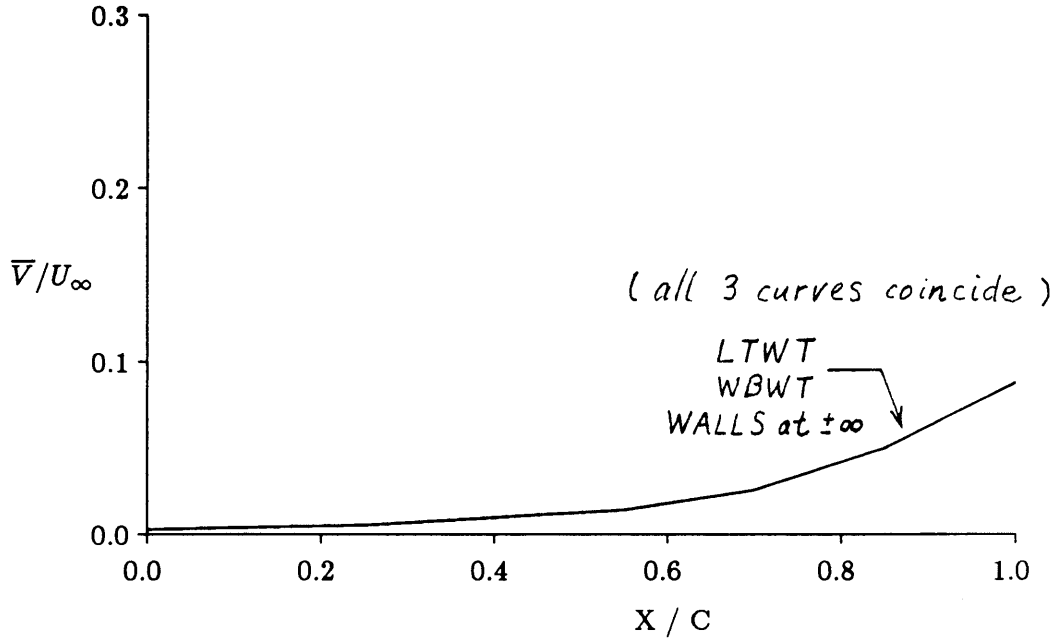


Figure 3.21: Tunnel wall effect with stationary cylinder

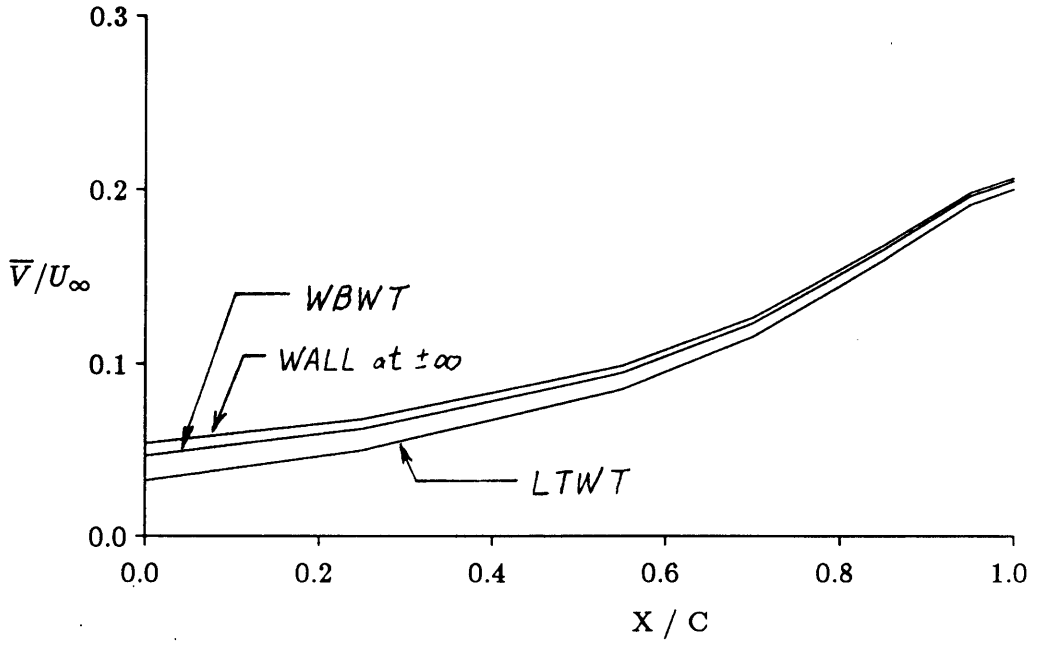


Figure 3.22: Calculation of time mean upwash at $k = 6.4$

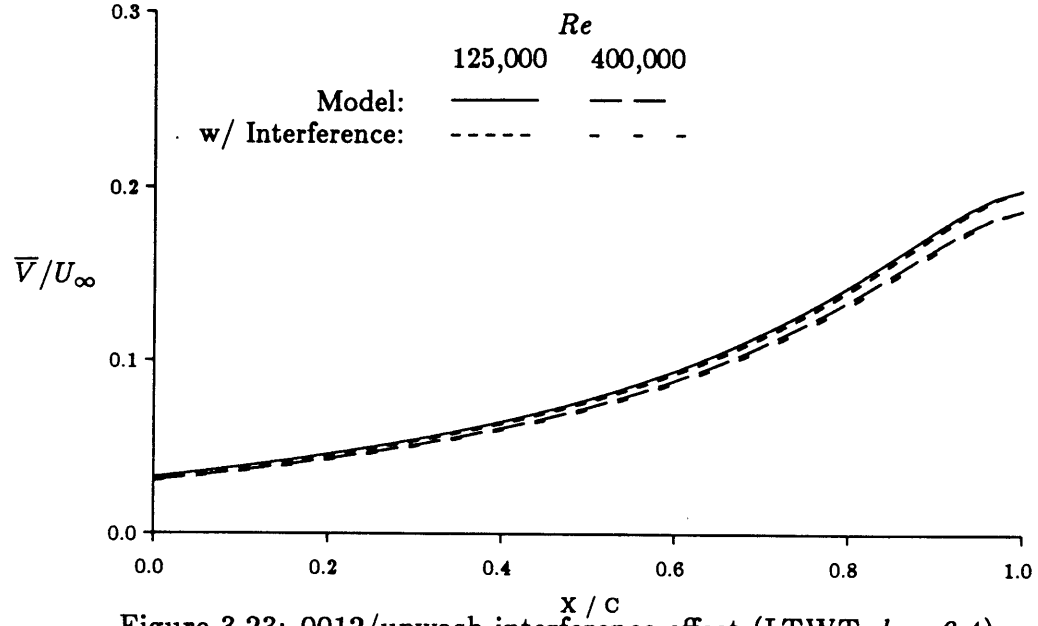


Figure 3.23: 0012/upwash interference effect (LTWT, $k = 6.4$)

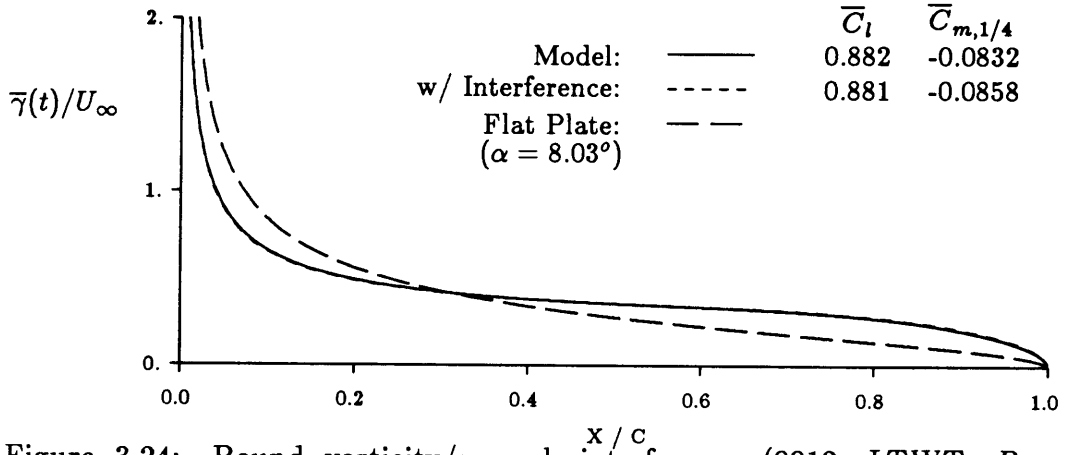


Figure 3.24: Bound vorticity/upwash interference (0012, LTWT, Re =125K, k =6.4)

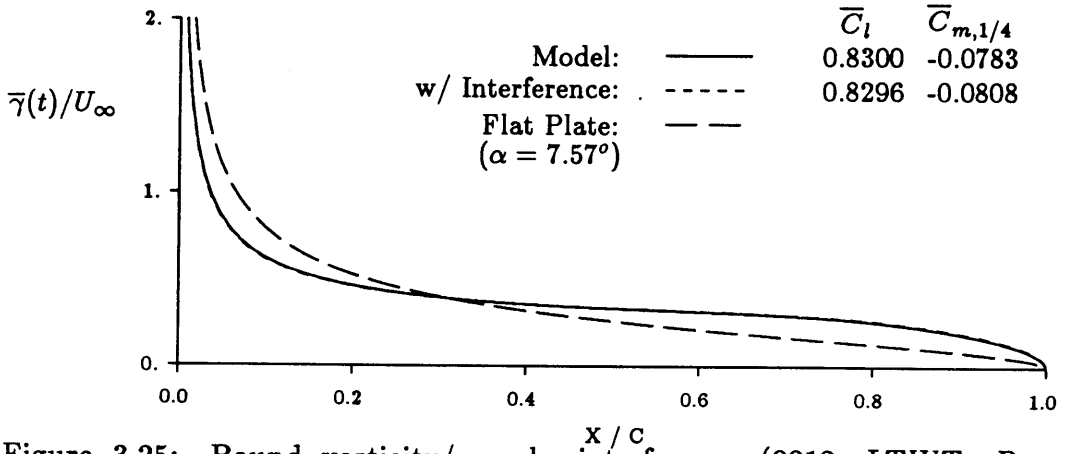


Figure 3.25: Bound vorticity/upwahs interference (0012, LTWT, Re =400K, k =6.4)

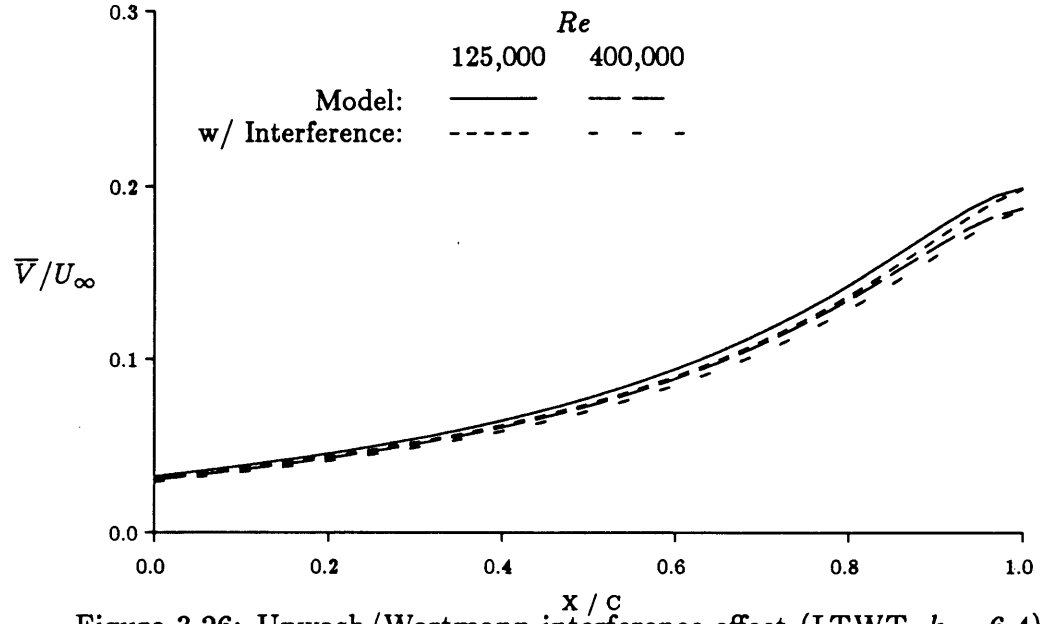


Figure 3.26: Upwash/Wortmann interference effect (LTWT, $k = 6.4$)

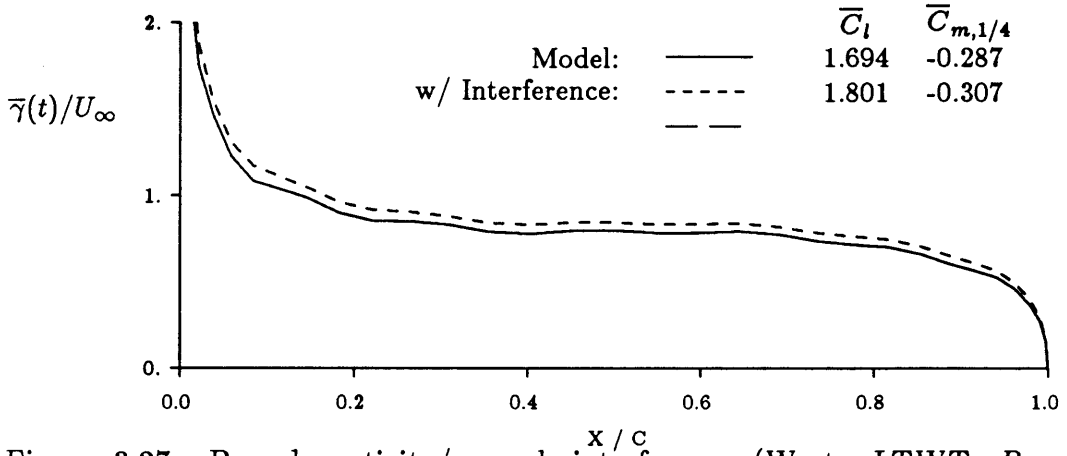


Figure 3.27: Bound vorticity/upwash interference (Wort., LTWT, Re =125K, k =6.4)

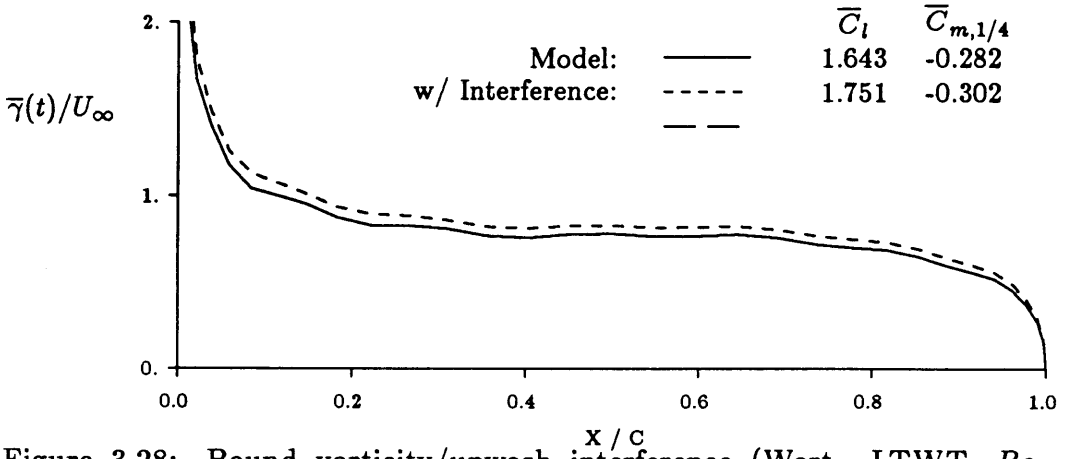


Figure 3.28: Bound vorticity/upwash interference (Wort., LTWT, Re =400K, k =6.4)

Chapter 4

Measured Airfoil Steady and Unsteady Surface Pressure

This chapter consists of presentation of the surface pressure results and discussions of major effects found. Tests are conducted at $\alpha = 0$ and 10 degrees, $Re = 125000$ and 400000, and reduced frequencies of 0.15, 0.5, 0.75, 1.0, 2.0, and 6.4 in both 0.05% (LTWT) and 0.8% (WBWT) free-stream turbulence levels. Pressure data are presented for steady flow, time mean unsteady flow, and amplitude and phase of unsteady flow at the fundamental frequency.

4.1 Steady external flow results

General characteristics of airfoils with a 'long' (on the order of the chord) separation bubble at low Reynolds numbers can be understood by studying the pressure field around the Wortmann FX63-137 airfoil. This is because the presence of a long separation bubble implies that the adverse pressure gradient is absent of sharp peak at cruise angles of attack. This usually corresponds to aft-loaded airfoils with trailing edge stall behavior. The Wortmann airfoil belongs to this classification.

Figures 4.1 and 4.2 present the pressure distributions in steady flow at $\alpha = 0^o$ in low and high turbulence environments, respectively. Figures 4.3 and 4.4 show corresponding data at $\alpha = 10^o$. Results for both Reynolds numbers are plotted

on each figure. Major effects found are related to Reynolds numbers, free-stream turbulence, and pressure gradient. Discussions of these effects on the geometry and general behavior of the separation bubble follow.

4.1.1 Reynolds number effects

An increase of Reynolds number from 125000 to 400000 causes transition, from laminar to turbulent flow in the separated laminar shear layer region, to occur further upstream. Figure 4.1 shows an abruptly increase of pressure on the suction surface near 80% chord for Re = 125000 and 70% for Re = 400000; at these locations, the process of flow transition from laminar to turbulence is completed and the turbulent flow begins to reattach. This interpretation is supported by Gault [29] who showed that "the position of transition in a bubble may be determined easily and accurately from pressure-distribution diagrams."

The consequence of earlier flow transition, as Reynolds number increases, is sooner reattachment as a turbulent boundary layer. The locations where the flow has completely reattached are near 90% and 75% chord for Re= 125000 and 400000 respectively. At these points, the pressure ceases to increase at the same rate as when the flow is reattaching, from 80-90% chord for Re= 125000 and 70-75% for Re = 400000. The newly reattached turbulent boundary layers continue downstream without separation, as implied by the lack of a pressure plateau.

4.1.2 Free-stream turbulence effects

The random flow fluctuation in the atmosphere is much less than the lowest turbulence level attainable by modern wind tunnels, which is about 0.05%. For this reason, it is important to study the effect of free-stream turbulence on the flow phenomenon under investigation [51] [52], especially when the effect is large. This answers the question: how can the data be applied to the flight environment? Such study is conducted in the present work by testing the airfoils in two free-stream turbulence levels – 0.05%(LTWT) and 0.8%(WBWT).

The effect of higher free-stream turbulence is to alter the process of flow transition. This is clear by comparing results for $Re = 400000$ tested in low turbulence level, figure 4.1, with results in high turbulence level, figure 4.2. In figure 4.1, a pressure plateau followed by an abrupt pressure increase signals the completion of boundary layer transition from a separated laminar shear layer to turbulent flow [29]. This trend is not clear from the pressure distribution of figure 4.2 for $Re = 400000$. Similar trend holds for a longer separation bubble, present at $Re = 125000$, but the location of completion of transition as inferred by the pressue distribution is more evident.

4.1.3 Pressure gradient effects

A higher adverse pressure gradient translates the bubble upstream and shortens its overall size. This is illustrated by comparing results of figures 4.1 and 4.3 for Wortmann at $\alpha = 0^o$ and 10^o respectively.

A region of over-expansion of pressure recovery near the reattachment region, 50% chord, is also observed at $Re = 125000$ (figure 4.3). The over-expansion is physical since uncertainty in C_p is only 2%, see appendix B for detail. This is an important flow feature in the empirical model of Dini *et el* [20]. The phenomenon of over-expansion is likely due to streamline curvature effect as the flow is reattaching as a turbulent boundary layer.

4.2 Definition of time mean and unsteady pressure coefficient

This section defines the time mean and unsteady pressure coefficients and their interpretations. The unsteady Bernoulli equation for a 2-D incompressible flow is

$$C_p(x,t) = 1 - \left(\frac{u_e(x,t)}{U_\infty}\right)^2 - \frac{2}{U_\infty^2}\frac{\partial \phi(x,t)}{\partial t} \tag{4.1}$$

where $\phi(x,t)$ is the velocity potential and $u_e(x,t)$ is the edge velocity which can be written as

$$\phi(x,t) = \overline{\phi}(x) + \tilde{\phi}(x)\ cos(\omega t + \varphi) \tag{4.2}$$

$$\begin{aligned} u_e(x,t) &= \frac{\partial \phi}{\partial x} \\ &= \frac{\partial \overline{\phi}}{\partial x} + \frac{\partial \tilde{\phi}}{\partial x}\ cos(\omega t + \varphi) \\ &= \overline{u}_e(x) + \tilde{u}_e(x)\ cos(\omega t + \varphi) \end{aligned} \tag{4.3}$$

For a more general periodic excitation, $u_e(x,t)$ and $\phi(x,t)$ consist of the sum of all Fourier components. Substituting (4.3) and (4.2) into (4.1) yields

$$\begin{aligned} C_p = \quad & 1 - \left(\frac{\overline{u}_e}{U_\infty}\right)^2 - 2\left(\frac{\overline{u}_e}{U_\infty}\right)\left(\frac{\tilde{u}_e}{U_\infty}\right)\ cos(\omega t + \varphi) \\ & - \left(\frac{\tilde{u}_e}{U_\infty}\right)^2\ cos^2(\omega t + \varphi) + 2\omega\frac{\tilde{\phi}}{U_\infty^2}\ sin(\omega t + \varphi) \end{aligned} \tag{4.4}$$

Since the unsteady excitation is periodic, define a time mean quantity as

$$\overline{f}(x) = \frac{1}{2\pi}\int_0^{2\pi} f(x,t)\ dt \tag{4.5}$$

and the first, or fundamental, harmonic as

$$\tilde{f}(x,t) = \frac{1}{2\pi}\int_0^{2\pi} f(x,t)\ e^{i\omega t}\ dt \tag{4.6}$$

The pressure coefficient can also be Fourier decomposed as

$$C_p(x,t) = \overline{C}_p(x) + \tilde{C}_{p1}\ cos(\omega t + \varsigma_1) + \tilde{C}_{p2}\ cos(2\omega t + \varsigma_2) + ... \tag{4.7}$$

Calculating for the time mean and the first harmonic of (4.4) according to (4.5) and (4.6) and equating the result with (4.7) gives

$$\overline{C}_p = 1 - \left(\frac{\overline{u}_e}{U_\infty}\right)^2 - \frac{1}{2}\left(\frac{\tilde{u}_e}{U_\infty}\right)^2 \tag{4.8}$$

$$\tilde{C}_{p1}\ cos(\omega t + \varsigma_1) = -2\left(\frac{\overline{u}_e}{U_\infty}\right)\left(\frac{\tilde{u}_e}{U_\infty}\right)\ cos(\omega t + \varphi) + 2\omega\frac{\tilde{\phi}}{U_\infty^2}\ sin(\omega t + \varphi) \tag{4.9}$$

$$\tilde{C}_{p2}\ cos(2\omega t + \varsigma_2) = -\frac{1}{2}\left(\frac{\tilde{u}_e}{U_\infty}\right)^2\ cos\,2(\omega t + \varphi) \tag{4.10}$$

Note the time mean pressure coefficient (4.8) is *not* simply governed by the steady Bernoulli equation with time mean variables but also depends on the square of the amplitude ratio as well; this additional term is due to non-linearity of pressure-velocity relation. The first harmonic of the unsteady pressure (4.9) is composed of the product of time mean and unsteady edge velocity (quasi-steady) and the product of frequency and unsteady velocity potential (high-frequency). For very low values of reduced frequency, the quasi-steady term dominates and the unsteady pressure is in phase with the motion of the edge velocity. In the high frequency limit, the other term dominates with a phase difference.

Some literature, see review by McCroskey [47], express the unsteady pressure coefficient as

$$C_p(x,t) = \overline{C}_p(x) + \tilde{C}_{p1c}\cos\omega t + \tilde{C}_{p1s}\sin\omega t + \tilde{C}_{p2}\cos(2\omega t + \varsigma_2) + \ldots \qquad (4.11)$$

Values for $\tilde{C}_{p1c}$ and $\tilde{C}_{p1s}$ are found by expanding (4.9), which yield

$$\begin{aligned}
\tilde{C}_{p1c} &= \tilde{C}_{p1}\cos\varsigma_1 \\
&= -2\left(\frac{\overline{u}_e}{U_\infty}\right)\left(\frac{\tilde{u}_e}{U_\infty}\right)\cos\varphi + 2\omega\frac{\tilde{\phi}}{U_\infty^2}\sin\varphi \qquad (4.12) \\
\tilde{C}_{p1s} &= \tilde{C}_{p1}\sin\varsigma_1 \\
&= 2\left(\frac{\overline{u}_e}{U_\infty}\right)\left(\frac{\tilde{u}_e}{U_\infty}\right)\sin\varphi + 2\omega\frac{\tilde{\phi}}{U_\infty^2}\cos\varphi \qquad (4.13)
\end{aligned}$$

Equations (4.12) and (4.13) are the in phase (real) and the quadrature (imaginary) components of the first harmonic, respectively.

In the context of this work, we shall use the definition of (4.7).

4.3 Time mean results

The time mean surface pressure on the NACA 0012 near the stall angle of attack, $\alpha = 10^o$, demonstrates effects of free-stream turbulence, reduced frequency, and Reynolds number. At $Re = 125000$, $k = 2.0$, and free-stream turbulence level of 0.8%(WBWT), figure 4.5 shows that i) the flow is attached near the leading edge

on the suction surface, ii) a hint of transition near 5% chord, iii) attached flow from 5% to 10% chord, and iv) separation further downstream. However, for the case of 0.5% free-stream turbulence level global separation on the suction surface is clear. These two pressure distributions illustrate the effect of free-stream turbulence on the ability of the separated shear layer to reattach (refer to the sketches inserted in figure 4.5). If the bubble is reattached, then the turbulent boundary layer persists downstream until the boundary layer separates again. If the bubble bursts then the flow separates with no reattachment.

However, at $Re = 400000$ and $k = 2.0$ (figure 4.7), the time mean pressure is free from global separation even for results obtained in LTWT. Comparison of figure 4.5 with figure 4.7 demonstrates the effect of Reynolds number on the pressure field near the stall angle of attack. Data suggest that the effect of increased in free-stream turbulence is analogous to increase in Reynolds numbers as far as separation or attachment of the time mean unsteady flow is concerned (figures 4.5 and 4.7). This is related to Gault's [29] idea for steady flow: "an increase in the free-stream turbulence reduces the extent of separated laminar flow in a manner somewhat analogous to an increase in the Reynolds number." Hence, the analogy for steady flow appears to be applicable for time mean unsteady flow as well, at least for small unsteady perturbation.

This trend is not so clear at higher reduced frequencies. At $k = 6.4$ and $Re = 400000$, figure 4.8 suggests that the suction surface time mean pressure in low turbulence level is again fully stalled, just as the case for $Re = 125000$, figure 4.6. The reason for this is not apparent. Cross examination of figures 4.5 and 4.7 with figures 4.6 and 4.8 reveals that for the 0012 at $\alpha = 10^o$ attachment of flow on the suction surface is more dependent on the reduced frequency at $Re = 400000$ than at $Re = 125000$.

To summarize other pressure data, the time mean lift is calculated. Figure 4.9 presents the ratio of measured time mean lift coefficient to the prediction from thin airfoil theory, calculated from time mean upwash data. Results obtained in LTWT

show the expected trend that $\overline{C}_l/\overline{C}_{l\,theory}$ increases with Reynolds number; thin airfoil airfoil theory is based on infinite Reynolds number. This increase appears to be a weak function of reduced frequency for $k \leq 2.0$.

4.4 Unsteady results

The ensemble averaged unsteady lift and moment coefficients for $Re = 125000$ and 400000, $k = 0.15$ and 2.0, free-stream turbulence levels of 0.05% and 0.8%, and both the NACA 0012 and Wortmann airfoils are presented in figures 4.10 to 4.11. Horizontal positions of ellipse is defined as t/T= 0 and 1.0. The potential upwash, at the leading edge position, is also shown as reference. The predictions of lift and moment from Theodorsen's theory [72] at fundamental frequency are shown by the dotted lines.

The unsteady lift and moment agree reasonably well with classical theory over all parameters studied. Several trends are worth noting. First, due to the characteristics of the unsteady flow generated by the ellipse, the slope is steeper during the first-half cycle than the second-half.[1] Secondly, for the results in the 0.05% turbulence level (LTWT), the fluctuations in C_l and C_m, are generally larger when the lift and moment are decreasing than increasing. This is due to the unsteady behavior of the separation bubble, especially near the transition region (compare figure 4.10c with 4.12). On the suction surface, the point of completion of flow transition translates from near 70% chord for $0 < t/T < 0.25$ to near 60% chord for $0.25 < t/T < 0.8$ and back to 70% chord for the remainder of the cycle. Note that the bottom surface also show fluctuations in the ensemble averaged pressure. Secondly, the results obtained in free-stream turbulence level of 0.8% (figures 4.11a and 4.11b) reveal that the fluctuation in C_l and C_m is greater than that obtained in lower turbulence environment. The primary reason is simply because of larger fluctuations in the free-stream. Ensemble averaging based on the convergence criterion of equation (2.1) is insufficient to smooth the fluctuations.

[1] First half cycle corresponds to $0^o \leq \alpha_e \leq 90^o$ ellipse angle of attack.

Comparison with unsteady thin airfoil theory is shown in figure 4.13. At $k = 0.15$, $\tilde{C}_l/\tilde{C}_{l\,theo}$ is about 0.95 for 0012 tested in LTWT at $Re = 400000$ and 0.92 for 0012 tested in the LTWT at $Re = 125000$. Note that results obtained in the WBWT is less that than in LTWT.

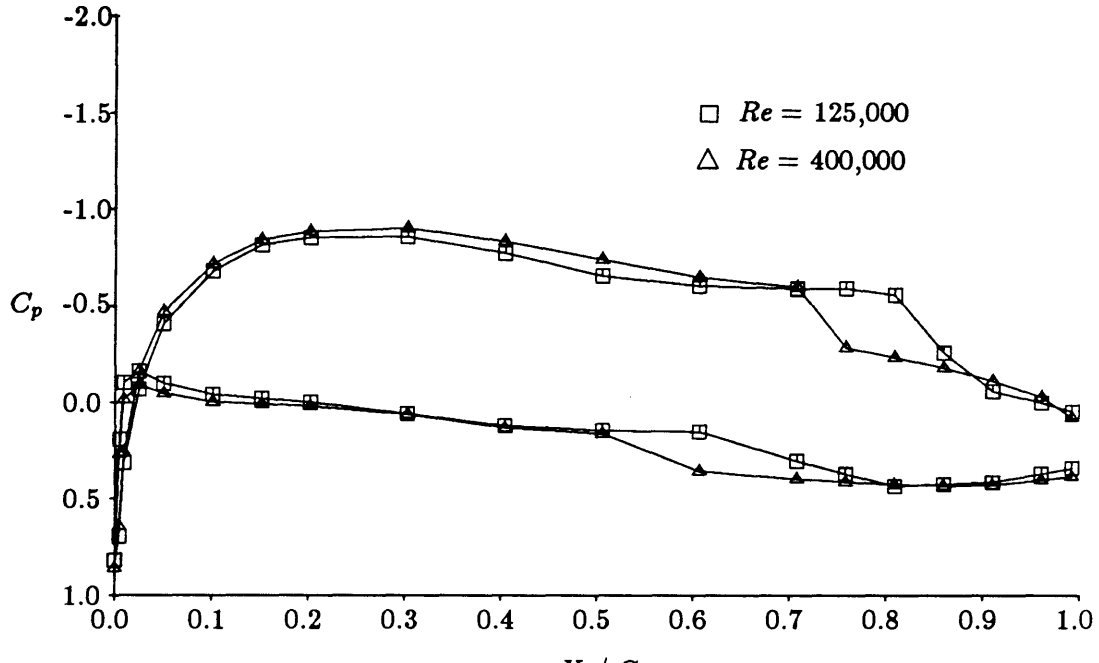


Figure 4.1: Wortmann pressure distribution in steady flow (LTWT, $\alpha = 0°$)

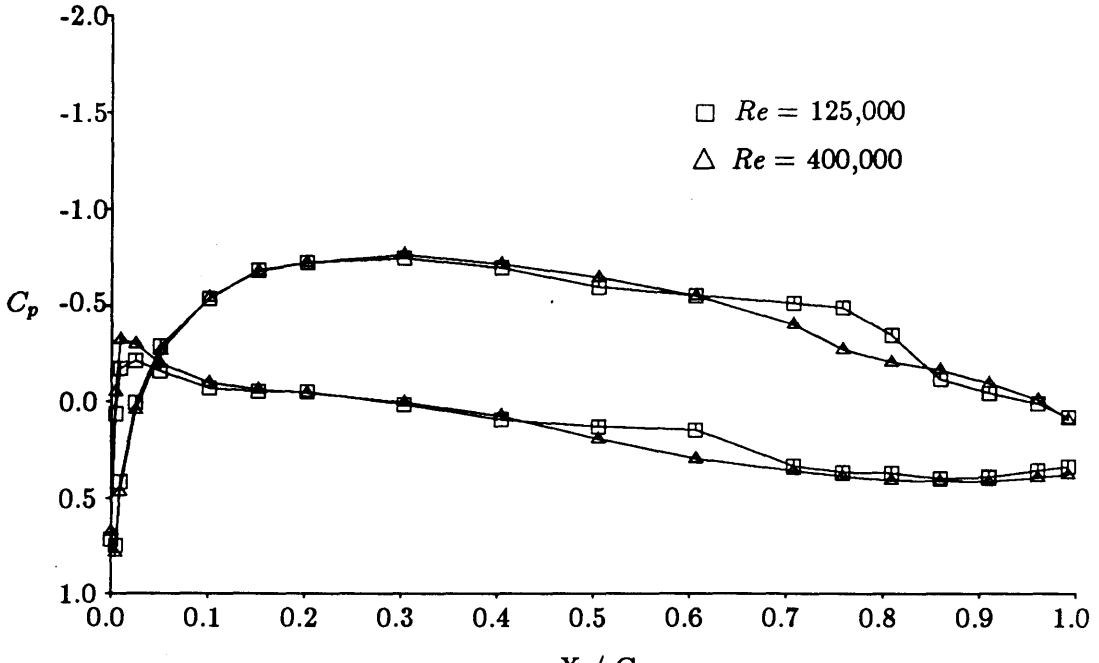


Figure 4.2: Wortmann pressure distribution in steady flow (WBWT, $\alpha = 0°$)

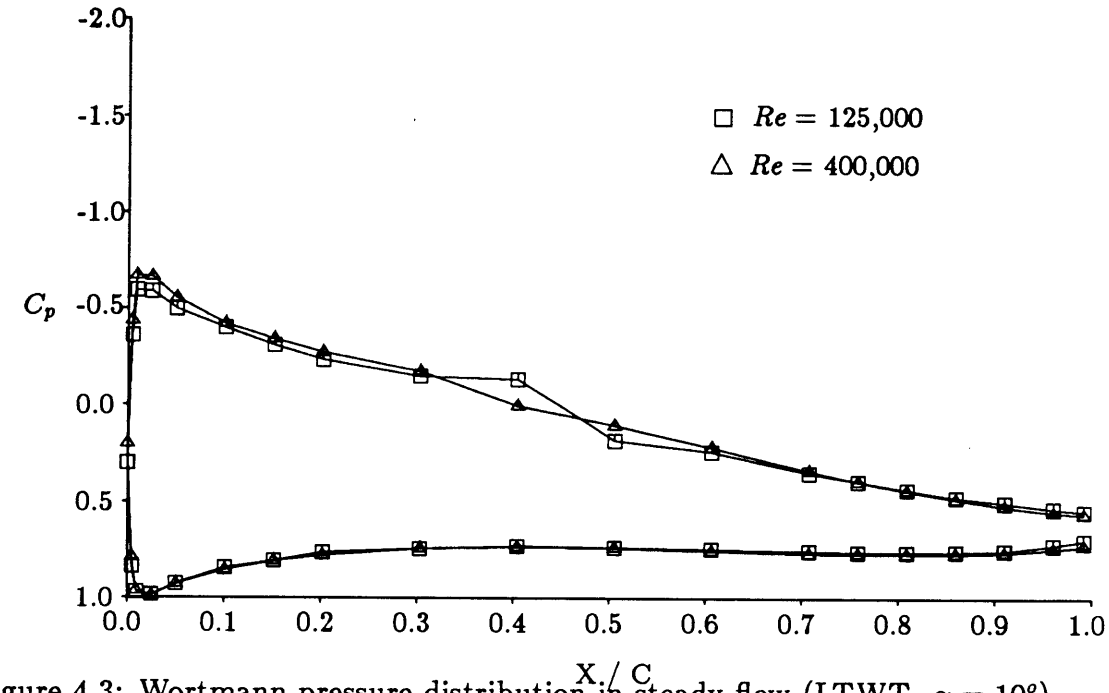


Figure 4.3: Wortmann pressure distribution in steady flow (LTWT, $\alpha = 10°$)

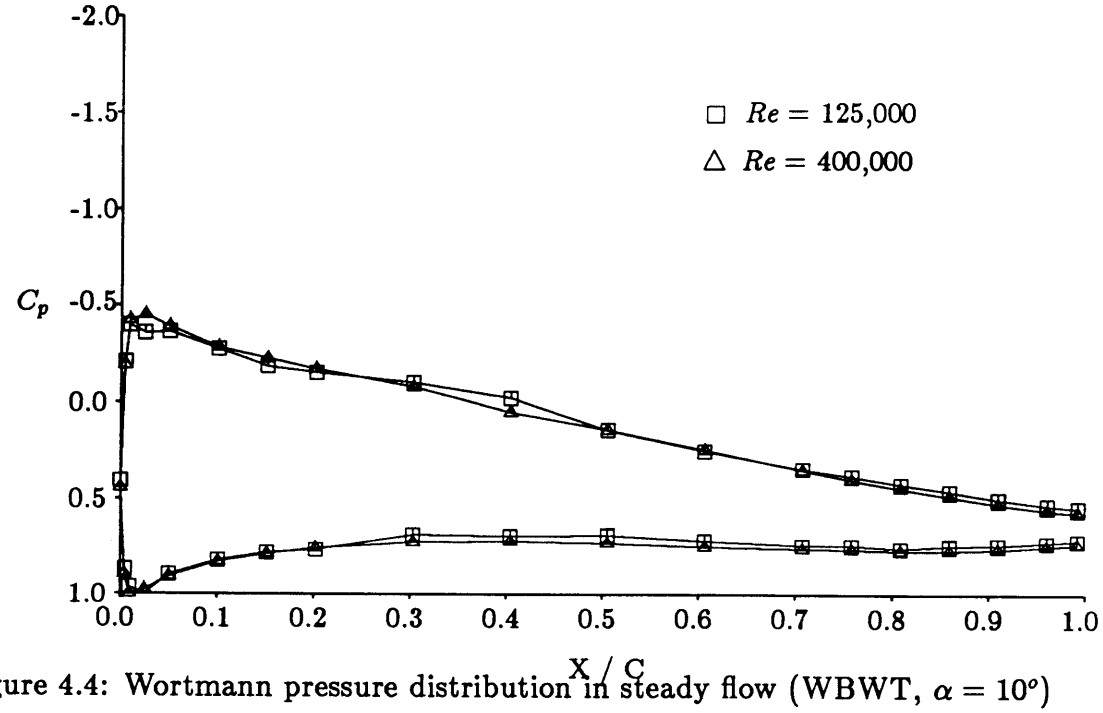


Figure 4.4: Wortmann pressure distribution in steady flow (WBWT, $\alpha = 10°$)

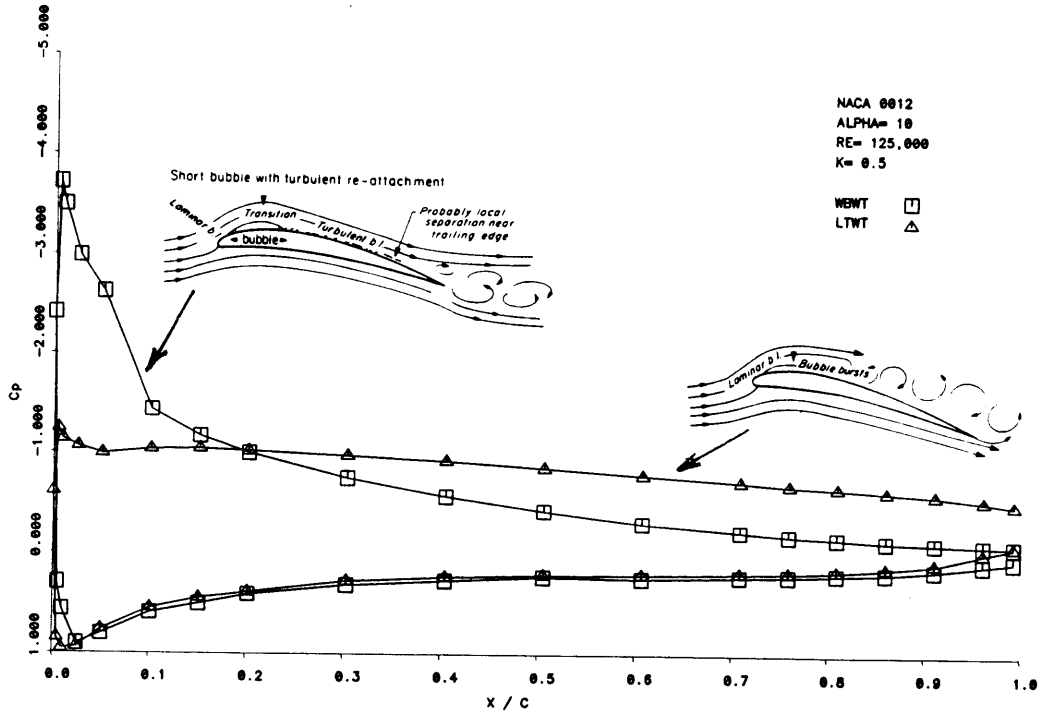


Figure 4.5: Time mean C_p (0012, $Re = 125000$, $\alpha = 10^o$, $k = 2.0$)

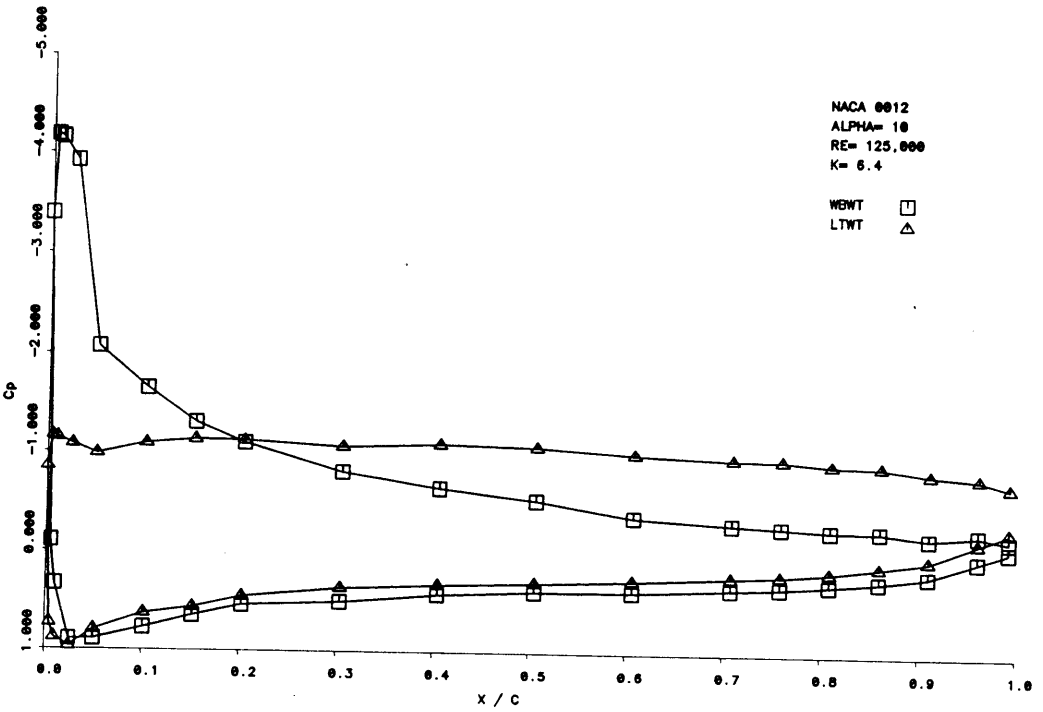


Figure 4.6: Time mean C_p (0012, $Re = 125000$, $\alpha = 10^o$, $k = 6.4$)

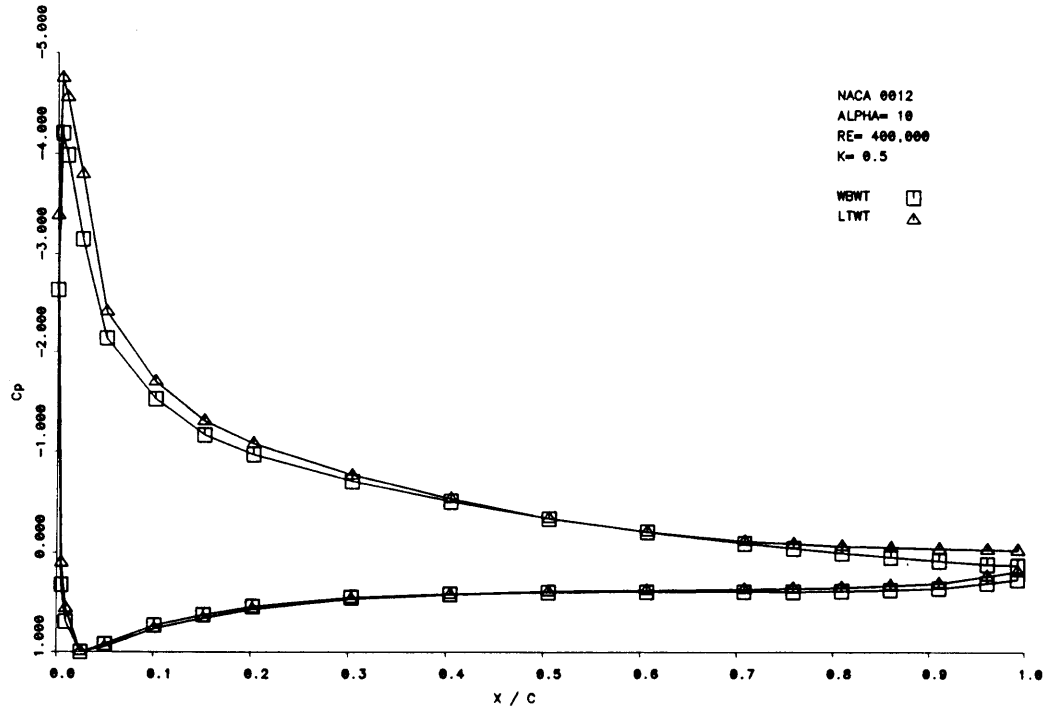


Figure 4.7: Time mean C_p (0012, $Re = 400000$, $\alpha = 10^o$, $k = 2.0$)

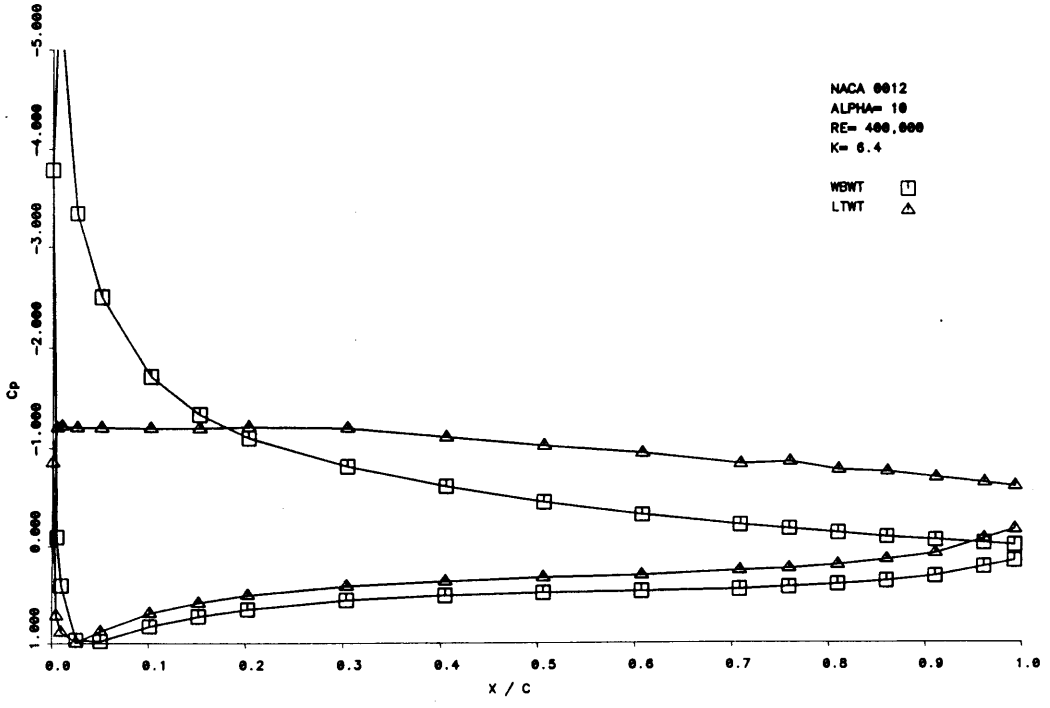


Figure 4.8: Time mean C_p (0012, $Re = 400000$, $\alpha = 10^o$, $k = 6.4$)

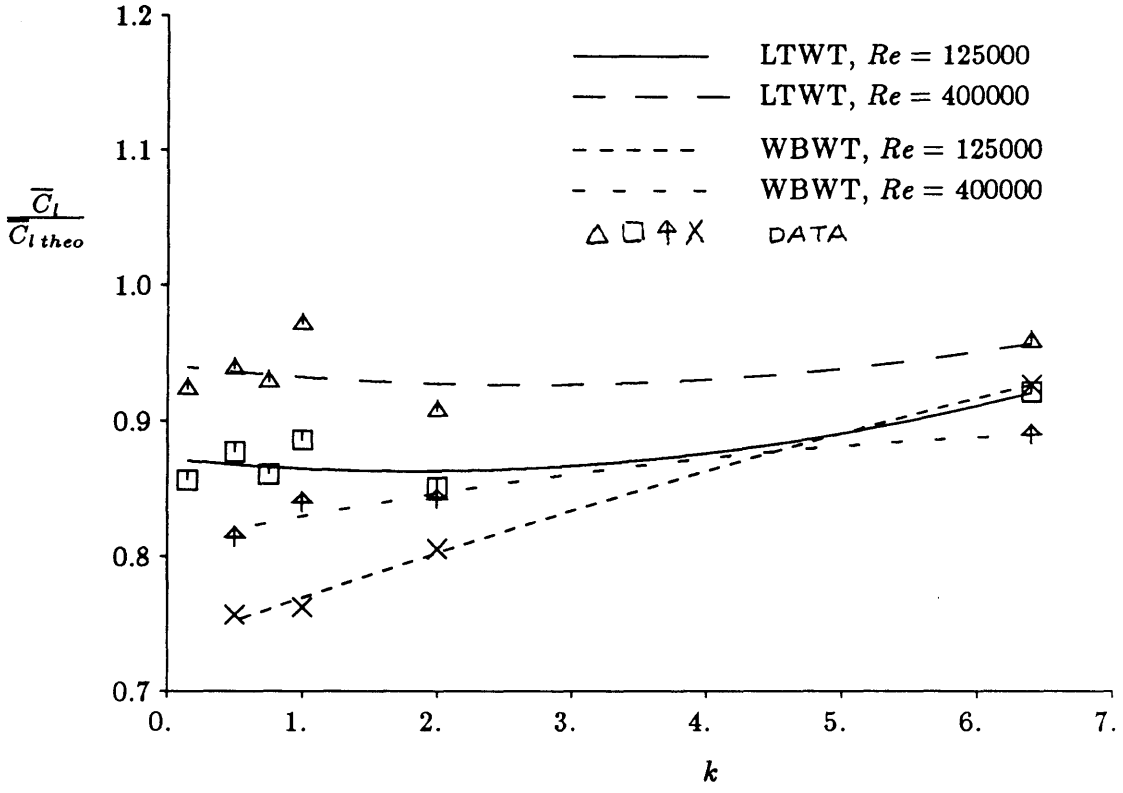


Figure 4.9: $\overline{C}_l/\overline{C}_{l\,theory}$ for both wind tunnels and Reynolds numbers (0012, $\alpha = 0°$)

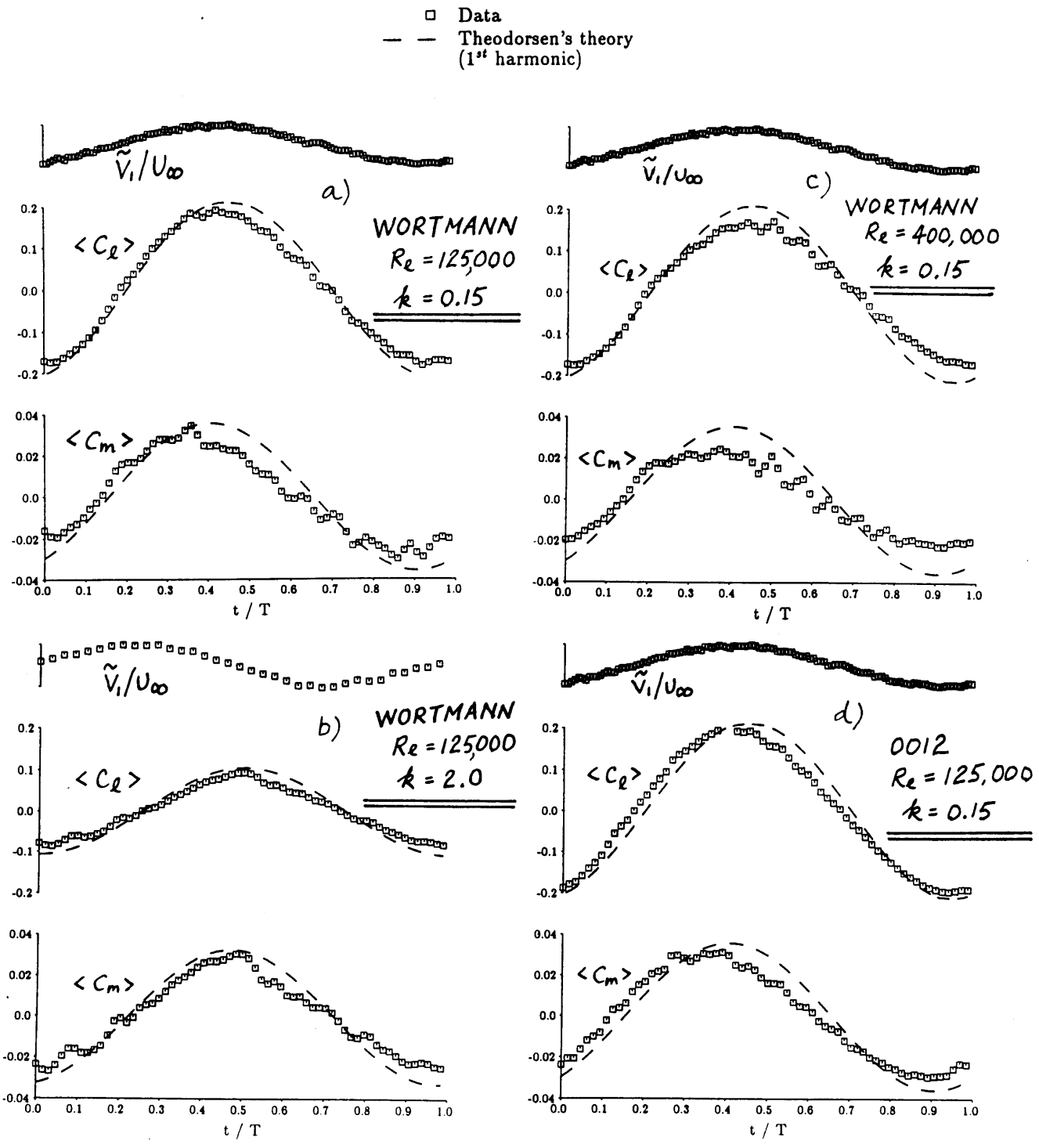


Figure 4.10: Unsteady lift and moment coefficients (ensemble averaged)

(0.05% tunnel turbulence level)

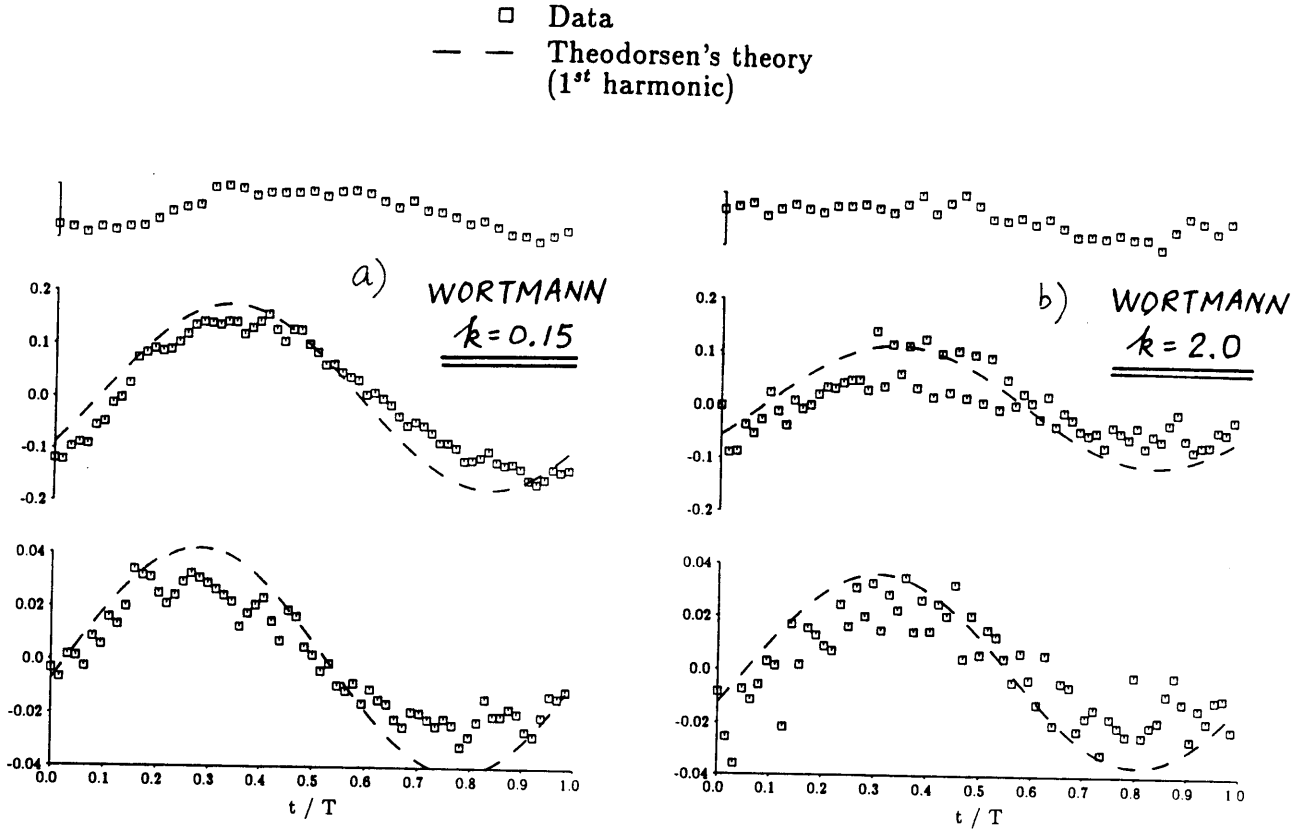


Figure 4.11: Unsteady lift and moment coefficients (ensemble averaged)

(0.8% tunnel turbulence level)

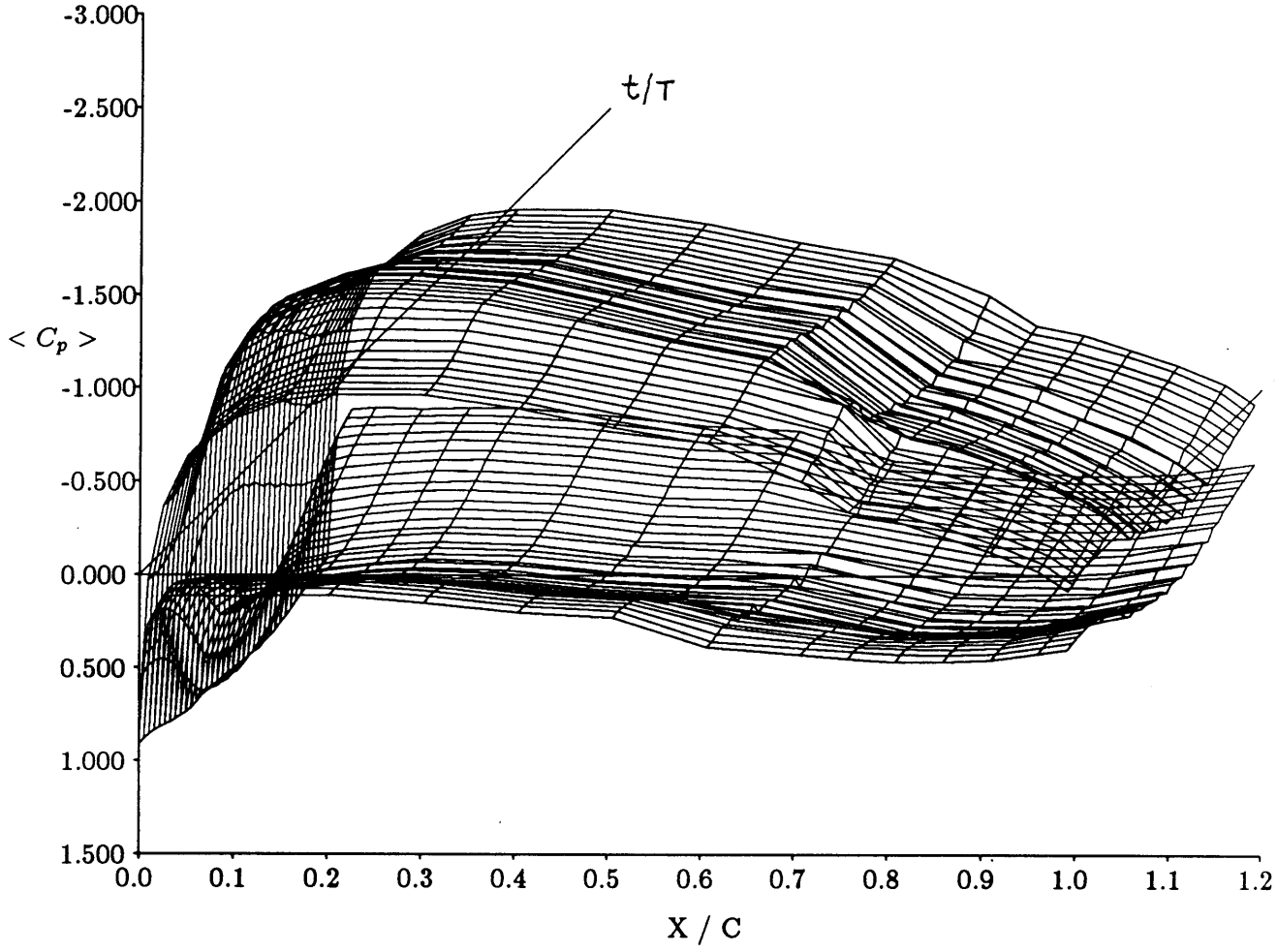


Figure 4.12: Ensemble averaged C_p over an unsteady period (Wortmann, LTWT, $Re = 400000$, $\alpha = 0°$, $k = 0.15$)

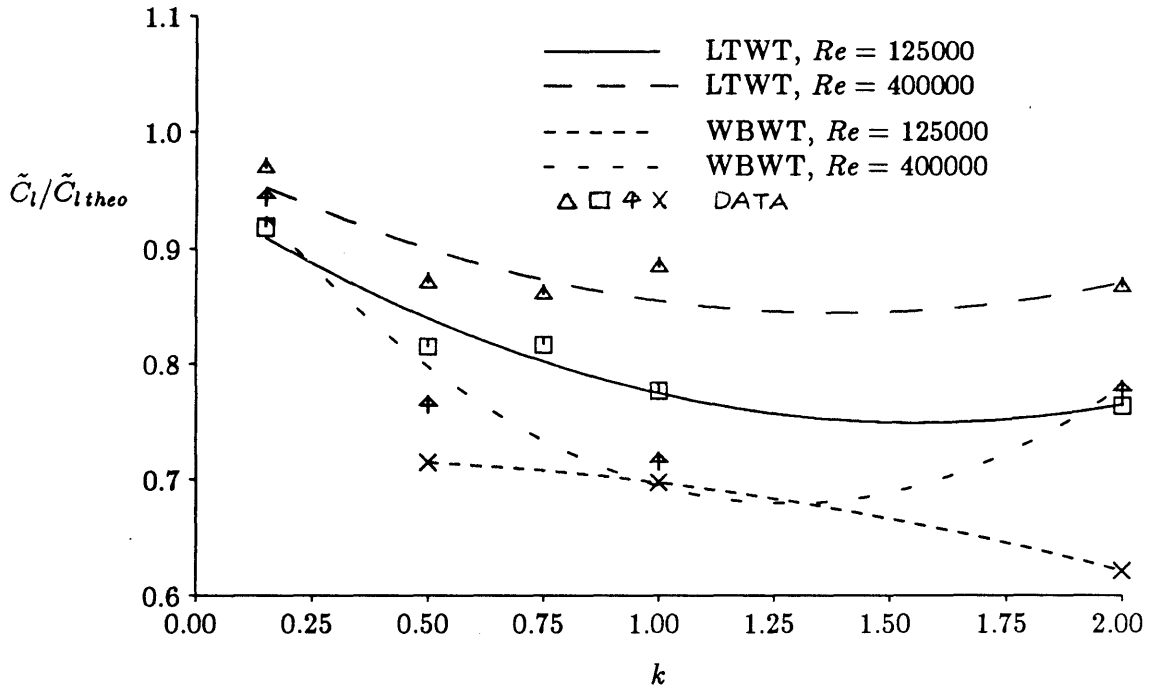


Figure 4.13: Ratio of measured amplitude of lift coefficient at fundamental frequency to the prediction of Theodorsen's theory (0012, $\alpha = 0^o$)

Chapter 5

Unsteady Flow aft of the Trailing Edge

Kutta and Joukowski independently proposed that the lift on an airfoil in a steady unseparated flow is given by potential flow theory with the unique value of the circulation that removes the inverse-square-root singularity in velocity for a cusped trailing edge. Batchelor [3] interprets this as that in the unsteady start-up phase the action of viscosity is such that, in the ultimate steady motion, viscosity can be explicitly ignored by implicitly incorporated in a single condition – known as the Kutta-Joukowski hypothesis. Hence the role of the Kutta condition is to set the bound circulation around the airfoil if no separation of flow occurs anywhere.

Much progress have been made in recent years in the theorectical understanding of the unsteady Kutta condition. Local interaction theory, or triple deck analysis, for boundary layers have shown that, within restricted parameter ranges, only those 'outer' potential flows that satisfy the Kutta condition are, in general, compatible (in the matched asymptotic expansion sense) with an acceptable multilayered 'inner' viscous structure. In this sense, the Kutta condition relates to the behavior of outer perturbations to a high Reynolds number flow as an edge or point of separation is approached. Crighton [18] reviewed these and other aspects of the unsteady Kutta condition in detail.

Numerous works [15] [63] [2] [26] [57] have been done in trying to understand the applicability of the classical Kutta-Joukowski condition in unsteady flow but results are contradicting. Commerford and Carter [15] investigated a circular arc airfoil at reduced frequency of 3.9 and concluded that the Kutta-Joukowski condition was satisfied. Their conclusion was based on the good correlation obtained between theory and pressure difference amplitude data at the 90% chord position. Satyanarayana and Davis [63] found that the Kutta-Joukowski was appropriate for reduced frequency of less than 0.6. For reduced frequency greater than 0.8, the measured loading in the trailing edge region was larger than predicted, with this difference increasing with reduced frequency. Also, Archibald [2] tested a flat plate and an airfoil at reduced frequency of 5.0 and concluded that the Kutta-Joukowski condition does not hold at this high reduced frequency. It is important to note that all these experiments deduce the validity of the Kutta-Joukowski condition based on pressure measurements which are at or upstream of the 95% chord. This is indeed very crude at best since length scales involved near the trailing edge are certainly much less than 5% of the chord hence casting serious doubts on the conclusions stated. Poling and Telionis [57] realized that one should really measure the velocity field rather than the pressure field but, due to physical constraint, was not able to have spatial resolution at least comparable to the trailing edge thickness.

The motivation of the present experiment is to provide additional insight into the validity of the Kutta-Joukowski condition in unsteady flow. The velocity field just aft of the NACA 0012 trailing edge, at $\alpha = 0^o$, was measured by the LDA. The experiment was conducted in 0.05% free-stream turbulence level (LTWT) at $Re = 125000$ and $k = 2.0$. This combination of flow parameters was chosen because the flow just aft of the trailing edge would less likely be smooth at low Reynolds numbers and at relatively high reduced frequencies.

5.1 The unsteady potential flow aft of the trailing edge position

Before investigating the flow field aft of the trailing edge, the potential flow field, *without the airfoil*, in the region of interest is first defined and will be used to aid interpretation of results. This section presents ensemble averaged streamlines, due to the upwash, leaving the trailing edge position. The streamlines are calculated from upwash data taken in the WBWT at Re = 125,000 and k = 2.0 (refer to Chapter 3 for detail on upwash). This set of data is used, rather than that in the LTWT, is because no data is availble downstream of $x/c = 1.0$ in the LTWT.

5.1.1 Formulation

To find the streamfunction passing through the trailing edge position, we need to perform path integration. With all length variables normalized by the chord and velocity by the free-stream, the streamfunction is defined by

$$\Psi(x,y,t) = \int_0^y u(x,y,t)dy - \int_{1.002}^{1.05} v(x,y,t)dx \tag{5.1}$$

With this definition, the streamlines extend just aft of the trailing edge position, $(x,y) = (1.002,0)$, to 5% chord downstream, the furthest downstream point of available upwash data. In order to perform the path integration using equation (5.1), the entire velocity field within the spatial extent must be known. However, upwash is measured at discrete locations along the chord only and velocities off the chordline are unknown. To solve for the unknown velocity field, consider the flow field to be 2-D, irrotational (since the region of investigation is upstream of the wake of the ellipse), i.e.

$$\frac{\partial u}{\partial y} = \frac{\partial v}{\partial x} \tag{5.2}$$

and incompressible (the free-stream Mach number is 0.09 and reduced frequency based on half chord of the ellipse is 0.4, hence $(kM)^2 = 0.0013$), i.e.

$$\frac{\partial u}{\partial x} + \frac{\partial v}{\partial y} = 0 \tag{5.3}$$

The Taylor series expansion for $u(x,y,t)$ in y is

$$u(x,y,t) = u(x,0,t) + \frac{\partial u}{\partial y}_{(x,0,t)} y + \frac{1}{2}\frac{\partial^2 u}{\partial y^2}_{(x,0,t)} y^2 + O(y^3) \tag{5.4}$$

Substituting equation (5.2) and (5.3) into (5.4), yields

$$u(x,y,t) = u(x,0,t) + \frac{\partial v}{\partial x}_{(x,0,t)} y - \frac{1}{2}\frac{\partial^2 u}{\partial x^2}_{(x,0,t)} y^2 + O(y^3) \tag{5.5}$$

The final form for the streamfunction is,

$$\Psi(x,y,t) = \int_0^y \left[u(x,0,t) + \frac{\partial v}{\partial x}_{(x,0,t)} y - \frac{1}{2}\frac{\partial^2 u}{\partial x^2}_{(x,0,t)} y^2 \right] dy - \int_{1.0}^{1.05} v(x,0,t)dx \tag{5.6}$$

Using equation (5.6) with ensemble averaged time as a parameter, the path integration scheme begins at $(x,y) = (1.002, 0)$ and take one step in δx and a series of steps in δy until a prescribed constant, say zero, value of Ψ is found. Then starts at the trailing edge position again and take two steps in δx and several steps in δy until the same constant is found. This procedure continues until $(x,y) = (1.05, 0)$ is reached. The streamline is the loci of points where the constant is obtained. The entire procedure is repeated for another ensemble averaged time. The experimental data are splined and second order schemes are used for computations.

5.1.2 Unsteady potential streamlines

The ensemble averaged potential streamlines aft of the trailing edge position, without the airfoil mounted, is presented in figure 5.1. The streamlines are shown at fixed phase, or ellipse rotation angle (legends indicate physical angle of ellipse). The streamlines clearly show that an upwash is present. Near the ellipse angle of attack of zero degree the streamline is essentially horizontal. At the ellipse angle of 60 degree the streamline is furthest from the chord; at this position, the distance between the trailing edge position and the surface of the ellipse is minimum. Hence the upwash ensemble averaged streamlines concur with physical understanding and little phase shift is observed.

It is important to note that figure 5.1 is the upwash streamlines which the airfoil experiences since the 0012/upwash interference effect is small (see Section 3.4). Note

also that the streamlines exceed the bisector angle formed by extension of the upper and lower surfaces, following the interpretaion of Basu and Hancock [4]. If figure 5.1 were the actual streamlines aft of the NACA 0012, the Kutta-Joukowski condition would not be valid. Hence, in order for the Kutta-Joukowski condition to hold in unsteady flow, the airfoil must develop bound circulation such that streamlines are within the bisector angle for all phases.

5.2 Experimental setup for study of unsteady Kutta condition

The unsteady flow field just aft of the NACA 0012 trailing edge is measured by the Laser Doppler anemometer. The position of the measurement volume closest to the trailing edge is $1mm$ downstream, which is 80% of the trailing edge thickness. This is critical for length scale reasons in this complicated flow region. In order to avoid beam obstruction at this streamwise location, the laser table is rotated horizontally by 1.55 degrees, the half angle of the beam, such that the u-component beam closer to the airfoil parallels the trailing edge. The beam focal volume has a resolution of 0.2mm which is sufficient for our purpose.

The measurement points can be deduced from figure 5.2. Nine points are used in both the transverse and streamwise directions. Note that streamwise spacing is even whereas the transverse is not, to be sure that streamlines are captured. The test was conducted in 0.05% tunnel turbulence level (LTWT) at Re= 125000 $\alpha = 0^o$ and k= 2. Only one value of k was studied due to the work load involved in making 81 measurements and time constraint. For each location, 120 ensembles were averaged.

5.3 The ensemble averaged streamlines aft of the trailing edge

Figures 5.3 and 5.4 show the ensemble averaged velocity vectors when the ellipse is at horizontal and 60 degree positions respectively. Just aft of the trailing edge, the boundary layers from the upper and lower surfaces can clearly be seen and they are attached, at least in the ensemble averaged sense. The lower boundary layer has a higher velocity due to closer proximity to the ellipse. Note that at ellipse angle of 60 degrees, the entire outer flow has a net upward vertical velocity.

Knowing the ensemble averaged u and v velocities at each measurement point, the ensemble averaged streamline is found by path integration using similar procedure as in section 5.1.2. The reason that streamlines are computed rather than streaklines or pathlines is one of simplicity. Since the velocity flow field is measured, the path integration is straight forward. Define the ensemble averaged streamfunction as

$$\hat{\Psi}(x,y,t) = \int_0^y \hat{u}(x,y,t)dy - \int_{1.002}^{1.2} \hat{v}(x,y,t)dx \tag{5.7}$$

The streamwise coordinate extends from 0.2% to 20% chord downstream of the trailing edge.

Figure 5.5 shows the ensemble averaged streamlines with magnification in the x direction for clearity. At horizontal ellipse position, the streamline is pratically horizontal and the streamline are furthest away from the chord when the ellipse is at 60 degree. Figure 5.6 presents the same ensemble averaged streamlines with full extend in the streamwise direction and hot wire measurements at ellipse angle of 0 and 90 degrees. Fletcher [27] measured the boundary layer velocity profiles at 94% chord and found that the time mean displacement thickness is 2.5 times the trailing edge thickness, as also shown in figure 5.6 for reference.

5.4 Discussions

The ensemble averaged streamline results suggest the following. First, the ensemble averaged streamlines are *in-phase* with the unsteady excitation (compare figure 5.1 with 5.5). This is in agreement with the triple deck analysis by Brown and Daniels [12] (as interpreted by Crighton [18], p. 419) for pitching or plunging airfoils. Brown and Daniels proved that for $S = \omega L/U_\infty \gg 1$, the flow everywhere in the vicinity of the trailing edge will be quasi-steady, with time entering only parametrically and flow at each instant given by the steady-incidence solutions of Brown and Stewartson [11]. Brown and Daniels also found that distinctive change occurs when time derivatives are brought into play in the viscous nonlinear lower deck, and this requires that the lower-deck thickness ($Re^{-5/8}L$) and the Stokes-layer thickness, $(\nu/\omega)^{1/2}$, be comparable and thus require $S = O(Re^{1/4})$. If $S \gg O(Re^{1/4})$, the oscillations may be too rapid to preserve the triple deck structure. For the present experiment, $S = 4$ and $Re^{1/4} = 18.8$ hence the local flow is in-phase with the excitation and the flow structure matches asymptotically throughout the entire flow region of the trailing edge.

The angle of the streamline is confined within the angle of the trailing edge which implies that the condition of smooth flow at the trailing edge is satisfied. This idea is from Maskell in Basu and Hancock [4] which simply state that for unsteady airfoil with finite trailing edge angle, vortices shed leaving the airfoil are tangential to the lower surface if $\frac{d\Gamma}{dt} > 0$ and tangential to the upper surface if $\frac{d\Gamma}{dt} < 0$, where Γ is the bounded circulation of the airfoil (see figure 5.7). Note that at ellipse angle of 0 degree, pressure data show that the lift is increasing hence vortices with opposite sign of that of bound vortices are shed. The situation is reversed when ellipse is passing 60 degrees. Hence the ensemble averaged streamlines suggest that the proper value of the circulation is set or the Kutta-Joukowski condition is satisfied, at least in the ensemble averaged sense.

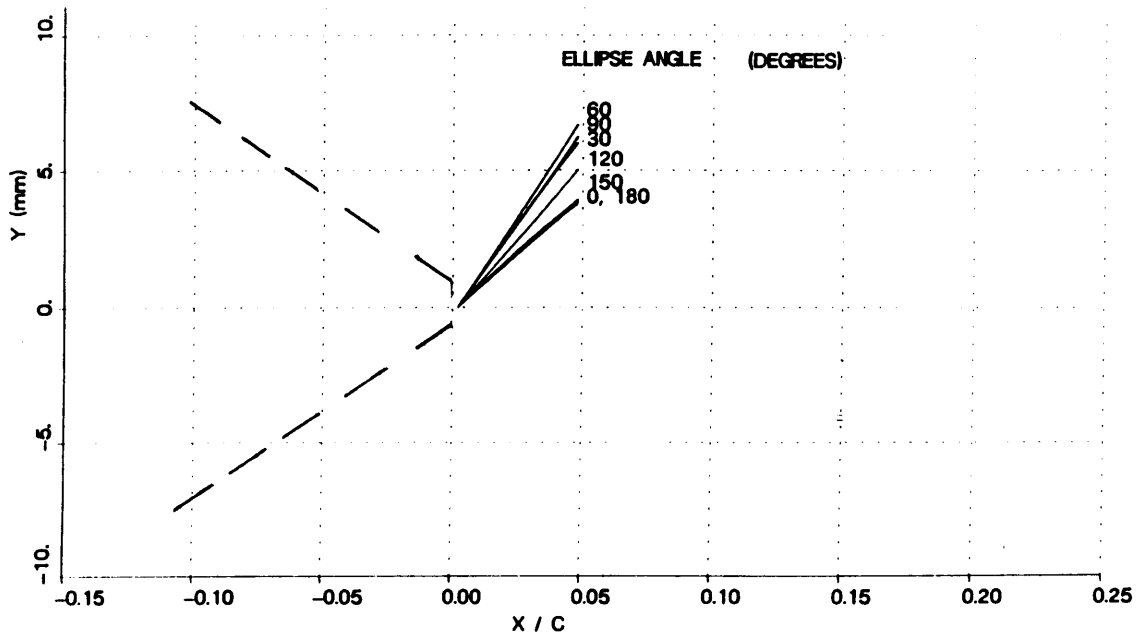
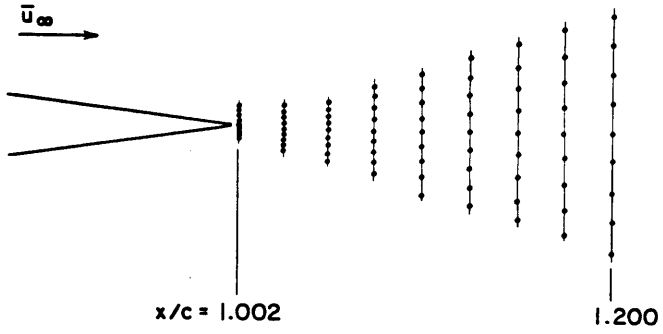


Figure 5.1: Upwash ensemble averaged streamlines without airfoil (WBWT, Re = 125,000, $k = 2.0$)



Measurement Location Points

x/c	$x - x_{T.E.}$ (mm)	ΔY (mm)
1.002	1.0	1.0
1.025	12.7	1.5
1.050	25.4	2.0
1.075	38.1	3.0
1.100	50.8	4.0
1.125	63.5	5.0
1.150	76.2	6.0
1.175	88.9	7.0
1.200	101.6	8.0

Figure 5.2: LDA measurement locations

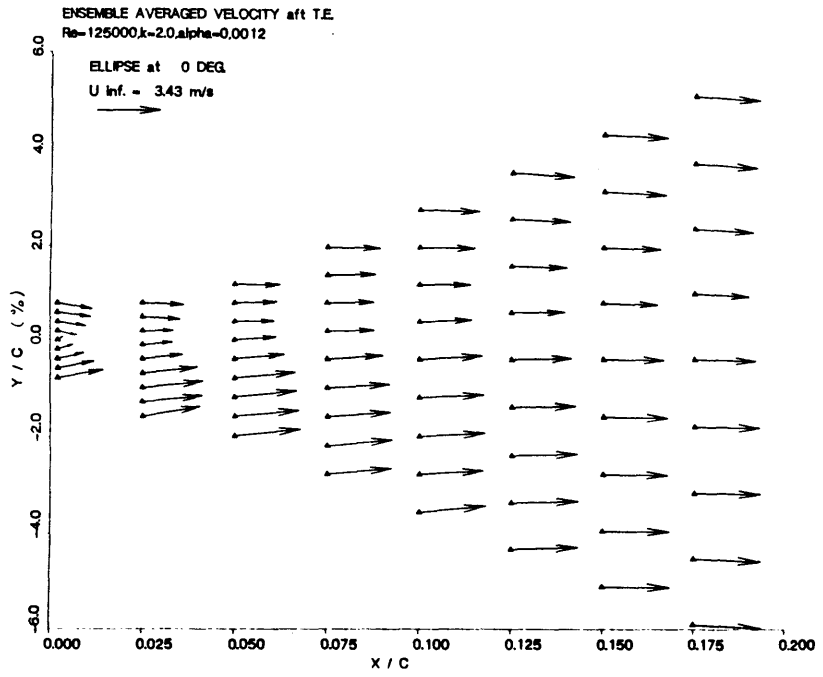


Figure 5.3: Ensemble averaged velocity vectors at ellipse of 0° (LTWT, Re = 125,000, $k = 2.0$)

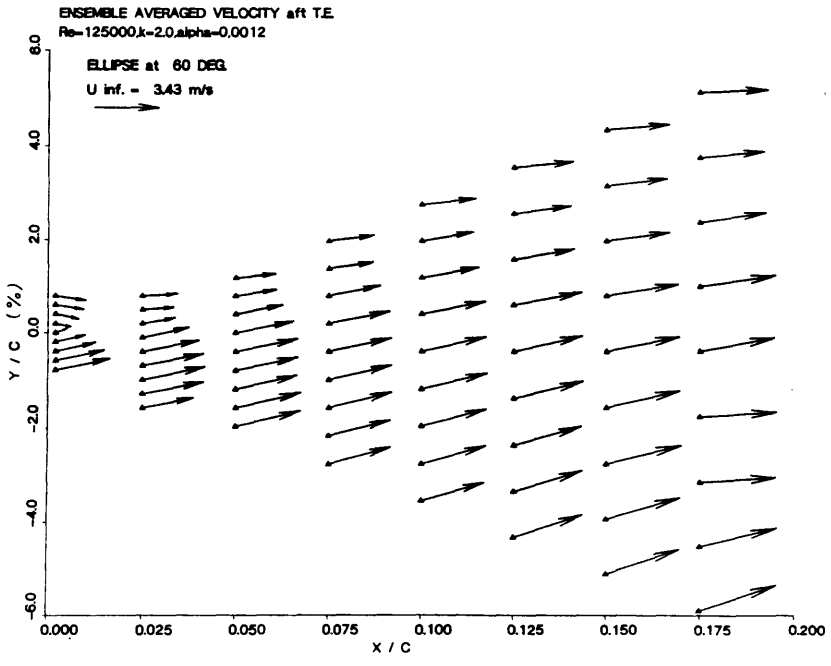


Figure 5.4: Ensemble averaged velocity vectors at ellipse of 60° (LTWT, Re = 125,000, $k = 2.0$)

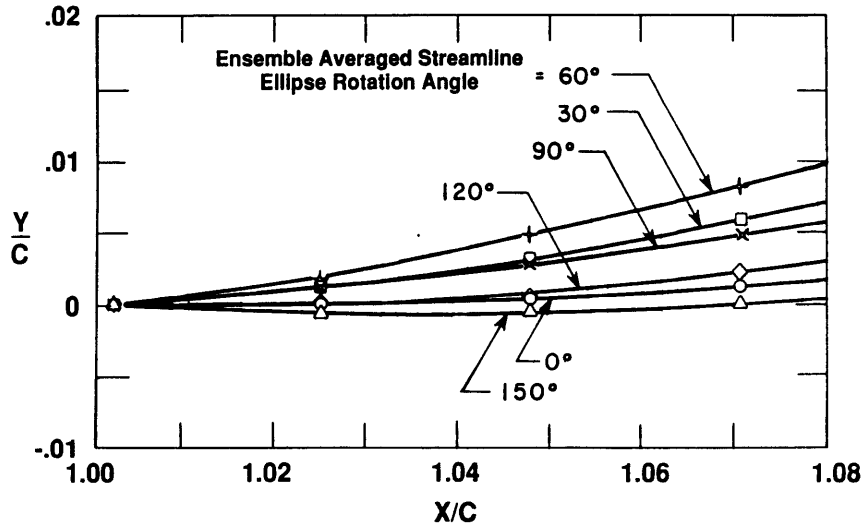


Figure 5.5: Ensemble averaged streamlines aft of 0012 trailing edge, enlarged for clearity (LTWT, Re = 125,000, k = 2.0)

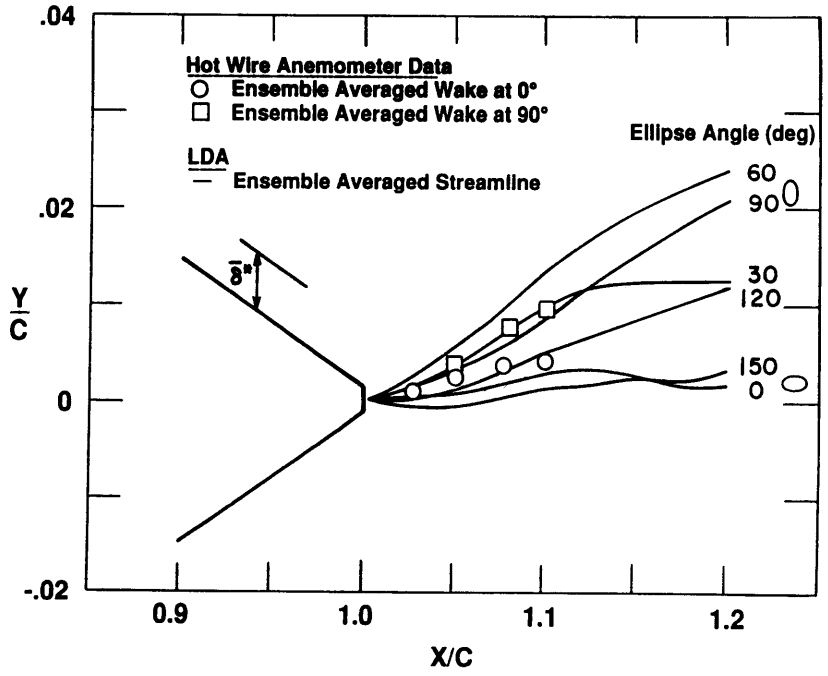


Figure 5.6: Ensemble averaged streamlines aft of 0012 trailing edge (LTWT, Re = 125,000, k = 2.0)

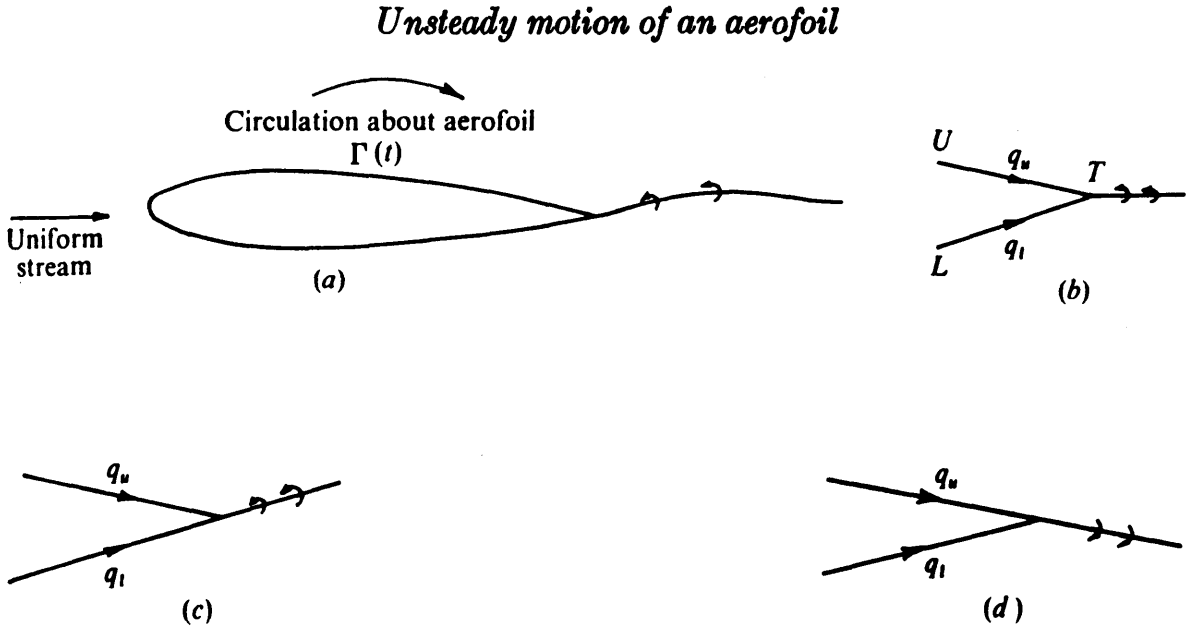


Figure 5.7: Maskell's model for streamlines leaving the trailing edge tangentially. (See Basu and Hancock)

Chapter 6

Dynamics of Laminar Separation Bubbles in *Steady* External Flow

This chapter focuses on the dynamics of laminar separation bubbles in steady external flow. The basic motivation is to investigate the balance of forces in the region of laminar separation and the validity of the assumptions in the boundary layer approximation. The present status of steady laminar boundary layer separation will first be briefly reviewed. The major effort is to examine the magnitude of terms in the x and y Navier-Stokes equations in the laminar separation region. The result of this study is applicable to analytical or numerical modeling of the forward portion of a laminar separation bubble. Test is conducted on the Wortmann FX63-137 airfoil at $\alpha = 0°$, Re =125000, and 0.05% tunnel turbulence level (LTWT).

6.1 Laminar boundary layers near separation – present status

F.T. Smith [68] recently reviewed the state of the art of steady and unsteady boundary-layer separation. For two-dimensional boundary-layer separation in steady external flow, he concluded that "separation is well accounted for overall and, following very recent studies, the nature of large-scale eddies seems on the verge of

being resolved as well." The Goldstein type singularity [31] at the point of laminar separation when calculating the boundary layer specifying the free-stream as a boundary condition has been a topic for research for many years. The basic mechanism is now considered understood as due to not allowing the free-stream condition, pressure or edge velocity, to be coupled with the calculation; this singularity is not a physical property of the flow. In fact, Leal's [36] results indicate that in the vicinity of separation the skin friction varies linearly with distance from the separation point, as predicted by Dean [19], and not as the square root of the distance, as would be the case if a Goldstein type singularity were to exist.

Recent works by Varty and Currie [76] and by Mathioulakis and Telionis [45] suggest that the boundary-layer approximation is valid through the point of laminar separation. These two works tested the flow over a cicular cylinder, hence used a cylindrical wall coordinate. Their examination of the boundary layer approximation is in the context of how well does the approximation apply in Cartesian coordinates as opposed to cylindrical.

6.2 Velocity profiles near laminar separation

The boundary layer on the suction surface of the Wortmann airfoil at $Re = 125000$ and $\alpha = 0^o$ in steady flow is measured by the LDA system. Data are taken at 48%, 50%, 52%, 54%, and 56% chord. The u-velocities are measured directly but the v-velocities are calculated numerically from the continuity equation; limited seeding in the transverse direction to the wall prevents direct LDA measurement of the v component. The x and y coordinates are parallel and normal to the wall, respectively.

Figures 6.1 and 6.2 present u and v velocity profiles near the point of laminar separation in steady flow. The u velocity profile clearly indicates the forward region of the laminar separation bubble; the location of the laminar separation point is closest to 51% chord. Note that there is a region of reverse flow near 55% chord.

The v velocity profile, figure 6.2, indicates that in the region forward and aft of laminar separation (near 48% and 55% chord, respectively) about 20% of the free-stream is ejecting into the potential region. Near laminar separation, about 25% to 30% of the free-stream is ejecting into the outer flow. Brown and Stewartson [10] explained this phenomenon as: "Here the main stream, which hiterto been in close contact with the body, suddenly, and for no obvious reason, breaks away, and downstream forms a region of eddying flow, which is usually turbulent even if the flow elsewhere is laminar, is set up." The amount of fluid ejection is probably much higher if the boundary layer were not to reattach further downstream.

The skin friction is shown in figure 6.3 and the displacement and momentun thicknesses are presented in figure 6.4. For this particular flow situation, the skin friction vanishes at 50.8% chord with the displacement thickness of 0.53% chord and momentum thickness of 0.13% chord. Figure 6.4 shows that the displacement thickness increases rapidly passing the point of laminar separation with the momentum thickness essentially increases at same rate as upstream. This means that the boundary layer is quickly thickening with no drastic increase of flow momentum deficit.

6.3 Values of terms in the Navier-Stokes equation near separation

The boundary layer approximation is known to be valid when the boundary layer is thin, Reynolds number is large, and no separation of flow occurs anywhere. In this case, the streamwise boundary layer equation becomes parabolic and the transverse equation is of the order of boundary layer thickness to chord and can be neglected. The natural question which arises in the context of the present work is how valid is the approximation at low chord Reynolds number, order of 10^5, in the region near laminar separation?

In answering these quesitons, data presented in the last section is used to cal-

culate velocity terms in the steady 2-D Navier-Stokes equation:

$$u^*\frac{\partial u^*}{\partial x^*} + v^*\frac{\partial u^*}{\partial y^*} = -\frac{1}{2}\frac{\partial C_p}{\partial x^*} + \frac{1}{Re}(\frac{\partial^2 u^*}{\partial x^{*2}} + \frac{\partial^2 u^*}{\partial y^{*2}}) \tag{6.1}$$

$$u^*\frac{\partial v^*}{\partial x^*} + v^*\frac{\partial v^*}{\partial y^*} = -\frac{1}{2}\frac{\partial C_p}{\partial y^*} + \frac{1}{Re}(\frac{\partial^2 v^*}{\partial x^{*2}} + \frac{\partial^2 v^*}{\partial y^{*2}}) \tag{6.2}$$

All lengths are normalized by the chord and velocities by the free-stream.

The values of terms in the x-momentum equation, corresponding to x/c= 48%, 50%, 52%, and 54% chord, are presented in figures 6.5 to 6.8. The displacement and momentum thicknesses are also drawn for reference. Several points are worth noting. First, the displacement thickness location (δ^*) divides regions where the viscous terms can be neglected; potential terms dominate for $y > \delta^*$ and viscous terms are also important for $y < \delta^*$. Secondly, extrema for the convection terms are also located near δ^*. The term $v^*\frac{\partial u^*}{\partial y^*}$ maximizes here mainly because $\frac{\partial u^*}{\partial y^*}$ peaks at the point of inflexion, which is near δ^*. The term $u^*\frac{\partial u^*}{\partial x^*}$ minimizes here due to a balance between the adverse pressure gradient and $v^*\frac{\partial u^*}{\partial y^*}$. Thirdly, from the numerics, the smallest term is $\frac{1}{Re}\frac{\partial^2 u^*}{\partial x^{*2}}$. A comparison of this term with the largest term in equation (6.1) will be studied later in the section. Fourthly, large variation of the streamwise pressure gradient, $\frac{1}{2}\frac{\partial C_p}{\partial x^*}$, of order of the convection terms, exists across boundary layer. This is inferred from the sum of $u^*\frac{\partial u^*}{\partial x^*}$ and $v^*\frac{\partial u^*}{\partial y^*}$, since the viscous terms are small in the outer portion of the boundary layer. This variation implies that $\frac{1}{2}\frac{\partial C_p}{\partial y^*}$ is not negligible.

The values of terms for the y-momentum equation are plotted in figures 6.9 to 6.12, corresponding to the same streamwise locations as in figures 6.5 to 6.8. The force balance in the y-momentum equation reveal many similarities as the x equation, but two points relate to laminar separation are worth noting. First, $v^*\frac{\partial v^*}{\partial y^*}$ maximizes near δ^*. Since $v^* > 0$, this implies $\frac{\partial v^*}{\partial y^*} > 0$; the fluid is ejecting towards the potential flow region. Secondly, $u^*\frac{\partial v^*}{\partial x^*}$ changes sign across laminar separation; with $u^* > 0$ for most region in the flow, the streamwise variation of the vertical velocity peaks near the laminar separation point. Thirdly, these plots also confirmed

X/C

	48%	50%	52%	54%
δ_1/C	.0004%	.015%	.046%	.032%
θ/C	.0001%	.022%	.080%	.18%

Table 6.1: Error in neglecting $\frac{1}{Re}\frac{\partial^2 u^*}{\partial x^{*2}}$, ϵ_t

X/C

	48%	50%	52%	54%
δ_1/C	15.7%	14.3%	19.9%	19.0%
θ/C	14.7%	13.7%	17.4%	21.7%

Table 6.2: Ratio of convection term in the y-momentum equation to that in the x-momentum equation, ϵ_y

that $\frac{1}{2}\frac{\partial C_p}{\partial y^*}$ is of the same order as the convection terms. This is due to streamline curvature effect near the region of separation.

If the boundary layer approximation is considered applicable in this flow region, $\frac{1}{Re}\frac{\partial^2 u^*}{\partial x^{*2}}$ must be small compared to other terms. In studying the magnitude of this term, the ratio of the absolute value of this term to the absolute value of the largest term in (6.1) is calculated, i.e.

$$\epsilon_t \equiv \left|\frac{1}{Re}\frac{\partial^2 u^*}{\partial x^{*2}}\right| / |largest\ \ term\ \ in\ \ eqn.\,(6.1)| \tag{6.3}$$

Hence ϵ_t can be considered as the trucation error if $\frac{1}{Re}\frac{\partial^2 u^*}{\partial x^{*2}}$ is neglected. This quantity is evaluated at two locations: the displacement thickness and the momentum thickness. At the displacement thickness, the largest term is $v^*\frac{\partial u^*}{\partial y^*}$ for all streamwise position studied. At the momentum thickness, $v^*\frac{\partial u^*}{\partial y^*}$ is still the largest term except in the well separated region, $x/c = 54\%$ chord, where $\frac{1}{Re}\frac{\partial^2 u^*}{\partial y^{*2}}$ dominates.

The results are tabulated in table 6.1, which suggests that $\frac{1}{Re}\frac{\partial^2 u^*}{\partial x^{*2}}$ is indeed negligible in the forward portion of the laminar separation bubble. Perhaps this

is not too surprising since the separation is quite mild. At $x/c = 54\%$ chord, the dividing streamline is about 0.25% chord above the wall or a 'separation angle', angle which the dividing streamline makes with the wall, of approximately 4.8°.

Another aspect of the boundary layer approximation is that the y-momentum equation is assumed to be of order boundary layer thickness compared to the x-momentum equation. To examine the magnitude of the y-momentum equation compared to the x-momentum equation, the ratio

$$\epsilon_y \equiv \left| v^* \frac{\partial v^*}{\partial y^*} \right| / \left| v^* \frac{\partial u^*}{\partial y^*} \right| \tag{6.4}$$

is computed. The result is tabulated in table 6.2. The calculation show that this ratio is about 14% to 22% near the laminar separation location; this is not small. Neglecting this term in calculating the boundary layer numerically will contribute error in the surface pressure since the normal pressure gradient is not taken into account.

In summary, the present effort proves that near the laminar separation region of a long (O(chord)) laminar separation bubble at low chord Reynolds numbers ($10^5 < Re < 10^6$),

- the displacement thickness location (δ^*) divides regions where the viscous terms can be neglected; potential terms dominate for $y > \delta^*$ and viscous terms are also important for $y < \delta^*$.
- the term $\frac{1}{Re}\frac{\partial^2 u^*}{\partial x^{*2}}$ can be ignored compared to other terms in the x-momentum equation.
- the convection terms in the y-momentum equation are 14% to 22% of the corresponding x-momentum equation.
- the pressure gradient terms are of the same order as the convection terms, i.e. $\frac{\partial C_p}{\partial x^*} \sim O(u^* \frac{\partial u^*}{\partial x^*})$ and $\frac{\partial C_p}{\partial y^*} \sim O(u^* \frac{\partial v^*}{\partial x^*})$.

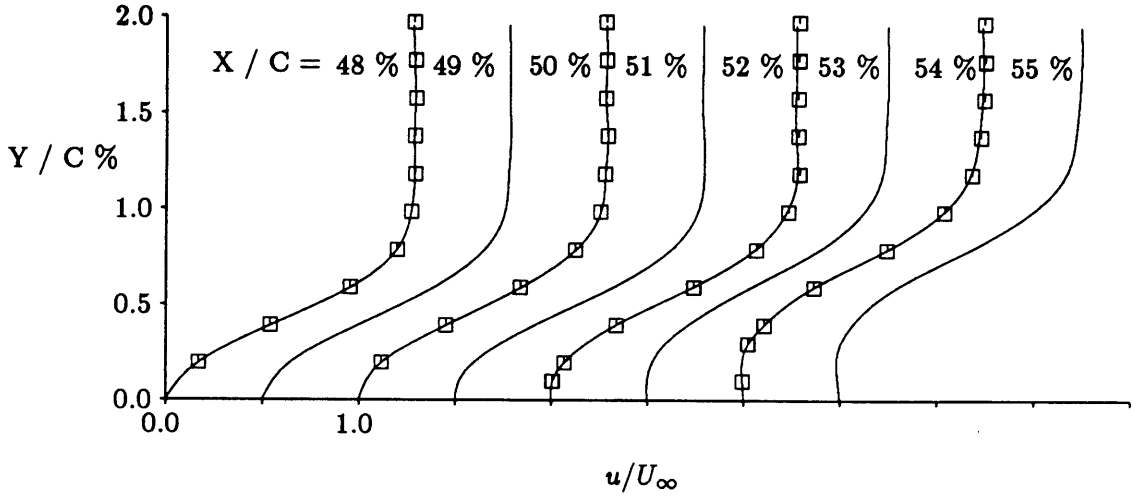


Figure 6.1: Steady boundary layer U-profile near laminar separation (Wortmann upper surface, LTWT, $Re = 125000$, $\alpha = 0^o$)

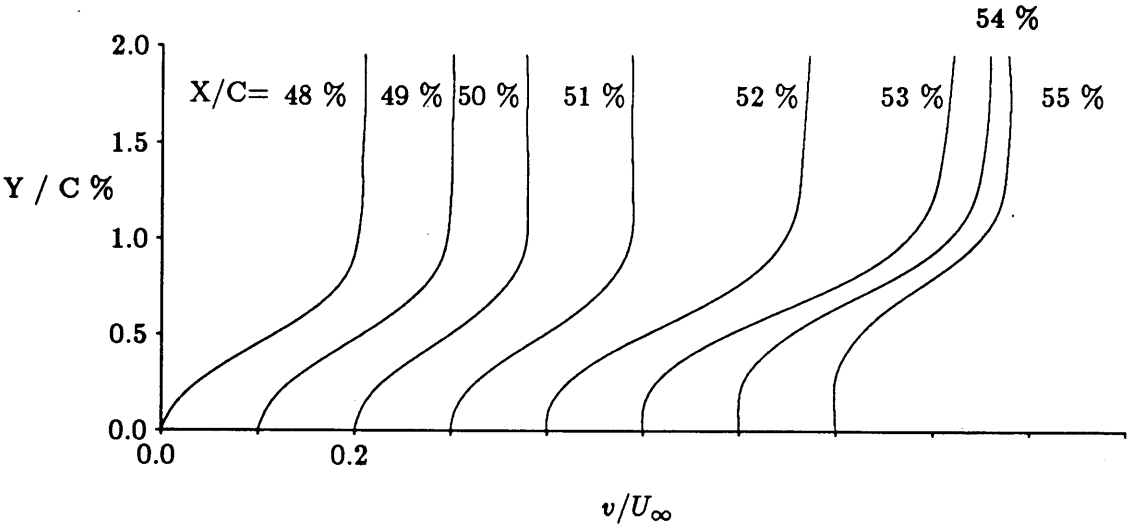


Figure 6.2: Steady boundary layer V-profile near laminar separation (Wortmann upper surface, LTWT, $Re = 125000$, $\alpha = 0^o$)

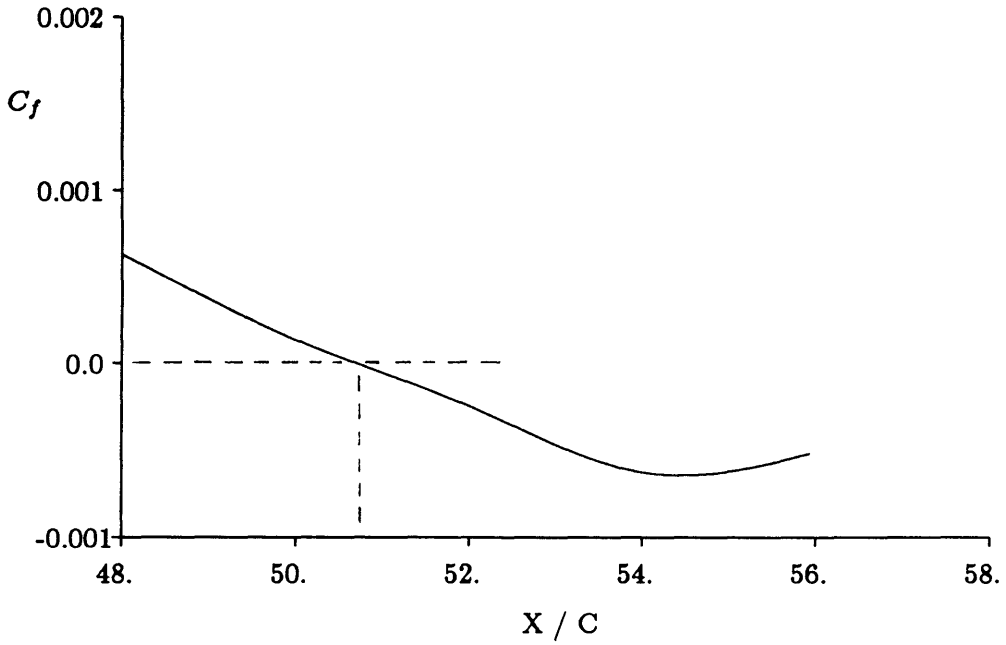


Figure 6.3: Skin friction of steady boundary layer near laminar separation (Wortmann upper surface, LTWT, $Re = 125000$, $\alpha = 0^o$)

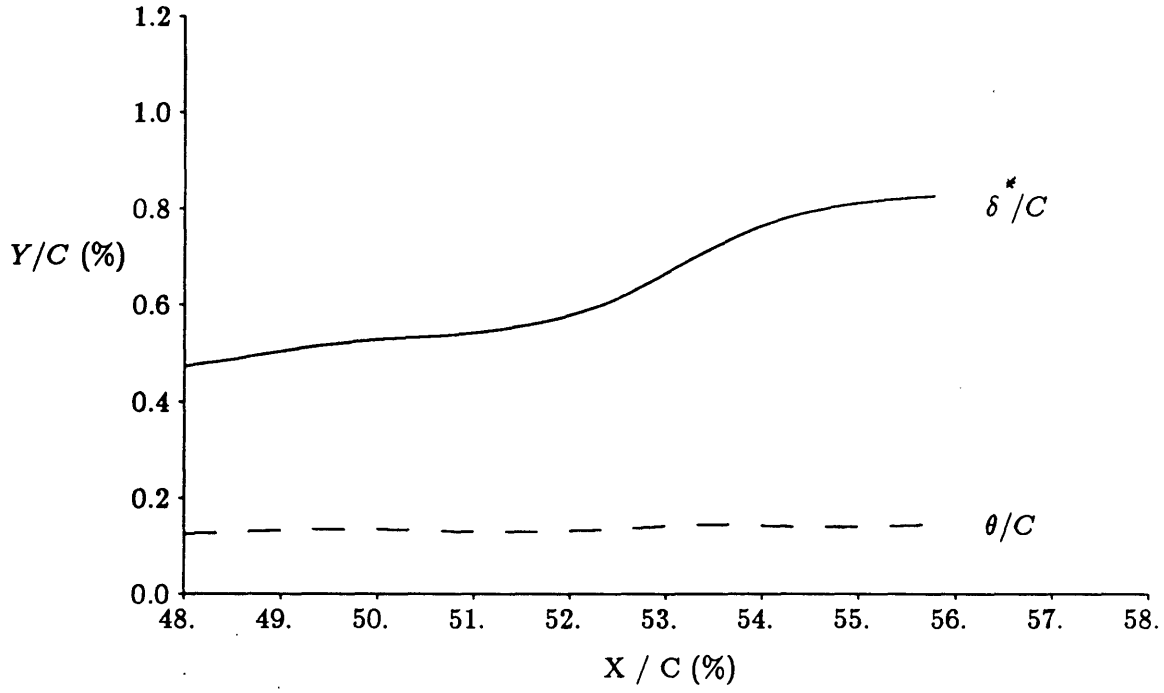


Figure 6.4: Steady boundary layer parameters near laminar separation (Wortmann upper surface, LTWT, $Re = 125000$, $\alpha = 0^o$)

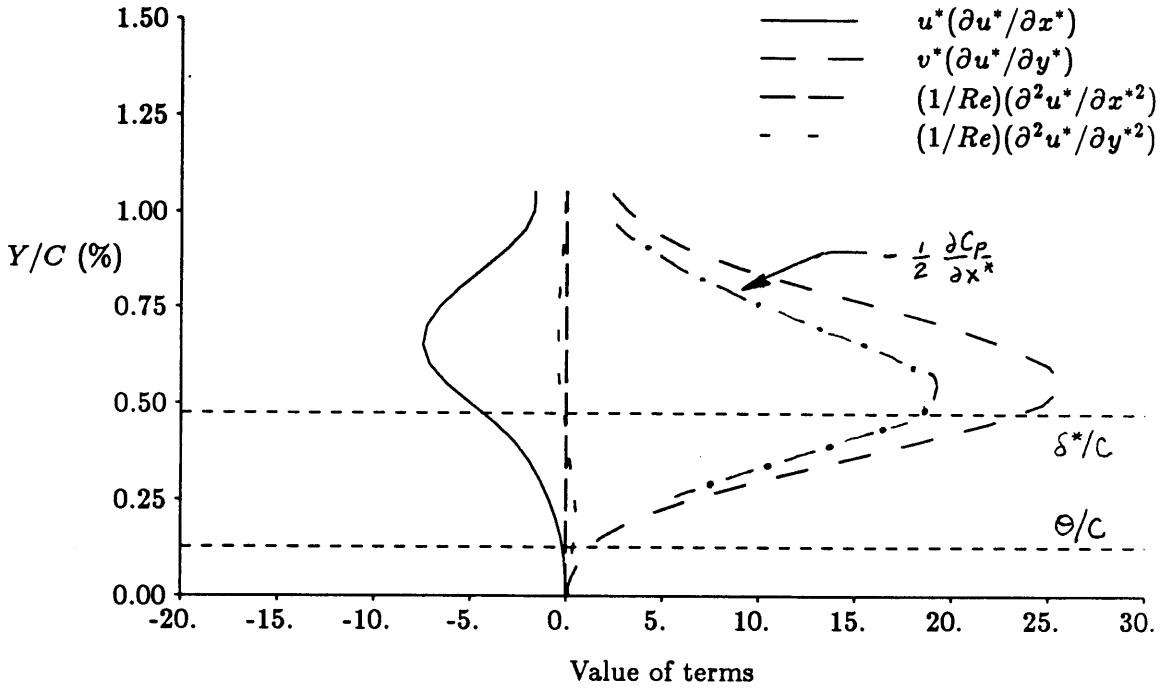


Figure 6.5: Values of terms in the X-momentun eq. (X/C= 48%) (Wortmann upper surface, LTWT, $Re = 125000$, $\alpha = 0^o$)

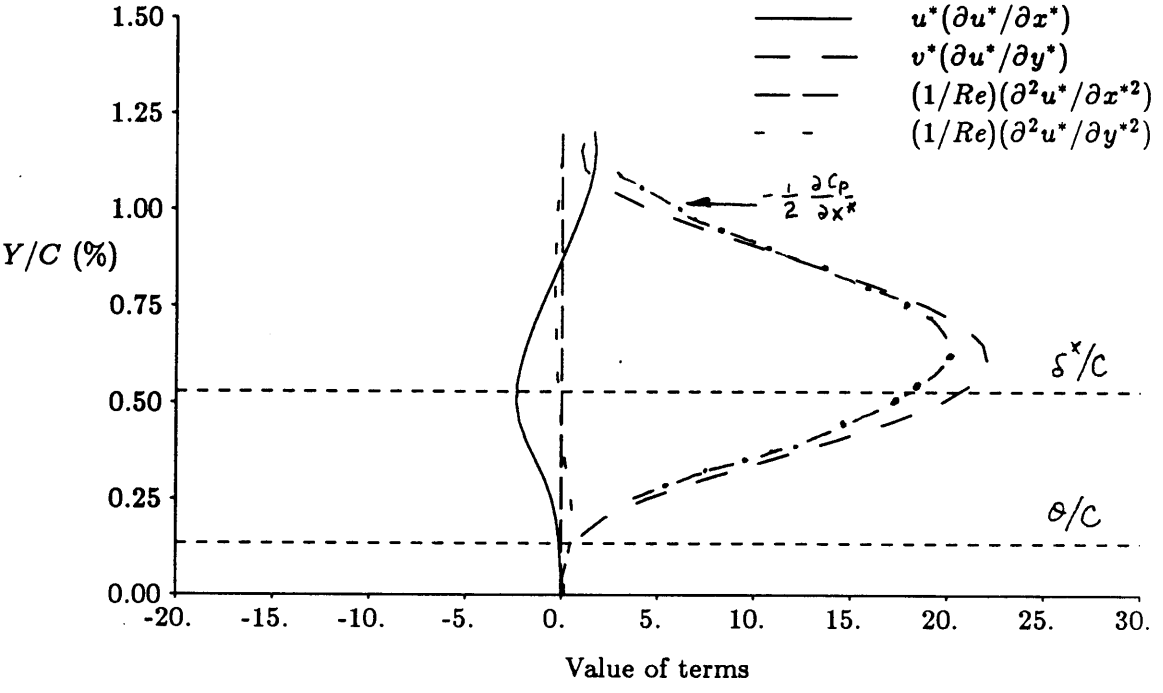


Figure 6.6: Values of terms in the X-momentun eq. (X/C= 50%) (Wortmann upper surface, LTWT, $Re = 125000$, $\alpha = 0^o$)

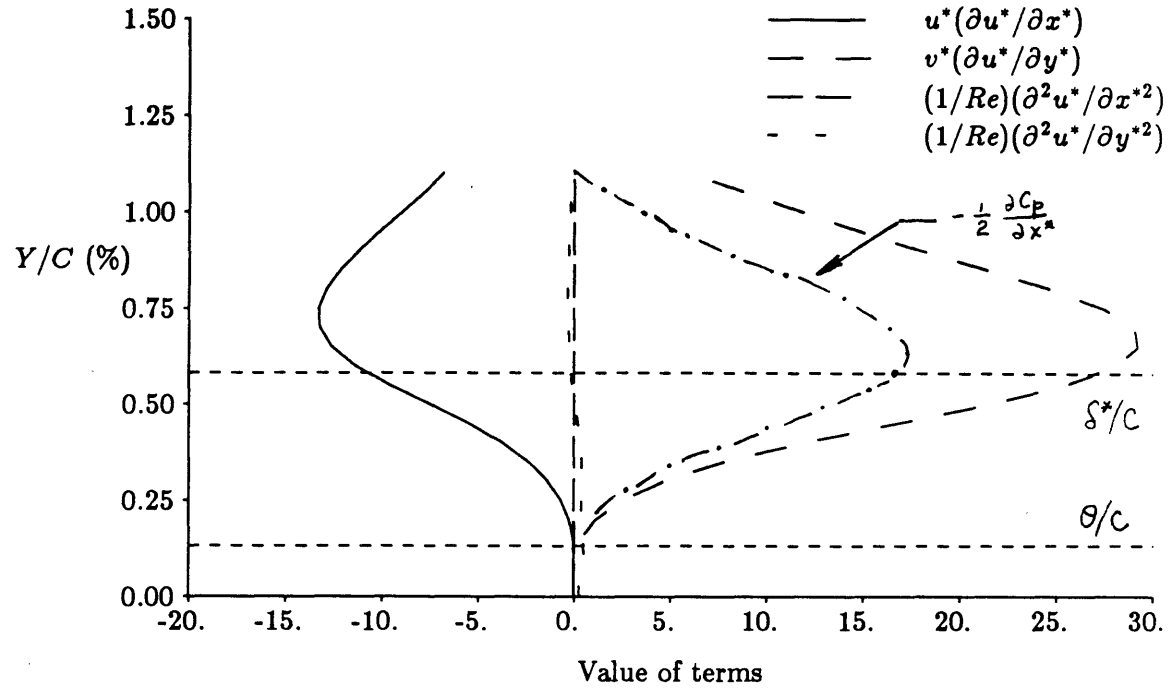


Figure 6.7: Values of terms in the X-momentumeq. (X/C= 52%) (Wortmann upper surface, LTWT, $Re = 125000$, $\alpha = 0^o$)

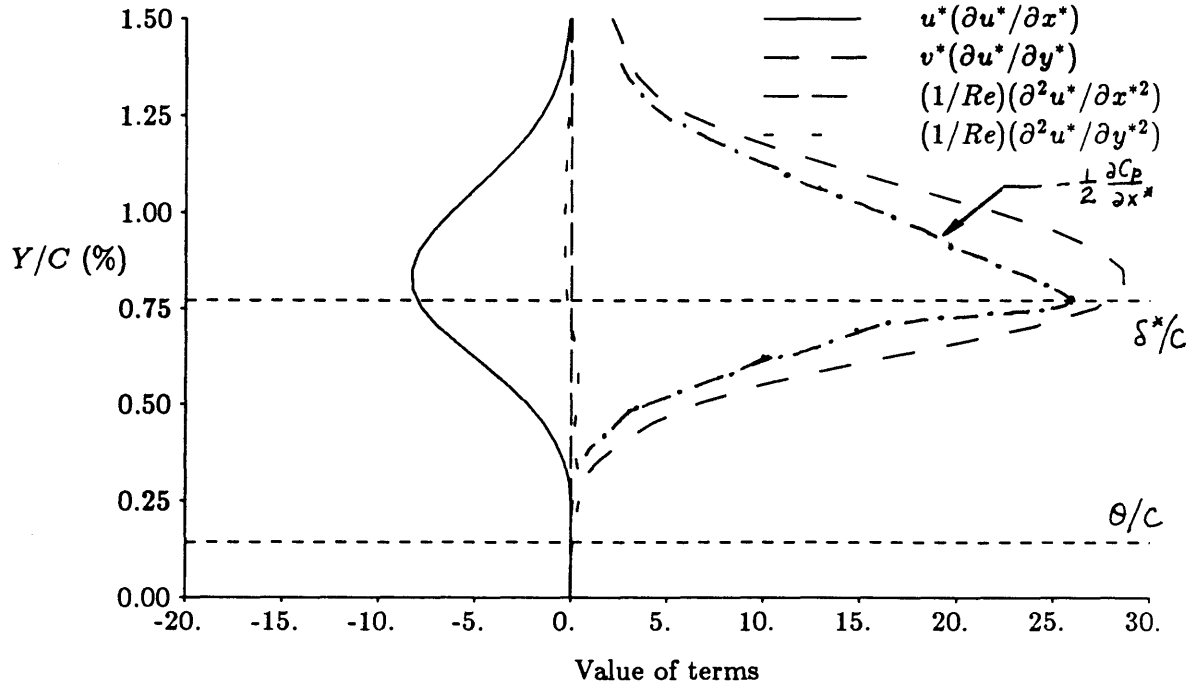


Figure 6.8: Values of terms in the X-momentumeq. (X/C= 54%) (Wortmann upper surface, LTWT, $Re = 125000$, $\alpha = 0^o$)

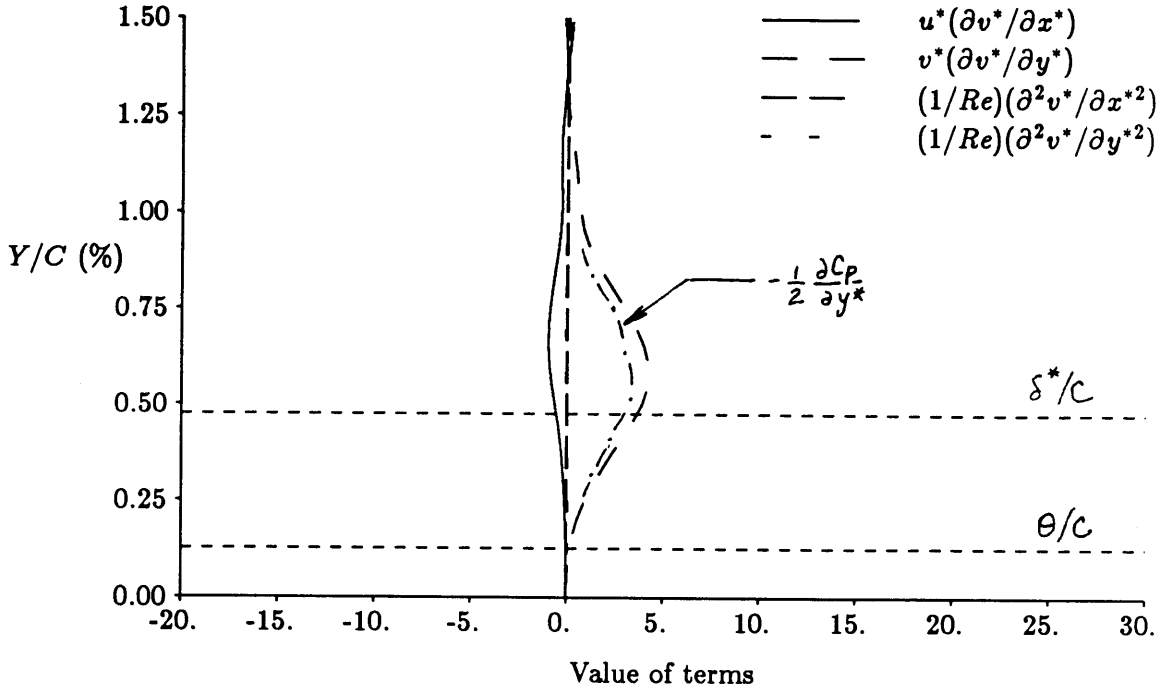


Figure 6.9: Values of terms in the Y-momentum eq. (X/C= 48%) (Wortmann upper surface, LTWT, $Re = 125000$, $\alpha = 0^o$)

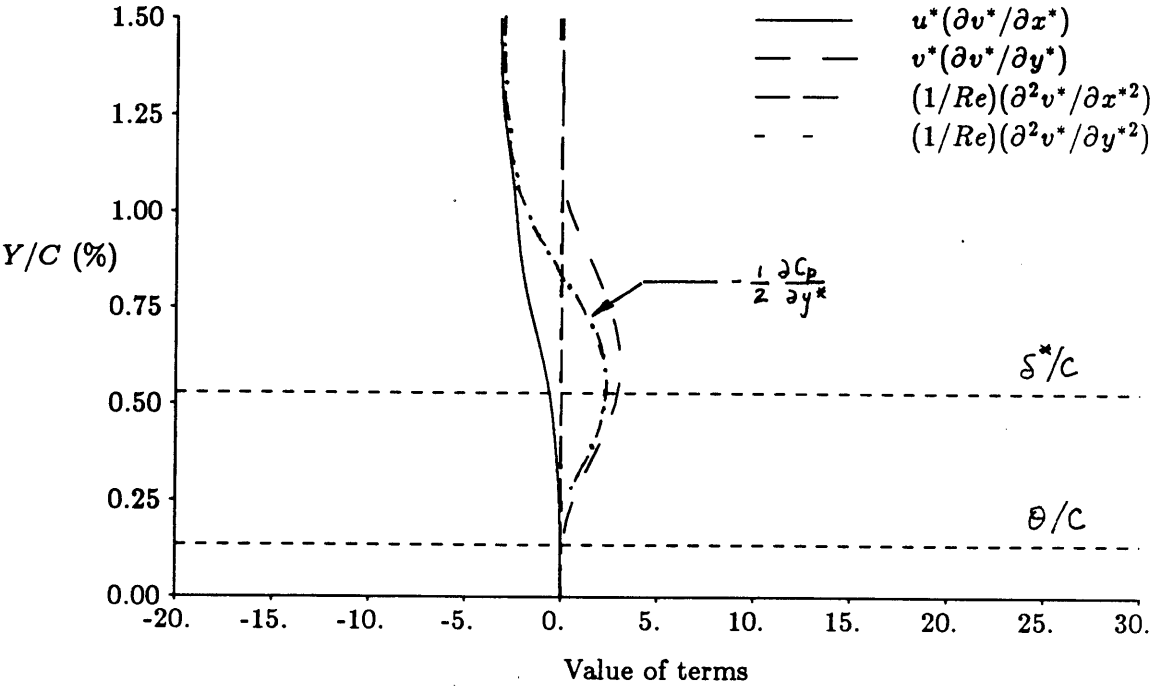


Figure 6.10: Values of terms in the Y-momentum eq. (X/C= 50%) (Wortmann upper surface, LTWT, $Re = 125000$, $\alpha = 0^o$)

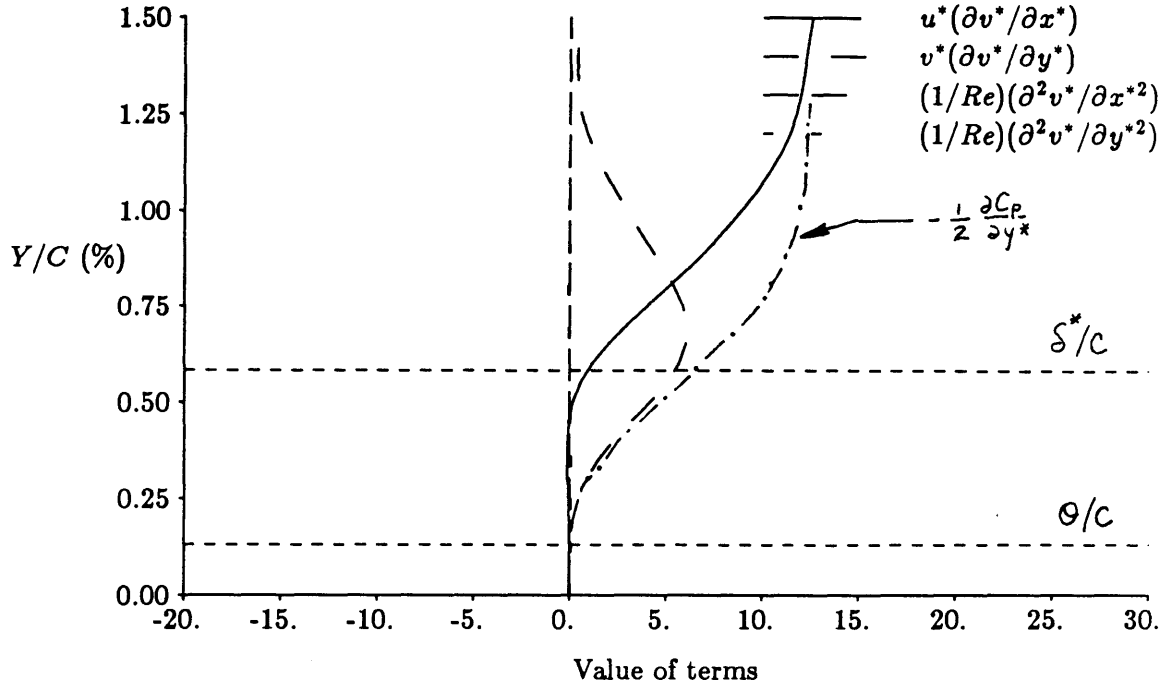


Figure 6.11: Values of terms in the Y-momentum eq. (X/C= 52%) (Wortmann upper surface, LTWT, $Re = 125000$, $\alpha = 0°$)

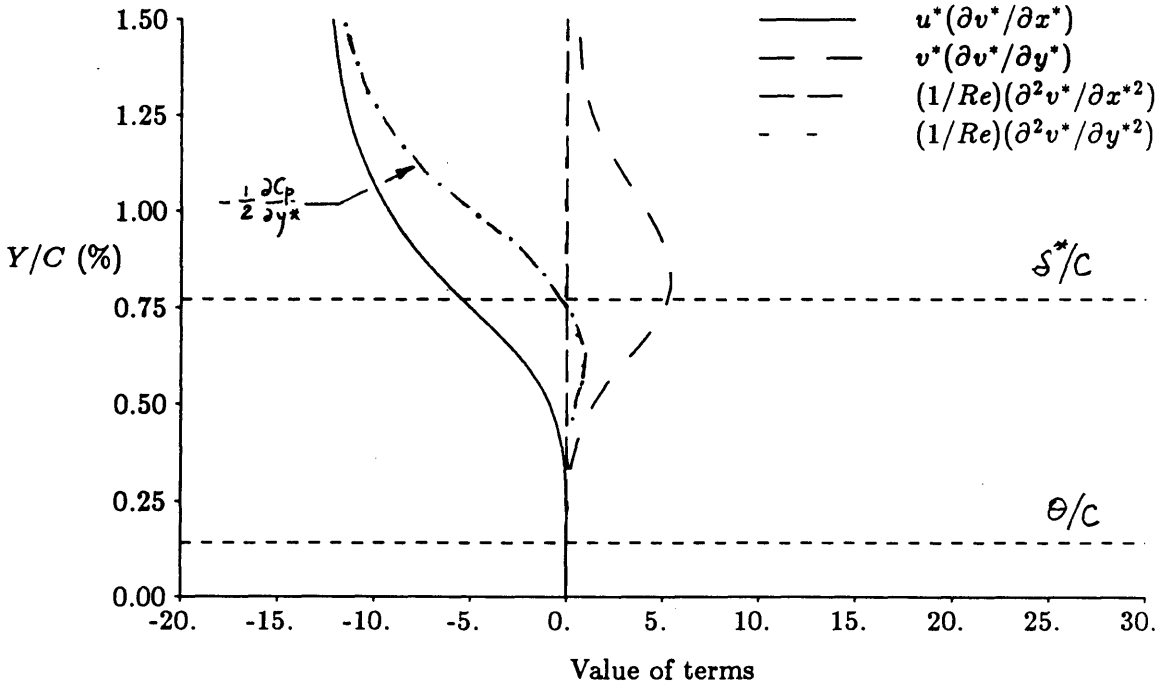


Figure 6.12: Values of terms in the Y-momentum eq. (X/C= 54%) (Wortmann upper surface, LTWT, $Re = 125000$, $\alpha = 0°$)

Chapter 7

Dynamics of Bubbles in *Unsteady* External Flow

With time as an additional independent variable, the boundary layer behavior exhibits many unexpected characteristics. Consider the response of a flat plate boundary layer with a small constant phase oscillating free-stream imposed on a steady stream, studied by Lighthill [37]. The pertinent reduced frequency parameter is $\omega x/U_\infty$. Figure 7.1 presents a sketch of the response of a boundary layer. The low frequency approximation is considered valid for $\omega x/U_\infty \leq 0.02$. This condition is chosen based on the phase lead of the skin friction with respect to the free-stream of less than 2 degrees. The high frequency approximation is valid for $\omega x/U_\infty \geq 0.6$ as derived by Lighthill. The boundary layer response is quasi-steady near the leading edge region and the high frequency limit apply sufficiently downstream. Hence, the boundary layer is in phase near the leading edge followed by a development of Stokes layer (Refer to Lighthill [37], Stuart [69], and Smith [68]). In the present work the boundary layer behavior is expected to lie in the intermediate to high frequency range, $(0.15 \leq k \leq 6.4)$.

The response of the forward portion of the bubble itself is contained under the research topic of *unsteady laminar separation.* In the early years of research in this field, it was believed that unsteady separation exhibit similar characteristics

as steady separation especially in defining the onset of flow separation. The idea of zero wall shear gave rise to the origin of separated wake flow downstream even in unsteady case was not uncommon. Breakthrough came in 1956 when Rott [62] presented an analysis of the unsteady flow in the vicinity of a stagnation point and observed that separation, in the sense of vanishing wall shear, was not expected. During the same year, Sears [66] proposed a generalized model postulating that the unsteady separation point was characterized by the simultaneous vanishing of velocity and shear at a point within the boundary layer as seen in a frame moving with the separation. Independently, Moore [49] in 1958 arrived at the same model describing separation as a point within the fluid. For an excellent review on the subject, refer to Williams [78] and Telionis [71].

The process of transition governs the behavior of the flow where the laminar separation bubble terminates. Due to the formation of vortical structures, the flow in this region is indeed very complex, especially in unsteady flow. Unlike steady flow where Tollmein-Schlichting waves only grow spatially, temporal growth also exists in unsteady flow. The flow field is further complicated due to the close proximity of the separated shear layer, where transition takes place, to the wall. Hot wire data [7], on the Wortmann suction surface at $Re = 105000$ and $\alpha = 7^o$, show that just upstream of the point of turbulent reattachment, where the shear layer is *furthest* away from the surface, the time mean boundary layer thickness is about 3% chord. In other words, the shear layer is not quite a *free* shear layer; it is bounded by the wall on one side. An attempt to predict the formation and extent of the transitional bubble in an unsteady external stream has been unsuccessful [9]. This is probably due to incomplete understanding of the transition process in conjunction with use of a time-average bubble model and the assumption that a separated laminar shear layer is similar to a free shear layer.

The purpose of this chapter is to study the effects of unsteadiness on the behavior of a laminar separation bubble. There are examples of external unsteadiness interacting with local behavior and drastically alter the flow structure. Acoustic wave

impinging on a globally separated airfoil can cause flow reattachment (Crighton [17] and Ahuja *et. al.* [1]). Tollmien-Schlichting waves can be attenuated with proper vibration of a flat plate in an otherwise steady flow (Gedney [30]). Vortex shedding on a cycular cylinder can be excited by external sound wave near the Strouhal frequency (Blevins [6]). The effect of imposed unsteadiness on the dynamics of a laminar separation bubble is a relatively unexplored area of low chord Reynolds number research.

Velocity profiles are measued by the Laser Doppler anemometer on the suction surface of the Wortmann airfoil at $Re = 125000$ and $k = 0.15$ and 2.0. These two reduced frequencies correspond to the intermediate frequency range, $k = 0.15$, and the high frequency approximation, $k = 2.0$, in the boundary layer response (see figure 7.1).

Data analyses reveal the following . First, secondary vorticity, of opposite sign to that of the unseparated boundary layer, exists within the boundary layer at $k = 0.15$. This phenomenon is not believed to have been documented previously. For $k = 2.0$, this flow feature is not observed. Secondly, the amplitude of unsteady velocity peaks within the boundary layer with maximum amplitude near six times that of the free-stream value for $k = 0.15$ and nine times for $k = 2.0$. Thirdly, a phase reversal is observed near the laminar separation region.

7.1 Unsteady laminar boundary layer near separation – present status

Perhaps the most active research on unsteady laminar boundary layer separation is being pursued by Prof. D.P. Telionis and his students at VPI&SU. In the last ten years, they have conducted a series of experiments on this phenomenon. Experimental setups consist of flow over i) a hump [34], ii) a flat plat with curved forward section [34], iii) a circular cylinder [45], and iv) an ellipse at an angle of attack [46]. The work of [34] consist mostly of detail flow visualization study on the

process of unsteady separation related to implusive acceleration and deceleration of the mean flow. Results reveal some fundamental similarities between these two types of imposed unsteady flow fields: i) the time scale which the flow require to adjust to its new pattern is of order L/U_∞, in qualitative agreement with the work of Tsahalis and Telionis [73], and ii) both flows exhibit strong influence on flow separation; a uniform acceleration essentially 'washes away' separation altogether where deceleration pushes separation upstream. Results for an oscillating external flow documented in [45] and [46] reveal the following. The work of [45] shows the local velocity amplitude is five times the amplitude at the edge of the boundary layer for Reynolds number, $U_\infty R/\nu$, of 71000, and reduced frequency, $\omega R/2U_\infty$, of 1.76. The phase also vary close to 100 degrees in the separated region compared to free-stream. The work of [46] tested at Reynolds number, based on major-axis $2a$, of 143000 and reduced frequency, $\omega a/U_\infty$, of 0.45 provide data for comparison with analytical and numerical results.

7.2 Measurement and discussions of unsteady velocity profiles near separation

The boundary layers on the suction surface at $\alpha = 0^o$ are measured using a two component LDA system. The external flow condition is $Re = 125000$, $k = 0.15$ (0.33 $Hz.$) and $k = 2.0$ (4.4 $Hz.$). The chordwise measurement locations are near the laminar separation point in steady flow, as suggested by the pressure plateau of figure 4.1. The emphasis is on the unsteady boundary layer behavior in the region of laminar separation.

7.2.1 Time mean velocity profiles

Figures 7.2 and 7.3 present the time mean unsteady streamwise boundary layer profiles for $k = 0.15$ and 2.0. The u-velocity profiles show that, in general, the region of reverse flow increases downstream. For $k = 0.15$ at 50% chord, there

exhibit an unusual feature near 0.5% above the surface. Close examination of the points above and below show that the slopes do not overlap suggesting that the feature is physical. This feature will be explored further in later sections.

7.2.2 Velocity amplitude and phase

Data analyses on the unsteady boundary layer profiles in the region of laminar separation reveal that the amplitude contour reaches a maximum within the boundary layer. Figures 7.4 and 7.5 present the amplitude contour for $k = 0.15$ and 2.0. The peak amplitude is about six times that of the amplitude at the edge of the boundary layer for $k = 0.15$ and about nine times for $k = 2.0$. As for comparison, the solution to the classical Stokes's oscillating plate problem (at high frequency limit) also exhibits an overshoot within the boundary layer but with a much smaller magnitude; the maximum amplitude ratio is about 1.07. Note that the path of the amplitude maxima above the wall increases downstream. This path corresponds to the path of the time mean inflection points, refer to figures 7.2 and 7.3.

The amplitude maxima have also been observed by Mathioulakis and Telionis [45]. Figure 7.6 present their amplitude contour result. Telionis [71] suggests that the amplitude maxima corresponds to the station of flow separation. Hence, it is believed that the large amplitude ratio is related to separation of flow but analytical proof is needed.

The phase response, with respect to that at the edge of the boundary layer, is plotted in figures 7.7 and 7.8 for $k = 0.15$ and 2.0, respectively. At $k = 0.15$, data show that the phase generally varies across the boundary layer. At 50% chord, the flow exhibits a drastic change in phase at 0.5% chord above the surface. (Recall that this the location where the time mean velocity profile shows an unusual flow feature.) At 52% chord, two large changes in phase are also observed at 0.2% and 1.2% chord above the wall. At $k = 2.0$, figure 7.8 shows the Stokes layer near the wall and a reversal in phase as separation is approached.

7.2.3 Ensemble averaged velocity profiles

The ensemble averaged data reveal that at $k = 0.15$ secondary vortices exist, within the boundary layer, as the primary vortices from the upstream boundary layer are leaving the surface. Figures 7.10 to 7.17 present ensemble averaged streamwise veloctiy profiles over most of an unsteady cycle, from $t/T = 0.00$ to 0.77. The evolution of the secondary vortices is clearly shown. Flow behavior for the rest of the cycle resembles that of $t/T = 0.77$.

To study this feature in greater detail, figures 7.18 to 7.25 show the ensemble averaged velocity vectors at 50% chord in a reference frame convecting with the velocity at the center of this feature. Vorticity opposite to that in the upstream boundary layer are clearly seen for portion of the cycle. Note that $\frac{\partial u}{\partial y} \gg \frac{\partial v}{\partial x}$ which is indicative that the secondary vortices are organized more like a vortex sheet than discrete point vortices.

7.2.4 Ensemble averaged vorticity contours

The question remaining is: Where did the observed secondary vortices come from? For a 2-D incompressible baratropic flow, a fluid particle can only change its vorticity through the action of viscosity, as governed by the vorticity dynamic equation. Hence, *the origin of the secondary vortices can only be from the wall.* So the question is: where along the wall are these vortices generated?

In steady flow, the entire boundary layer upstream of the laminar separation point possess only one sign of vorticity with no mechanism to alter it. In the laminar separated region, the path of maximum negative velocity divides the flow distinctly into two regions of opposite vorticity, *with no vorticity with opposite sign within the other.* Therefore, it is reasoned that the presence of vorticity with opposite must be related to the dynamics of the unsteady boundary layer. There are two possible regions where opposite vortices may exist in unsteady flow: near the stagnation point and near the laminar separation point. As these points oscillate responding to changes in the unsteady boundary layer, negative vorticity may exist in the region

where it is predominatly positive, or vice versa. This argument is actually suggested by Moore [50] for the boundary layer with a moving separation point (see figure 7.33).

Ensemble averaged vorticity contours are computed to study the evolution of vorticity in the boundary layer[1] in hope of tracing the origin of the secondary vortices. The experimental data are splined and secondary order schemes are used in numerically differentiation. The vorticity is normalized by $\omega^* = U_\infty/C$ and contours of $100\omega^*$ are plotted. Figures 7.26 to 7.32 present the results corresponding to $t/T = 0$, 3.5%, 7%, 10.5%, 14%, 17.5%, and 22%, respectively.

This sequence of ensemble averaged vorticity contours clearly show the temporal evolution of the opposite vorticity region. At $t/T = 0$, there is little evidence of any unusual feature. Eventually, the region of opposite vorticity decreases in strength and reaches a value of $100\omega^* = -0.2$ at $t/T = 21\%$. Note that concurrent to the development of this feature, contour islands are formed above. Unfortunately, the spatial resolution is insufficient to trace the origin of the secondary vortices from the wall.

[1]Prof. Giles deserves credit for encouraging this method of analysis.

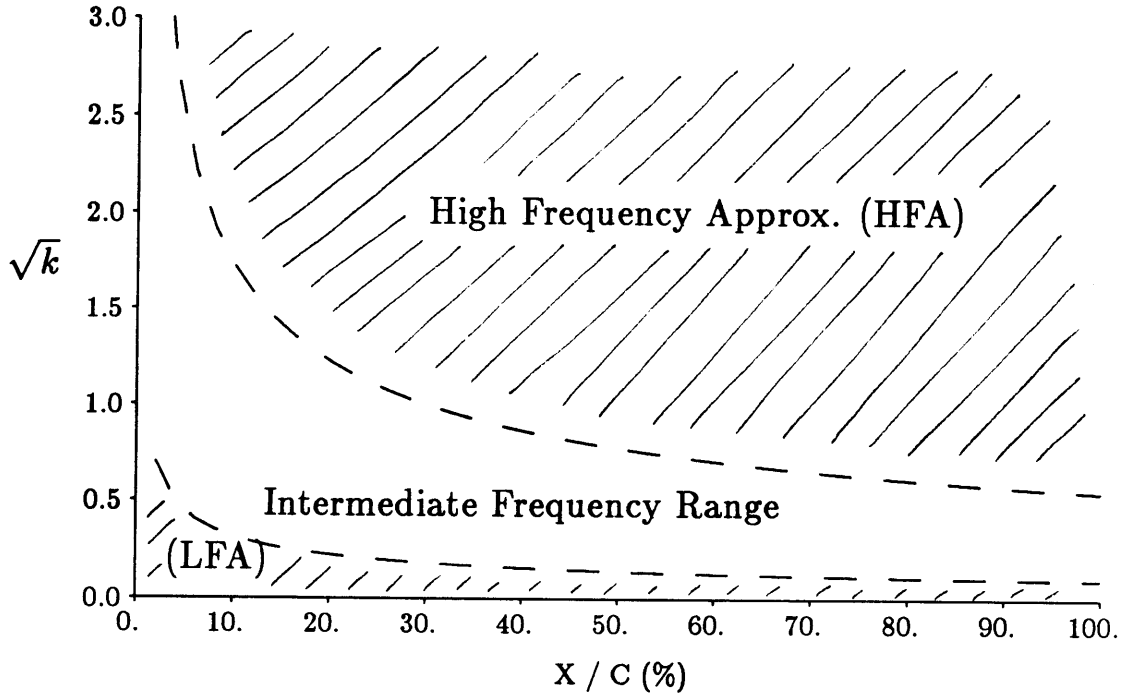


Figure 7.1: Low and High Frequency Approximations for an unsteady flat plate boundary layer Lighthill (1954) (LFA: $\omega x/U_\infty \leq 0.02$, HFA: $\omega x/U_\infty \geq 0.6$)

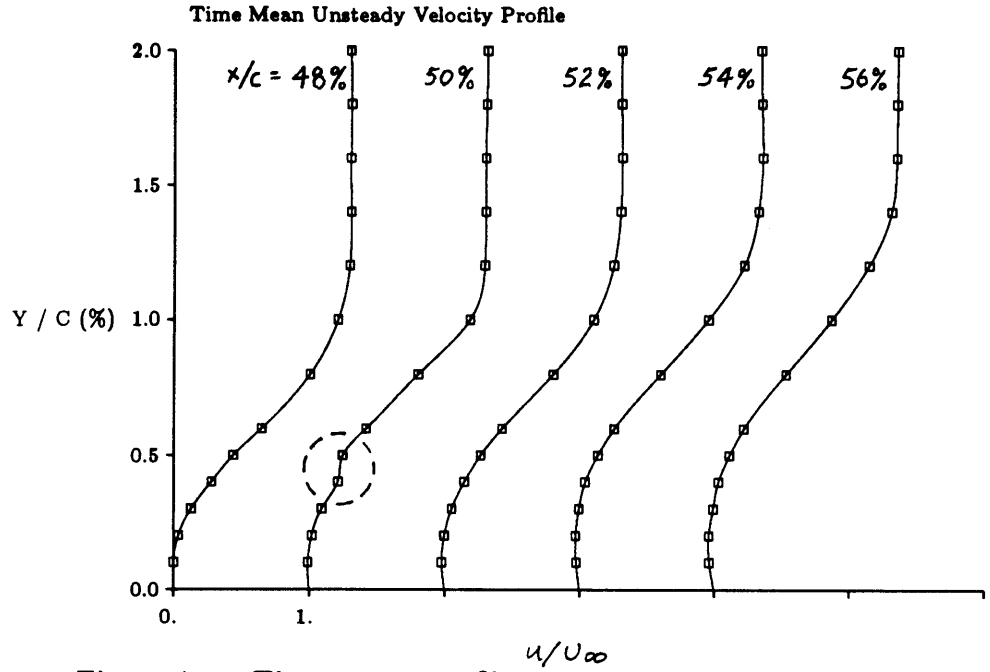


Figure 7.2: Time mean profile (Wortmann upper surface, LTWT, $Re = 125000$, $\alpha = 0°$, $k = 0.15$)

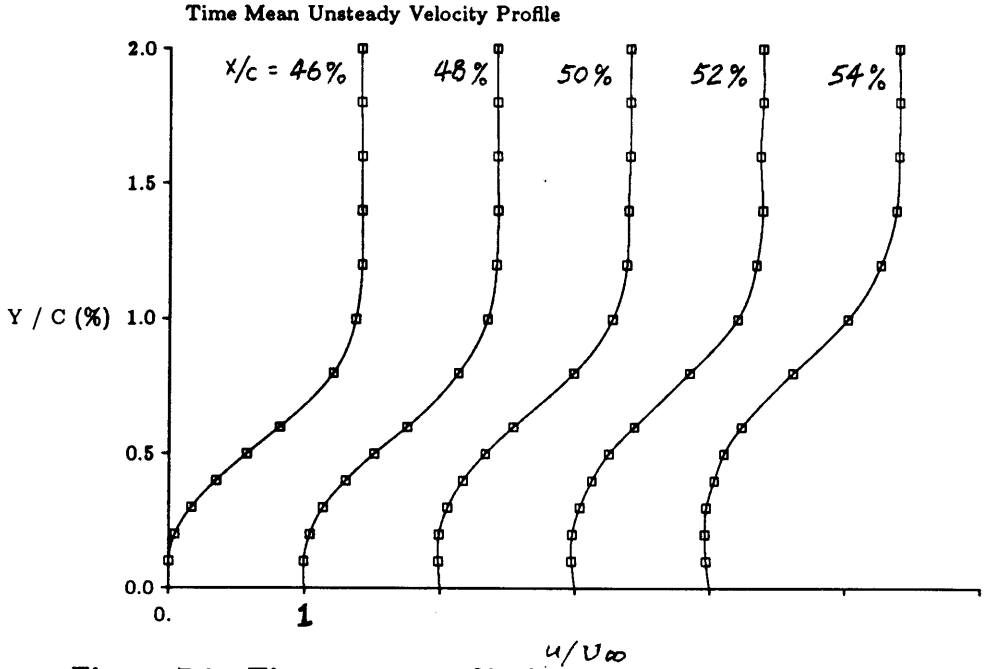


Figure 7.3: Time mean profile (Wortmann upper surface, LTWT, $Re = 125000$, $\alpha = 0°$, $k = 2.0$)

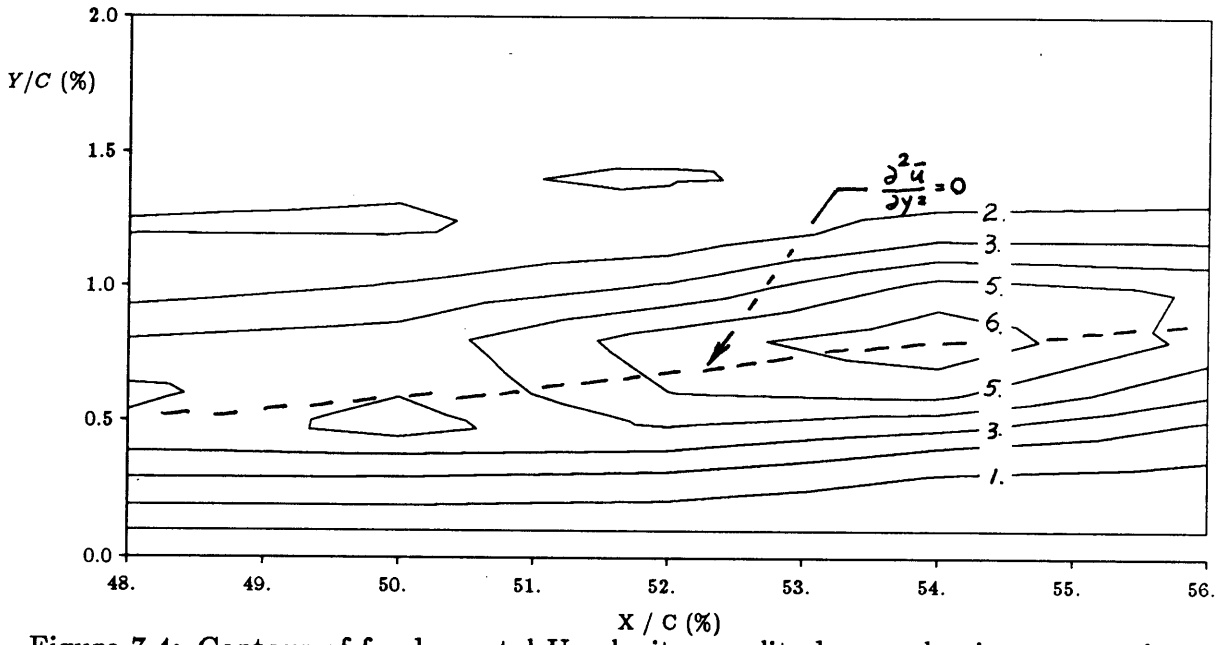


Figure 7.4: Contour of fundamental U-velocity amplitude near laminar separation normalized by local free-stream fundamental amplitude (Wortmann upper surface, LTWT, $Re = 125000$, $\alpha = 0^o$, $k = 0.15$)

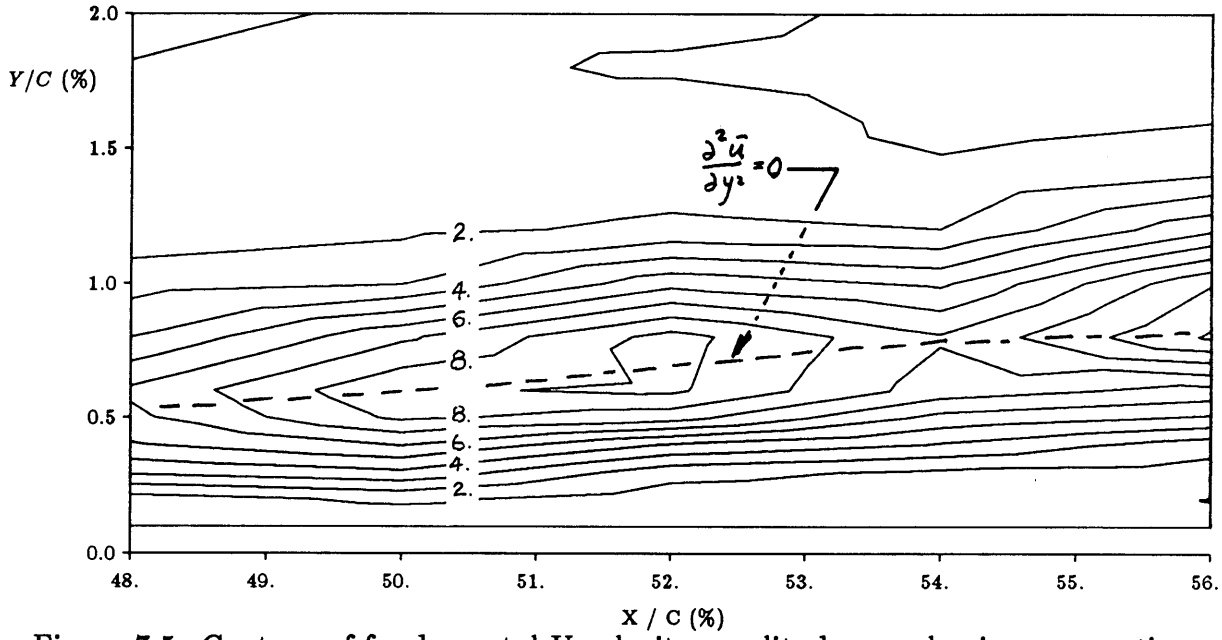


Figure 7.5: Contour of fundamental U-velocity amplitude near laminar separation normalized by local free-stream fundamental amplitude (Wortmann upper surface, LTWT, $Re = 125000$, $\alpha = 0°$, $k = 2.0$)

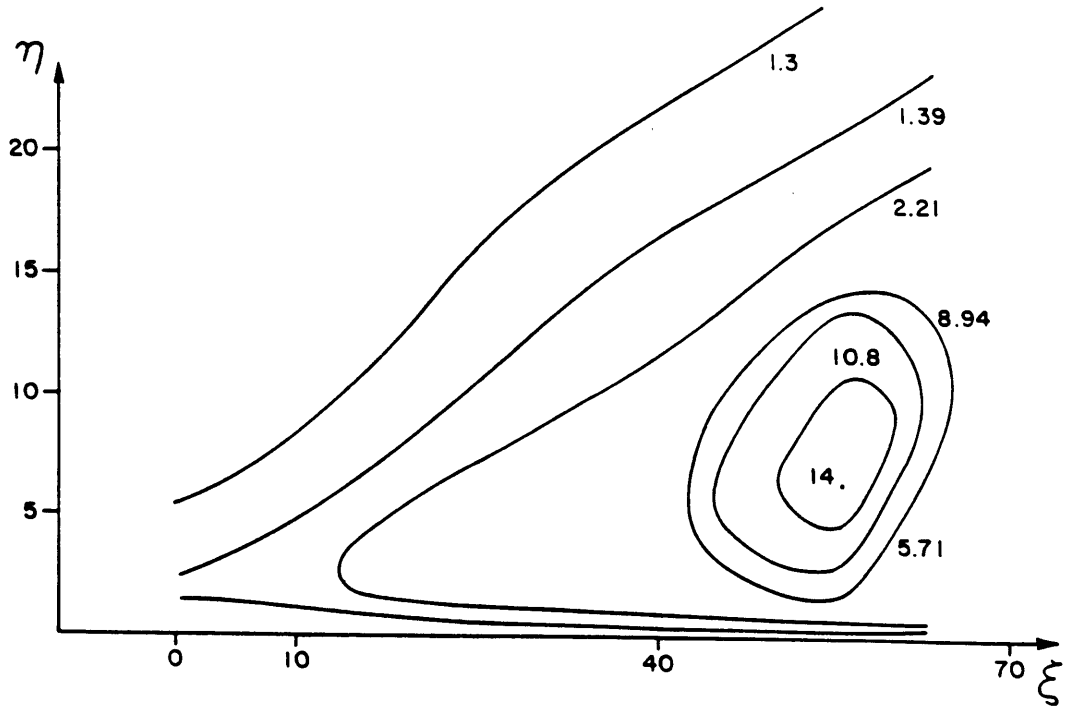


Figure 7.6: Curves of constant amplitude of oscillation in the neighborhood of separation for $f = 0.2Hz.$ obtained experimentally by Mezaris and Telionis (1980). The numbers in the figure denote the ratio of the velocity amplitude over the corresponding amplitude at the edge of the viscous region.

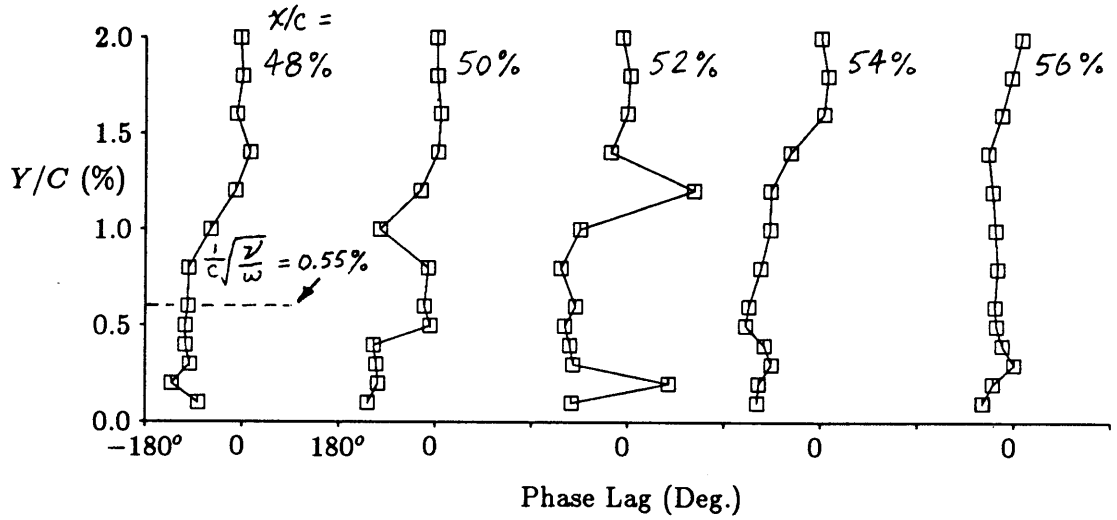


Figure 7.7: Phase Lag of U-velocity at fundamental freq. near laminar separation (Wortmann upper surface, LTWT, $Re = 125000$, $\alpha = 0^o$, $k = 0.15$)

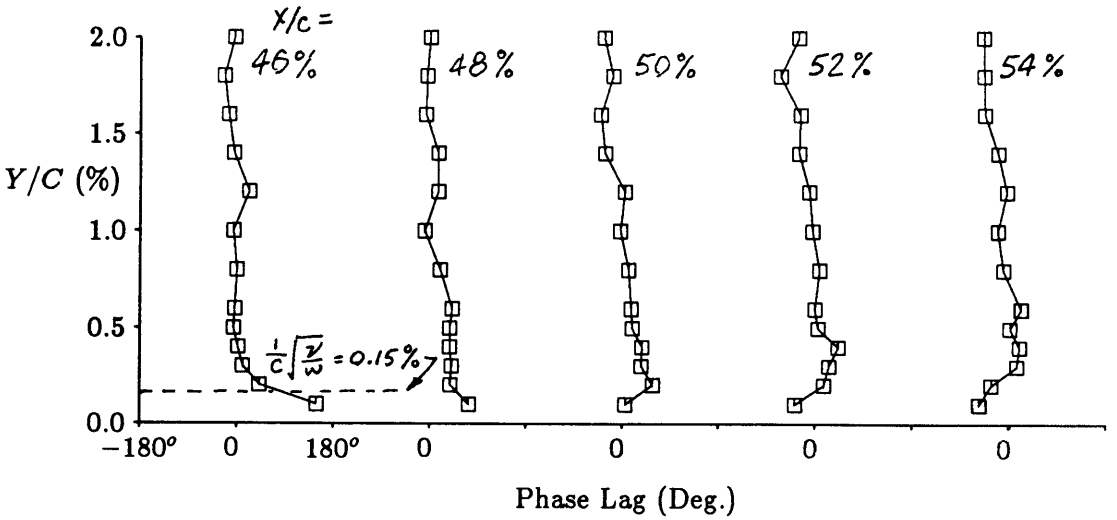


Figure 7.8: Phase Lag of U-velocity at fundamental freq. near laminar separation (Wortmann upper surface, LTWT, $Re = 125000$, $\alpha = 0^o$, $k = 2.0$)

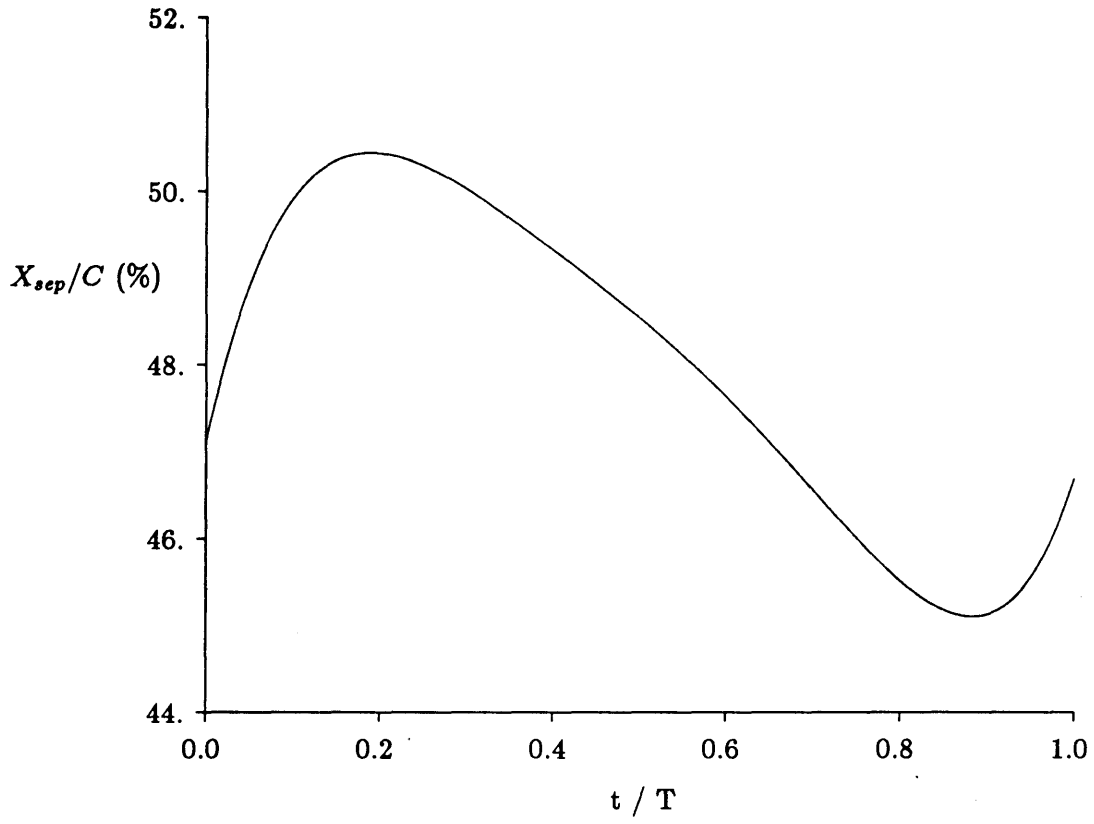


Figure 7.9: Excursion of laminar separation location (Wortmann upper surface, LTWT, $Re = 125000$, $\alpha = 0^o$, $k = 0.15$)

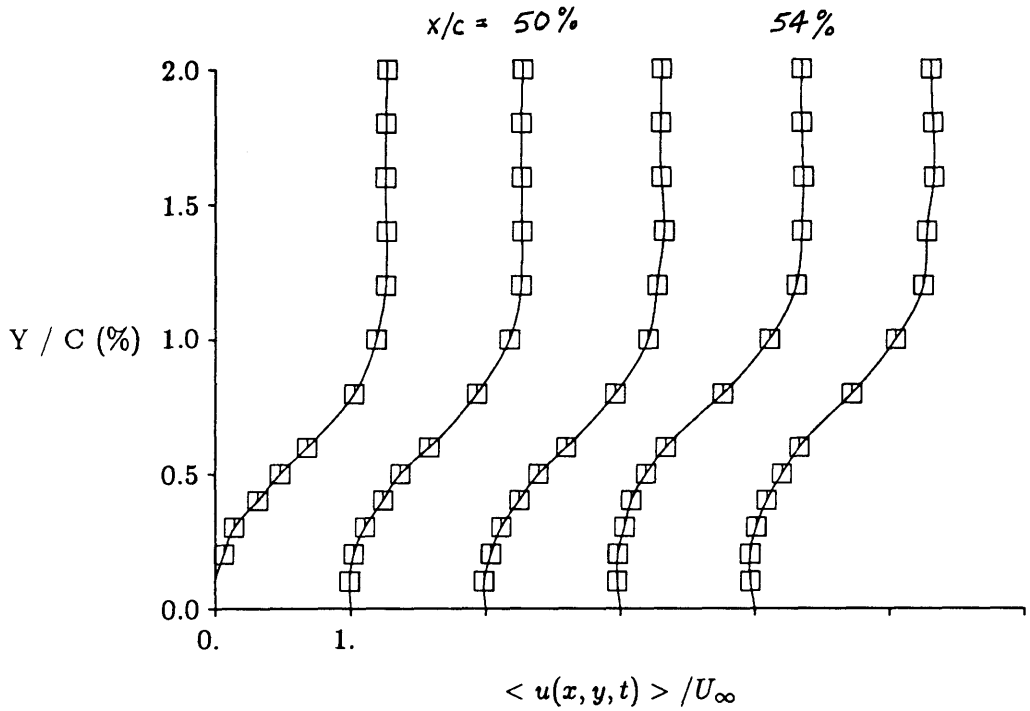


Figure 7.10: Ensemble Averaged U-velocity at $t/T = 0.00$ (Wortmann upper surface, LTWT, $Re = 125000$, $\alpha = 0^o$, $k = 0.15$)

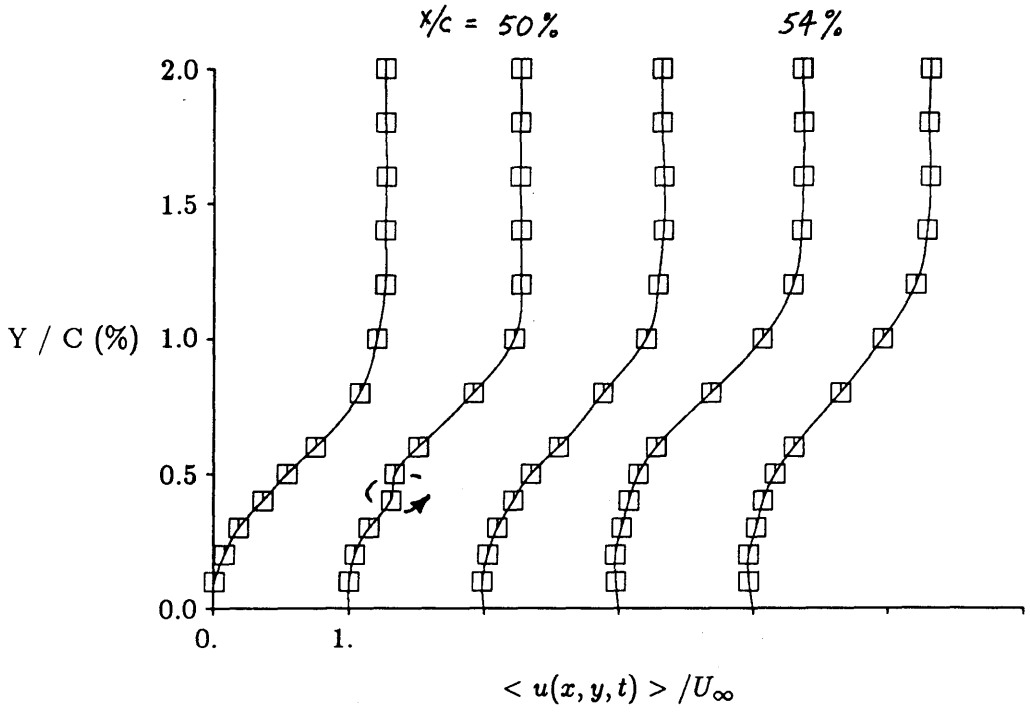


Figure 7.11: Ensemble Averaged U-velocity at $t/T = 0.11$ (Wortmann upper surface, LTWT, $Re = 125000$, $\alpha = 0^o$, $k = 0.15$)

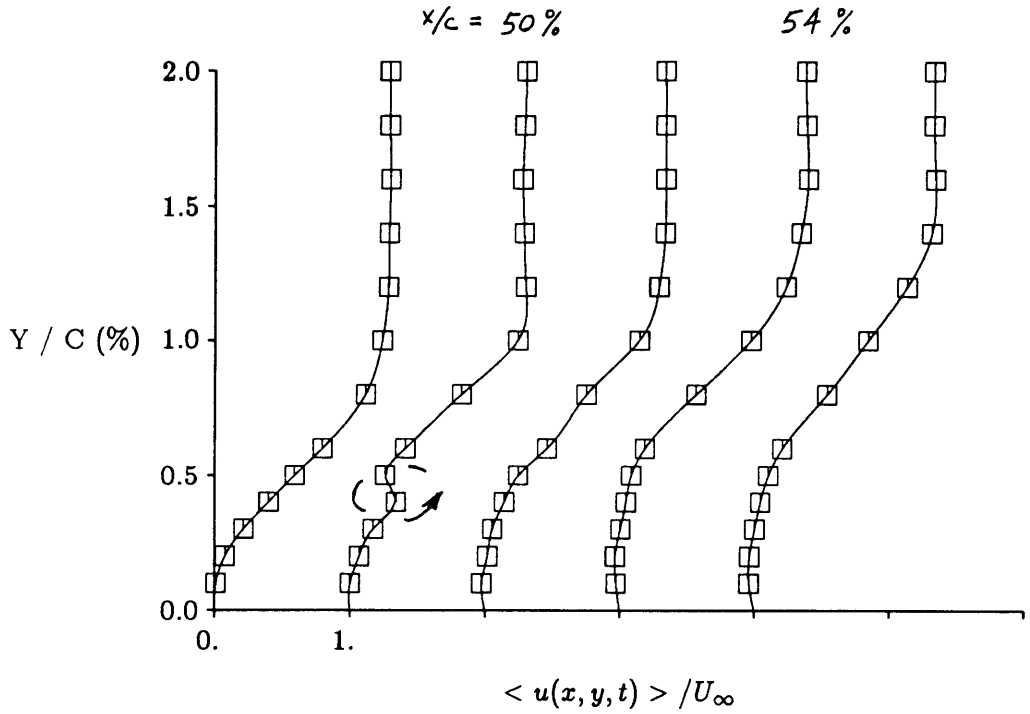


Figure 7.12: Ensemble Averaged U-velocity at $t/T = 0.22$ (Wortmann upper surface, LTWT, $Re = 125000$, $\alpha = 0^o$, $k = 0.15$)

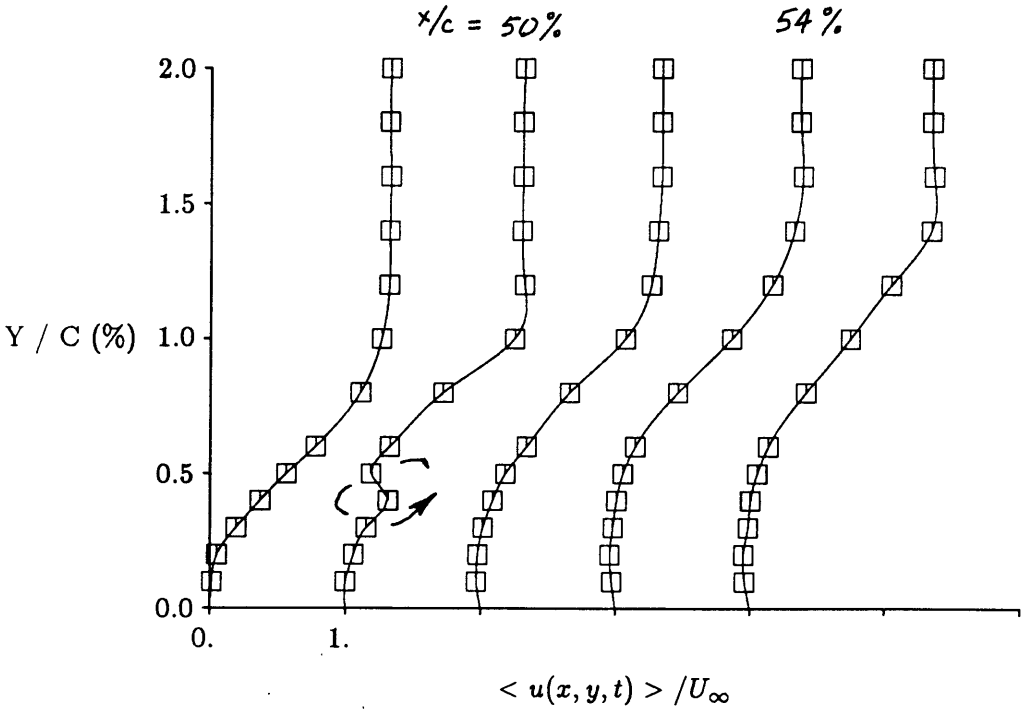


Figure 7.13: Ensemble Averaged U-velocity at $t/T = 0.33$ (Wortmann upper surface, LTWT, $Re = 125000$, $\alpha = 0^o$, $k = 0.15$)

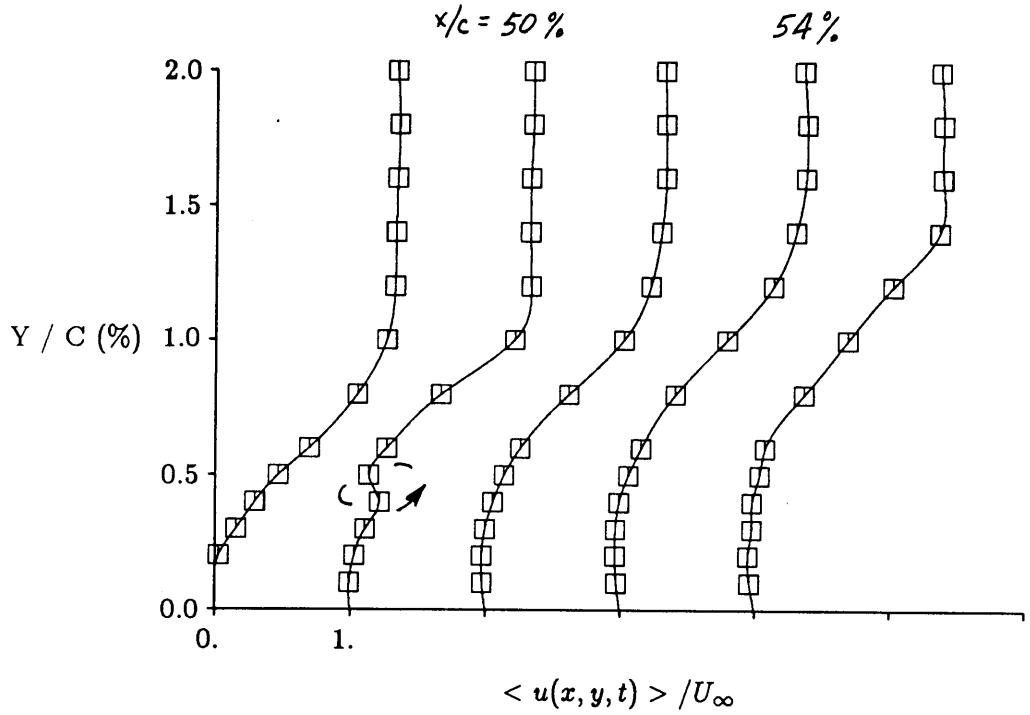


Figure 7.14: Ensemble Averaged U-velocity at $t/T = 0.44$ (Wortmann upper surface, LTWT, $Re = 125000$, $\alpha = 0^o$, $k = 0.15$)

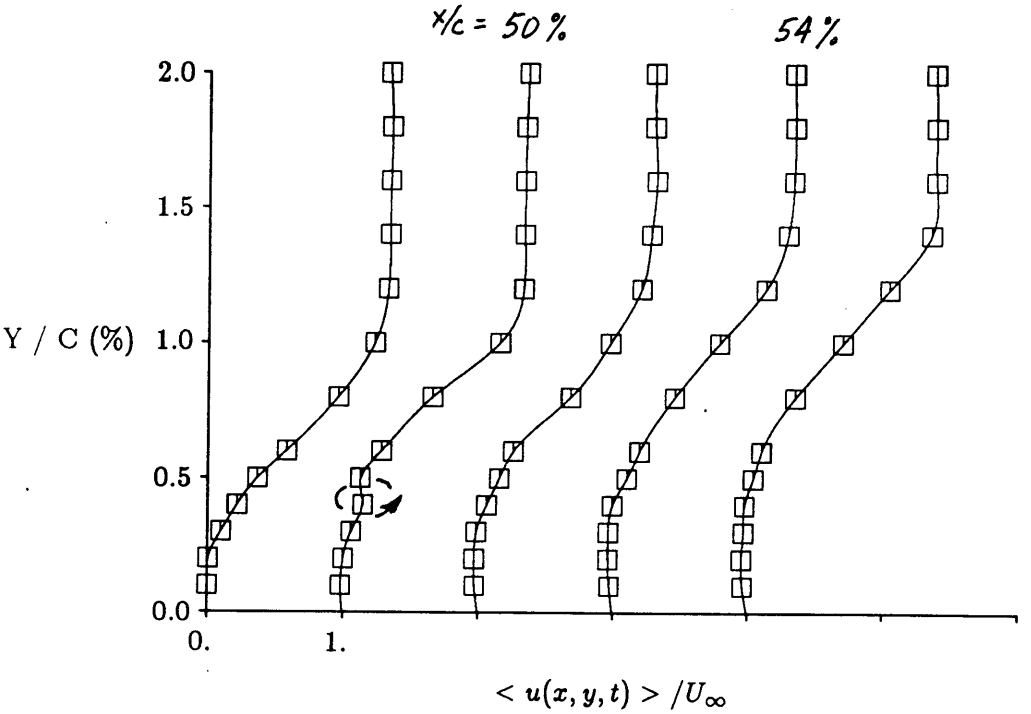


Figure 7.15: Ensemble Averaged U-velocity at $t/T = 0.55$ (Wortmann upper surface, LTWT, $Re = 125000$, $\alpha = 0^o$, $k = 0.15$)

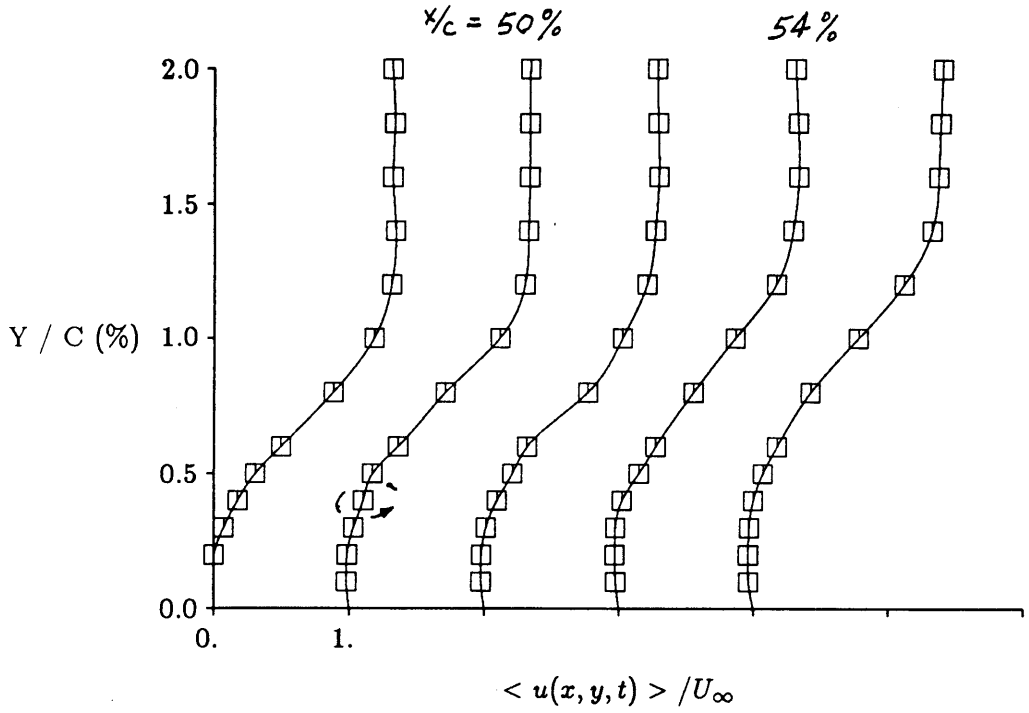


Figure 7.16: Ensemble Averaged U-velocity at $t/T = 0.66$ (Wortmann upper surface, LTWT, $Re = 125000$, $\alpha = 0^o$, $k = 0.15$)

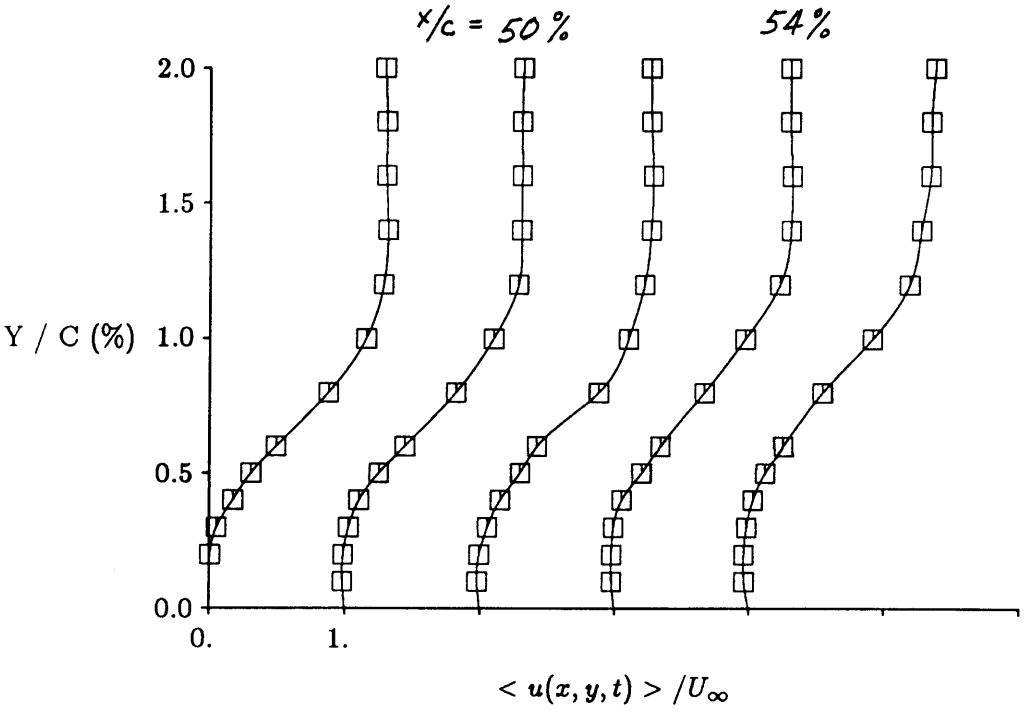


Figure 7.17: Ensemble Averaged U-velocity at $t/T = 0.77$ (Wortmann upper surface, LTWT, $Re = 125000$, $\alpha = 0^o$, $k = 0.15$)

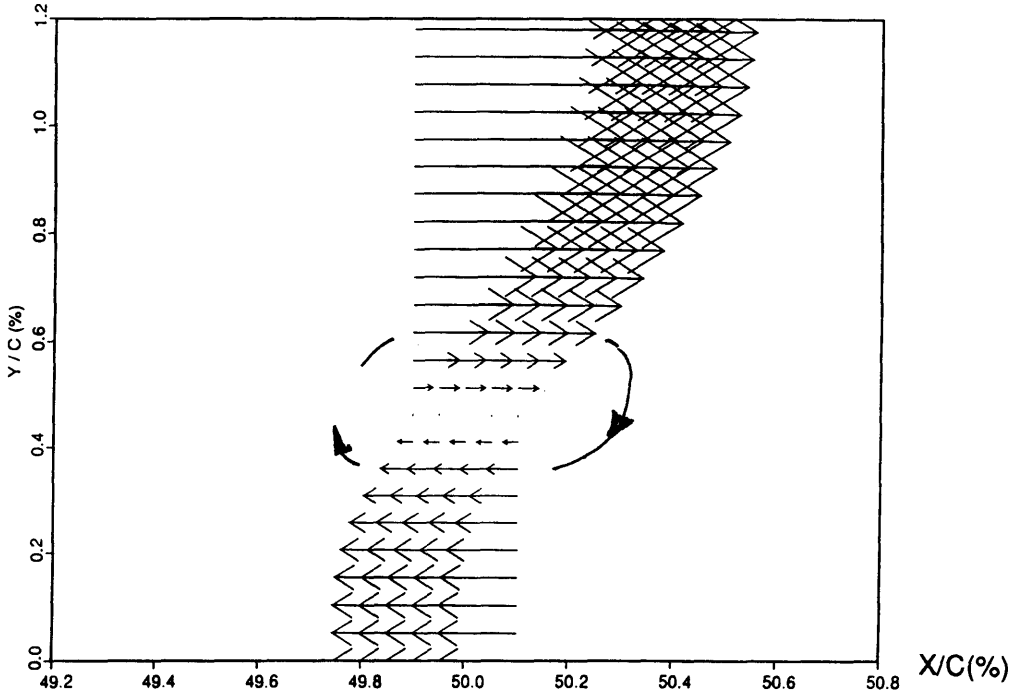


Figure 7.18: Ensemble averaged velocity vectors near x/c= 0.5 and at $t/T = 0$ in moving frame. (Wortmann upper surface, LTWT, $Re = 125000$, $\alpha = 0^o$, $k = 0.15$)

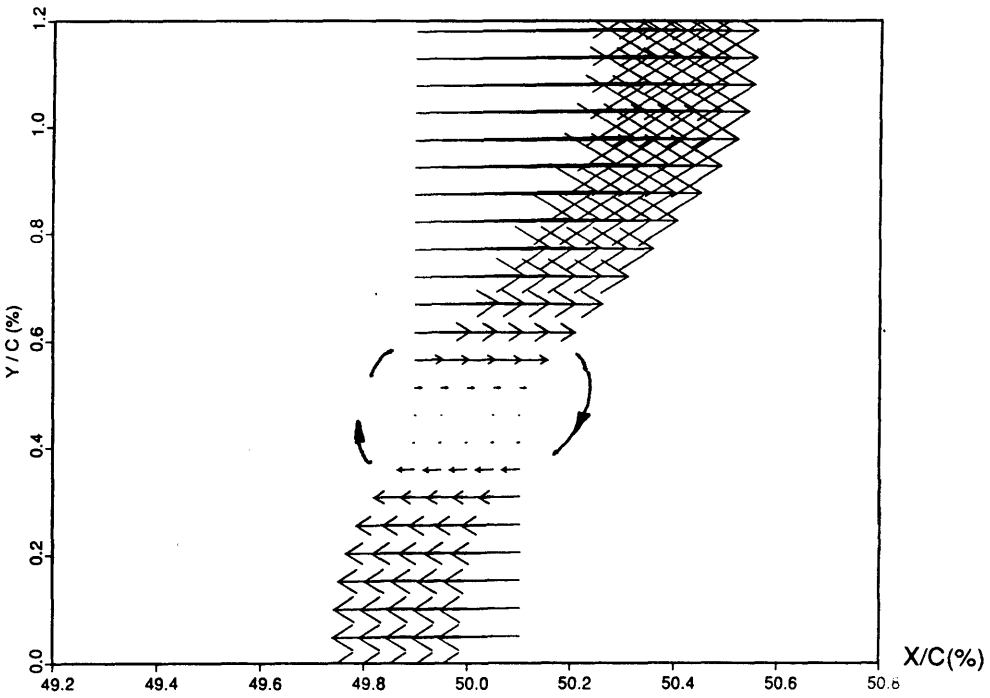


Figure 7.19: Ensemble averaged velocity vectors near x/c= 0.5 and at $t/T = 11\%$ in moving frame. (Wortmann upper surface, LTWT, $Re = 125000$, $\alpha = 0^o$, $k = 0.15$)

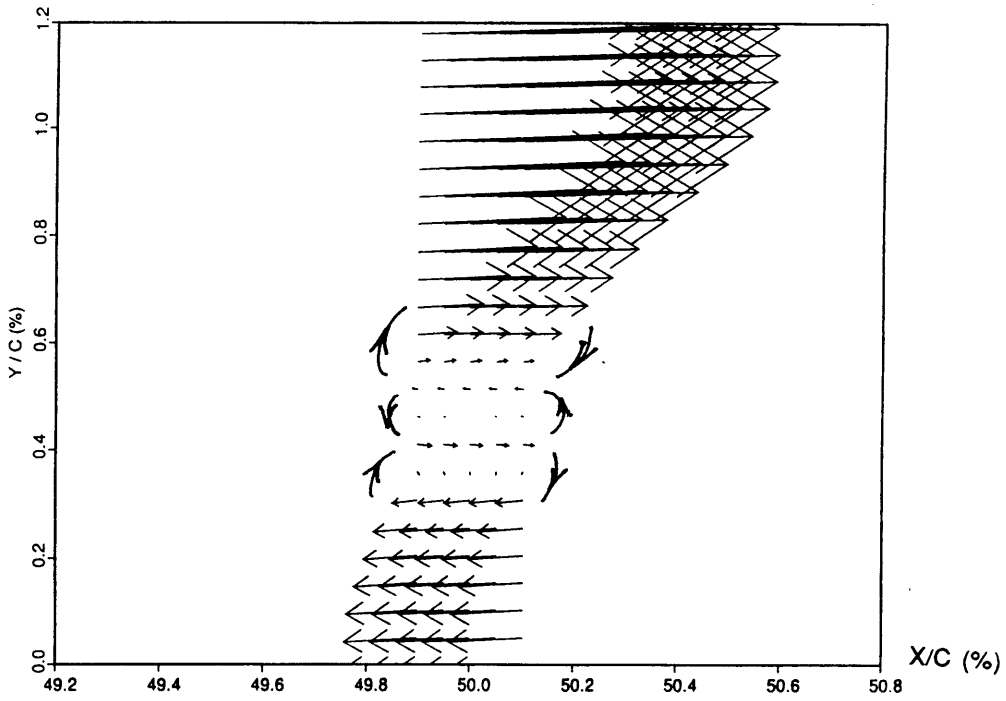


Figure 7.20: Ensemble averaged velocity vectors near x/c= 0.5 and at t/T = 22% in moving frame. (Wortmann upper surface, LTWT, Re = 125000, α = 0°, k = 0.15)

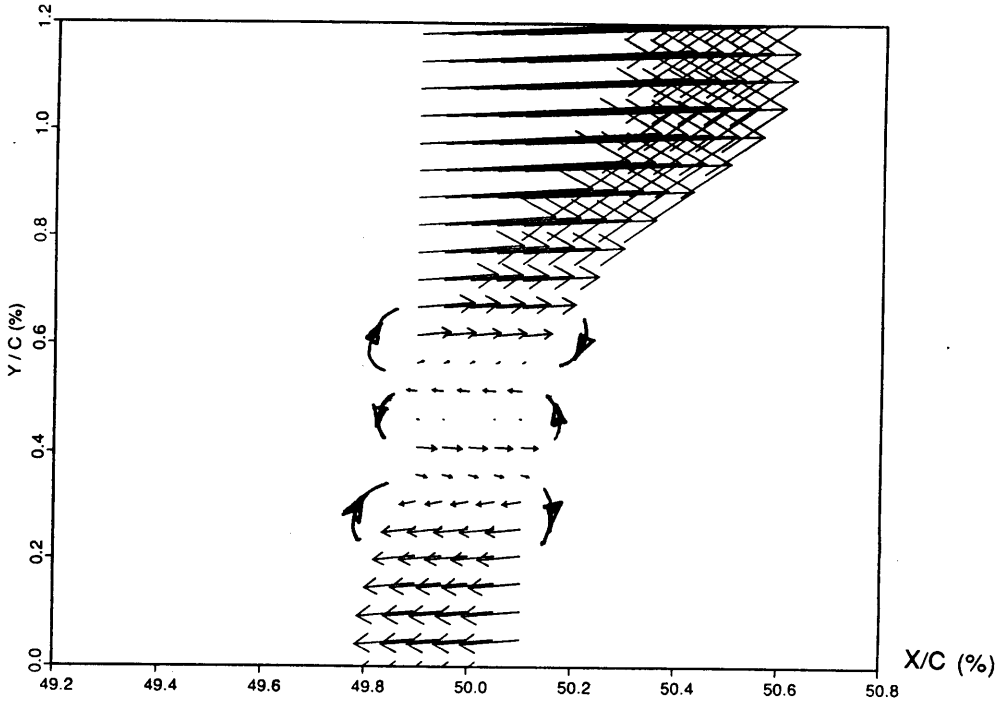


Figure 7.21: Ensemble averaged velocity vectors near x/c= 0.5 and at t/T = 33% in moving frame. (Wortmann upper surface, LTWT, Re = 125000, α = 0°, k = 0.15)

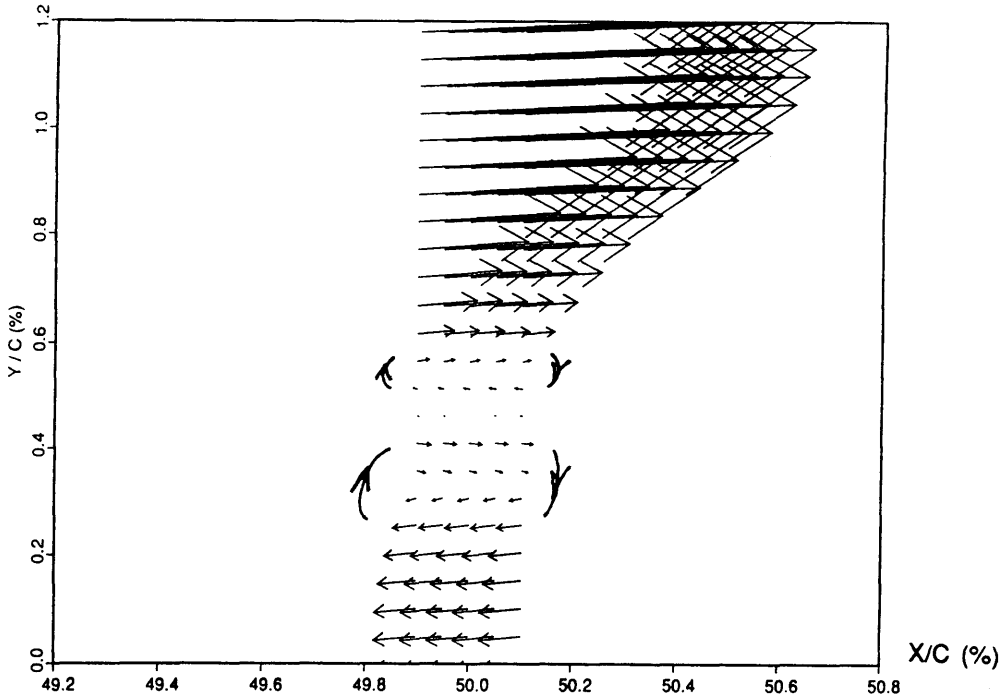


Figure 7.22: Ensemble averaged velocity vectors near x/c= 0.5 and at t/T = 44% in moving frame. (Wortmann upper surface, LTWT, Re = 125000, α = 0°, k = 0.15)

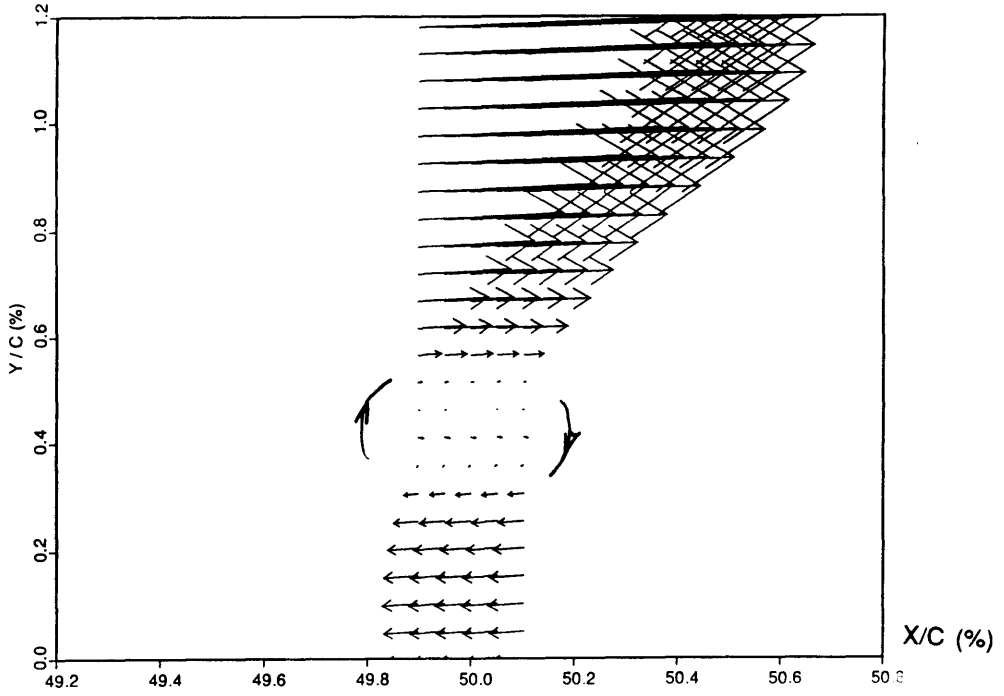


Figure 7.23: Ensemble averaged velocity vectors near x/c= 0.5 and at t/T = 55% in moving frame. (Wortmann upper surface, LTWT, Re = 125000, α = 0°, k = 0.15)

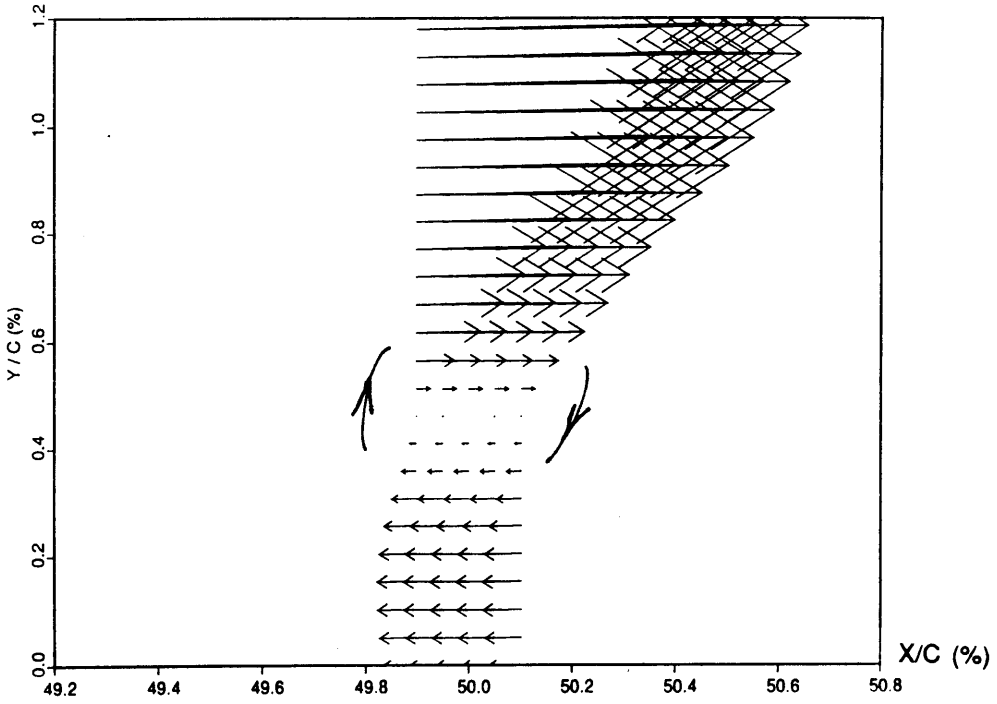


Figure 7.24: Ensemble averaged velocity vectors near x/c= 0.5 and at t/T = 66% in moving frame. (Wortmann upper surface, LTWT, Re = 125000, α = 0°, k = 0.15)

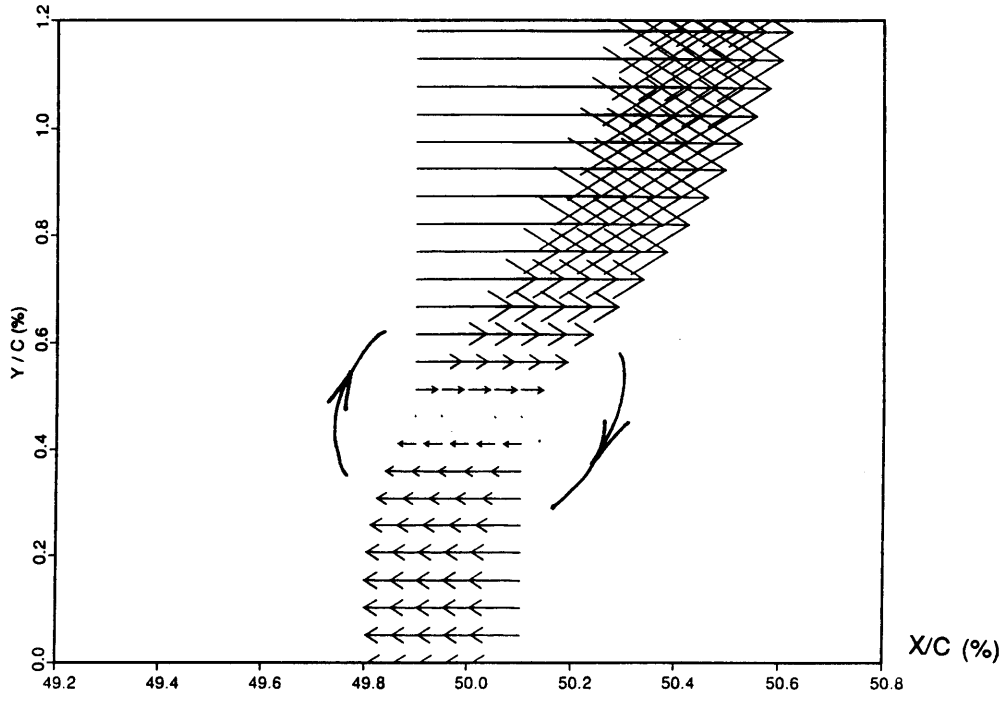


Figure 7.25: Ensemble averaged velocity vectors near x/c= 0.5 and at t/T = 77% in moving frame. (Wortmann upper surface, LTWT, Re = 125000, α = 0°, k = 0.15)

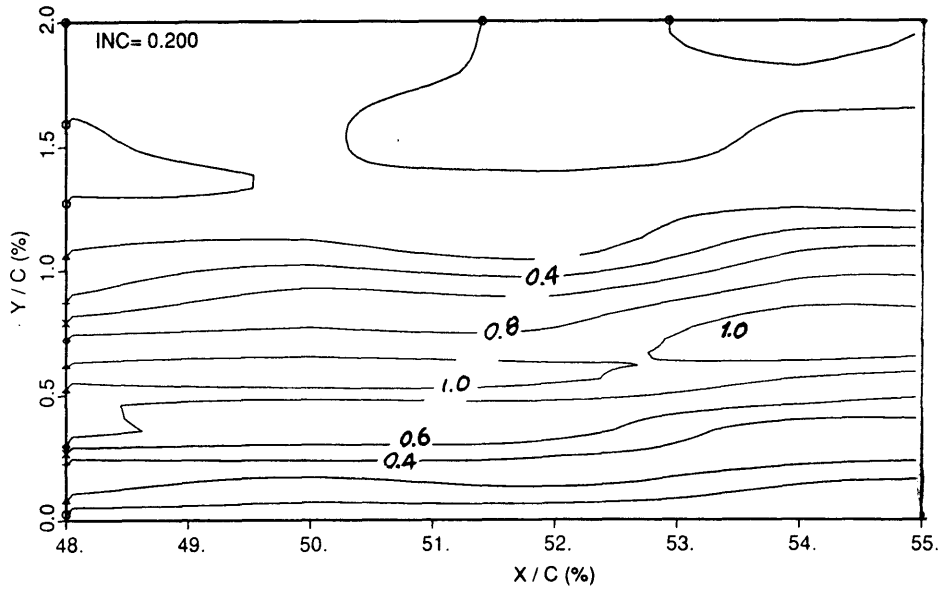


Figure 7.26: Ensemble averaged vorticity contour at $t/T = 0$ (Wortmann upper surface, LTWT, $Re = 125000$, $\alpha = 0^o$, $k = 0.15$)

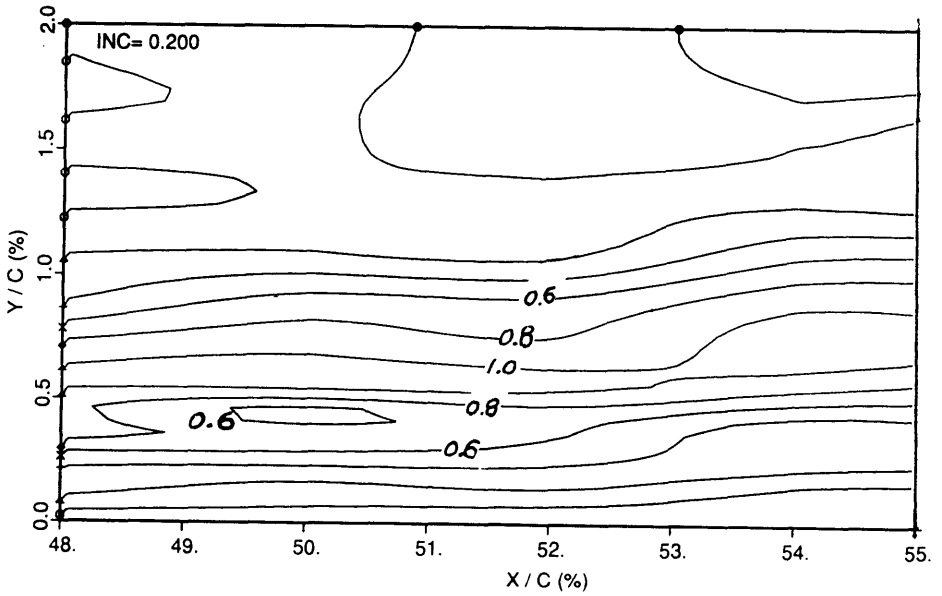


Figure 7.27: Ensemble averaged vorticity contour at $t/T = 3.5\%$ (Wortmann upper surface, LTWT, $Re = 125000$, $\alpha = 0^o$, $k = 0.15$)

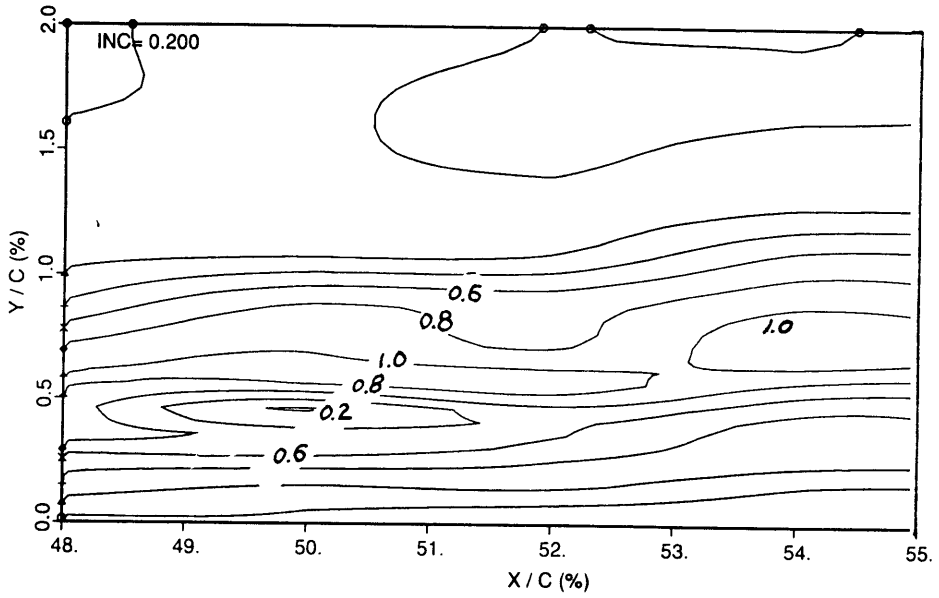


Figure 7.28: Ensemble averaged vorticity contour at $t/T = 7\%$ (Wortmann upper surface, LTWT, $Re = 125000$, $\alpha = 0°$, $k = 0.15$)

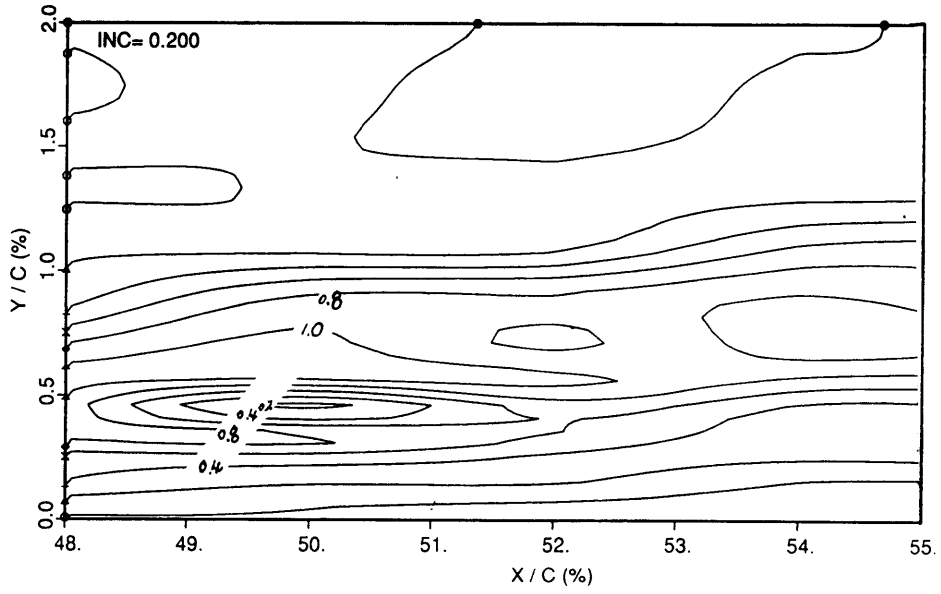


Figure 7.29: Ensemble averaged vorticity contour at $t/T = 10.5\%$ (Wortmann upper surface, LTWT, $Re = 125000$, $\alpha = 0°$, $k = 0.15$)

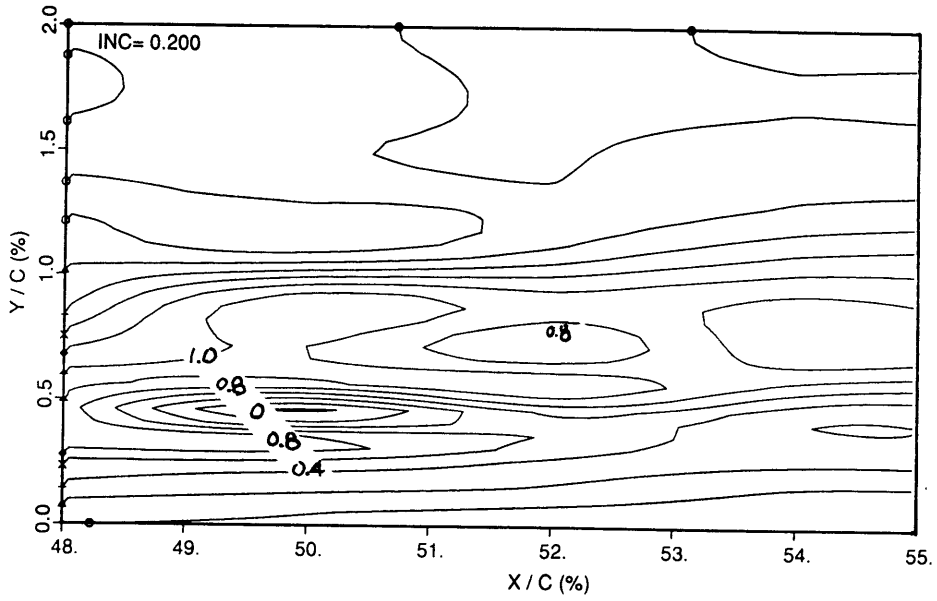


Figure 7.30: Ensemble averaged vorticity contour at $t/T = 14\%$ (Wortmann upper surface, LTWT, $Re = 125000$, $\alpha = 0^o$, $k = 0.15$)

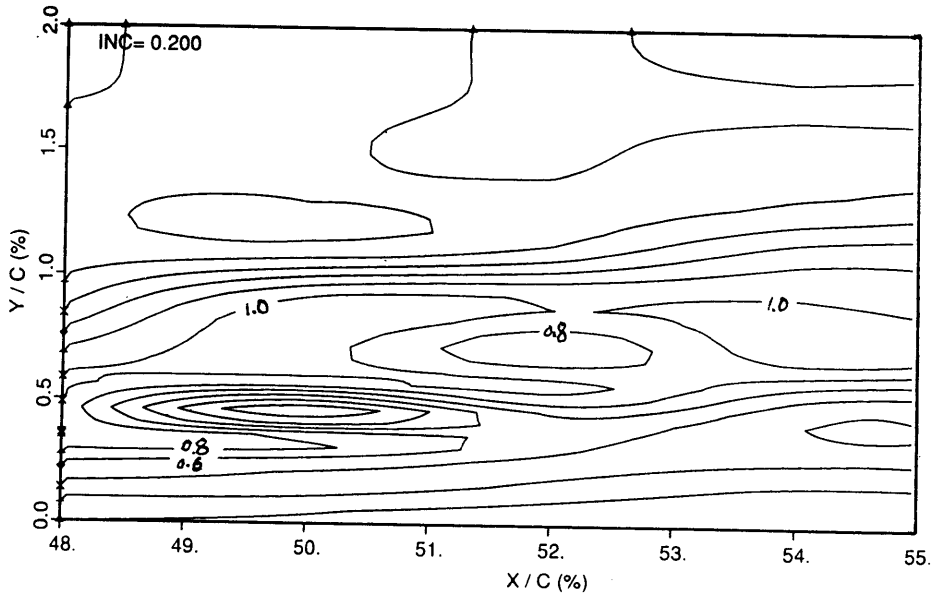


Figure 7.31: Ensemble averaged vorticity contour at $t/T = 17.5\%$ (Wortmann upper surface, LTWT, $Re = 125000$, $\alpha = 0^o$, $k = 0.15$)

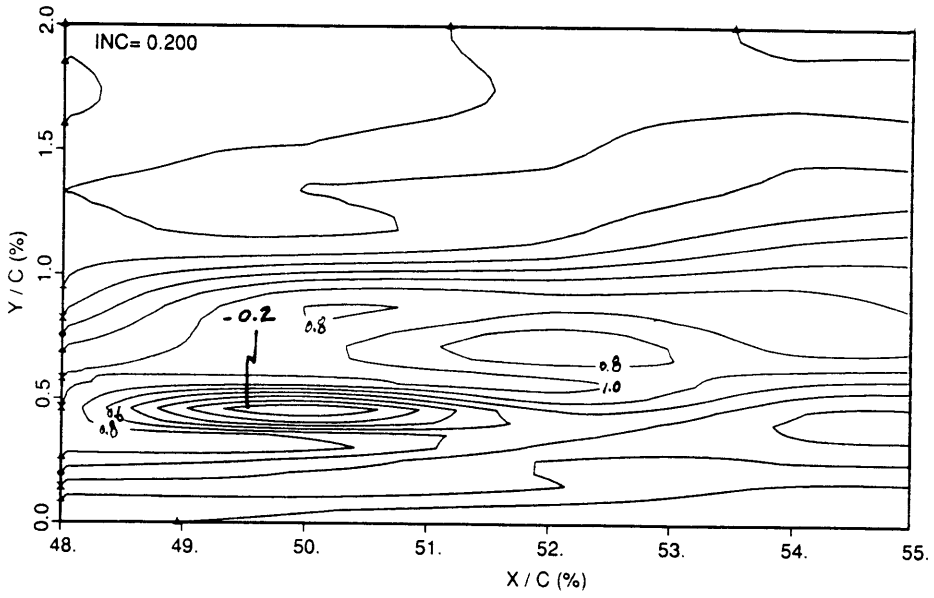


Figure 7.32: Ensemble averaged vorticity contour at $t/T = 22\%$ (Wortmann upper surface, LTWT, $Re = 125000$, $\alpha = 0°$, $k = 0.15$)

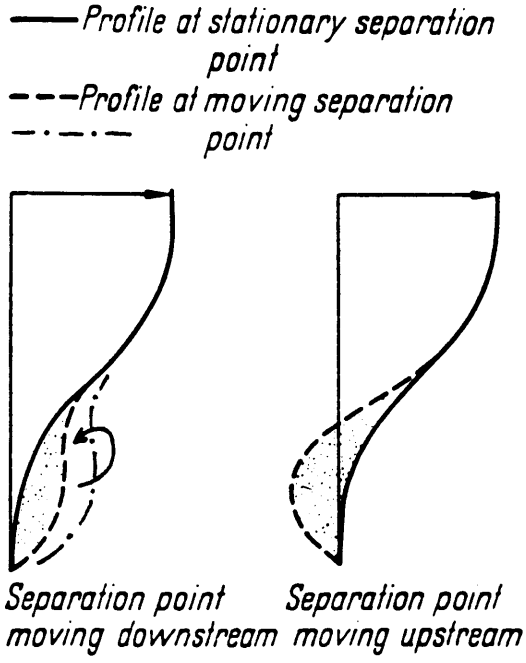


Figure 7.33: Moore's postulated velocity profiles for unsteady separation on a fixed wall. Moore (1958)

Chapter 8

Summary and Conclusions

This experimental investigation concerns steady and unsteady aerodynamics and fluid mechanics phenomena at low chord Reynolds numbers ($Re \sim O(10^5)$). The focuses of this work are to examine i) the response of the surface pressure near the laminar separation bubble to Reynolds number, angle of attack, unsteadiness, and free-stream turbulence ii) the validity of the unsteady Kutta condition, iii) the balance of forces near laminar separation in steady flow, and iv) the boundary layer behavior near laminar separation in unsteady flow. Tests are conducted on Wortmann FX63-137 and NACA 0012 airfoils at $\alpha = 0^o$ and 10^o, $Re = 125000$ and 400000, and reduced frequencies ($k = \omega C/2U_\infty$) of 0.15, 0.5, 0.75, 1.0, 2.0, and 6.4 in both 0.05% (LTWT) and 0.8% (WBWT) free-stream turbulence levels. The unsteady excitation is essentially constant phase along the chord. Surface pressure and LDA velocity measurements are made. A summary of the findings follows.

8.1 Steady pressure results

The Wortmann FX63-137 airfoil represents a general class of low Reynolds number airfoils with a 'long' ($\sim O(chord)$) separation bubble. The suction surface pressure in steady flow at $\alpha = 0^o$ and tunnel turbulence level of 0.05% reveals that an increase of Reynolds number from 125000 to 400000 causes flow transition in the separated laminar shear layer to occur further upstream (figure 4.1). The

consequence of earlier flow transition is proportionally sooner reattachment as a turbulent boundary layer. Hence, the overall length of a laminar separation bubble is shortened, from 30% chord at Re =125000 to 20% chord at Re =400000, with increase in Reynolds number. The newly reattached turbulent boundary layers for both Reynolds numbers continue downstream without turbulent separation.

At $\alpha = 10^o$, the separation bubble translates upstream and shortens its overall size (compare figures 4.1 with 4.3). At 125000, the location where completion of transition moves from near 80% chord at $\alpha = 0^o$ to 40% chord at $\alpha = 10^o$ and shrinks from 30% to 20% chord in length. A region of over-expansion of pressure recovery at the turbulent reattachment region, near 50% chord, is also observed at Re = 125000 (figure 4.3). This phenomenon is due to streamline curvature effect as the flow is reattaching as a turbulent boundary layer.

The net effect of free-stream turbulence is to alter the process of flow transition. At low turbulence level, surface pressure distribution shows distinctly that flow transition occurs near 70% chord for Re = 400000 (figure 4.1); no clear sign of this can be inferred from pressure data taken in high turbulence environment (figure 4.2).

8.2 Unsteady pressure results

The time mean surface pressure of a NACA 0012 near the stall angle of attack, $\alpha = 10^o$, demonstrates the effects of free-stream turbulence, reduced frequency, and Reynolds number. At Re = 125000, k = 2.0 and a free-stream turbulence level of 0.8%(WBWT), figure 4.5 shows that i) the flow is attached near the leading edge on the suction surface, ii) a hint of transition near 5% chord, iii) attached flow from 5% to 10% chord, and iv) separation further downstream. However, for the case of 0.05% free-stream turbulence level (LTWT) the flow separates globally on the suction surface. These two pressure distributions illustrate the effect of free-stream turbulence on the ability of the separated shear layer to reattach near the stall angle of attack.

Reynolds number also plays an important role near stall. At $Re = 125000$, time mean results at other reduced frequencies, $0.15 \leq k \leq 6.4$, also exhibit the two flow states, partially attached or globally separated, depending on the free-stream turbulence level. However, at $Re = 400000$ and $k \leq 2.0$, the time mean pressure is free from global separation even for results obtained in the low turbulence environment (compare figure 4.5 with 4.7).

For the 0012 near the stall angle of attack, data suggest that the effect of an increase in free-stream turbulence is analogous to increase in Reynolds numbers as far as separation or attachment of the time mean unsteady flow is concerned (figures 4.5 and 4.7). This is related to Gault's [29] idea for steady flow: "an increase in the free-stream turbulence reduces the extent of separated laminar flow in a manner somewhat analogous to an increase in the Reynolds number." Hence, the analogy for steady flow appears to be applicable for the time mean unsteady flow as well, at least for small unsteady perturbation.

The unsteady lift and moment agree within 10% in amplitude and 10° in phase with Theodorsen's theory [72] over all parameters studied. Several trends are worth noting from the ensemble averaged pressure results (figure 4.10). First, for the results in the 0.05% turbulence level (LTWT), the fluctuations in C_l and C_m, are generally larger when the lift and moment are decreasing than increasing. This is due to unsteady behavior of the separation bubble, especially near transition (compare figure 4.10c with 4.12). Secondly, the results obtained in free-stream turbulence level of 0.8% (figures 4.11a and 4.11b) reveal that the fluctuation in C_l and C_m is greater than that obtained in lower turbulence environment. The primary reason is simply because of larger fluctuations in the free-stream. Ensemble averaging based on the convergence criterion of equation (2.1) is insufficient to smooth the fluctuations.

8.3 Unsteady flow aft of the trailing edge

The motivation is to investigate the validity of the Kutta-Joukowski condition in unsteady flow. The velocity just aft of the NACA 0012 trailing edge, at $\alpha = 0^o$ $Re = 125000$, $k = 2.0$ and 0.05% tunnel turbulence level, is measured by LDA. This combination of flow parameters is chosen because the flow leaving the trailing edge is less likely to be smooth with relatively thick boundary layers at low chord Reynolds number and at high reduced frequency.

The ensemble averaged streamline results suggest the following. First, the ensemble averaged streamlines are *in-phase* with the unsteady excitation (compare figure 5.1 with 5.5). This is in agreement of triple deck analysis by Brown and Daniels [12] (as interpreted by Crighton [18], p. 419) for pitching or plunging airfoils. Secondly, *the streamlines are confined within the trailing edge angle* which implies that the condition of smooth flow at the trailing edge is satisfied.[1] This idea is from Maskell [4] which means for unsteady airfoil with bound circulation Γ and finite trailing edge angle, vortices shed leaving the airfoil are tangential to the lower surface if $\frac{d\Gamma}{dt} > 0$ and tangential to the upper surface if $\frac{d\Gamma}{dt} < 0$ (figure 5.7). Hence the results suggest that the proper value of the circulation is set or the unsteady Kutta-Joukowski condition appears to be satisfied, at least in the ensemble averaged sense.

8.4 Balance of forces near laminar separation in steady flow

The dynamics of a 'long' ($\sim O(chord)$) laminar separation bubble in steady flow is studied by examining the balance of forces in the region of laminar separation and, hence, the validity of the assumptions in the boundary layer approximation. The magnitude of terms in the x and y Navier-Stokes equations near the laminar

[1] Unlike a cusped, airfoils with finite trailing edge angle enjoy some flexibility in the flow leaving the trailing edge to be considered 'smooth'.

separation point are calculated using LDA velocity data. The result of this study is applicable to analytical or numerical modeling of the forward portion of a laminar separation bubble. Boundary layer is measured on the suction surface of the Wortmann FX63-137 airfoil at $\alpha = 0°$, Re =125000, and 0.05% (LTWT) tunnel turbulence level.

For the forces in the x direction, four observations are made. First, the displacement thickness location (δ^*) divides regions where the viscous terms can be neglected; potential terms dominate for $y > \delta^*$ and viscous terms are also important for $y < \delta^*$ (figures 6.5 to 6.8). Secondly, extrema for the convection terms are also located near δ^*. The term $v^* \frac{\partial u^*}{\partial y^*}$ maximizes here mainly because $\frac{\partial u^*}{\partial y^*}$ peaks at the point of inflexion, which is near δ^*. The term $u^* \frac{\partial u^*}{\partial x^*}$ minimizes here due to a balance between the adverse pressure gradient and $v^* \frac{\partial u^*}{\partial y^*}$. Thirdly, the numerics indicate that the smallest term in the x-momentum equation is $\frac{1}{Re} \frac{\partial^2 u^*}{\partial x^{*2}}$ (see below). Fourthly, large variation of the streamwise pressure gradient, $\frac{1}{2} \frac{\partial C_p}{\partial x^*}$, of order of the convection terms, exists across the boundary layer. This variation implies that $\frac{1}{2} \frac{\partial C_p}{\partial y^*}$ is not negligible.

The force balance in the y-momentum equation (figure 6.9 to 6.12) reveals many similarities to the x equation, but two points relate to laminar separation are worth noting. First, $v^* \frac{\partial v^*}{\partial y^*}$ maximizes near δ^*. Since $v^* > 0$, this implies $\frac{\partial v^*}{\partial y^*} > 0$; the fluid is ejecting towards the potential flow region. Secondly, $u^* \frac{\partial v^*}{\partial x^*}$ changes sign across laminar separation; with $u^* > 0$ for most region in the flow, the streamwise variation of the vertical velocity peaks near laminar separation.

More detail examination of the balance of forces is focused on i) the magnitude of $\frac{1}{Re} \frac{\partial^2 u^*}{\partial x^{*2}}$ compared to the largest term in the 2-D x-momentum equation and ii) the magnitude of $v^* \frac{\partial v^*}{\partial y^*}$ compared to $v^* \frac{\partial u^*}{\partial y^*}$. These points are relevant to the validity of the boundary layer approximations. First, the ratio

$$\epsilon_t \equiv \left| \frac{1}{Re} \frac{\partial^2 u^*}{\partial x^{*2}} \right| / \left| largest\ term\ in\ 2-D\ x-momentum\ eqn.\ (eqn.\ 6.1) \right| \quad (8.1)$$

is calculated; ϵ_t can be considered as the truncation error if $\frac{1}{Re} \frac{\partial^2 u^*}{\partial x^{*2}}$ is neglected.

Results suggest that $\epsilon_t < 0.2\%$ in the reverse flow region but $\epsilon_t \ll 0.05\%$ in the attached flow region (table 6.1). Hence, $\frac{1}{Re}\frac{\partial^2 u^*}{\partial x^{*2}}$ can indeed be ignored in modeling the flow near laminar separation.

To examine the magnitude of the y-momentum equation compared to the x-momentum equation, the ratio of the convection terms

$$\epsilon_y \equiv \left| v^* \frac{\partial v^*}{\partial y^*} \right| / \left| v^* \frac{\partial u^*}{\partial y^*} \right| \tag{8.2}$$

is computed. The results (table 6.2) show that this ratio is about 14% to 22% near the laminar separation location; this is not small. Neglecting the y-momentum equation entirely in calculating the boundary layer numerically will contribute to error in the surface pressure result since the normal pressure gradient is not taken into account.

8.5 Unsteady laminar separation

In this work, the effect of unsteadiness on the behavior of the boundary layer near separation is also studied. Velocity profiles are measued by LDA on the Wortmann airfoil suction surface at Re= 125000 and k= 0.15 and 2.0. These two reduced frequencies correspond to the intermediate frequency range, $k = 0.15$, and the high frequency approximation, $k = 2.0$, in the boundary layer behavior (figure 7.1, Lighthill [37]).

Data analyses reveal the following . First, periodic secondary vortices, of opposite sign of the primary boundary layer, exist within the boundary layer at $k = 0.15$. This phenomenon is not believed to have been documented previously. Velocity vectors in a frame fixed with the core of the secondary vortices (figures 7.18 to 7.25) show that they resemble a vortex sheet more so than isolated vortices, since $\left|\frac{\partial u}{\partial y}\right| \gg \left|\frac{\partial v}{\partial x}\right|$. Ensemble averaged vorticity contour results (figure 7.26 to 7.32) show temporal but not spatial development of vortical regions due to insufficient data resolution. The origin of the secondary vortices is most likely due to unsteady motion of the laminar separation point. For $k = 2.0$, this flow feature is not observed.

Secondly, the velocity amplitude (figures 7.4 and 7.5) peaks within the boundary layer with a magnitude near six times the amplitude at the edge-velocity for $k = 0.15$ and nine times for $k = 2.0$. The locations of the maxima correspond to the points of inflexion. This suggest that the boundary layer near inflexion is most responsive to the periodic pressure variation.

Thirdly, phase results confirm that the boundary layer behavior is in the intermediate frequency range for $k = 0.15$ and high frequency range for $k = 2.0$ (figures 7.7 and 7.8). At $k = 0.15$, data show that the phase generally varies across the boundary layer. At 50% chord and 0.5% chord above the wall, corresponds to the location of the secondary vortices, the flow exhibits a significant change in phase. At $k = 2.0$, the phase is essentially constant across the outer layer with a Stokes region near the wall. Streamwise variation of 180^o in phase exists across the separation point; the flow direction is reversed.

8.6 Conclusions

In light of the objectives of this experimental study stated in Section 1.4, the following conclusions are drawn for steady and unsteady flow at low chord Reynolds numbers. (Each item following corresponds to the question in Section 1.4)

1. The unsteady thin airfoil theory (e.g. Theodorsen [72]) is a good design tool to calculate the unsteady forces at Reynolds numbers as low as 125000; difference of C_l between measurement and prediction is within 10% in amplitude and 10^o in phase (figure 4.10). Higher harmonics are present due to the motion of the transition region. The ratio of fluctuation in C_l, or C_m, to its fundamental amplitude is about 15% (figure 4.10c).

2. The fluid mechanics of flow transition, from separated laminar shear layer to turbulence, dominate the behavior and geometry of a laminar separation bubble. The process of transition is shown to be sensitive to all parameters

studied – Reynolds number, unsteadiness, and pressure gradient. In general, an increase in the free-stream turbulence level causes earlier flow transition, analogous to an increase in Reynolds number. Near the stall angle of attack, the tunnel turbulence level can determine whether the flow is attached or globally separated.

3. The ensemble averaged streamlines leaving the trailing edge of a NACA 0012 at Re= 125000 and k = 2.0 are within the trailing edge angle and in-phase with the unsteady excitation. The unsteady Kutta-Joukowski condition holds at this flow condition, at least in the ensemble averaged sense and to the accuracy that the Kutta condition holds in steady viscous flow.

4. Near the laminar separation point in steady flow, examination of terms in the momentum equations show $\frac{1}{Re}\frac{\partial^2 u^*}{\partial x^{*2}}$ is less than 0.2% of $v^*\frac{\partial u^*}{\partial y^*}$. The convection terms in the y-momentum equation is 14% to 22% of the corresponding x equation terms. The transverse pressure gradient has the same order of magnitude as the convection terms. Above the boundary layer displacement thickness all viscous terms can be neglected.

5. In the intermediate frequency range (k = 0.15) for boundary layer response, secondary vorticity, having opposite sign to that of unseparated boundary layer, are found near the laminar separation point. This is likely due to unsteady motion of the separation point. In the high frequency approximation (k = 2.0) this feature is not found. The fundamental amplitude of the local flow within the bounday layer peaks at the point of inflexion.

8.7 Recommendations

In view of the questions that this work has addressed, further studies are recommended in the following areas. First, refined unsteady boundary layer measurements are needed to determine the mechanics of generation of the secondary vortices. This study should allow direct correlation of secondary vortices time history with the

motion of the unsteady separation point. Further insight into this phenomenon may advance the understanding of dynamic stall or other flow phenomena in which unsteady separation plays a key role.

Secondly, the effect of free-stream turbulence has been shown to be important in altering the process of flow transition, especially near stall angle of attack. Presently, this effect is only inferred from surface pressure distribution. Steady and unsteady boundary layer data in the separated shear layer region, where flow transition occurs, are needed. This will better quantify the effect of tunnel turbulence on the unsteady boundary layer.

Bibliography

[1] Ahuja, K.K. and Burrin, R.H. *Control of Flow Separation by Sound.* AIAA 84-2298.

[2] Archibald F.S. *Unsteady Kutta Condition at High Values of Reduced Frequency Parameter.* J. of Aircraft, **12**, no. 6, 1975, p545-550.

[3] Batchelor, G.K. *An Introduction to Fluid Dynamics.* Cambridge: Cambridge University Press, 1967, p615.

[4] Basu, B.C. and Hancock, G.J. *The Unsteady Motion of a Two-Dimensional Airfoil in Incompressible Inviscid Flow.* J. Fluid Mechanics, **87**, 1978, p159-178.

[5] Bisplinghoff, R.L., Ashley, H., and Halfman, R.L., *Aeroelasticity*, Addison Wesley Publishing Co., Reading, Mass., 1955, p277.

[6] Blevins, R. *The Effect of Sound on Vortex Shedding from Cylinders.* J. Fluid Mech., **161**, 1985.

[7] Brendel, M., *Experimental Study of the Boundary Layer on a Low Reynolds Number Airfoil in Steady and Unsteady Flow,* Ph.D. Thesis, University of Notre Dame, 1986, p267.

[8] Brendel, M. and Mueller, T.J., *Boundary Layer Measurements on an Airfoil at a Low Reynolds Number in an Oscillating Freestream,* AIAA Journal, **26**, No.3, Mar. 1988, p257-263.

[9] Brendel, M. and Mueller, T.J. *Transition Phenomena on Airfoils Operating at Low Chord Reynolds Numbers in Steady and Unsteady Flow.* 4*th* Symposium on Numerical and Physical Aspects of Aerodynamic Flows, edited by T. Cebeci, Jan. 16-19, 1989.

[10] Brown, S.N. and Stewartson, K. *Laminar Separation.* Ann. Rev. Fluid Mech., **1**, 1969, p45-72.

[11] Brown, S.N. and Stewartson, K. *Trailing-edge Stall.* J. Fluid Mechanics, **42**, 1970, p561-584.

[12] Brown, S.N. and Daniels, P.G. *On the Viscous Flow about the Trailing Edge of a Rapidly Oscillating Plate.* J. Fluid Mechanics, **67**, 1975, p743-761.

[13] Carmichael, B.H. *Low Reynolds Number Airfoil Survey.* NASA CR-165803, Nov. 1981.

[14] Cebeci, T. and McIlvaine, M. *An Interactive Boundary-Layer Stability-Transition Approach for Low Reynolds-Number Airfoils.* Proceedings of the Conference on Low Reynolds Number Aerodynamics, Edited by Thomas Mueller, June 1989.

[15] Commerford, G.L. and Carta, F.O. *Unsteady Aerodynamic Response of a Two-Dimensional Airfoil at High Reduced Frequency.* AIAA J, **12**, 1974, p43-48.

[16] Covert, E.E. and Drela, M. *Low Speed Aerodynamics in the Reynolds Number Range of 20,000 to 200,000.* Interim Report, ONR Contract No. N00014-82-K-0310. 1982.

[17] Crighton, D.G. *Acoustics as a Branch of Fluid Mechanics.* J. Fluid Mech., **106**, 1981, p261-298.

[18] Crighton, D.G. *The Kutta Condition in Unsteady Flow.* Ann. Rev. of Fluid Mechanics, **17**, 1985, p411-445.

[19] Dean, W.R. *Note on the Motion of Liquid near a Position of Separation.* Proc. Cambridge Philos. Soc., **46**, 1950, p293-306.

[20] Dini, P. and Maughmer, M.D. *A Computationally Efficient Modelling of Laminar Separation Bubbles.* Proceedings of the Conference on Low Reynolds Number Aerodynamics, Edited by Thomas Mueller, June 1989.

[21] Drela, M., *Two-Dimensional Transonic Aerodynamic Design and Analysis Using the Euler Equations,* Ph.D Thesis, M.I.T., 1985.

[22] Drela, M. *XFOIL: An Analysis and Design System for Low Reynolds Number Airfoils.* Proceedings of the Conference on Low Reynolds Number Aerodynamics, Edited by Thomas Mueller, June 1989.

[23] Dryden, H.L., Schubauer, G.B., Mock, W.C. Jr., and Skramstad, H.K., *Measurements of Intensity and Scale of Wind-Tunnel Turbulence and their Relation to the Critical Reynolds Number of Spheres*, NACA TN 581, 1937.

[24] Eppler, R. and Somers, D.M. *A Computer Program for the Design and Analysis of Low-Speed Airfoils.* NASA TM-80210, 1980.

[25] Finaish, F., Freymuth, P. and Bank, W. *Streamwise and Spanwise Vortical Patterns Visualized over Airfoils in Unsteady Flow.* Proceedings of the Conference on Low Reynolds Number Aerodynamics, Edited by T.J. Mueller, June 1985, p269-280.

[26] Fleeter, S. *Trailing Edge Conditions for Unsteady Flows at High Reduced Frequency.* AIAA J, **18**, 1980, p497-503.

[27] Fletcher, M.J. *Reynolds Number Effects on the Unsteady Aerodynamic Behavior of an NACA 0012 Airfoil.* S.M. Thesis, Dept. of Aeronautics and Astronautics, M.I.T., 1986.

[28] Gaster, M. *On the Stability of Parallel Flows and the Behavior of Laminar Separation Bubbles.* Ph.D. Thesis, University of London. Also see British ARC R&M **3595**, 1969.

[29] Gault, D.E., *An Experimental Investigation of Regions of Separated Laminar Flow*, NACA TN 3505, 1955, p52-60.

[30] Gedney, C.J. *The Cancellation of a Sound-Excited Tollmien-Schlichting Wave with Plate Vibration.* Phy. of Fluids, **26**, May 1983.

[31] Goldstein, S. *Fluid Mechanics in the First Half of this Century.* Annual Rev. of Fluids Mechanics, **1**, 1969, p1-28.

[32] Jones, B.M. *An Experimental Study of the Stalling of Wings.* NACA Reports and Memoranda No. **1588**, Dec. 1933.

[33] Kline, S.J., and McClintock, F.A., *Describing Uncertainties in Single-Sample Experiments*, Mech. Eng., Jan. 1953, p3.

[34] Koromilas, C.A. *Unsteady Laminar Separation: an Experimental Study.* J. Fluid Mech., **97**, part 2, 1980, p347-384.

[35] Krause, E., Erhardt, G. and Schweitzer, B. *Experiments on Unsteady Flows About Wing Sections.* Proceedings of the Conference on Low Reynolds Number Aerodynamics, Edited by T.J. Mueller, June 1985, p255-268.

[36] Leal, L.G. *Steady Separated Flow in a Linearly Decelerated Free-Stream.* J. Fluid Mech., **59**, 1973, p513-35.

[37] Lighthill, M.J. *The Response of Laminar Skin Friction and Heat Transfer to Fluctuations in the Stream Velocity.* Proc. Roy. Soc. London, **224A**, 1954, p1-23.

[38] Lissaman, P.B.S. *Low-Reynolds-Number Airfoils.* Annual Rev. of Fluids Mechanics, **15**, 1983, p223-240.

[39] Liu, X. *Documentation of the LDV System.* Internal Report, Gas Turbine Laboratory, March 1987.

[40] Liu, Xiu, Wo, Andrew, and Covert, Eugene E., *Unsteady Streamlines Near the Trailing Edge of an NACA 0012 Airfoil at a Reynolds Number of 125,000*, AIAA Journal, **28**, No. 1, Jan. 1990, p169-70.

[41] Lorber, P.F. and Covert, E.E., *Unsteady Airfoil Pressures Produced by Periodic Aerodynamic Interference,* AIAA Journal, **20**, No.9, Sept. 1982, p1153-59.

[42] Lorber, P.F *Turbulent Boundary Layers on an Airfoil in Unsteady Flow.* Ph.d thesis, M.I.T., May 1984.

[43] Mack, L. *Transition and Laminar Instability*, JPL Publication N77-24058 (or NASA-CP-153203), May 1977, p48.

[44] Mangus, J. *Measurement of Drag and Bursting Frequency Downstream of Tandem Spanwise Ribbons in a Turbulent Boundary Layer*, MIT SM Thesis in Aeronautics and Astronautics, 1984.

[45] Mathioulakis, D.S. and Telionis, D.P. *Velocity and Vorticity Distributions in Periodic Separating Laminar Flow.* J. Fluids Mech., **184**, 1987, p303-333.

[46] Mathioulakis, D.S. and Telionis, D.P. *Pulsating Flow over an Ellipse at an Angle of Attack.* J. Fluid Mech., **201**, 1989, p99-121.

[47] McCroskey, W.J. *Unsteady Airfoils.* Ann. Rev. Fluid Mechanics, **14**, 1982, p285-311.

[48] McCullough, G.B. and Gault, D.E. *Examples of Three Representative Types of Airfoil-Section Stall at Low Speed.* NACA TN-2502, 1951.

[49] Moore, F.K. *On the Separation of the Unsteady Laminar Boundary Layer.* Boundary-Layer Research, Berlin:Springer, edited by H.G. Görtler, 1958, p296-310.

[50] Moore, T.W.F. *Some Experiments on the Reattachment of a Laminar Boundary Layer Separating from a Rearward Facing Step on a Flat Plate Airfoil.* Journal of the Royal Aero. Soc., Nov. 1960.

[51] Mueller, T. et.al., *Influence of Free Stream Disturbances on Low Reynolds Number Airfoil Experiments*, Experiments in Fluids, **1**, no.1, June 1983, p3-13.

[52] Mueller, T.J. *Low Reynolds Number Vehicles.* AGARDograph No. **288**, 1985.

[53] Obremski, H.J., Morkovin, M.V., and Landahl, M., *A Portfolio of Stability Characteristics of Incompressible Boundary Layers*, AGARDograph **134**, March 1969.

[54] Owen, P.R. and Klanfer, L. *On the Laminar Boundary Separaton from the Leading Edge of a Thin Airfoil.* Aero. Res. Council CP-220, 1953.

[55] Panton, R.L. *Incompressible Flow.* Wiley & Sons, Inc., New York, 1984.

[56] Pfenniger, W. *Experimental Investigation of an Airfoil with High Lift to Drag Ratios at Low Reynolds Numbers.* Report No. BLC-84 Northrop Aircraft Inc., Feb. 1956.

[57] Poling, D.R. and Telionis, D.P. *The Response of Airfoils to Periodic Disturbances - The Unsteady Kutta Condition.* AIAA J, **24**, no. 2, 1986, p193-199.

[58] Potter, M.C. and Foss, J.F. *Fluid Mechanics.* Great Lakes Press, Inc., 1982.

[59] Prandtl, L. and Tietjens, O.G. *Applied Hydro- and Aeromechanics.* McGraw-Hill, 1934.

[60] Ratelle, J.P., *Unsteady Boundary Layer Flow Reversal in a Longitudinally Oscillating Flow,* USAF-FJSRL, SRL-TR-78-0006, 1978.

[61] Reed, H. and Pauley, L. *An Analysis of Unsteady, Two-dimensional Separation Bubbles.* Proceedings of Aerodynamics at Low Reynolds Numbers International Conference, The Royal Aeronautical Society, October 1986.

[62] Rott, N. *Unsteady Viscous Flow in the Vicinity of a Stagnation Point.* Q. Appl. Math., **13**, 1956, p444-451.

[63] Satyanarayana, B and Davis, S.S. *Experimental Studies of Unsteady Trailing Edge Conditions.* AIAA J, **16**, 1978, p125-129.

[64] Saxena, L.S., *An Experimental Investigation of Oscillating Flows Over an Airfoil,* Ph.D Thesis, Illinois Institute of Technology, 1977.

[65] Schmitz, F.W. *Aerodynamics of the Model Airplane. Part I, Airfoil Measurements.* Redstone Scientific Information Center, 1941.

[66] Sears, W.R. *Some Recent Developments in Airfoil Theory.* J. Aero. Sci., **23**, 1956, p490-499.

[67] Sears, W.R. *Unsteady Motion of Airfoils with Boundary-Layer Separation.* AIAA Journal, **8**, Feb. 1976, p216-220.

[68] Smith, F.T. *Steady and Unsteady Boundary-Layer Separation.* Ann. Rev. Fluid Mech., **18**, 1986, p197-220.

[69] Stuart, J.T. In *Recent Research of Unsteady Boundary Layers*, edited by E.A. Eichelbrenner, **1**, p1-46.

[70] Sumantran, V., Sun, Z., and Marchman, J.F.III, *Acoustic and Turbulence Influence on Low- Reynolds Number Wing Pressure Distributions.* Proceedings of the Conference on Low Reynolds Number Airfoil Aerodynamics, U. Nortre Dame, June 1985.

[71] Telionis, D.P. *Review - Unsteady Boundary Layers Separated and Attached*, J. Fluids Eng., **101**, March 1979, p29-43.

[72] Theodorsen, T., *General Theory of Aerodynamic Instability and the Mechanism of Flutter*, NACA Report **496**, 1935.

[73] Tsahalis, D.TH. and Telionis, D.P. AIAA J., **12**, 1974, p1469.

[74] Vaczy, Carol M., *Unsteady Separated Flow Fields Around a NACA 0012 Airfoil*, MIT SM Thesis in Aeronautics and Astronautics, June 1984.

[75] van Ingen, J.L. *Theoretical and Experimental Investigations of Incompressible Laminar Boundary Layers with and withour Suction.* Technological University, Delft, Netherlands, Oct. 1965.

[76] Varty, R.L. and Currie, I.G. *Measurements near a Laminar Separation Point.* J. Fluids Mech., **138**, 1984, p1-19.

[77] von Karman, T. and Sears, W. *Airfoil Theory for Non-Uniform Motion.* J. of Aero. Sci., **5**, No. 10, August 1938, p379-390.

[78] Williams, J.C. III *Incompressible Boundary-Layer Separation.* Ann. Rev. Fluid Mech., **9**, 1977, p113-144.

[79] Wo, A.M. and Covert, E.E., *On the Effects of Wind Tunnel Turbulence on Steady and Unsteady Airfoil Characteristics, 4th* Symposium on Numerical and Physical Aspects of Aerodynamic Flows, edited T. Cebeci, Jan. 16-19, 1989.

[80] Wo, A.M. and Covert, E.E. *Unsteady Aerodynamics of Wortmann FX63-137 Airfoil at Low Reynolds Numbers.* Proceedings of the Conference on Low Reynolds Number Aerodynamics. June 1989.

Appendix A

Uncertainties in Laser Doppler Anemometer measurements

There are three primary sources of uncertainty in data obtained by the LDA. Firstly, there is an uncertainty in measuring the Doppler frequency. This is due to many factors inherent in the LDA system – optics are not aligned properly causing beams do not intersect symmetrically at the probe volume, uncertainties in the photo detection devices, uncertainties in the particle countering process, etc. Secondly, uncertainty in positioning the probe volume in the flow field. This is especially critical in flow regime where gradient of velocity is large. Thirdly, one of the disadvantages of the LDA is that particle velocity is actually measured, the natural question is how well do the particles follow the flow field? This question is more critical for unsteady flow than for steady flow due to the inertia of a particle. I shall now discuss each of these aspects.

A check of the accuracy of the LDA is performed by Dr. Xiao-Liu Liu. Dr. Liu measured the velocity at a point on the face of a rotating gear over a range of frequency between $524Hz.$ and $2863Hz.$. Five measurements were made for both blue and green beams at each frequency. The percentage difference between the LDA measurement and calculated gear velocity ranges from 0.08% to 0.31% for the green beam and from 0.05% to 0.18% for the blue beam. The average difference is

0.18% for the green and 0.09% for the blue beam. This is considered sufficient for the present work. Refer to documentation by Liu [39] for detail.

The second source of uncertainty arises from positioning the probe volume. The resolution in the traverse mechanism is $0.01mm$. The most severe velocity gradient measured is in the laminar boundary layers. Assuming a Blasius profile, with boundary layer thickness of 1% chord, uncertainty of $0.01mm$, or 0.002% chord for an airfoil with chord of $500mm$, in the region just above the wall gives an uncertainty of 0.33% in velocity.

How well does a particle follow an unsteady flow field? A model is used to answer this question. Assume a spherical particle is submerged in an oscillating flow field, the differential equation is

$$m_p \frac{du_p}{dt} = 6\pi\mu a(u(t) - u_p) \tag{A.1}$$

where m_p, u_p, and a is the mass, velocity, and diameter of the partial respectively, and $u(t)$ is the unsteady external flow. Equation (A.1) says the drag, assuming $\rho ua/\mu \leq 1$, balances the acceleration of the particle. This differential equation models only the response of a partial due to unsteadiness in the flow field; acceleration due to spatial velocity variation is neglected. Let the unsteady external velocity be oscillating in time,

$$u(t) = u_o sin\,\omega t \tag{A.2}$$

Equation (A.1) can be written as

$$\frac{d\,u_p}{dt} + \omega_p u_p = \omega_p u_o sin\,\omega t \tag{A.3}$$

where

$$\omega_p = \frac{6\pi\mu a}{m_p} \tag{A.4}$$

is the frequency scale depending on the size and mass of the particle. Assuming u_p takes the form

$$u_p(t) = Au_o\, sin\,(\omega t - \phi) \tag{A.5}$$

and solve for A and ϕ. I obtain,

$$A = \left[\left(\frac{\omega_p^2}{\omega^2+\omega_p^2}\right)^2 + \left(\frac{\omega\omega_p}{\omega^2+\omega_p^2}\right)^2\right]^{\frac{1}{2}} \tag{A.6}$$

$$tan\,\phi = \frac{\omega}{\omega_p} \tag{A.7}$$

Hence, amplitude attenuation is a function of the imposed unsteady frequency and the inherent frequency scale of the particle. Phase shift depends on the ratio of two frequencies. As seeds for the flow field, I used vaporized 50% ethelene glycol and 50% water solution. Typical size of a vapor particle is a few micron and the density is very close to that of water. Assume $a = 5\mu m$ and density to be that of water, $\omega_p = 2\ x\ 10^4\, rad/s$. At the highest frequency test, Reynolds number 400000 and k= 6.4, $\omega = 282\, rad/s$. Calcuations give A= 0.9999 and $\frac{\omega}{\omega_p}$ = 0.014 or 0.81°.

Using (A.2) and (A.5), define the difference between the particle and fluid velocity as

$$\begin{aligned}\frac{\triangle u}{u_o} &= \frac{u}{u_o} - \frac{u_p}{u_o} \\ &= sin\,\omega t - A\,sin\,(\omega t - \phi)\end{aligned}$$

It follows that the $r.m.s.$ error is

$$\begin{aligned}\sqrt{\overline{\left(\frac{\triangle u}{u_o}\right)^2}} &= \left[\frac{1}{2\pi}\int_0^{2\pi}\left(\frac{\triangle u}{u_o}\right)^2 dt\right]^{1/2} \\ &= \frac{1}{\sqrt{2}}\left(1 - 2A\,cos\phi + A^2\right)^{1/2}\end{aligned} \tag{A.8}$$

Table (A.1) summarizes the error in the LDA measurements which shows that vapor particles indeed follow the unsteady flow field quite well under the condition studied.

Summing the $r.m.s.$ error in table (A.1) with uncertainties due to laser optics (0.14%), average of green and blue beam, and due to positioning of beam (0.33%), the total uncertainties in LDA measurement is tabulated in table (A.2).

Note that the total error in the LDA velocity data has a minimum of 0.36% with maximum of about 1%. At low reduced frequencies, $k \leq 2$, largest contribution to

Reduced Frequency

	6.4	2.0	1.0	.75	0.5	.15
Re = 125,000	.31%	.098%	.049%	.035%	.024%	.007%
Re = 400,000	1.00%	.31%	.16%	.12%	.077%	.024%

Table A.1: Percentage *r.m.s.* error in LDA data due to difference between particle motion and fluid motion.

Reduced Frequency

	6.4	2.0	1.0	.75	0.5	.15
Re = 125,000	.48%	.37%	.36%	.36%	.36%	.36%
Re = 400,000	1.06%	.48%	.39%	.38%	.37%	.36%

Table A.2: Total percentage *r.m.s.* error of LDA measured velocity

the total error is due to positioning of the probe volume. For $k \geq 2$, error due to finite inertia of vapor particles causing them not following the unsteady flow field faithfully begins to dominate.

Appendix B

Uncertainties in pressure data

The airfoil surface pressure is measured by two $\pm 0.1 psid$ Setra differential pressure transducers, one for each surface, mounted within the airfoil. The static pressure from the pitot-static probe in the free-stream is used as the camber pressure for the transducer. The total pressure is also connected to the transducers for calibration purpose. The calibration for the transducers is performed by comparing the dynamic pressure, difference between the total and static pressure, measured by the transducers with that measured by a baratron. Hence the baratron serves as the reference pressure for the entire pressure measurement system.

The calculation for uncertainty in the pressure measurement is based on single sample analysis of Kline and McClintock [33]. Let the result of a desired measurement be R, which can be expressed as

$$R = R(x_1, x_2, ..., x_n) \tag{B.1}$$

The uncertainty in R is

$$W_R = \left[\sum_{i=1}^{n} \left(\frac{\partial R}{\partial x_i} W_i \right)^2 \right]^{1/2} \tag{B.2}$$

where W_i is the uncertainty due to x_i. Since our data acquisition process is based on consecutive sampling, the estimation of uncertainty is conservative.

The pressure data, steady and unsteady, are processed and presented in the form

of pressure coefficient which is calculated as follows.

$$C_p = \frac{(C/V)\, G_t\, [(V/P)_t\, (p - p_\infty)_t + V_d]\, (CB)}{(C/V)\, G_b\, (V/P)_b\, (p_o - p_\infty)_b} \tag{B.3}$$

where

C/V = analog to digital Counts/Volt (2048 counts = 10 volts)

G_t = Gain of transducer amplifying circuitry

G_b = Gain of baratron amplifying circuitry

$(V/P)_t$ = Volts/psi conversion of transducer

$(V/P)_b$ = Volts/psi conversion of baratron

V_d = transducer drift voltage

$(p - p_\infty)_t$ = pressure output of transducer

$(p_o - p_\infty)_t$ = dynamic pressure output of transducer

$(p_o - p_\infty)_b$ = dynamic pressure output of baratron

(CB) = Calibration constant

and the calibration constant is

$$(CB) = \frac{(C/V)\, G_b\, (V/P)_b\, (p_o - p_\infty)_b}{(C/V)\, G_t\, [(V/P)_t\, (p_o - p_\infty)_t + V_d]} \tag{B.4}$$

Equation (B.3) says that analog voltage output from the transducer, $[(V/P)_t\, (p - p_\infty)_t + V_d]$, is amplified by the gain, G_t, and converted into digital form via (C/V). This value of count is then multiplied by the value of count for the calibration constant, (CB), determined prior to data acquisition. The result is then divided by the value of count corresponding to the dynamic pressure as measured by the baratron.

Substituting (B.4) into (B.3) and using (B.2), the fractional uncertainty in the instanteous C_p is

$$\frac{W_{C_p}}{C_p} = \left[2\left(\frac{W_{(p_o-p_\infty)_b}}{(p_o - p_\infty)_b}\right)^2 + \left(\frac{W_{(p_o-p_\infty)_t}}{(p_o - p_\infty)_t}\right)^2 + \left(\frac{W_{(p-p_\infty)_t}}{(p - p_\infty)_t}\right)^2 + 4\left(\frac{W_{C/V}}{C/V}\right)^2 + 2\left(\frac{W_{(V/P)_t}}{(V/P)_t}\right)^2 + 2\left(\frac{W_{V_d}}{V_d}\right)^2 \right]^{1/2} \tag{B.5}$$

where uncertainties in G_t, G_b, and $(V/P)_b$ are assumed to be negligible; the gains simply amplifies the uncertainties but not contribute to it and the baratron analog

conversion is very linear with near zero hysteresis. The calculation of each uncertainty term in (B.5) follows. The analysis presented takes into account only major contribution to the overall uncertainty in pressure coefficient, of which measurement errors dominate due to low velocities involved at low Reynolds numbers.

1) Uncertainties in $(p_o - p_\infty)_b$:

The dynamic pressure is measured by a pitot-static probe and read by the baraton. The probe is located about 0.5 chord upstream and 1.5 chord above the leading edge in the WBWT, 0.5 chord upstream and 1.0 chord above in the LTWT. Oscillascope trace of the dynamic pressure indicates maximum temporal variation of about 0.2% at lowest reduced frequency of 0.15. At $k = 6.4$, the temporal variation is negligible probably due to signal attenuation within the tubing. The location of the probe is about 10 boundary layer thicknesses from the upper tunnel walls. Hence, the dynamic pressure is considered steady and measures true free-stream dynamic pressure. The spatial variation of cross-sectional flow in the wind tunnel is assumed small. The major contributions to the uncertainty in the dynamic pressure are due to uncertainties in i) calculation of U_∞ and ii) setting the tunnel speed at U_∞.

The velocity is calculated from the definition of Reynolds number and density from perfect gas law. Hence,

$$(p_o - p_\infty)_b = \frac{1}{2}\left(\frac{p_\infty}{RT_\infty}\right)\left(\frac{Re\,\nu}{c}\right)^2 \tag{B.6}$$

Using (B.2), the fractional uncertainty in $(p_o - p_\infty)_b$ is

$$\frac{W_{(p_o-p_\infty)_b}}{(p_o - p_\infty)_b} = \left[\left(\frac{W_{p_\infty}}{p_\infty}\right)^2 + \left(\frac{W_{T_\infty}}{T_\infty}\right)^2 + 4\left(\frac{W_\nu}{\nu}\right)^2\right]^{1/2} + \frac{W_{U_{\infty\,tunnel}}}{U_{\infty\,tunnel}} \tag{B.7}$$

2) Uncertainties in $(p_o - p_\infty)_t$:

Since the first order approximation to the uncertainty for the dynamic pressure as measured by the baratron, $(p_o - p_\infty)_b$, in (B.7) is independent of instrumentation,

it follows

$$\frac{W_{(p_o-p_\infty)_t}}{(p_o-p_\infty)_t} = \frac{W_{(p_o-p_\infty)_b}}{(p_o-p_\infty)_b} \tag{B.8}$$

3) Uncertainties in $(p-p_\infty)_t$:

a) Steady flow :

The uncertainty in $(p-p_\infty)_t$ for steady flow is estimated using linear theory,

$$(p-p_\infty)_t = (p_o-p_\infty)_b\, 4\alpha\sqrt{\frac{1-x}{1+x}} \tag{B.9}$$

Assuming negligible uncertainty in spatial location compared to measurement error, the fractional uncertainty is

$$\frac{W_{(p-p_\infty)_t}}{(p-p_\infty)_t} = \left[\left(\frac{W_{(p_o-p_\infty)_b}}{(p_o-p_\infty)_b}\right)^2 + \left(\frac{W_\alpha}{\alpha}\right)^2\right]^{1/2} \tag{B.10}$$

Substituting (B.7) into (B.10), yields

$$\begin{aligned}\frac{W_{(p-p_\infty)_t}}{(p-p_\infty)_t} = \Bigg\{ & \left(\frac{W_{p_\infty}}{p_\infty}\right)^2 + \left(\frac{W_{T_\infty}}{T_\infty}\right)^2 + 4\left(\frac{W_\nu}{\nu}\right)^2 + \left(\frac{W_{U_{\infty\,tunnel}}}{U_{\infty\,tunnel}}\right)^2 + \\ & 2\left(\frac{W_{U_{\infty\,tunnel}}}{U_{\infty\,tunnel}}\right)\left[\left(\frac{W_{p_\infty}}{p_\infty}\right)^2 + \left(\frac{W_{T_\infty}}{T_\infty}\right)^2 + 4\left(\frac{W_\nu}{\nu}\right)^2\right]^{1/2} + \\ & \left(\frac{W_\alpha}{\alpha}\right)^2\Bigg\}^{1/2}\end{aligned} \tag{B.11}$$

b) Unsteady flow (Amplitude):

The measurement uncertainty in the result of amplitude of pressure coefficient at, say, fundamental excitation frequency, $\tilde{C}_{p1}$, are mainly due to amplitude attenuation for finite pressure tubing length. Calibration of the tubings show amplitude attenuation, figure 2.8, to be approximately linear from 0 to 2% in the frequency range of 0 to $40Hz.$, the maximum frequency tested for the first harmonic. This calibration is applied to the unsteady pressure data. Hence, the second order correction should be negligible and the uncertainty for amplitude of unsteady pressure is assumed to be same as that for the steady pressure data.

c) Unsteady flow (Phase) :

The uncertainties in phase lag results from measurement error are due to finite pressure tubing and resolution in the photo detection setup in timing the position of the ellipse. The first order uncertainty due tubing dynamics is corrected and secondary uncertainties will be assumed small. Measurement indicates uncertainty in the timing mechanism of 1/16 inch over 2.5 inch radius. Hence the uncertainty in the phase is approximately,

$$W_\varphi = \pm 1.5^o \tag{B.12}$$

4) Uncertainties in $(V/P)_t$:

The analog output of the transducer is very linear with hysteresis of about 0.1% according to manufacturer's specification. So we shall assume

$$\frac{W_{(V/P)_t}}{(V/P)_t} = 0.001 \tag{B.13}$$

5) Uncertainties in V_d:

The drift of the transducer is mainly a function of temperature change. In the test section of LTWT, the temperature over the duration of one set of pressure data is approximately $T_\infty = 70 \pm 0.2^o F$. As first order approximation, assume that the drift is linear with temperature change, hence

$$\begin{aligned} \left(\frac{W_{V_d}}{V_d}\right)_{LTWT} &= \frac{0.2}{460+70} \\ &= 0.0004 \end{aligned} \tag{B.14}$$

For the WBWT, the temperature variation is larger since the test section is not thermally shielded from the outdoor environment. The variation is measured to be $T_\infty = 80 \pm 2^o F$. Hence

$$\begin{aligned} \left(\frac{W_{V_d}}{V_d}\right)_{WBWT} &= \frac{2}{460+80} \\ &= 0.004 \end{aligned} \tag{B.15}$$

6) Uncertainties in C/V:

The uncertainty in the analog to digital conversion is mainly due to truncation

in digital representation. The A/D conversion is 2048 counts per 10 volts. For $Re = 125000$, $(p_o - p_\infty)$ corresponds to 0.5 volts which is 102 counts. Hence,

$$\left(\frac{W_{C/V}}{C/V}\right)_{125k} = \frac{1}{102} = 0.010 \qquad \text{(B.16)}$$

For $Re = 400000$, $(p_o - p_\infty)$ corresponds to 2.0 volts which is 409 counts. Hence,

$$\left(\frac{W_{C/V}}{C/V}\right)_{400k} = \frac{1}{409} = 0.0024 \qquad \text{(B.17)}$$

7) Other uncertainties:

Additional uncertainties are:

$p_\infty = 30.00 \pm .02$ *inch Hg.*

$\nu = .000157 \pm 1.11x10^{-7}\ ft^2/sec$ for LTWT

$\nu = .000157 \pm 1.11x10^{-6}\ ft^2/sec$ for WBWT

The uncertainties in the kinematic viscosity is based on temperature variation within the test section, as estimated in part 5.

Substituting (B.7) to (B.17) into (B.5) yields

$$\frac{W_{C_p}}{C_p} = \left\{ 4\left(\frac{W_{p_\infty}}{p_\infty}\right)^2 + 4\left(\frac{W_{T_\infty}}{T_\infty}\right)^2 + 16\left(\frac{W_\nu}{\nu}\right)^2 + 4\left(\frac{W_{U_{\infty\ tunnel}}}{U_{\infty\ tunnel}}\right)^2 + 8\left(\frac{W_{U_{\infty\ tunnel}}}{U_{\infty\ tunnel}}\right)\left[\left(\frac{W_{p_\infty}}{p_\infty}\right)^2 + \left(\frac{W_{T_\infty}}{T_\infty}\right)^2 + 4\left(\frac{W_\nu}{\nu}\right)^2\right]^{1/2} + \left(\frac{W_\alpha}{\alpha}\right)^2 + 4\left(\frac{W_{C/V}}{C/V}\right)^2 + 2\left(\frac{W_{(V/P)_t}}{(V/P)_t}\right)^2 + 2\left(\frac{W_{V_d}}{V_d}\right)^2 \right\}^{1/2} \qquad \text{(B.18)}$$

Tables (B.1) and (B.2) summarize the uncertainties for experiments in LTWT and WBWT respectively.

	$\frac{W_{T_\infty}}{T_\infty}$	$\frac{W_\nu}{\nu}$	$\frac{W_{U_{\infty\ tunnel}}}{U_{\infty\ tunnel}}$	$\frac{W_{C/V}}{C/V}$	$\frac{W_{V_d}}{V_d}$
Re = 125,000	.00040	.00071	.010	.010	.00040
Re = 400,000	.00040	.00071	.0050	.0024	.00040

Table B.1: Fractional uncertainties for tests in LTWT

	$\frac{W_{T_\infty}}{T_\infty}$	$\frac{W_\nu}{\nu}$	$\frac{W_{U_{\infty\ tunnel}}}{U_{\infty\ tunnel}}$	$\frac{W_{C/V}}{C/V}$	$\frac{W_{V_d}}{V_d}$
Re = 125,000	.0040	.0071	.010	.010	.0040
Re = 400,000	.0040	.0071	.0050	.0024	.0040

Table B.2: Fractional uncertainties for tests in WBWT

Substituting values from tables (B.1) and (B.2) into (B.18), table (B.3) is constructed. The percentage uncertainties in the pressure data are shown in table (2.2). Uncertainties of about 2% in C_p for the results in 0.05% free-stream turbulence level (LTWT) is certainly acceptable. The larger uncertainties in the WBWT is primarily due to temperature variation over a test period (the tests were conducted over the summer) causing uncertainties in the free-stream velocity, for a fixed Reynolds number, which give rise to uncertainties in the pressure data.

	LTWT	WBWT
Re = 125,000	2.3%	5.1%
Re = 400,000	1.3%	4.1%

Table B.3: Fractional uncertainties in C_p, $\frac{W_{C_p}}{C_p}$, in both tunnels and Reynolds numbers

Appendix C

Formulation for the chordwise distribution of angle attack

The unsteady flow generator used in this work is somewhat unconventional; an rotating ellipse is placed aft and below trailing edge position of the airfoil. The distance between the rotating axis of the ellipse to the trailing edge is 0.33 chord. The induced upwash by the unsteady flow generator on the airfoil can be interpreted as chordwise variation of angle of attack. The following analysis determines the Fourier decomposition of this chordwise variation.

Let the streamwise and vertical velocity induced by the unsteady flow generator along the chordline location without the airfoil mounted be represented by

$$u(x,0,t) = \overline{u}(x,0,t) + \sum_{n=1}^{\infty} \tilde{u}_n cos(n\omega t + \varsigma_n) \tag{C.1}$$

$$v(x,0,t) = \overline{v}(x,0,t) + \sum_{n=1}^{\infty} \tilde{v}_n cos(n\omega t + \eta_n) \tag{C.2}$$

Similarly, let the chordwise distribution of angle of attack be

$$\alpha(x,0,t) = \overline{\alpha}(x,0,t) + \sum_{n=1}^{\infty} \tilde{\alpha}_n cos(n\omega t + \beta_n) \tag{C.3}$$

At any instant in time, the local angle of attack is defined as

$$\begin{aligned} \alpha &\equiv tan^{-1}\left(\frac{v}{u}\right) \\ &= \frac{v}{u} + O\left(\frac{v}{u}\right)^3 ;\ for\ \left(\frac{v}{u}\right)^2 < 1 \end{aligned} \tag{C.4}$$

The higher order term can be neglected since data show $(\overline{v}/\overline{u})^2$, being largest at the trailing edge position, is about 3% and only 0.2% at the leading edge location.

Using (C.1) and (C.2) and substituting into (C.4),

$$\begin{aligned}\frac{v}{u} = & \frac{\overline{v}(x,0,t)+\sum_{n=1}^{\infty}\tilde{v}_n\, cos(n\omega t+\eta_n)}{\overline{u}(x,0,t)+\sum_{n=1}^{\infty}\tilde{u}_n\, cos(n\omega t+\varsigma_n)} \\ = & \frac{\overline{v}/\overline{u}}{1+\sum_{n=1}^{\infty}(\tilde{u}_n/\overline{u})\, cos(n\omega t+\varsigma_n)}+\frac{\tilde{v}_1/\overline{u}\, cos(\omega t+\eta_1)}{1+\sum_{n=1}^{\infty}(\tilde{u}_n/\overline{u})\, cos(n\omega t+\varsigma_n)}+ \\ & \frac{\tilde{v}_2/\overline{u}\, cos(2\omega t+\eta_2)}{1+\sum_{n=1}^{\infty}(\tilde{u}_n/\overline{u})\, cos(n\omega t+\varsigma_n)}+\ldots \end{aligned} \tag{C.5}$$

Binomial series expanding each term above gives

$$\begin{aligned}\frac{v}{u} = & \left(\frac{\overline{v}}{\overline{u}}+\frac{\tilde{v}_1}{\overline{u}}\, cos(\omega t+\eta_1)+\frac{\tilde{v}_2}{\overline{u}}\, cos(2\omega t+\eta_2)+\ldots\right)* \\ & \left[1-\left(\frac{\tilde{u}_1}{\overline{u}}\, cos(\omega t+\varsigma_1)+\frac{\tilde{u}_2}{\overline{u}}\, cos(2\omega t+\varsigma_2)+\ldots\right)+\right. \\ & \left.\left(\frac{\tilde{u}_1}{\overline{u}}\, cos(\omega t+\varsigma_1)+\frac{\tilde{u}_2}{\overline{u}}\, cos(2\omega t+\varsigma_2)+\ldots\right)^2+\ldots\right] \end{aligned} \tag{C.6}$$

The square bracket on the right-hand-side of (C.6) contains terms due to temporal and spatial variation of streamwise velocity along the chord. To examine the order of magnitude of these terms, figures (C.1) to (C.4) show the chordwise distribution of streamwise time mean velocity and several harmonics for LDV data taken in Low Turbulence Wind Tunnel without the airfoil mounted. Data taken in WBWT is similar in order of magnitude. Tables (C.1) and (C.2) are also constructed based on the figures for reduced frequencis of 0.15 and 6.4. Overall, the streamwise velocity amplitude ratios are small with the exception of the amplitude of fundamental frequency at the leading edge for $k = 0.15$. For the sake of simplification in the the representation of chordwise distribution of angle of attack, the terms in the square bracket of (C.6 will be approximated as unity.

Finally, equating (C.3) with (C.6) and taking the approximation for the streamwise veloctiy into account, the Fourier amplitude and phase of the chordwise distribution of angle of attach are identified as

$$\overline{\alpha} = \frac{\overline{v}}{\overline{u}} \tag{C.7}$$

	$\tilde{u}_1/\overline{u}$	$\tilde{u}_2/\overline{u}$	$\tilde{u}_3/\overline{u}$
Leading edge	0.78%	0.05%	0.01%
Trailing edge	4.7%	0.93%	0.7%

Table C.1: Upwash amplitude ratio for $k = 0.15$ ($Re = 125{,}000$, LTWT)

	$\tilde{u}_1/\overline{u}$	$\tilde{u}_2/\overline{u}$	$\tilde{u}_3/\overline{u}$
Leading edge	0.09%	0.05%	0.01%
Trailing edge	1.5%	0.15%	0.02%

Table C.2: Upwash amplitude ratio for $k = 6.4$ ($Re = 125{,}000$, LTWT)

$$\tilde{\alpha}_1 = \frac{\tilde{v}_1}{\overline{u}} \tag{C.8}$$

$$\tilde{\alpha}_2 = \frac{\tilde{v}_2}{\overline{u}} \tag{C.9}$$

$$\beta_n = \eta_n \tag{C.10}$$

which are the first order terms. Note that if the upwash is larger, then additional terms in $\overline{\alpha}$, $\tilde{\alpha}_1$, and $\tilde{\alpha}_2$ exist, due to taking appropriate weighted average of eqaution (C.6).

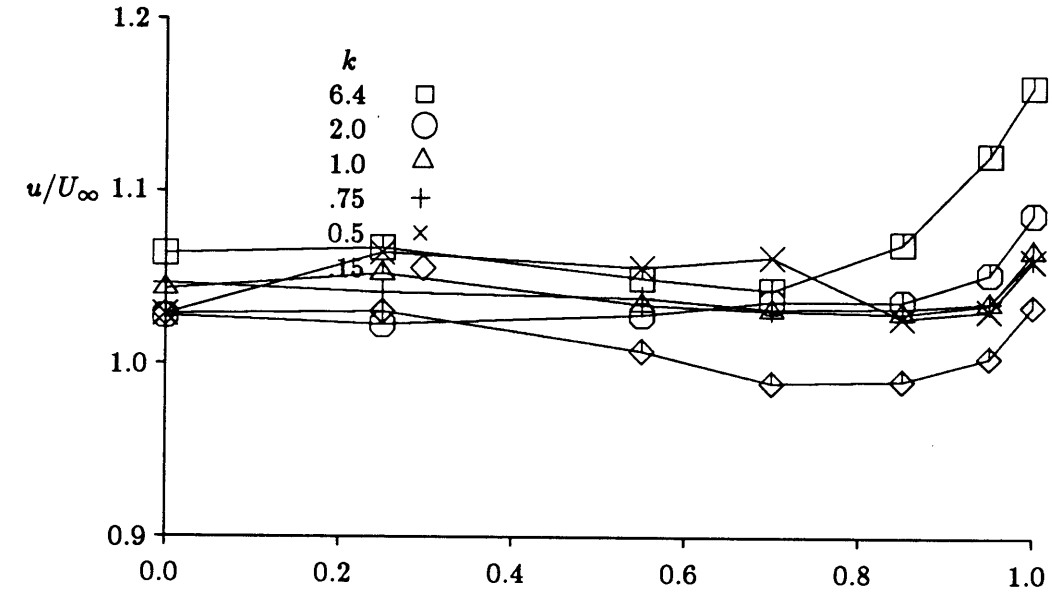


Figure C.1: Chordwise time mean U-velocity ($Re = 125000$, LTWT)

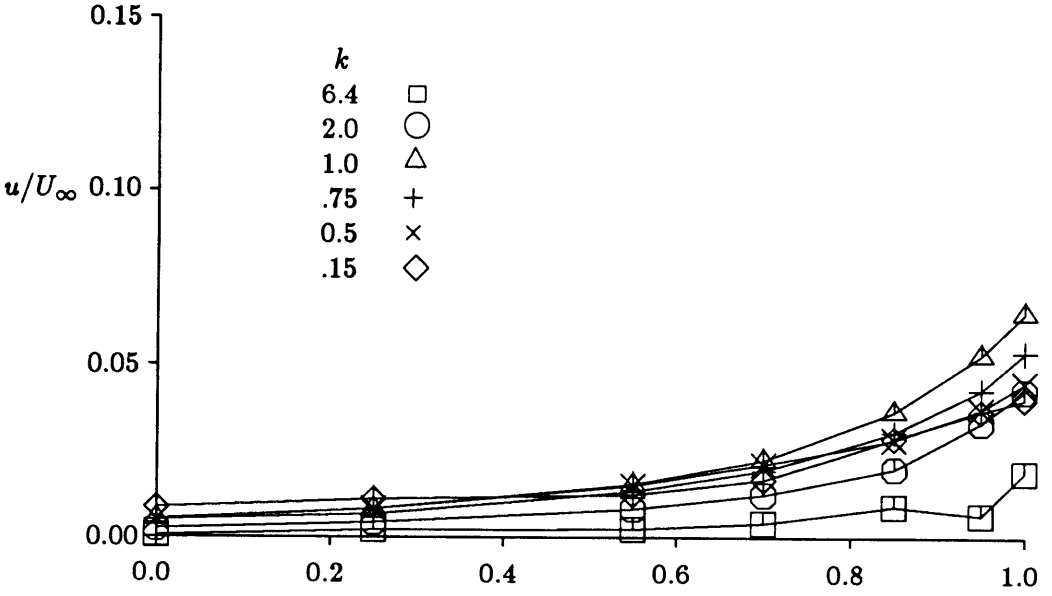


Figure C.2: Chordwise amplitude of U-velocity at fundamental freq. ($Re = 125000$, LTWT)

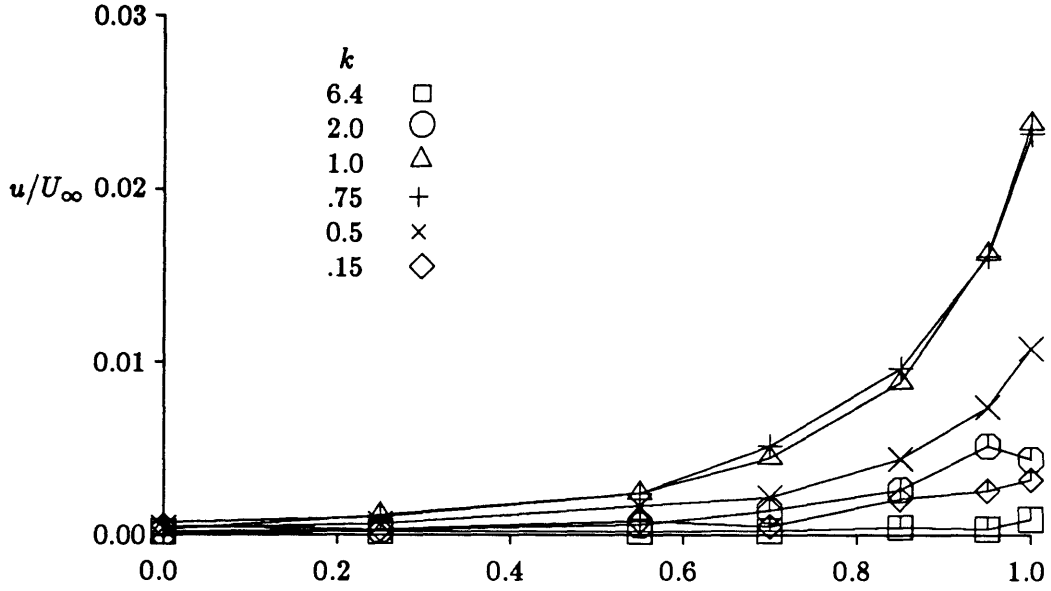


Figure C.3: Chordwise amplitude of U-velocity at 2^{nd} harmonic (Re = 125000, LTWT)

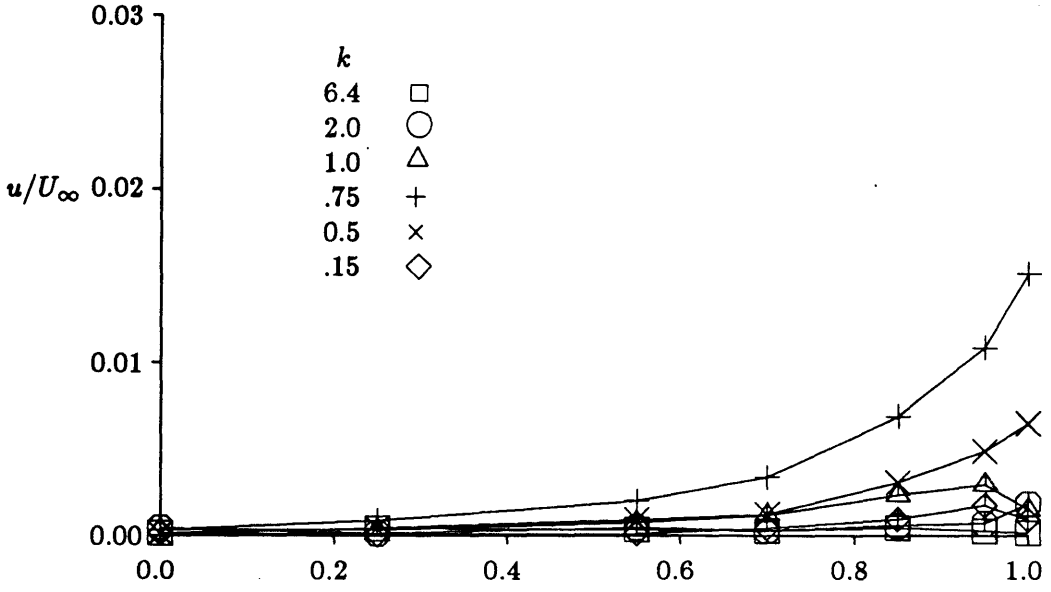


Figure C.4: Chordwise amplitude of U-velocity at 3^{rd} harmonic (Re = 125000, LTWT)

Appendix D

Theorectical time mean and unsteady airfoil pressure

D.1 Time mean difference pressure

The theorectical time mean difference pressure is calculated using thin airfoil theory. The measured potential upwash is used as input. These calculations serve as comparison with measured surface pressure data.

Results of this calculation are presented in figures D.1 to D.4 for the 0012 airfoil and in figures D.5 to D.8 for the Wortmann airfoil. Each set of figure consists of tunnel turbulence level of 0.05% and 0.8%, Re = 125000 and 400000, and $0.15 \leq k \leq 6.4$. The reduced frequency effect on time mean loading for both airfoils are very similar; loading increases with reduced frequency. This is expected since data show that upwash increases with reduced frequency. Note that $\overline{C}_{m,1/4}$, quarter chord moment coefficient with nose up positive, is much smaller for the Wortmann than the 0012 due to difference in loading distribution.

D.2 Unsteady pressure–Theodorsen's unsteady airfoil theory

The problem of thin airfoil in small unsteady motion in an otherwise uniform free-stream was the subject of intense investigation beginning in the early 1930s with flutter prediction as the main motivation. The first complete solution was published by Theodorsen [72] in 1935 which separates the resulting lift into an illuminating circulatory and non-circulatory parts. Many workers such as Glauert, Ellenberger, Küssner and others also came to the same conclusion later. See Blisplinghoff et al. [5] for references.

Ashley [5] rederived Theodorsen's results and obtained an expression for the amplitude of the difference pressure distribution based on the amplitude of the vertical velocity along the chord. This form is suitable for the present investigation since the upwash velocities that the airfoil sees are measured. The goal of the analysis is to compare the linear unsteady airfoil theory with data. In the present work, presentation of details of derivation is not deemed necessary and only the final results and methods for calculation is outlined.

For an airfoil in periodic motion with vertical velocity

$$w(x,t) = Re(\tilde{w}(x)e^{i\omega t}) \tag{D.1}$$

and loading

$$\triangle p(x,t) = Re(\triangle \tilde{p}(x)e^{i\omega t}) \tag{D.2}$$

The expression for the amplitude of the unsteady differnece pressure is :

$$\begin{aligned}\frac{-\triangle\tilde{p}(x)}{\rho U} = \; & (2/\pi)\;\; [1-C(k)]\sqrt{\frac{1-x}{1+x}}\int_{-1}^{1}\sqrt{\frac{1+\xi}{1-\xi}}\tilde{w}(\xi)d\xi + \\ & (2/\pi)\;\; \int_{-1}^{1}\left[\sqrt{\frac{1-x}{1+x}}\sqrt{\frac{1+\xi}{1-\xi}}\frac{1}{(x-\xi)} - ik\Lambda(x,\xi)\right]\tilde{w}(\xi)\,d\xi\end{aligned} \tag{D.3}$$

where

$$\Lambda(x,\xi) = \frac{1}{2}ln\left[\frac{1-x\xi+\sqrt{1-\xi^2}\sqrt{1-x^2}}{1-x\xi-\sqrt{1-\xi^2}\sqrt{1-x^2}}\right] \tag{D.4}$$

and $C(k)$ is the famous Theodorsen's function.

A few notes on equation D.3 is in order. In steady motion, $C(0) = 1$, the second term on the right hand side alone accounts for the chordwise distribution of difference pressure, which is of the same form as the vorticity distribution on the flat plate at small angle of attack. See equation 3.19. Additionally, it is indeed interesting that the (1- $C(k)$) term which accounts for the pressure variation associated with the wake also has the same form as flat plat loading in steady flow.

The methodology in applying Theodorsen's theory to our data is to Fourier decompose the measured upwash along the chordline in time and Chebyshev polynomial decompose in space. That is,

$$w(x,t) = \sum_{j=0}^{\infty} \sum_{m=0}^{\infty} \left[A_{mj} cos(m\omega t) + B_{mj} sin(m\omega t) \right] T_j(x) \tag{D.5}$$

where

$$T_j(x) = cos[j(cos^{-1}(x))] \tag{D.6}$$

For example, $T_0(x) = 1, T_1(x) = -x, T_2(x) = 2x^2 - 1$ etc. Then, integration of equation D.3 using the well known Glauert integral, leads to an analytic solution in the form of finite and infinity series with fast decaying terms. Hence, the chordwise distribution of unsteady difference pressure is found by simply summing terms.

The beauty of this particular form of decomposition arises from the nature of our unsteady excitation. Being basically periodic with small higher harmonic terms, the dominant Fourier term is the coefficient at the fundamental frequency. Standard Fast Fourier Transform (FFT) code is used for this purpose. In the spatial domain, the rotating ellipse is essentially a vortex with periodically varying strength which induces a $1/r^n$ type velocity decay. Hence, it can be represented by just a few terms of Chebyshev polynomials. In fact, for most cases, the 5^{th} order term is 3 orders of magnitude smaller than the 4^{th} term! However, there is a constraint on values of x namely that it has to have a cosine distribution rather than, say, evenly spaced. But for our airfoil, this constrain is actually welcomed since pressure gradients are expected to be steepest at the leading and trailing edges. Typical CPU time for 32

points on the airfoil is only about half a minute on a μVax. The lesson well learned from decomposing the upwash is simply know the signal at hand and use the right mathematical tool.

Figures D.9 to D.12 present results for the calculated unsteady airfoil loading. The most prominent feature is that unsteady loading decreases with reduced frequency for all cases. Also, at low reduced frequencies loading is more aft than that of high reduced frequencies. This trend is consistent with the unsteady upwash data which show a decrease in amplitude with increase in reduced frequency.

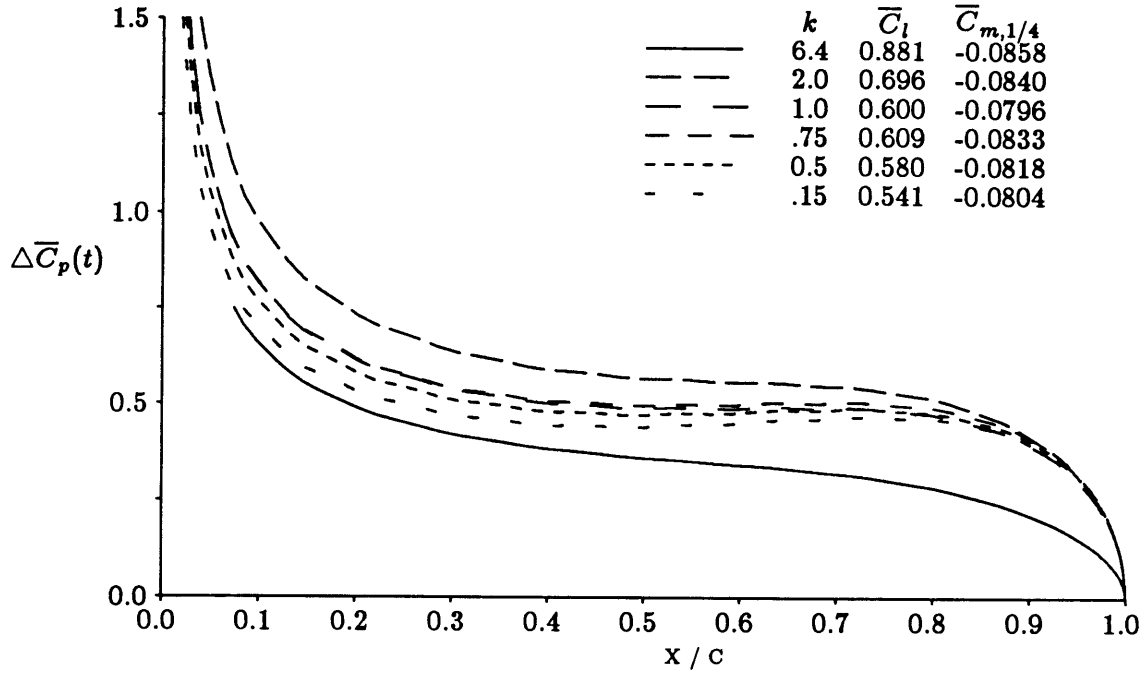


Figure D.1: Calculated time mean loading (0012 in LTWT, $Re = 125{,}000$)

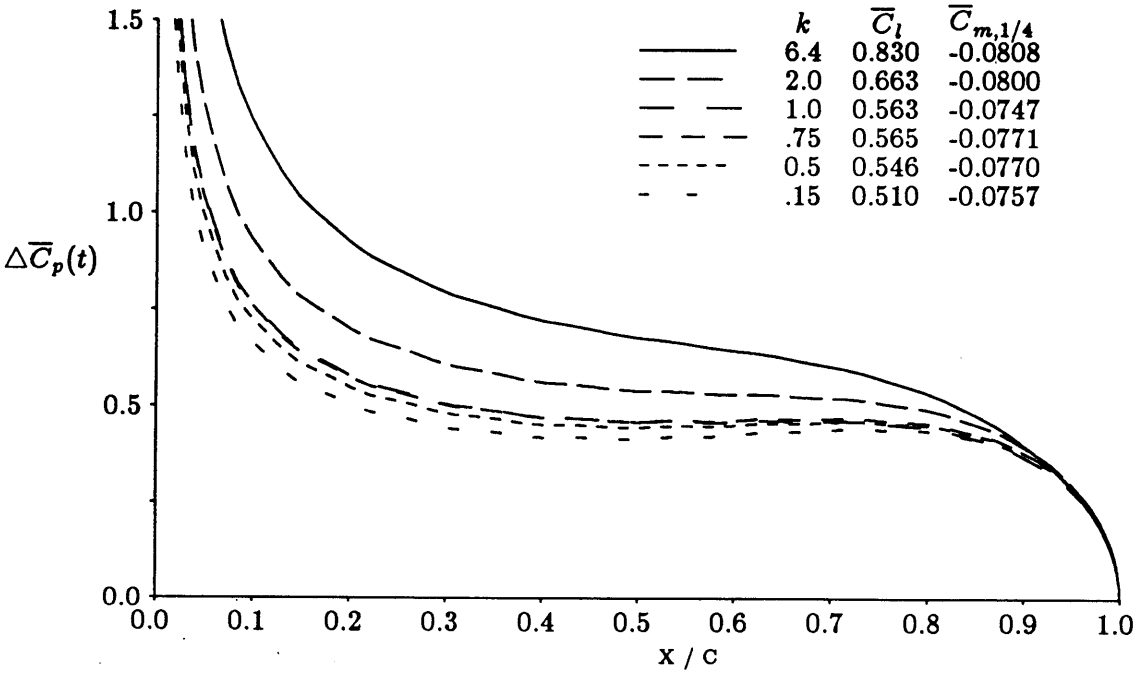


Figure D.2: Calculated time mean loading (0012 in LTWT, $Re = 400{,}000$)

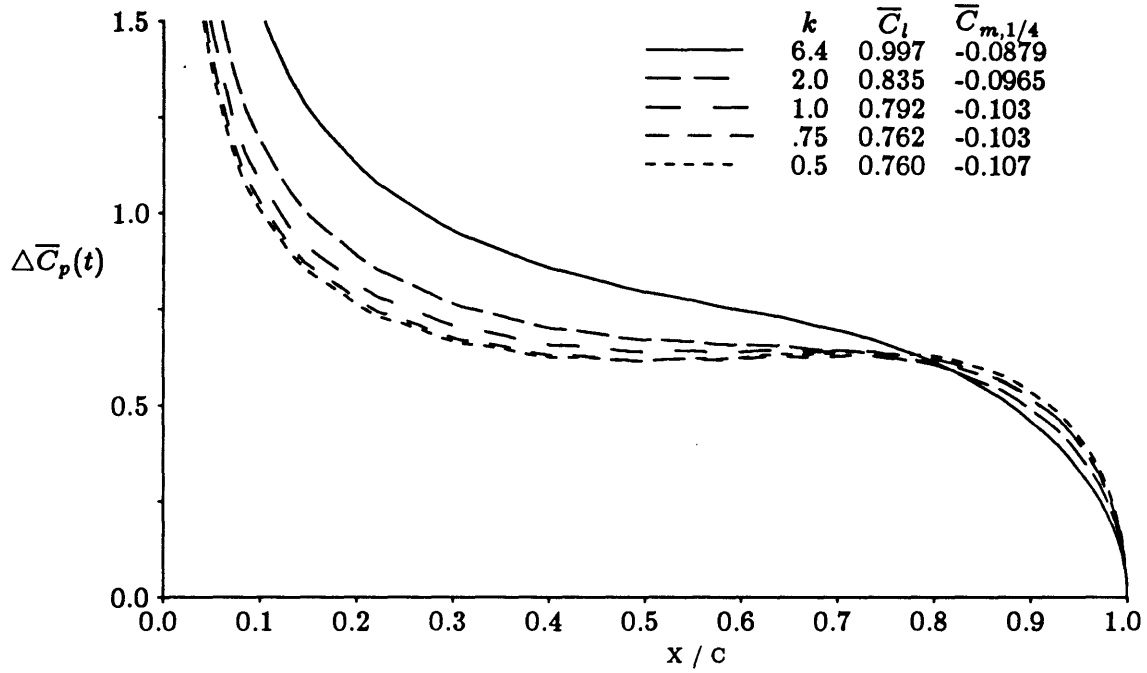


Figure D.3: Calculated time mean loading (0012 in WBWT, $Re = 125{,}000$)

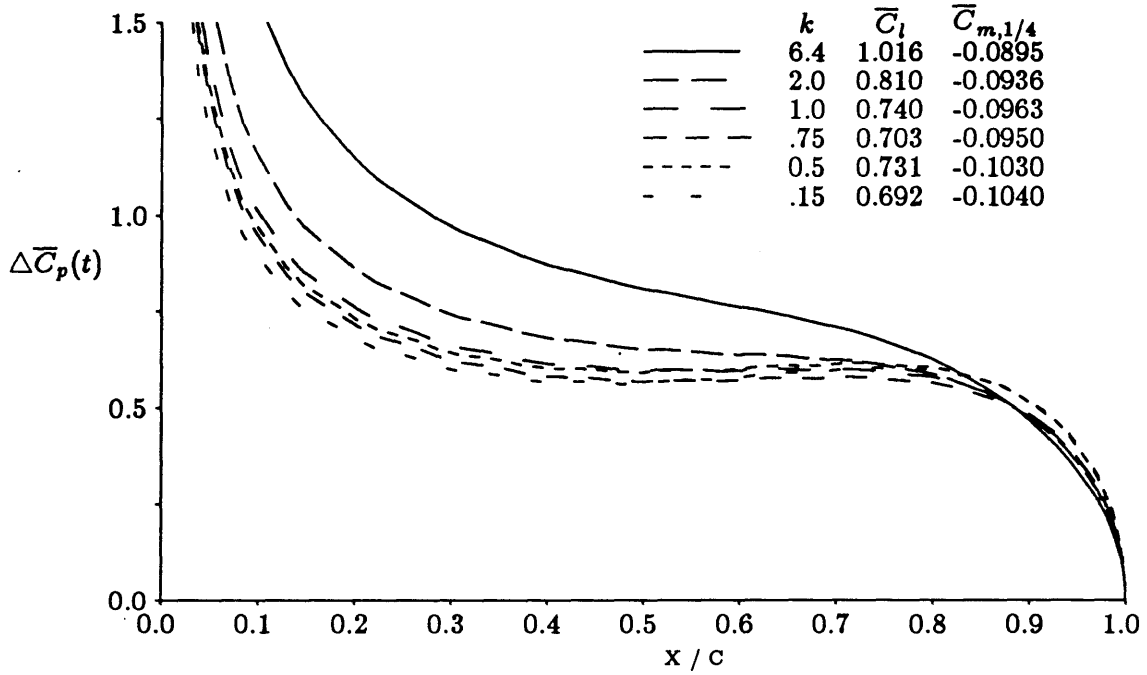


Figure D.4: Calculated time mean loading (0012 in WBWT, $Re = 400{,}000$)

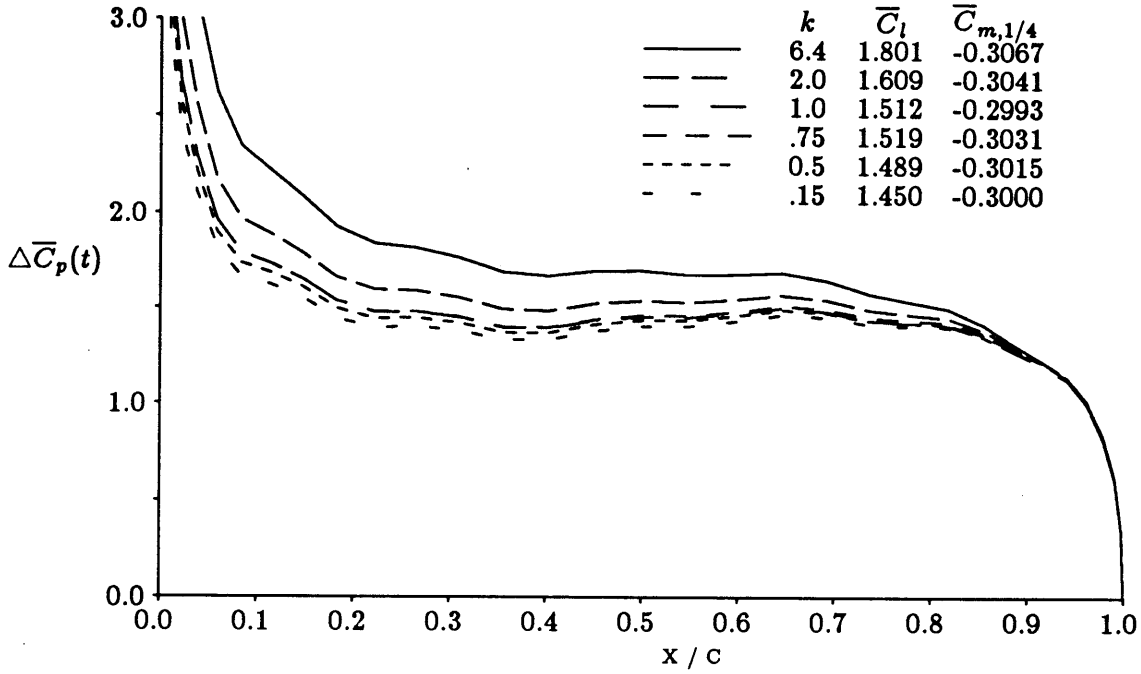


Figure D.5: Calculated time mean loading (Wort. in LTWT, $Re = 125{,}000$)

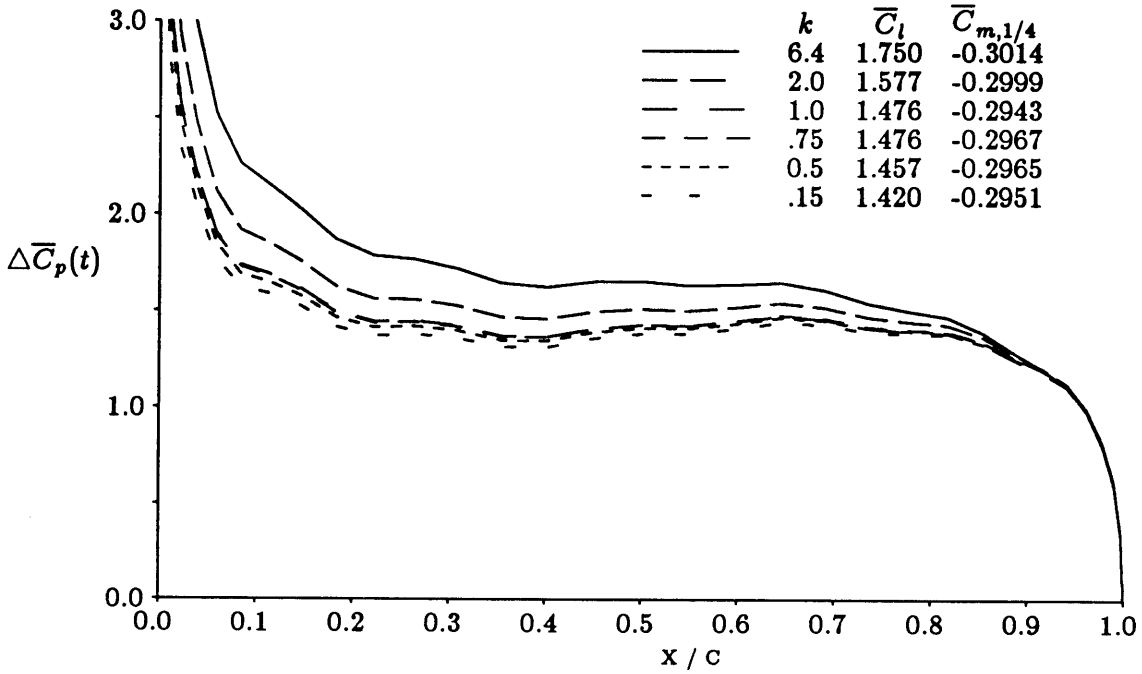


Figure D.6: Calculated time mean loading (Wort. in LTWT, $Re = 400{,}000$)

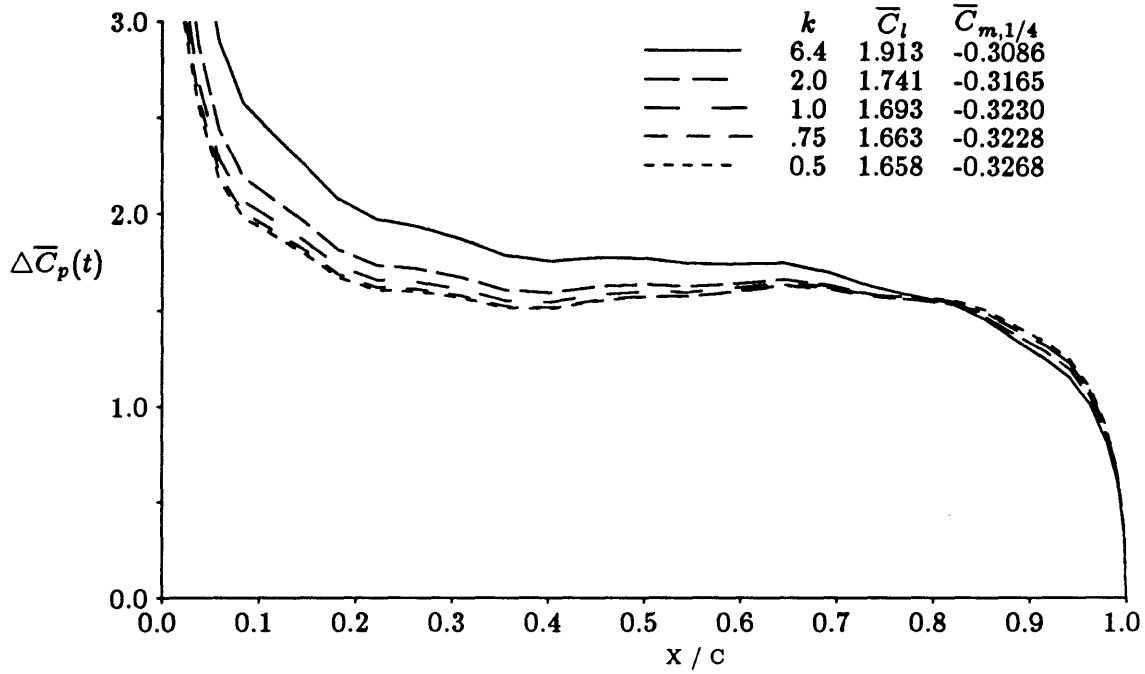


Figure D.7: Calculated time mean loading (Wort. in WBWT, Re = 125,000)

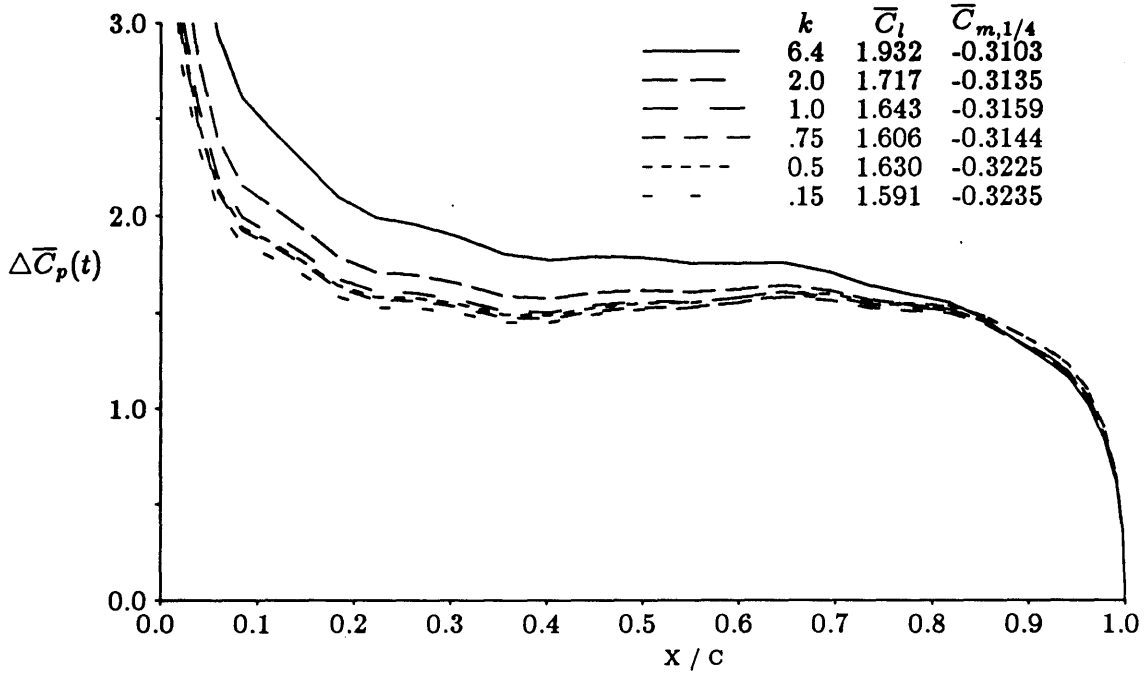


Figure D.8: Calculated time mean loading (Wort. in WBWT, Re = 400,000)

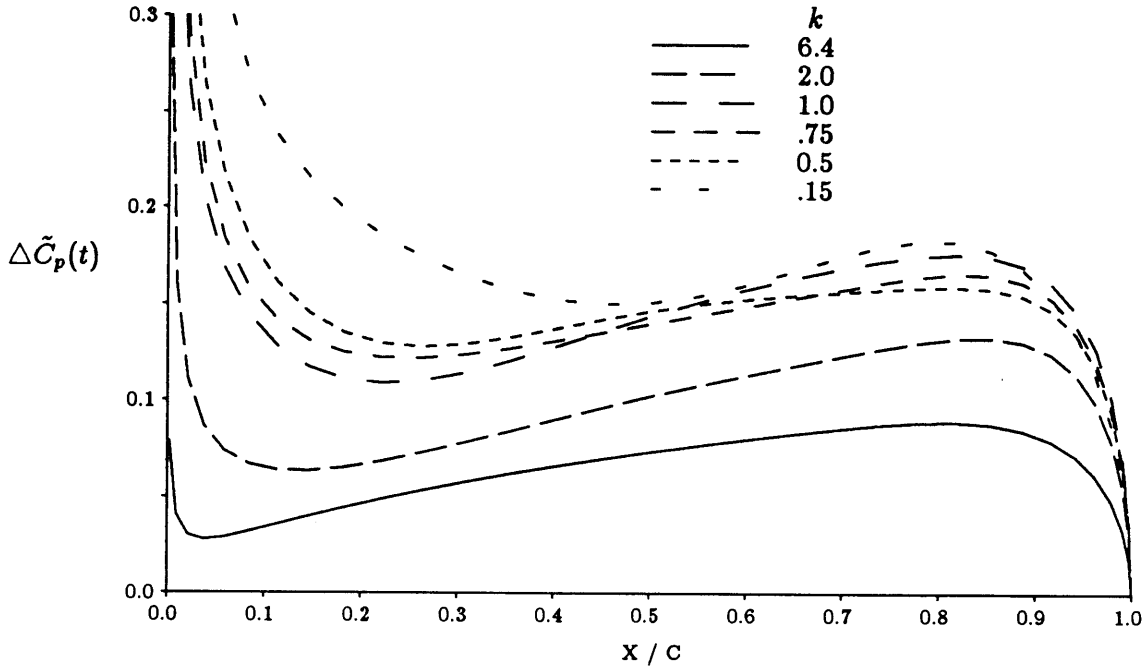


Figure D.9: Calculated loading amplitude at fund. frequency (LTWT, Re = 125,000)

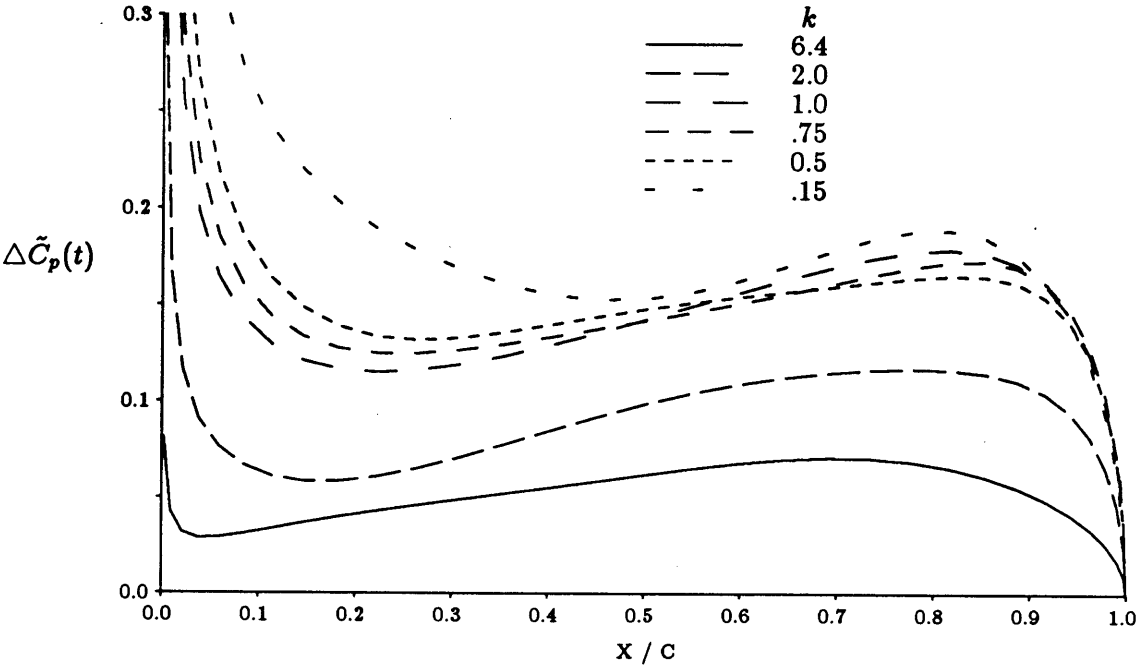


Figure D.10: Calculated loading amplitude at fund. frequency (LTWT, Re = 400,000)

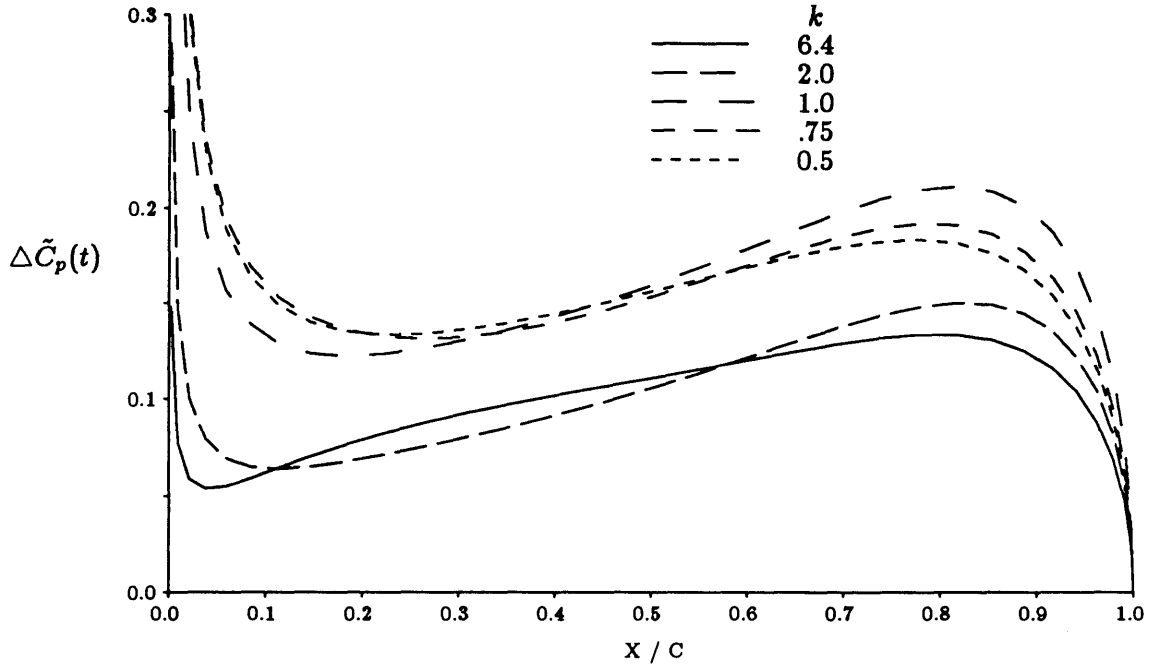


Figure D.11: Calculated loading amplitude at fund. frequency (WBWT, Re = 125,000)

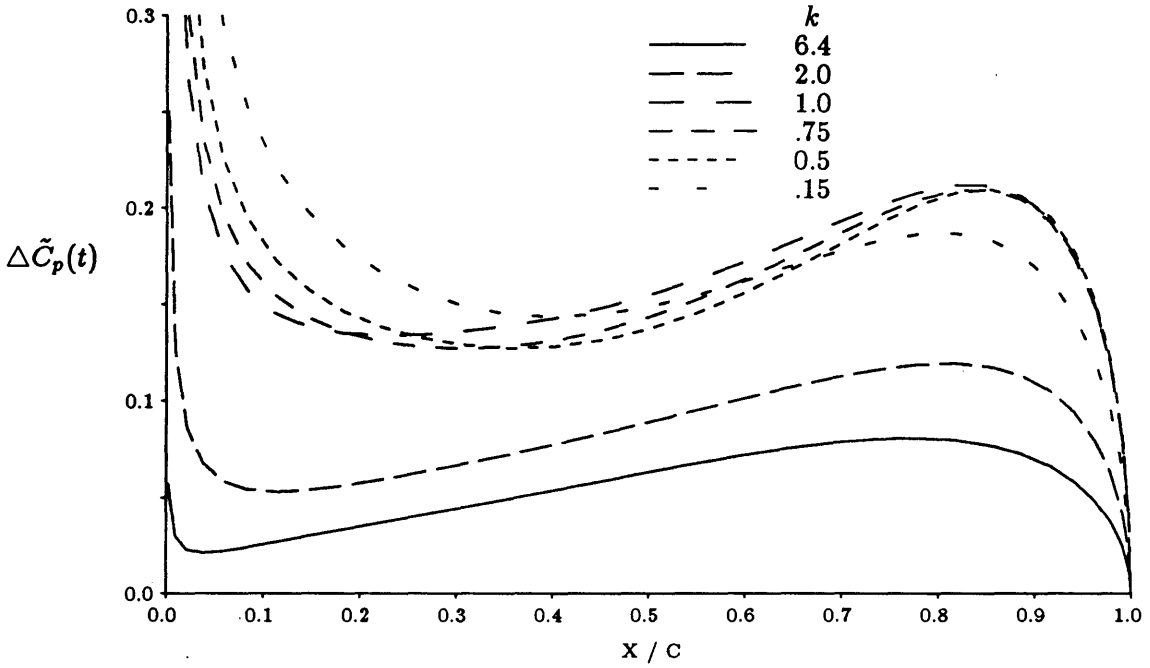


Figure D.12: Calculated loading amplitude at fund. frequency (WBWT, Re = 400,000)

Appendix E

Unsteady pressure data

This appendix presents the unsteady pressure data taken in 0.05% free-stream turbulence level (LTWT). Data includes Wortmann FX63-137 and NACA 0012 at $\alpha = 0^o$, Re = 125000 and 400000, and k = 0.15, 0.5, 0.75, 1.0, 2.0, 6.4. The pressure coefficients are normalized by the upwash (without the airfoil) angle of attack at the trailing edge position. This is determined from the upwash data in Chapter 3. Tables (E.1) and (E.2) summarized this data.

Plots are organized such that each page shows the amplitude and phase of pressure coefficient at fundamental frequency, $\tilde{C}_{p1}$ and ς, and the amplitude of pressure coefficient at 2^{nd} harmonic, $\tilde{C}_{p2}$; the definitions are given in equations (4.9) and (4.10).

Reduced Frequency

	6.4	2.0	1.0	.75	0.5	.15
Re = 125,000	0.210	0.184	0.166	0.166	0.170	0.158
Re = 400,000	0.189	0.171	0.153	0.152	0.154	0.147

Table E.1: Time mean upwash angle of attack at the trailing edge, $\overline{\alpha}_{te}$ (radian), in 0.05% free-stream turbulence(LTWT)

Reduced Frequency

	6.4	2.0	1.0	.75	0.5	.15
$Re = 125{,}000$	0.0169	0.0514	0.0788	0.0770	0.0762	0.0722
$Re = 400{,}000$	0.0143	0.0437	0.0776	0.0799	0.0783	0.0747

Table E.2: Upwash angle of attack of fundamental harmonic at the trailing edge, $\tilde{\alpha}_{te}$ (radian), in 0.8% free-stream turbulence(WBWT)

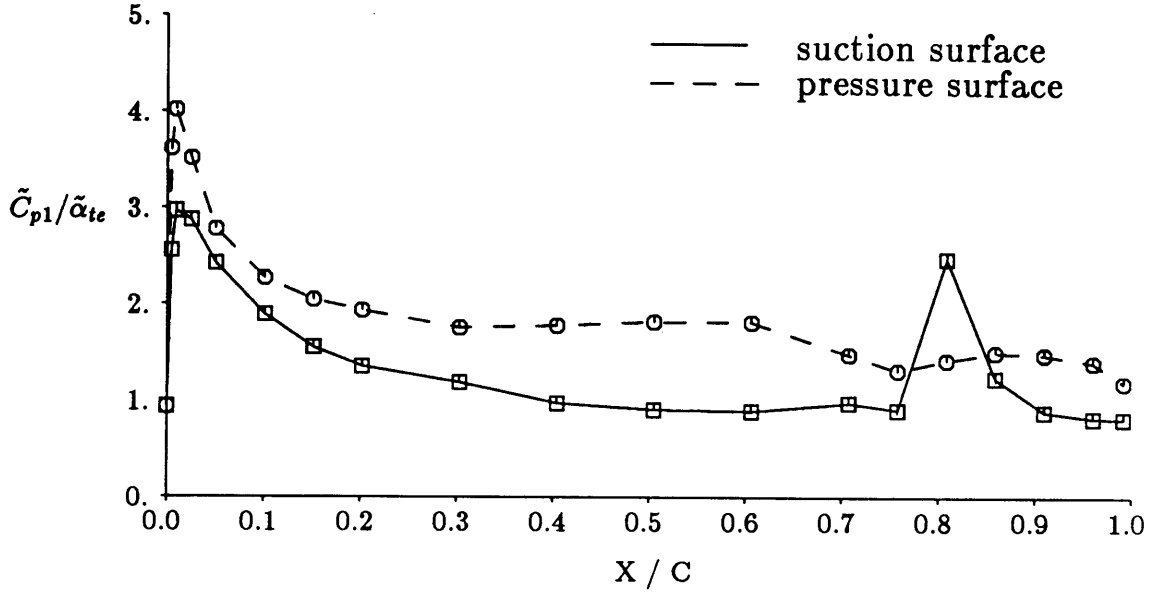


Figure E.1: Amplitude of C_p at fundamental frequency (Wortmann, LTWT, Re = 125000, $\alpha = 0^o$, $k = 0.15$)

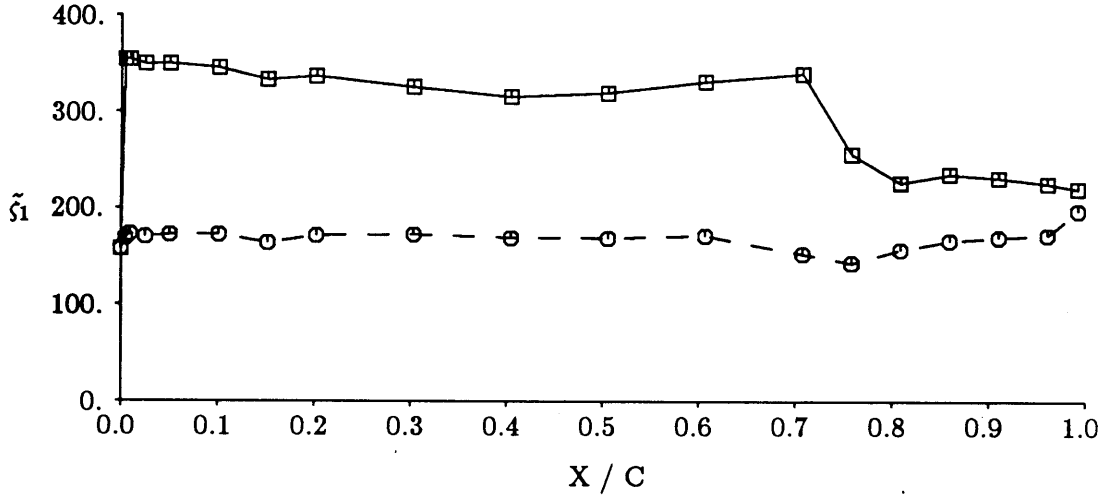


Figure E.2: Phase of C_p at fundamental frequency (Wortmann, LTWT, Re = 125000, $\alpha = 0^o$, $k = 0.15$)

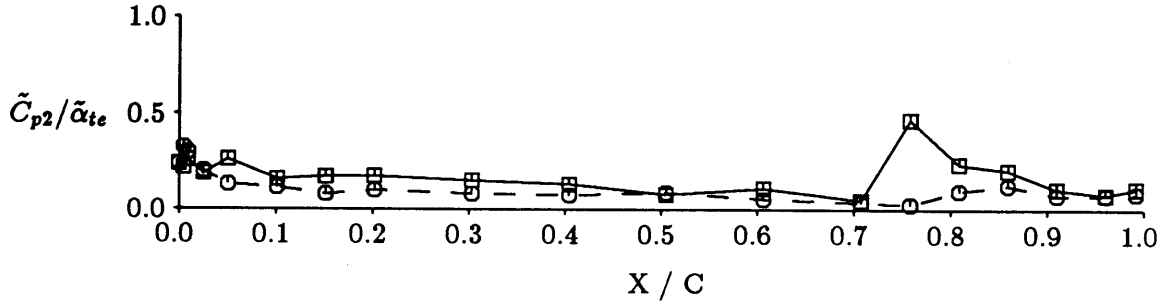


Figure E.3: Amplitude of C_p at 2^{nd} harmonic (Wortmann, LTWT, Re = 125000, $\alpha = 0^o$, $k = 0.15$)

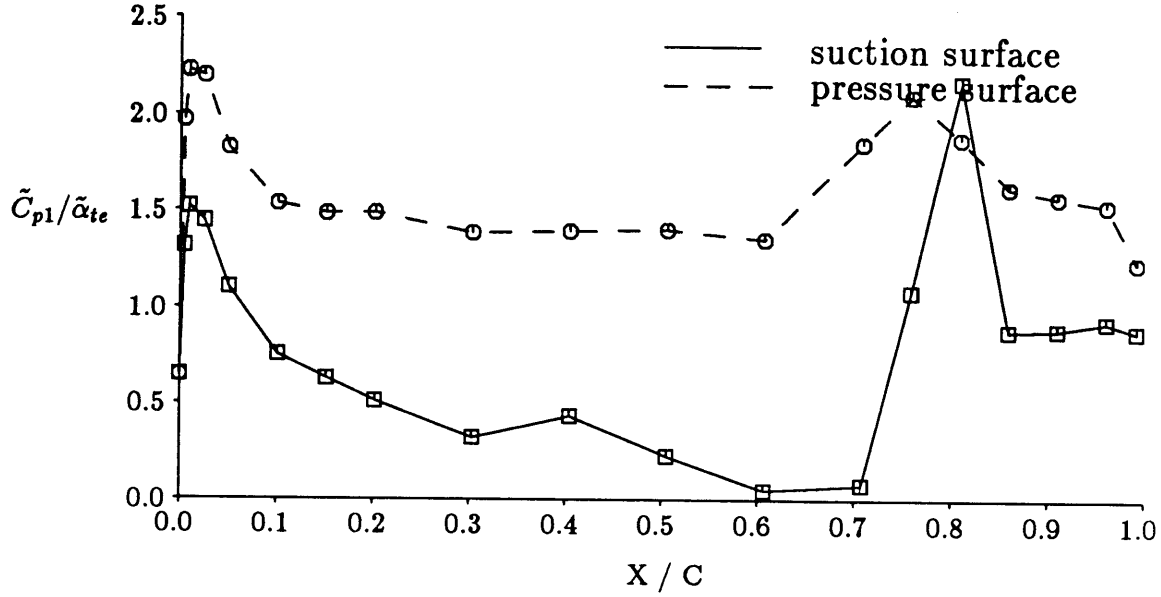


Figure E.4: Amplitude of C_p at fundamental frequency (Wortmann, LTWT, Re = 125000, $\alpha = 0^o$, $k = 0.5$)

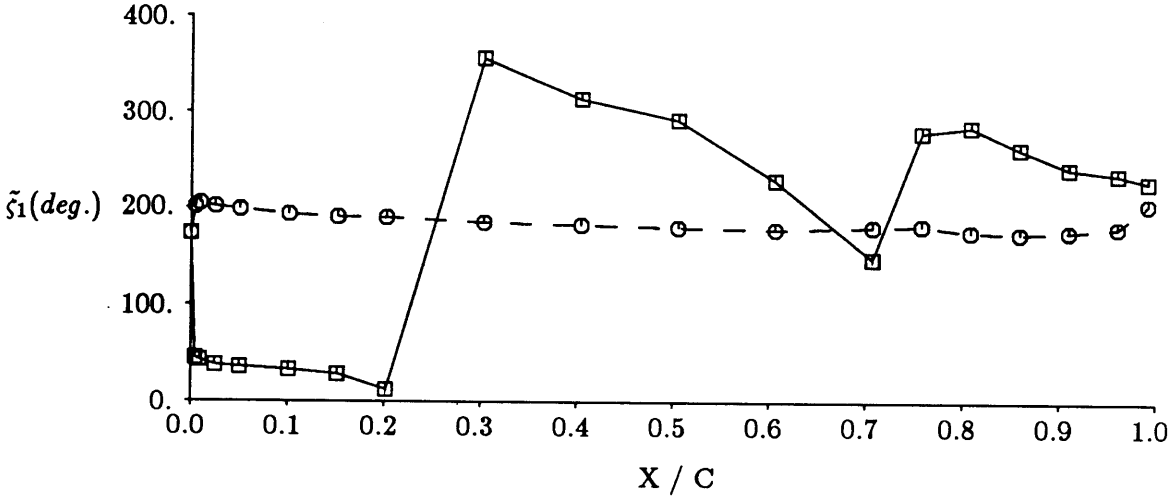


Figure E.5: Phase of C_p at fundamental frequency (Wortmann, LTWT, Re = 125000, $\alpha = 0^o$, $k = 0.5$)

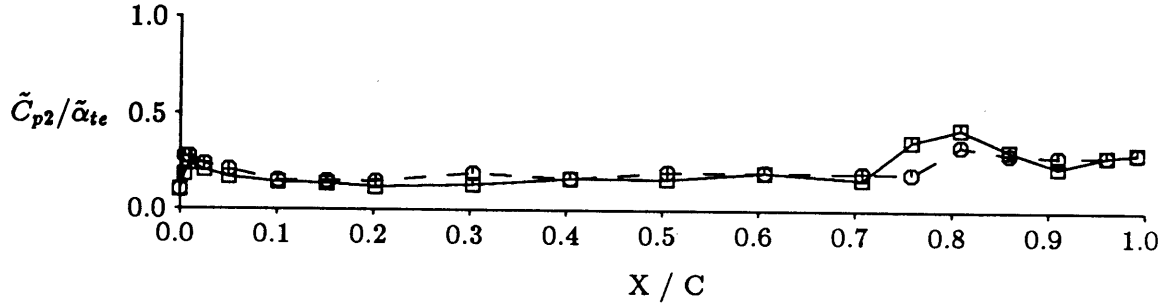


Figure E.6: Amplitude of C_p at 2^{nd} harmonic (Wortmann, LTWT, Re = 125000, $\alpha = 0^o$, $k = 0.5$)

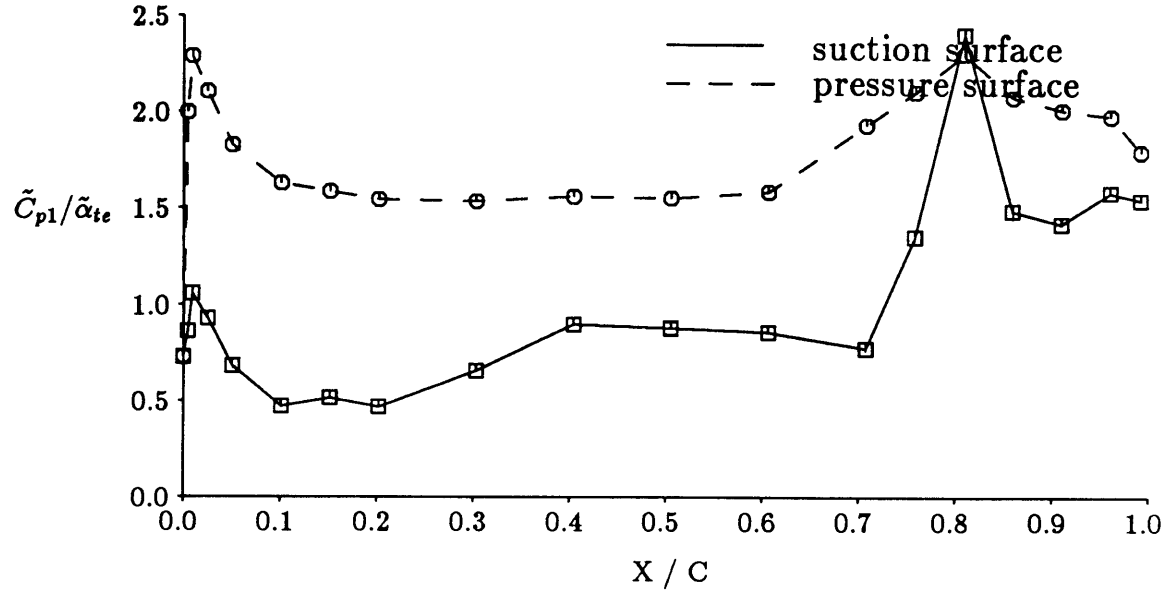


Figure E.7: Amplitude of C_p at fundamental frequency (Wortmann, LTWT, Re = 125000, $\alpha = 0^o$, $k = 0.75$)

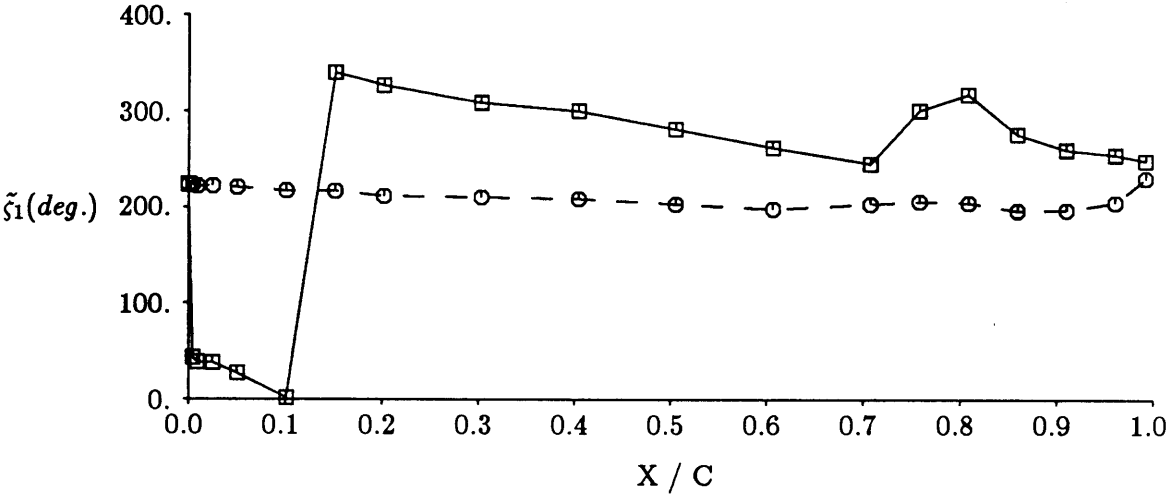


Figure E.8: Phase of C_p at fundamental frequency (Wortmann, LTWT, Re = 125000, $\alpha = 0^o$, $k = 0.75$)

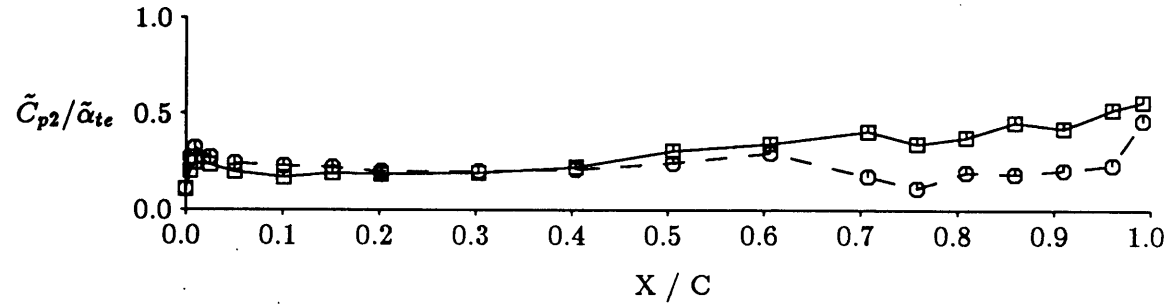


Figure E.9: Amplitude of C_p at 2^{nd} harmonic (Wortmann, LTWT, Re = 125000, $\alpha = 0^o$, $k = 0.75$)

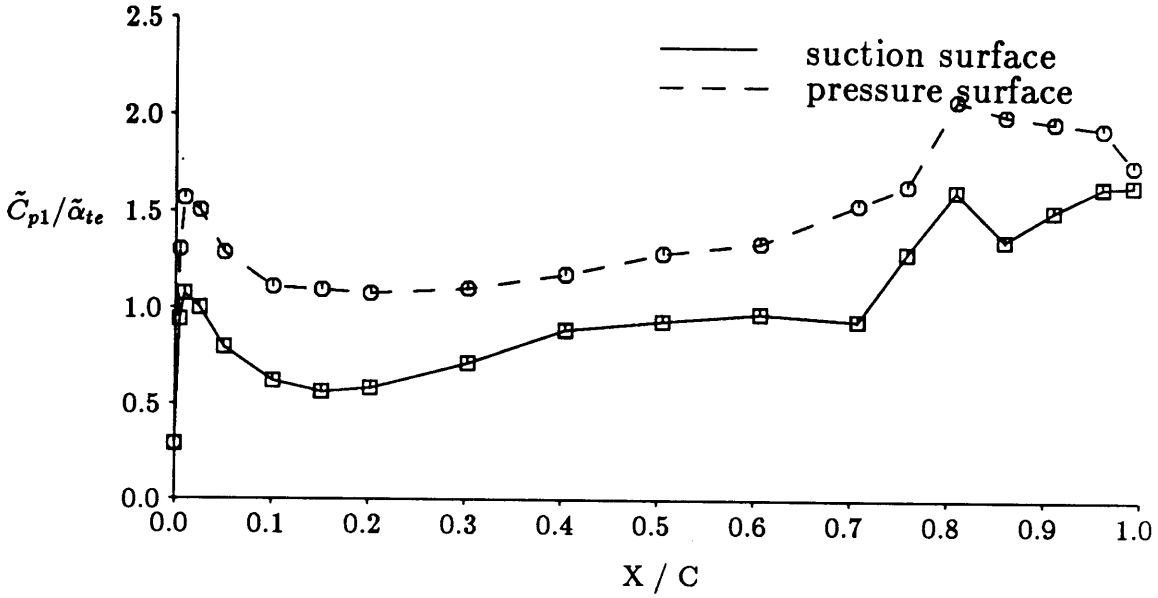


Figure E.10: Amplitude of C_p at fundamental frequency (Wortmann, LTWT, Re = 125000, $\alpha = 0^o$, $k = 1.0$)

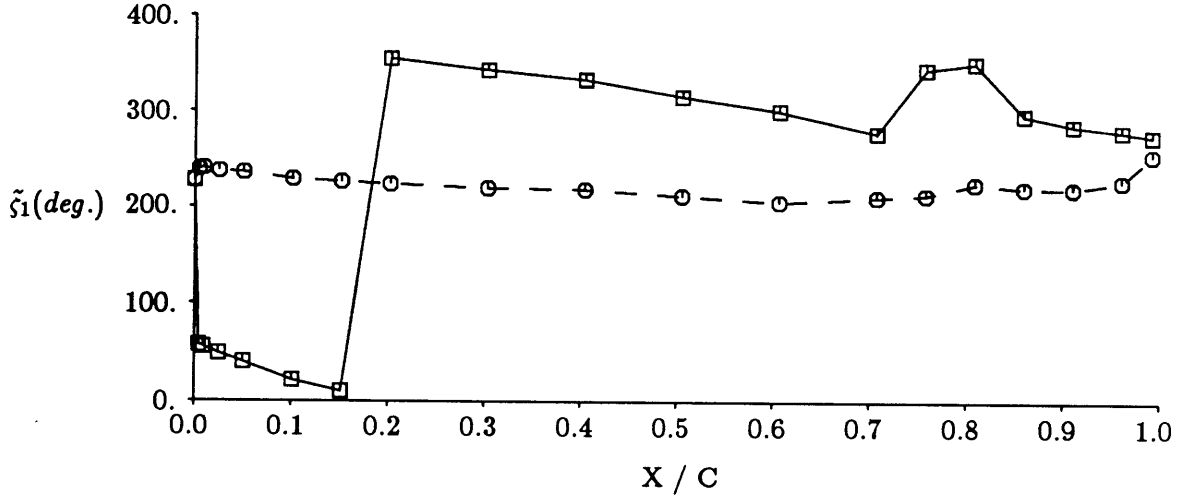


Figure E.11: Phase of C_p at fundamental frequency (Wortmann, LTWT, Re = 125000, $\alpha = 0^o$, $k = 1.0$)

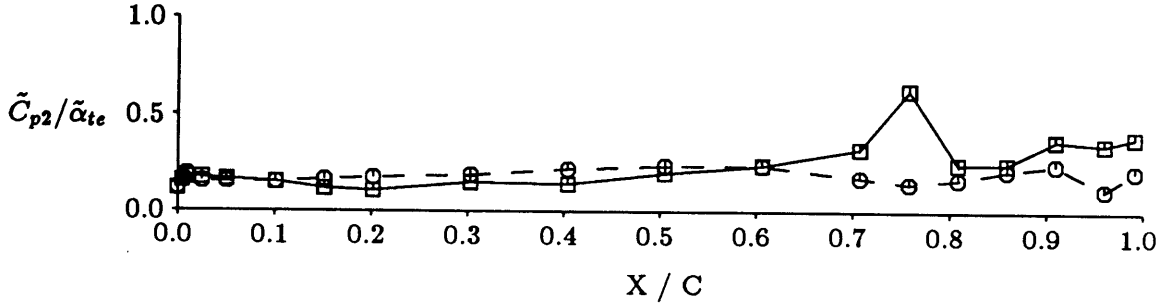


Figure E.12: Amplitude of C_p at 2^{nd} harmonic (Wortmann, LTWT, Re = 125000, $\alpha = 0^o$, $k = 1.0$)

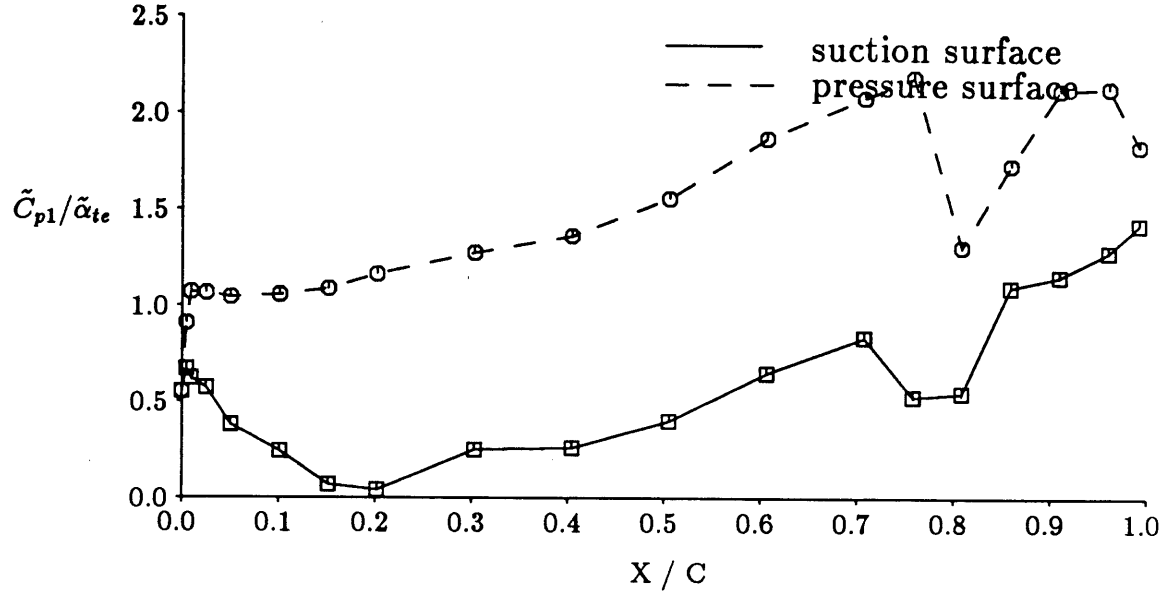


Figure E.13: Amplitude of C_p at fundamental frequency (Wortmann, LTWT, Re = 125000, $\alpha = 0^o$, $k = 2.0$)

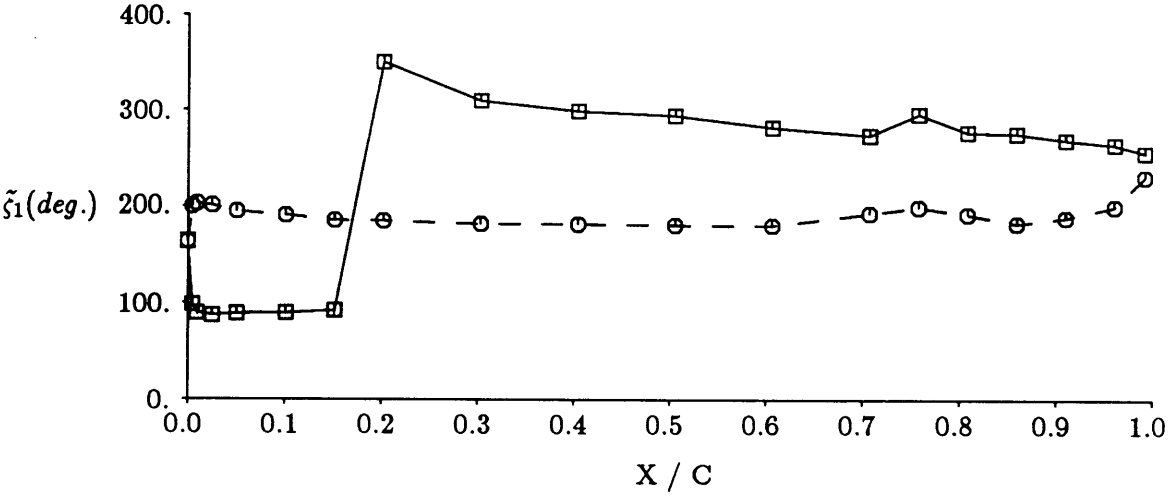


Figure E.14: Phase of C_p at fundamental frequency (Wortmann, LTWT, Re = 125000, $\alpha = 0^o$, $k = 2.0$)

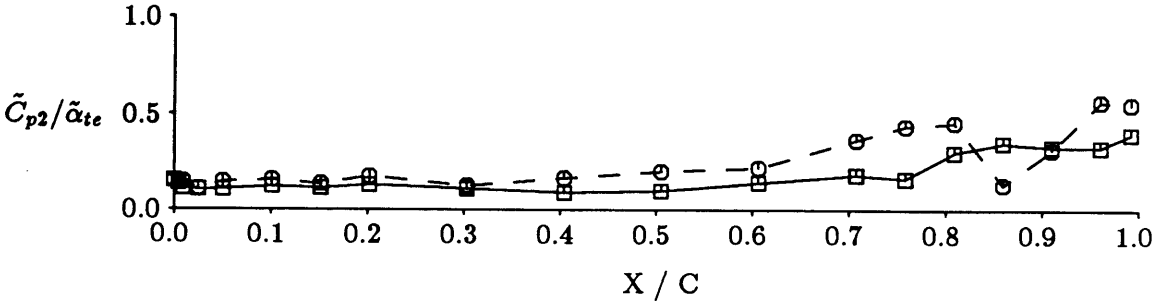


Figure E.15: Amplitude of C_p at 2^{nd} harmonic (Wortmann, LTWT, Re = 125000, $\alpha = 0^o$, $k = 2.0$)

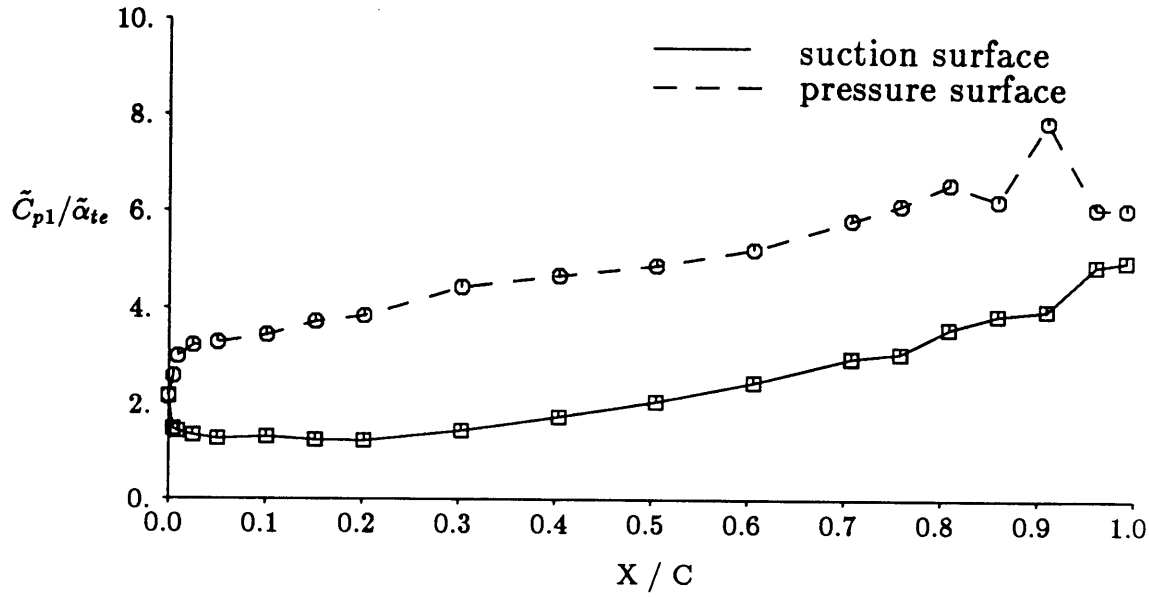


Figure E.16: Amplitude of C_p at fundamental frequency (Wortmann, LTWT, Re = 125000, $\alpha = 0^o$, $k = 6.4$)

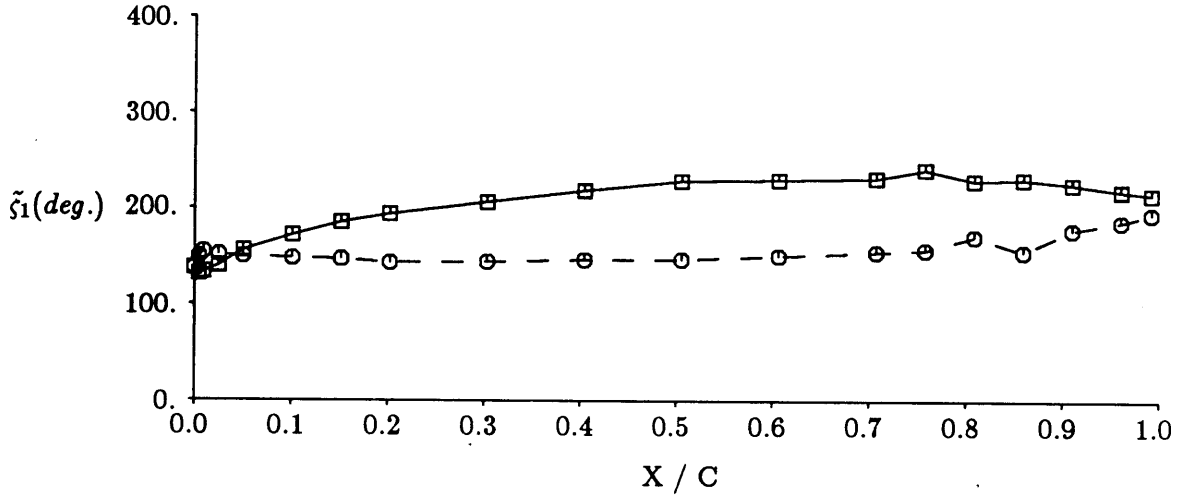


Figure E.17: Phase of C_p at fundamental frequency (Wortmann, LTWT, Re = 125000, $\alpha = 0^o$, $k = 6.4$)

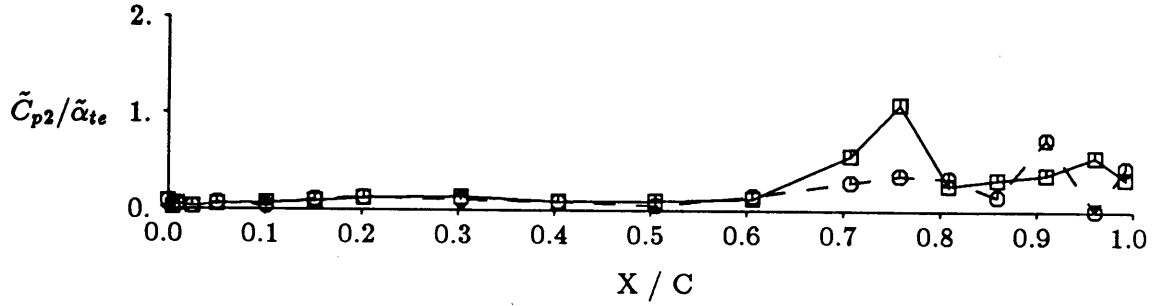


Figure E.18: Amplitude of C_p at 2^{nd} harmonic (Wortmann, LTWT, Re = 125000, $\alpha = 0^o$, $k = 6.4$)

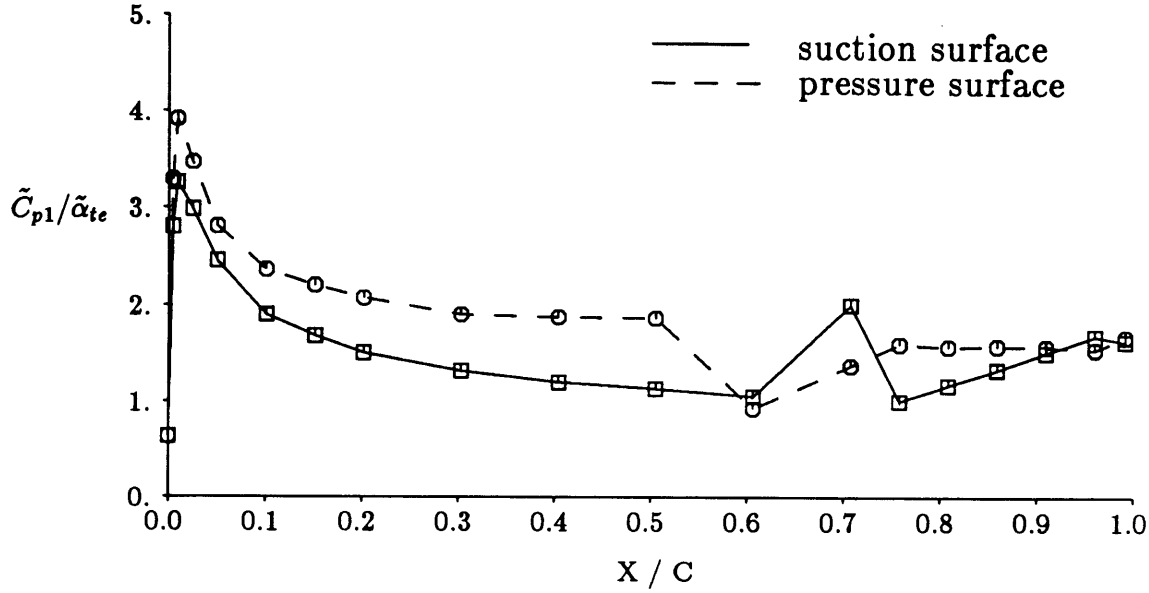


Figure E.19: Amplitude of C_p at fundamental frequency (Wortmann, LTWT, Re = 400000, $\alpha = 0^o$, $k = 0.15$)

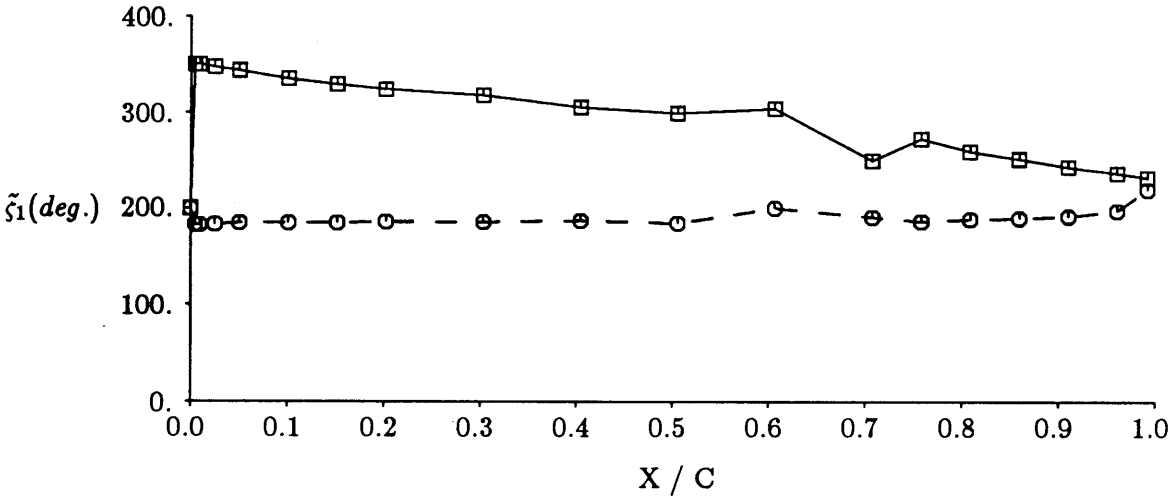


Figure E.20: Phase of C_p at fundamental frequency (Wortmann, LTWT, Re = 400000, $\alpha = 0^o$, $k = 0.15$)

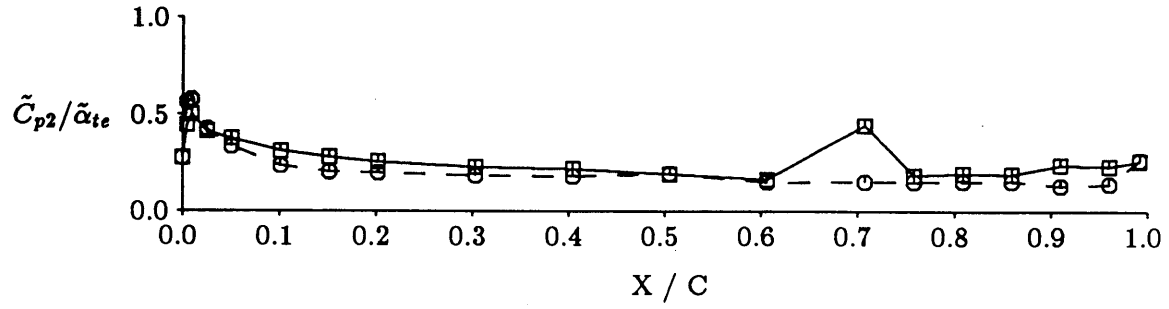


Figure E.21: Amplitude of C_p at 2^{nd} harmonic (Wortmann, LTWT, Re = 400000, $\alpha = 0^o$, $k = 0.15$)

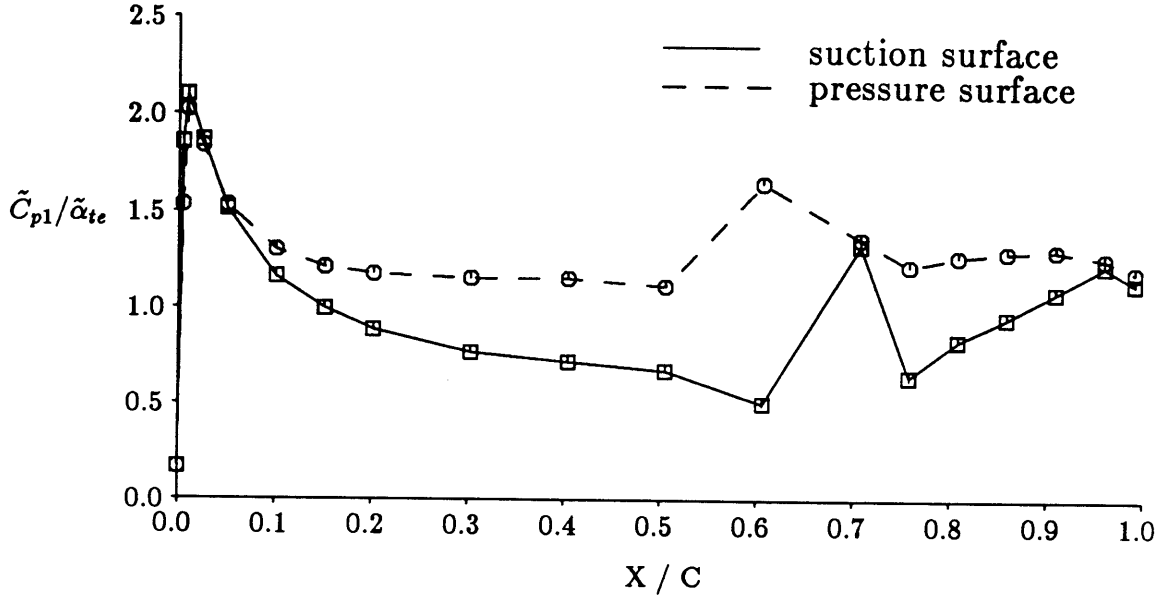


Figure E.22: Amplitude of C_p at fundamental frequency (Wortmann, LTWT, Re = 400000, $\alpha = 0^o$, $k = 0.5$)

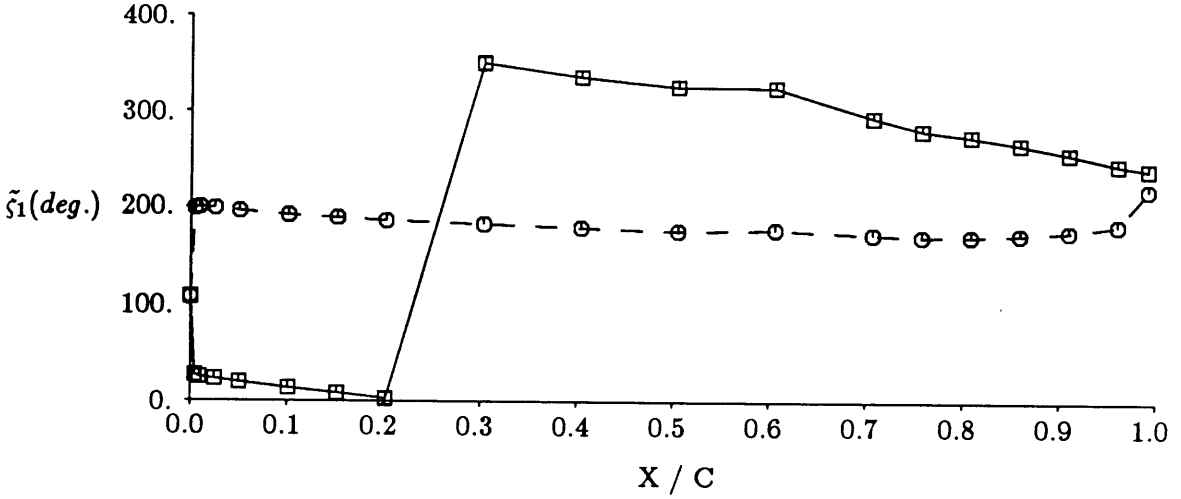


Figure E.23: Phase of C_p at fundamental frequency (Wortmann, LTWT, Re = 400000, $\alpha = 0^o$, $k = 0.5$)

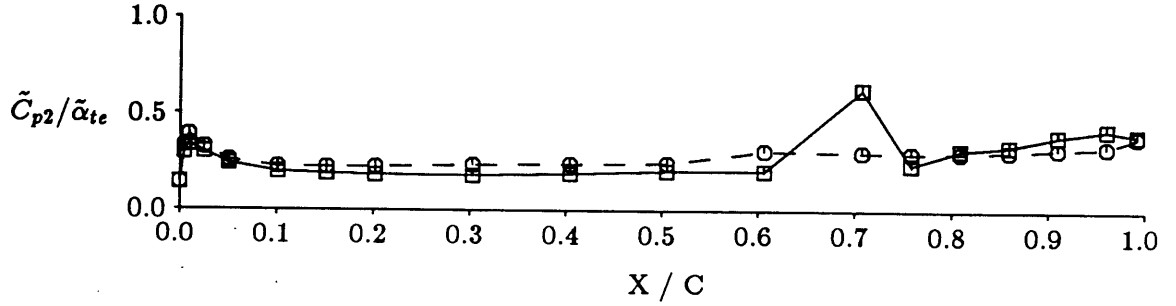


Figure E.24: Amplitude of C_p at 2^{nd} harmonic (Wortmann, LTWT, Re = 400000, $\alpha = 0^o$, $k = 0.5$)

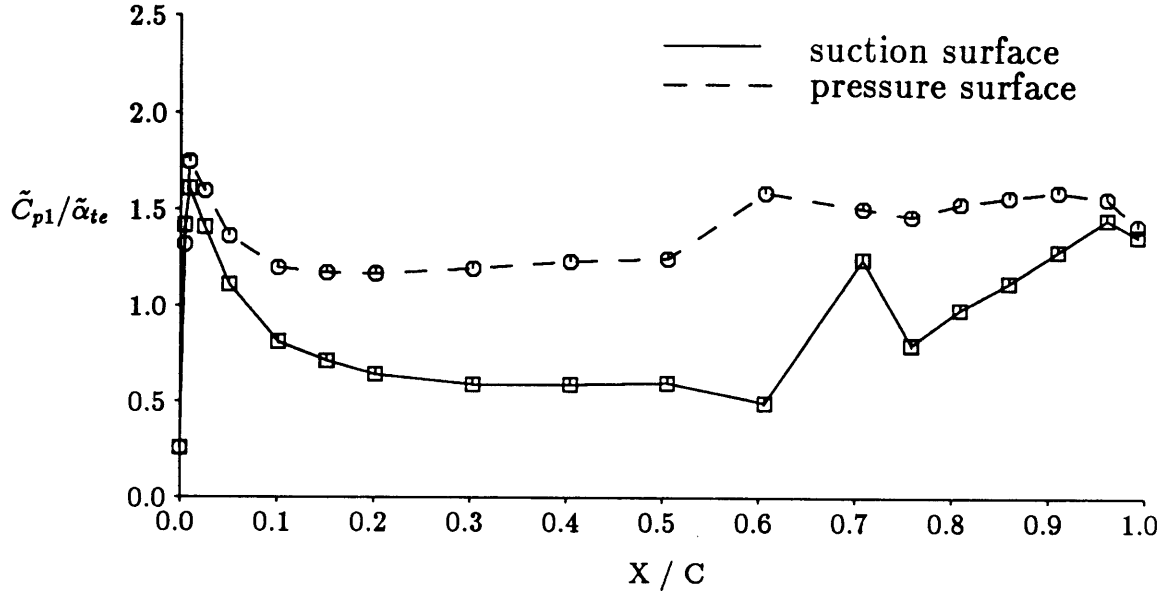


Figure E.25: Amplitude of C_p at fundamental frequency (Wortmann, LTWT, Re = 400000, $\alpha = 0^o$, $k = 0.75$)

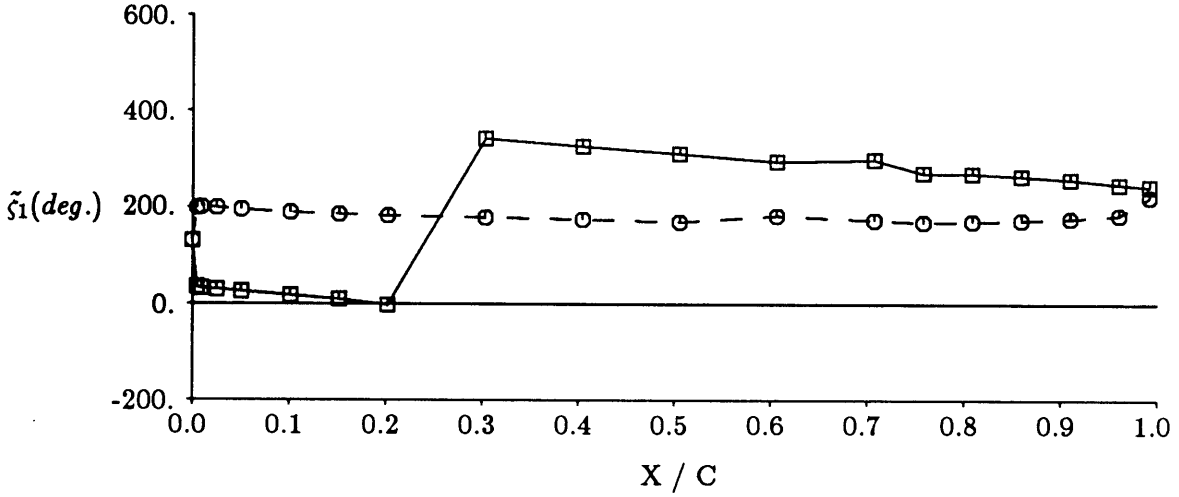


Figure E.26: Phase of C_p at fundamental frequency (Wortmann, LTWT, Re = 400000, $\alpha = 0^o$, $k = 0.75$)

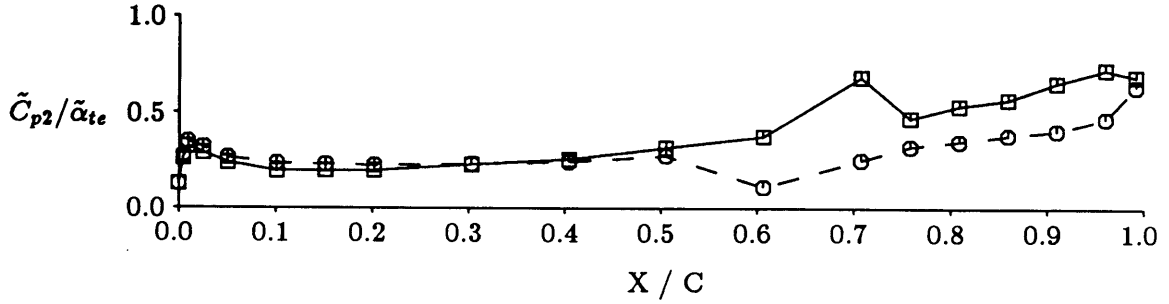


Figure E.27: Amplitude of C_p at 2^{nd} harmonic (Wortmann, LTWT, Re = 400000, $\alpha = 0^o$, $k = 0.75$)

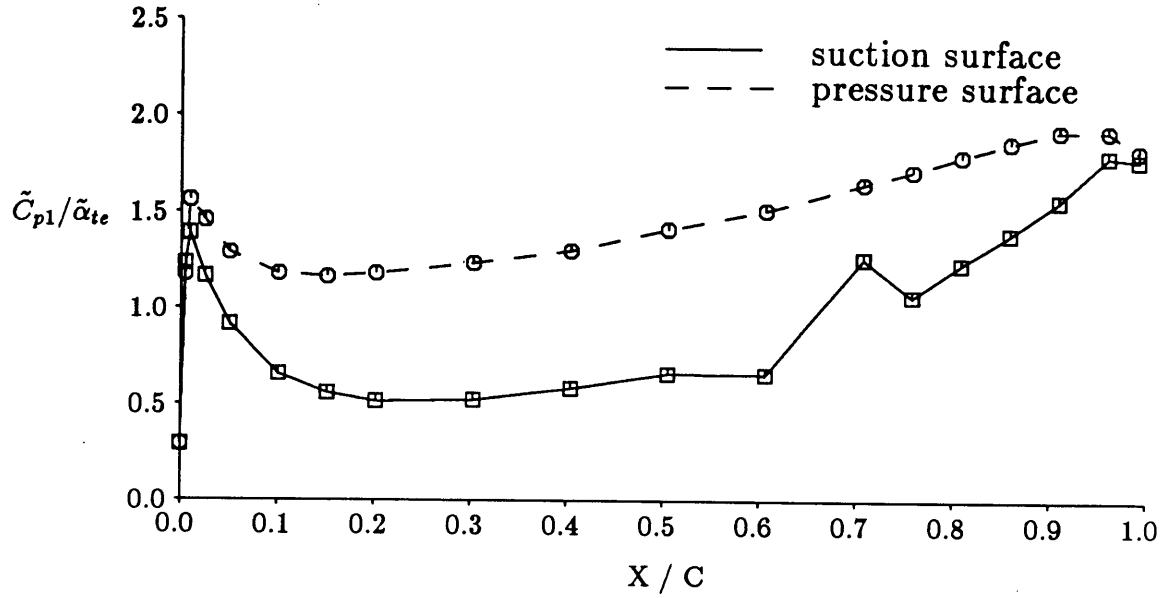


Figure E.28: Amplitude of C_p at fundamental frequency (Wortmann, LTWT, Re = 400000, $\alpha = 0^o$, $k = 1.0$)

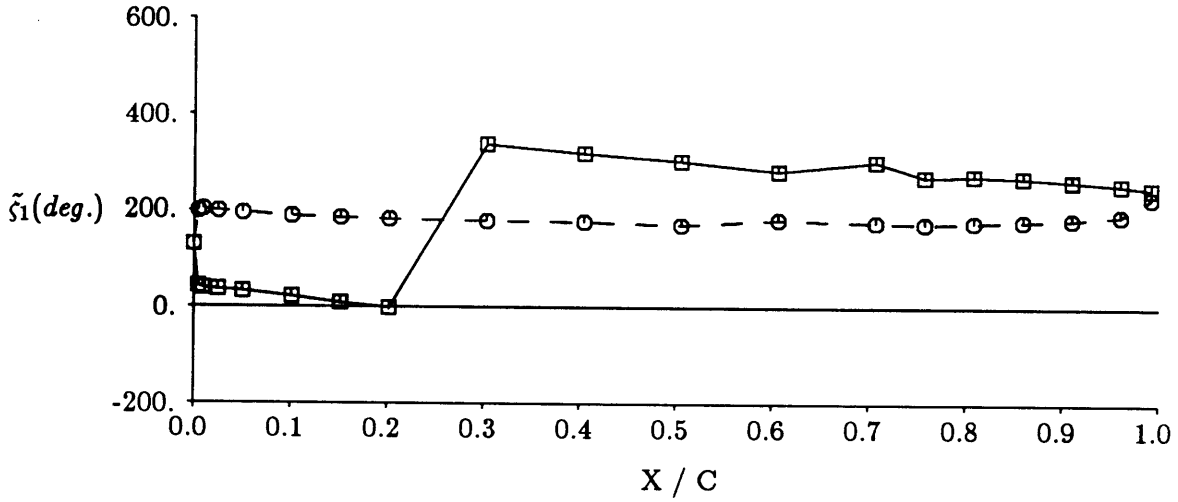


Figure E.29: Phase of C_p at fundamental frequency (Wortmann, LTWT, Re = 400000, $\alpha = 0^o$, $k = 1.0$)

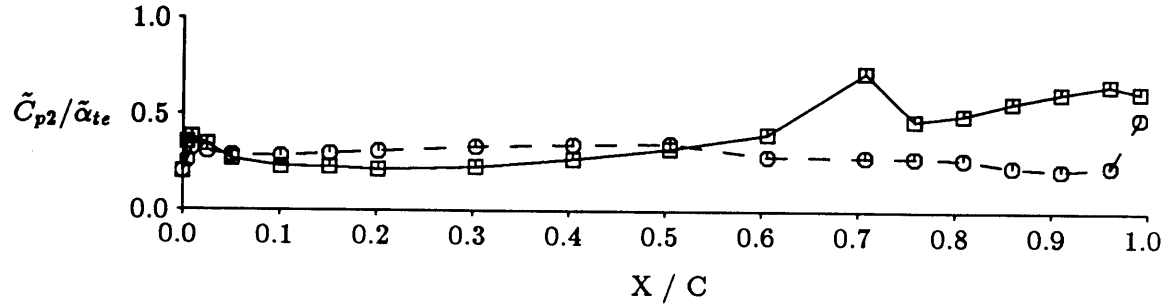


Figure E.30: Amplitude of C_p at 2^{nd} harmonic (Wortmann, LTWT, Re = 400000, $\alpha = 0^o$, $k = 1.0$)

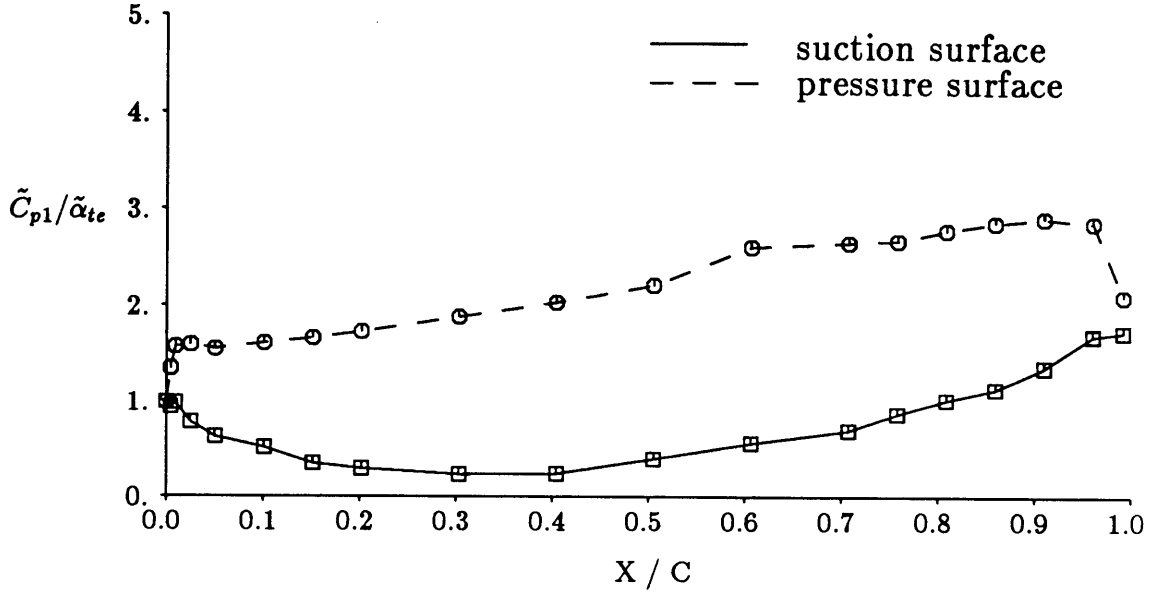


Figure E.31: Amplitude of C_p at fundamental frequency (Wortmann, LTWT, Re = 400000, $\alpha = 0°$, $k = 2.0$)

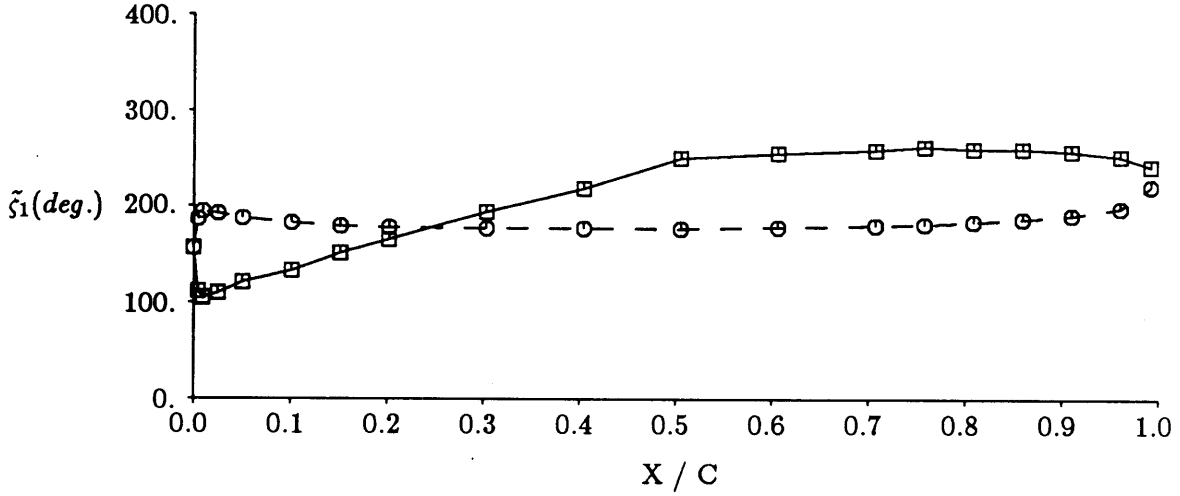


Figure E.32: Phase of C_p at fundamental frequency (Wortmann, LTWT, Re = 400000, $\alpha = 0°$, $k = 2.0$)

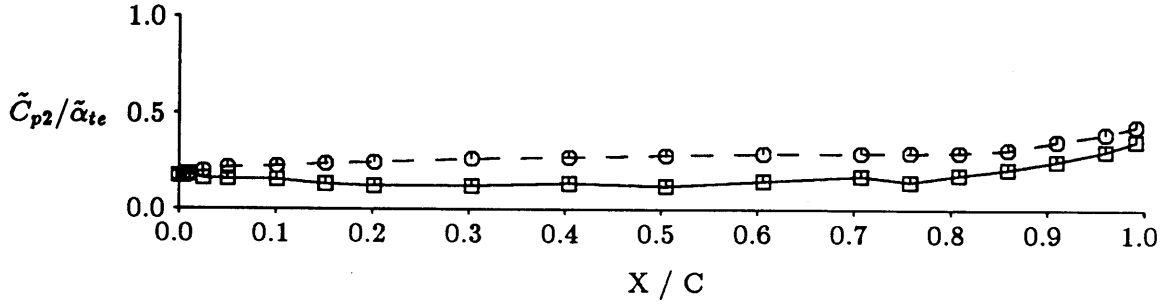


Figure E.33: Amplitude of C_p at 2^{nd} harmonic (Wortmann, LTWT, Re = 400000, $\alpha = 0°$, $k = 2.0$)

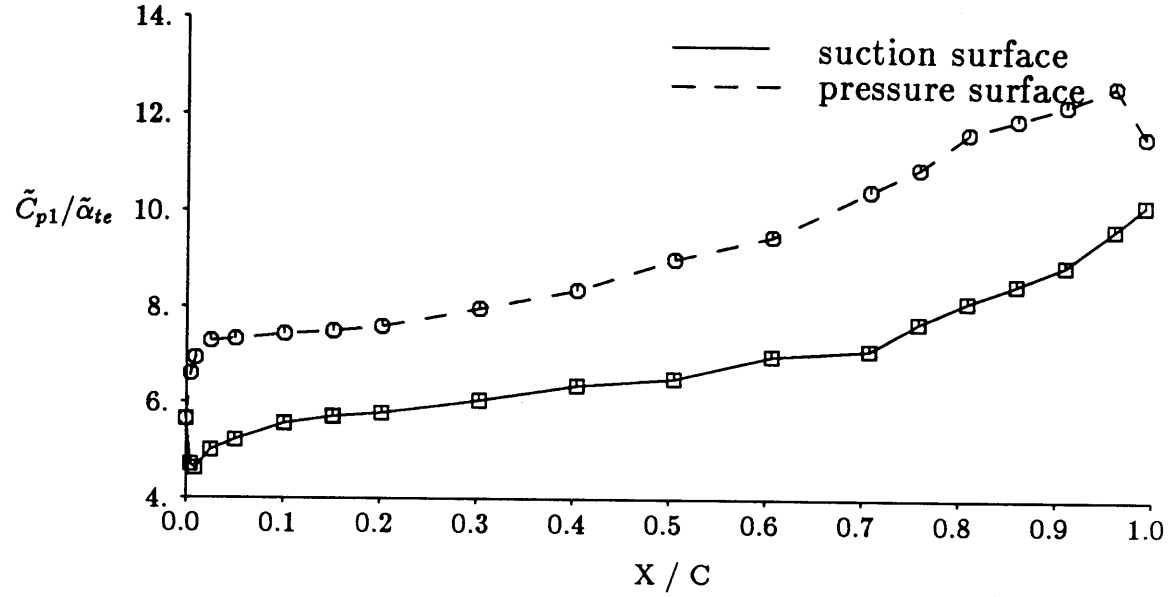


Figure E.34: Amplitude of C_p at fundamental frequency (Wortmann, LTWT, Re = 400000, $\alpha = 0°$, $k = 6.4$)

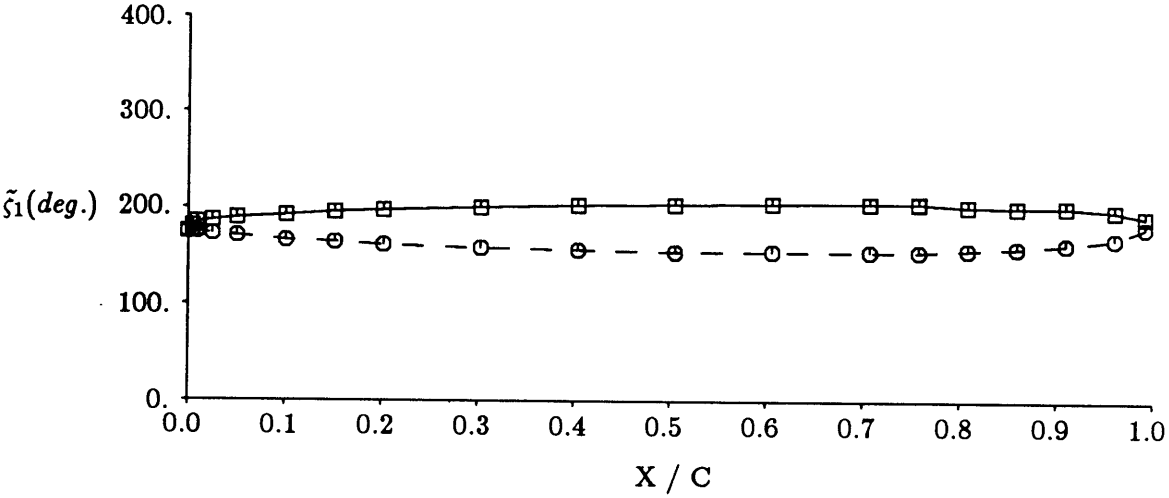


Figure E.35: Phase of C_p at fundamental frequency (Wortmann, LTWT, Re = 400000, $\alpha = 0°$, $k = 6.4$)

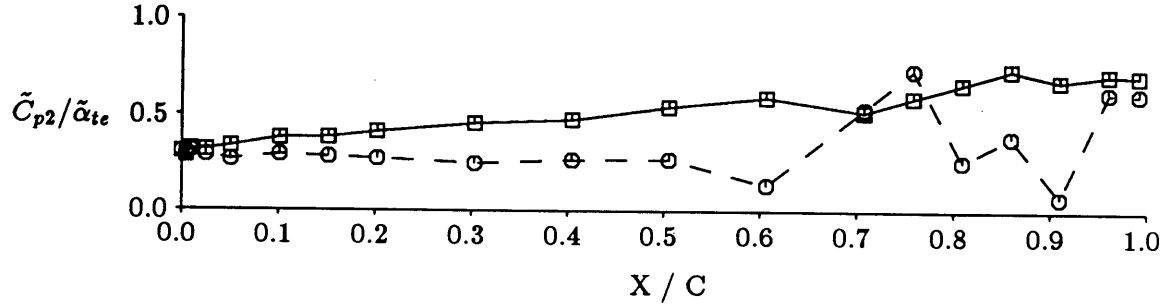


Figure E.36: Amplitude of C_p at 2^{nd} harmonic (Wortmann, LTWT, Re = 400000, $\alpha = 0°$, $k = 6.4$)

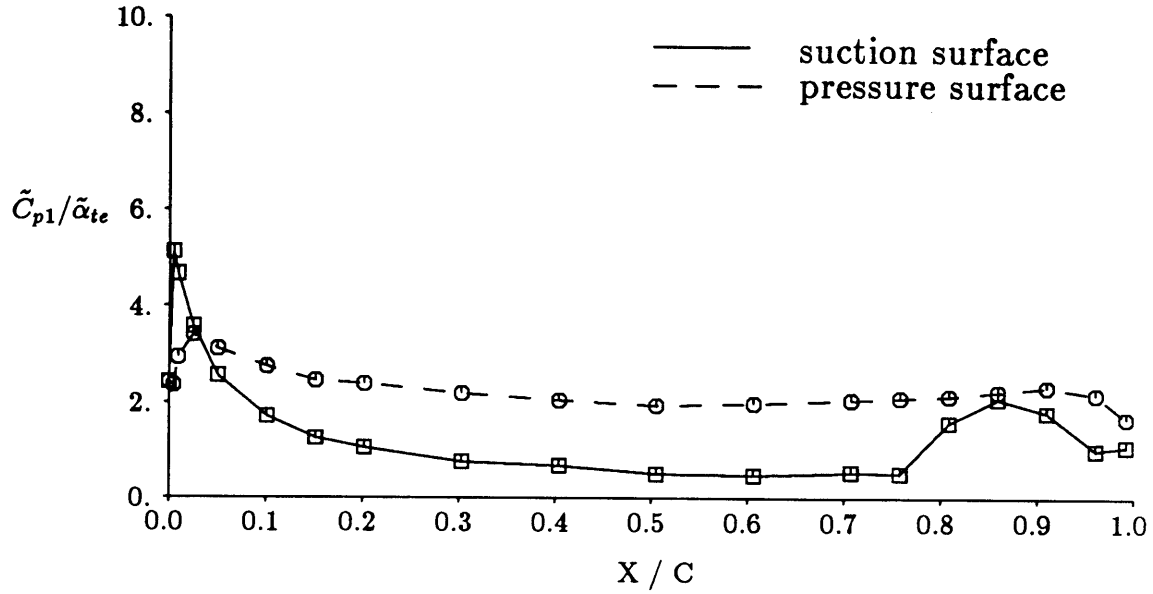


Figure E.37: Amplitude of C_p at fundamental frequency (0012, LTWT, Re = 125000, $\alpha = 0^o$, $k = 0.15$)

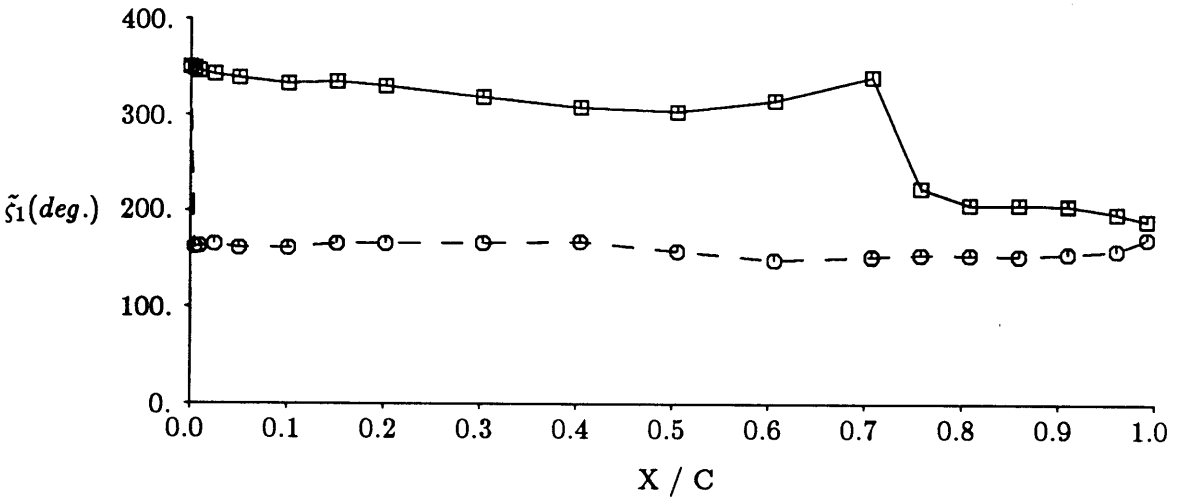


Figure E.38: Phase of C_p at fundamental frequency (0012, LTWT, Re = 125000, $\alpha = 0^o$, $k = 0.15$)

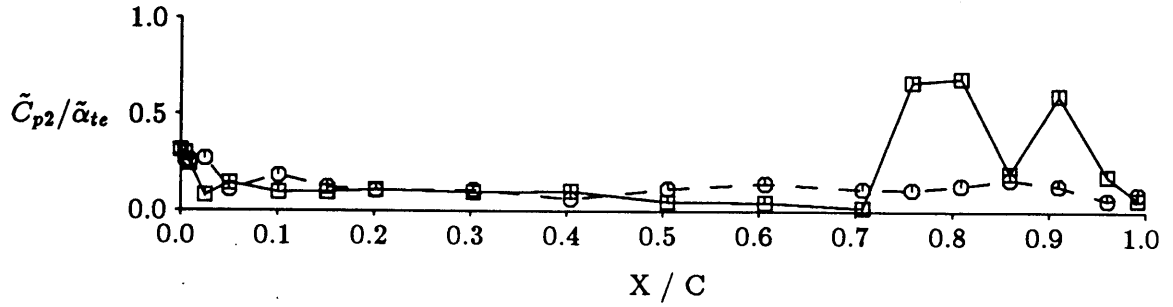


Figure E.39: Amplitude of C_p at 2^{nd} harmonic (0012, LTWT, Re = 125000, $\alpha = 0^o$, $k = 0.15$)

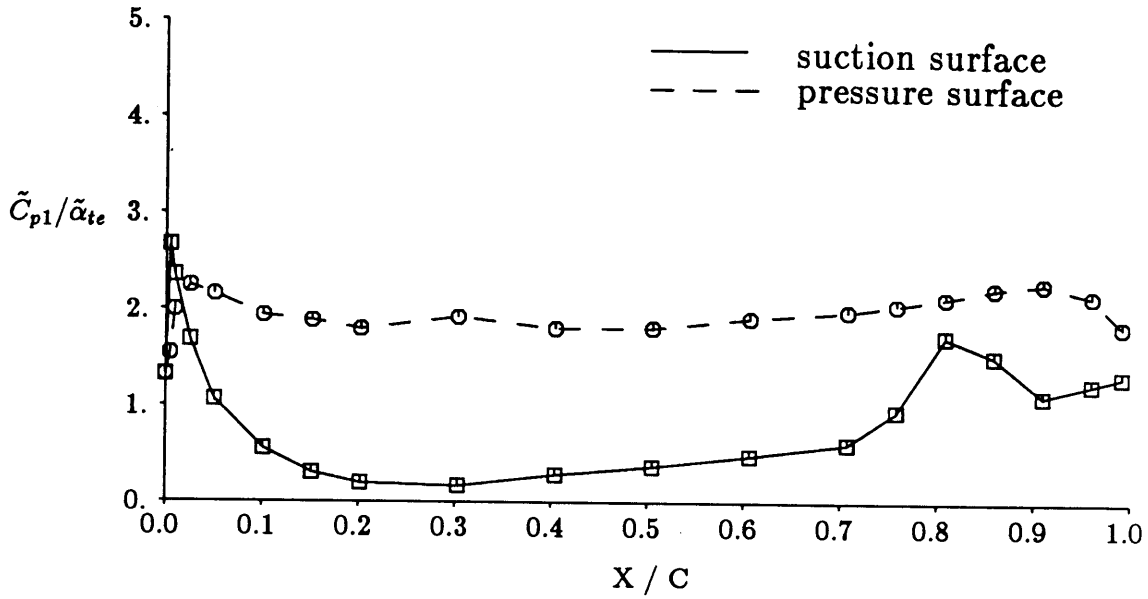


Figure E.40: Amplitude of C_p at fundamental frequency (0012, LTWT, Re = 125000, $\alpha = 0°$, $k = 0.5$)

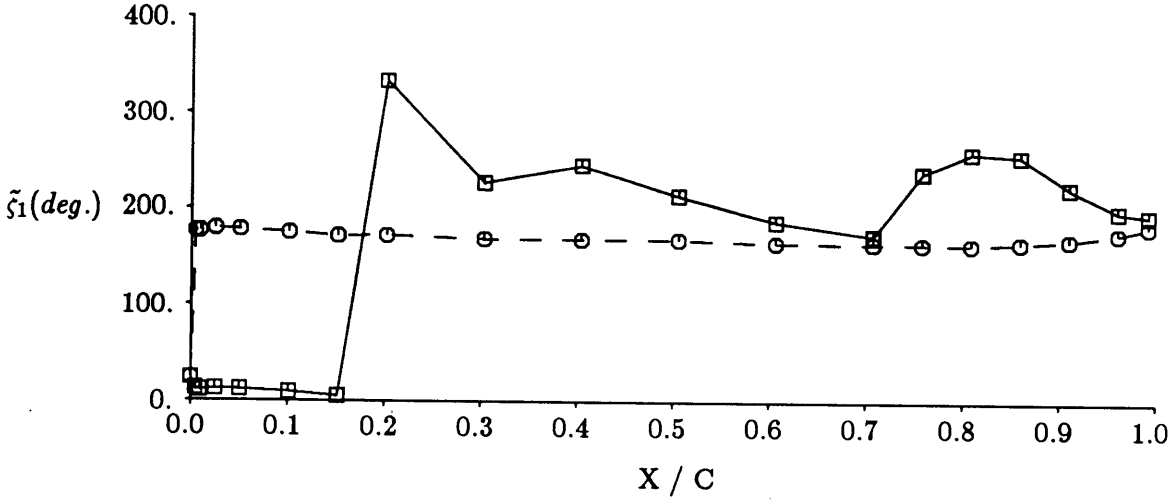


Figure E.41: Phase of C_p at fundamental frequency (0012, LTWT, Re = 125000, $\alpha = 0°$, $k = 0.5$)

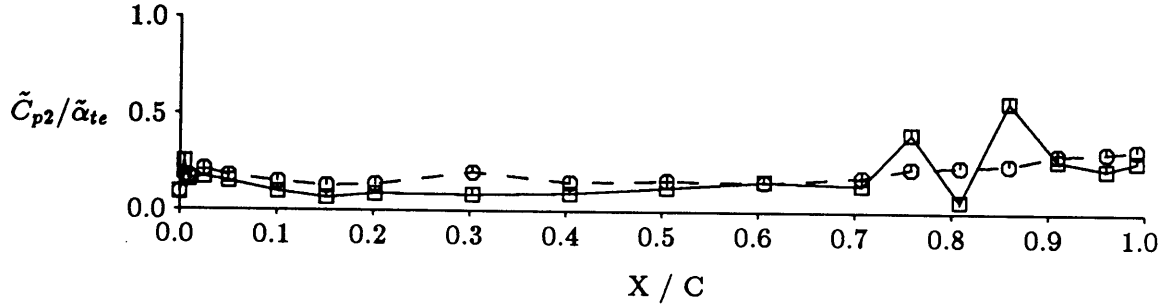


Figure E.42: Amplitude of C_p at 2^{nd} harmonic (0012, LTWT, Re = 125000, $\alpha = 0°$, $k = 0.5$)

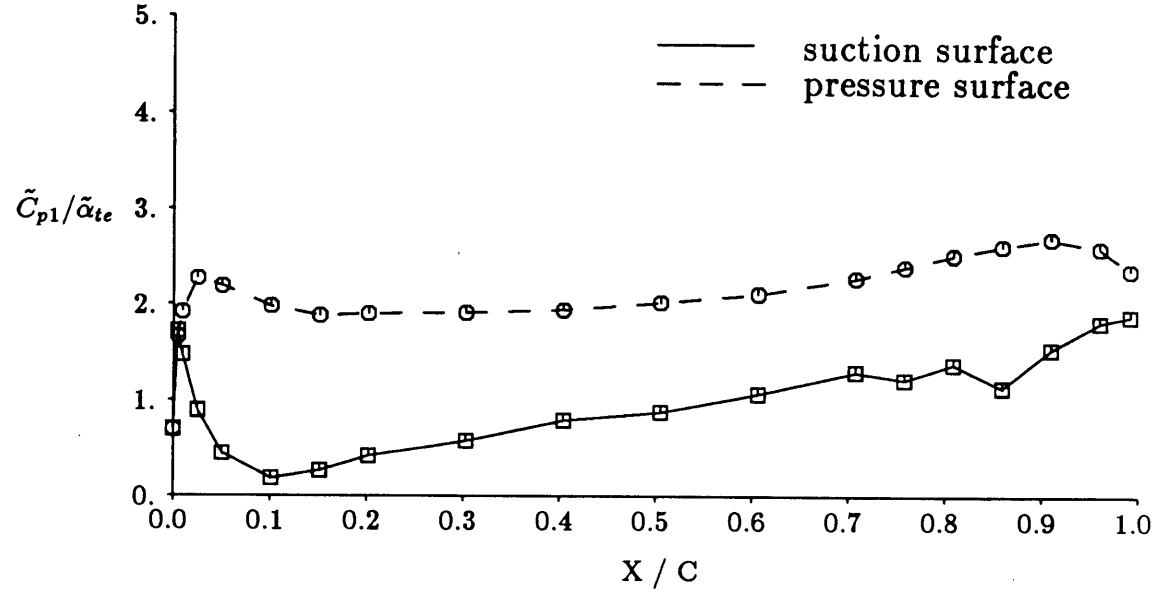


Figure E.43: Amplitude of C_p at fundamental frequency (0012, LTWT, Re = 125000, $\alpha = 0^o$, $k = 0.75$)

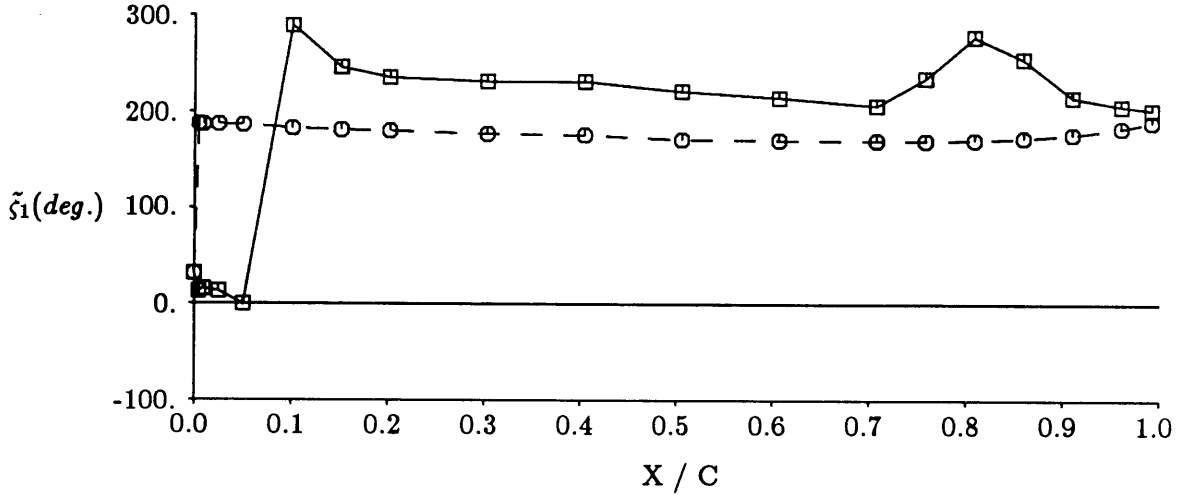


Figure E.44: Phase of C_p at fundamental frequency (0012, LTWT, Re = 125000, $\alpha = 0^o$, $k = 0.75$)

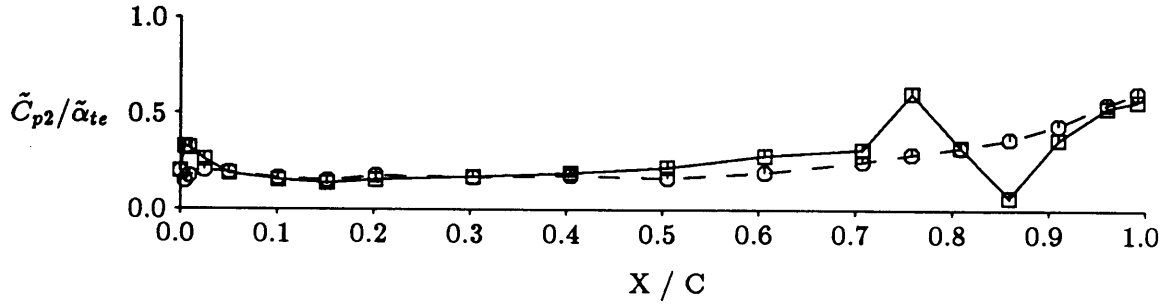


Figure E.45: Amplitude of C_p at 2^{nd} harmonic (0012, LTWT, Re = 125000, $\alpha = 0^o$, $k = 0.75$)

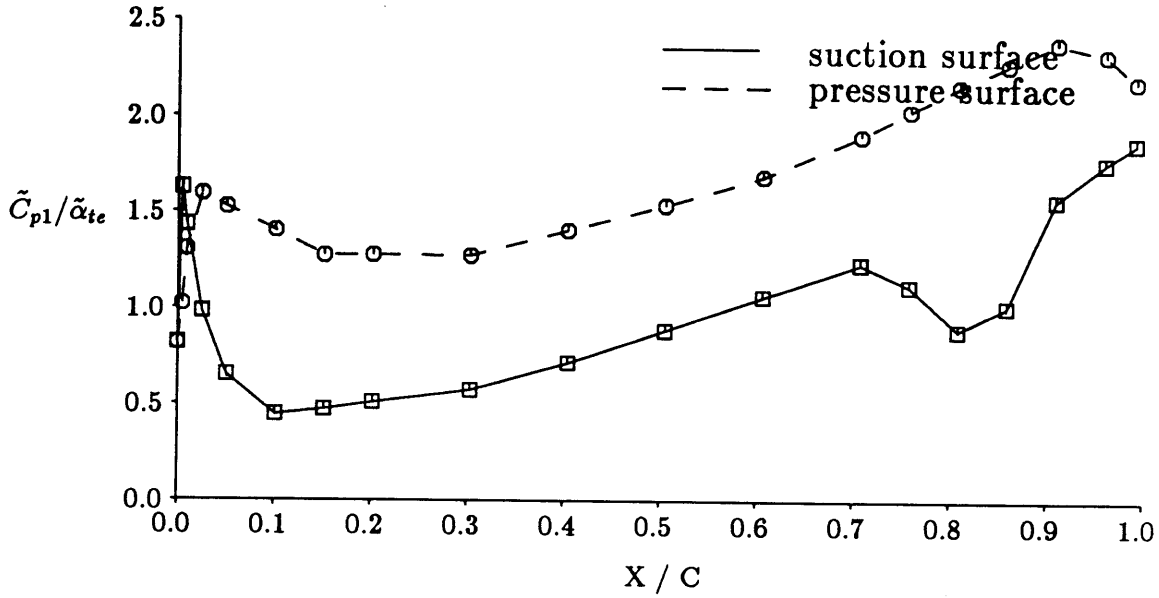


Figure E.46: Amplitude of C_p at fundamental frequency (0012, LTWT, Re = 125000, $\alpha = 0^o$, $k = 1.0$)

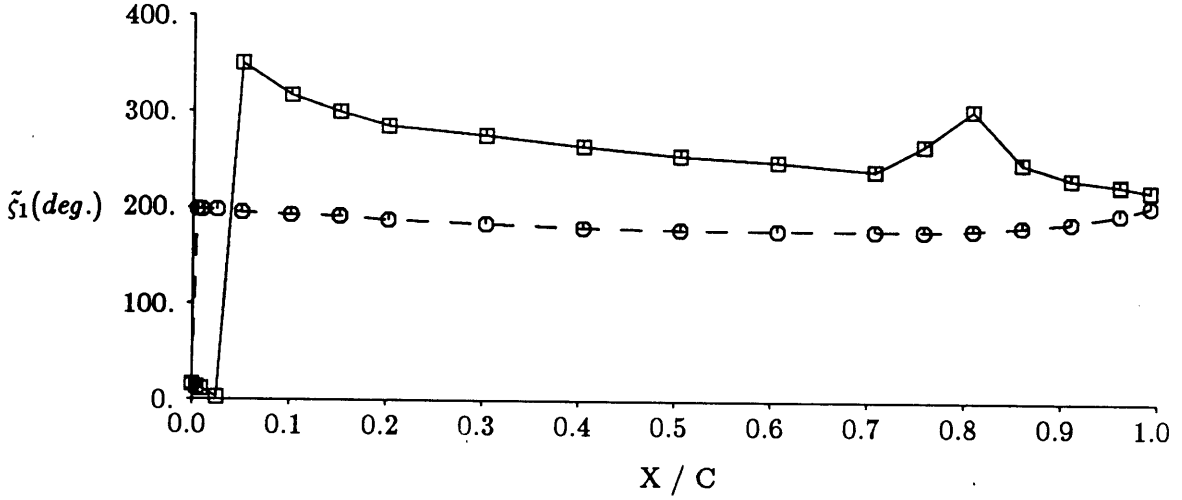


Figure E.47: Phase of C_p at fundamental frequency (0012, LTWT, Re = 125000, $\alpha = 0^o$, $k = 1.0$)

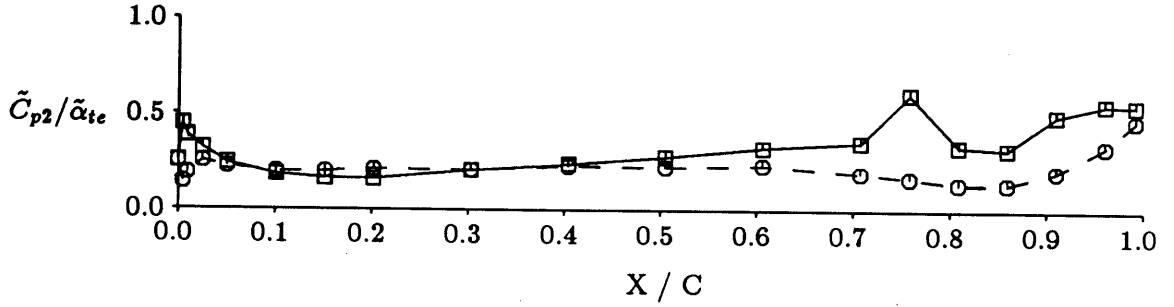


Figure E.48: Amplitude of C_p at 2^{nd} harmonic (0012, LTWT, Re = 125000, $\alpha = 0^o$, $k = 1.0$)

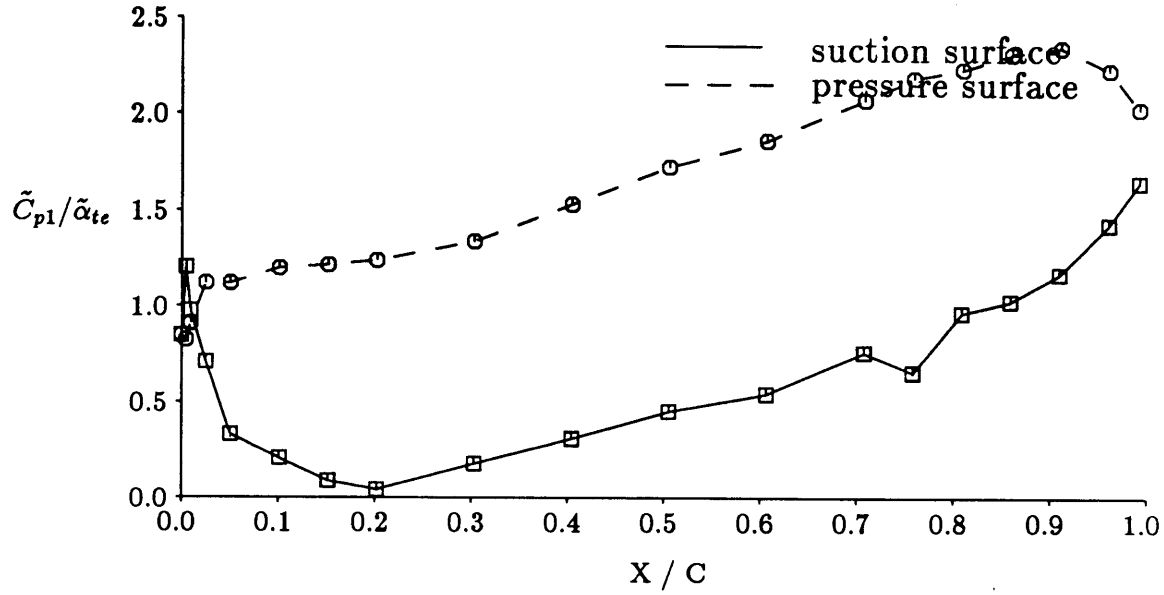


Figure E.49: Amplitude of C_p at fundamental frequency (0012, LTWT, Re = 125000, $\alpha = 0^o$, $k = 2.0$)

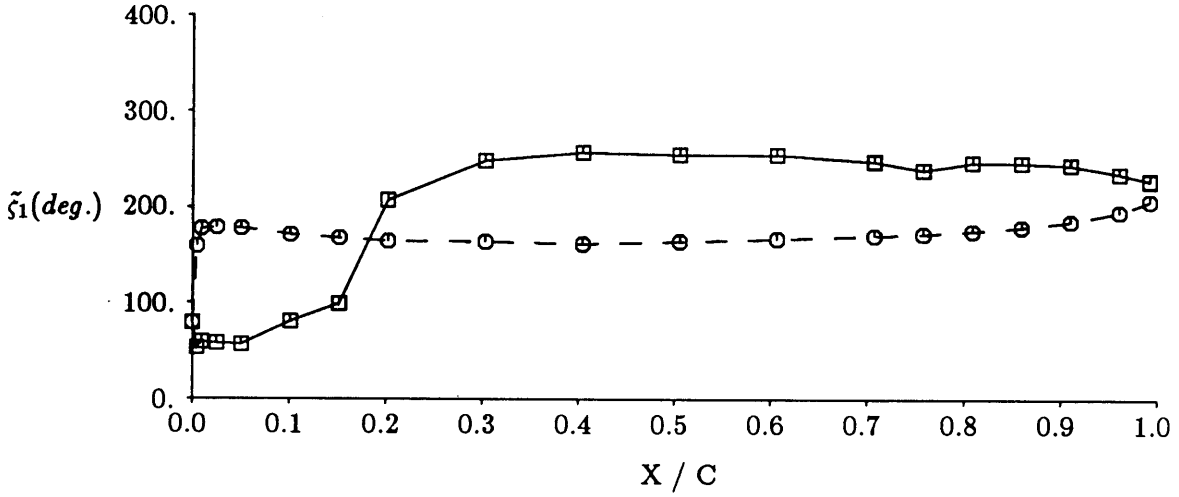


Figure E.50: Phase of C_p at fundamental frequency (0012, LTWT, Re = 125000, $\alpha = 0^o$, $k = 2.0$)

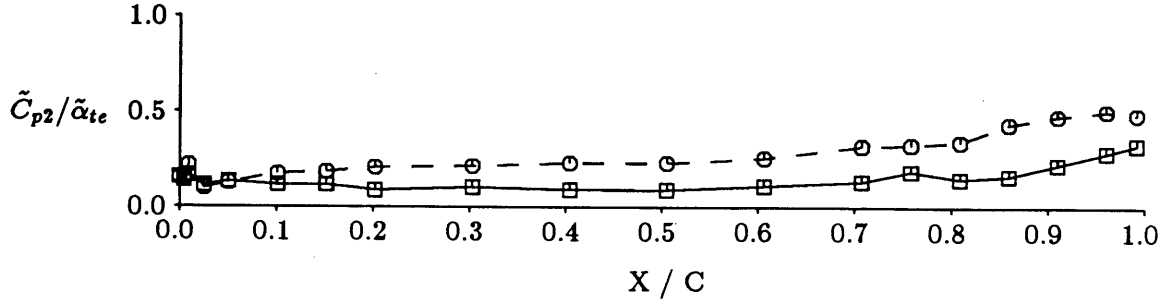


Figure E.51: Amplitude of C_p at 2^{nd} harmonic (0012, LTWT, Re = 125000, $\alpha = 0^o$, $k = 2.0$)

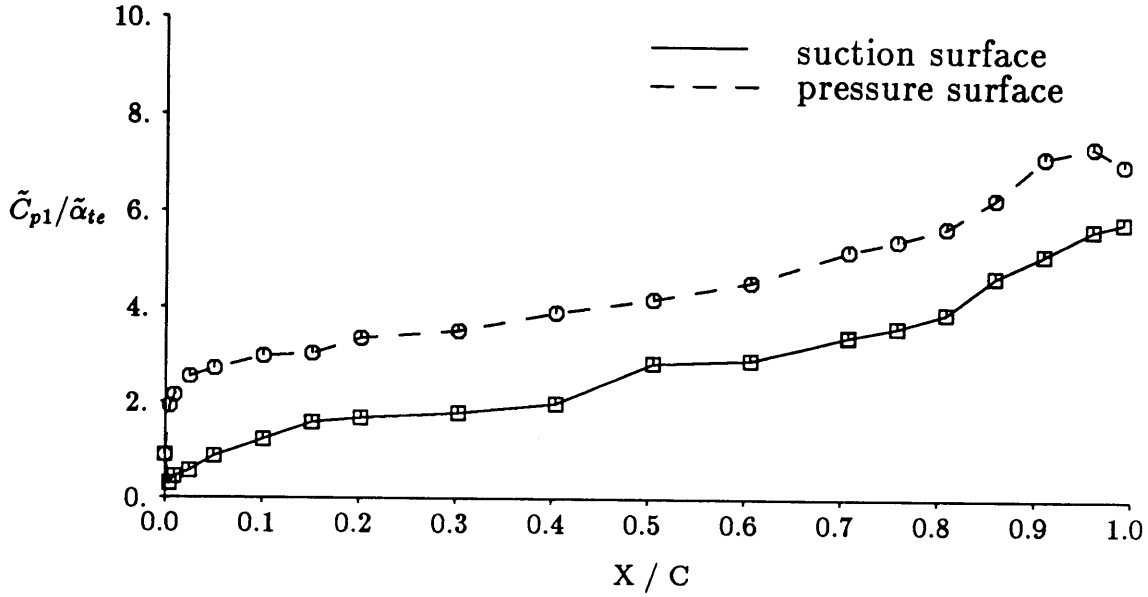


Figure E.52: Amplitude of C_p at fundamental frequency (0012, LTWT, Re = 125000, $\alpha = 0^o$, $k = 6.4$)

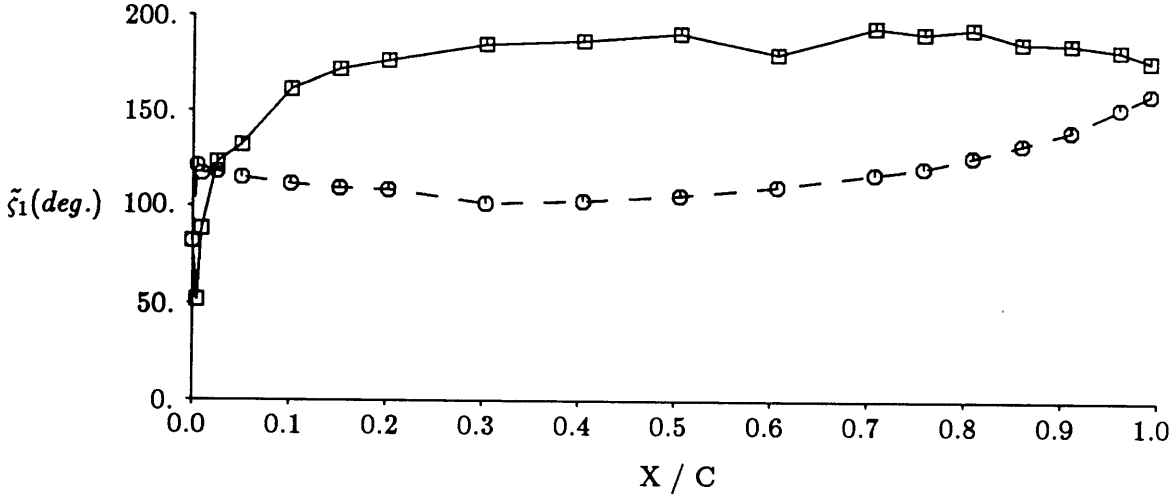


Figure E.53: Phase of C_p at fundamental frequency (0012, LTWT, Re = 125000, $\alpha = 0^o$, $k = 6.4$)

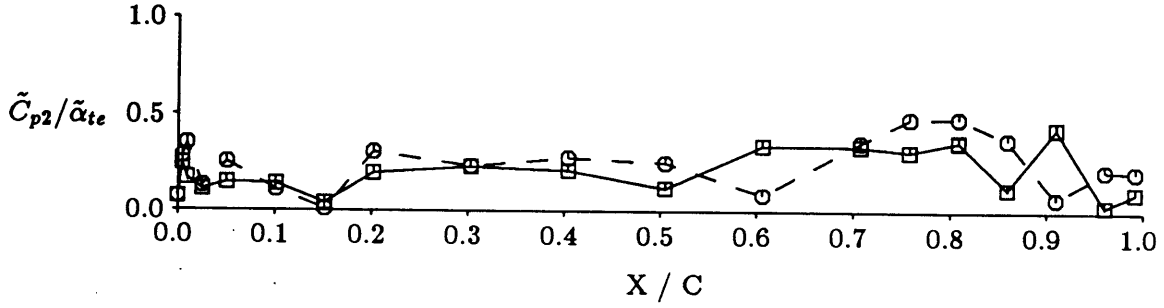


Figure E.54: Amplitude of C_p at 2^{nd} harmonic (0012, LTWT, Re = 125000, $\alpha = 0^o$, $k = 6.4$)

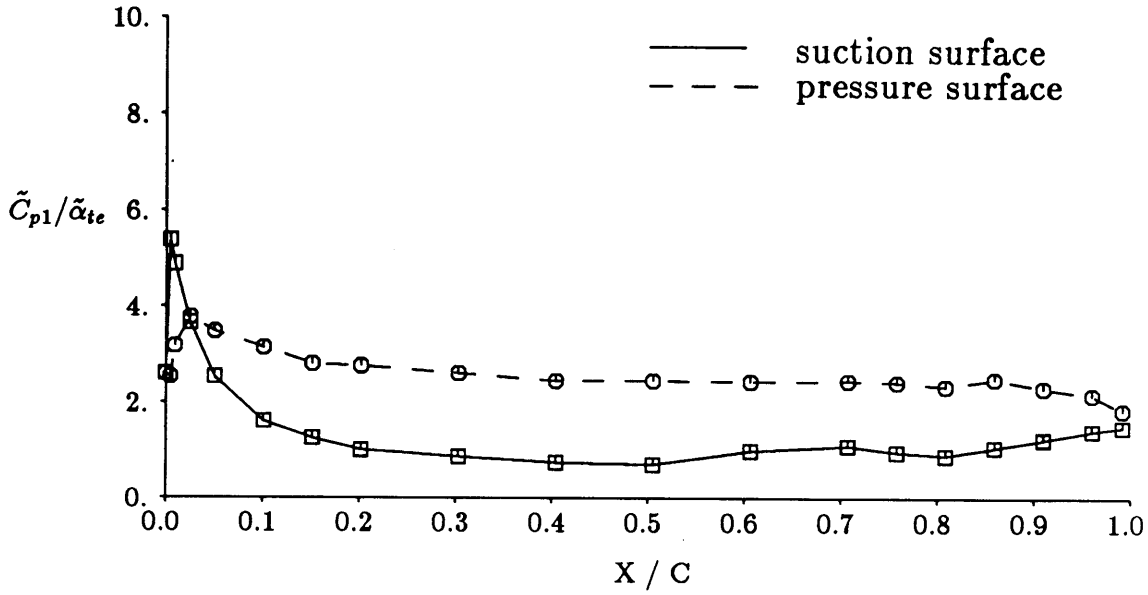


Figure E.55: Amplitude of C_p at fundamental frequency (0012, LTWT, Re = 400000, $\alpha = 0°$, $k = 0.15$)

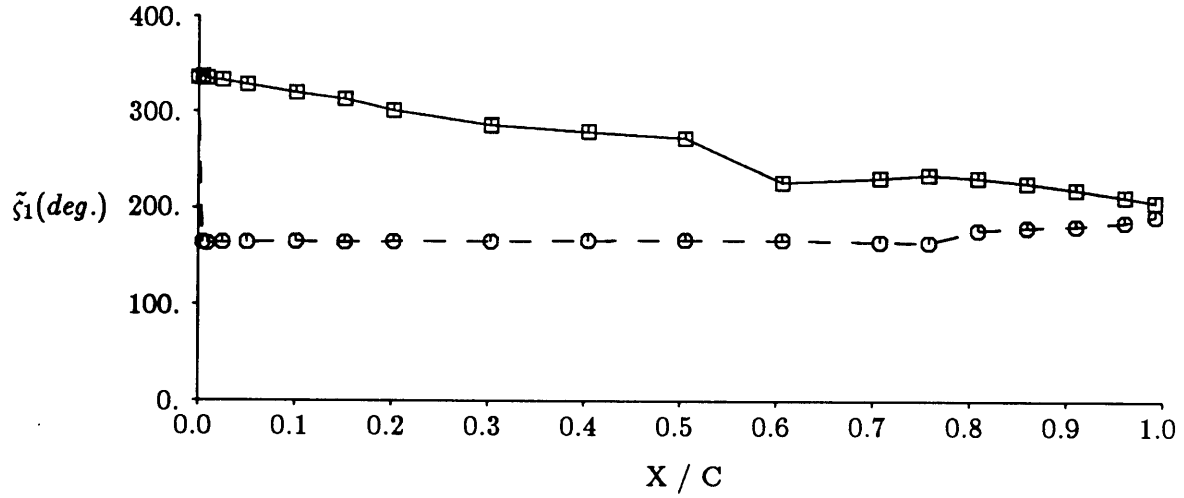


Figure E.56: Phase of C_p at fundamental frequency (0012, LTWT, Re = 400000, $\alpha = 0°$, $k = 0.15$)

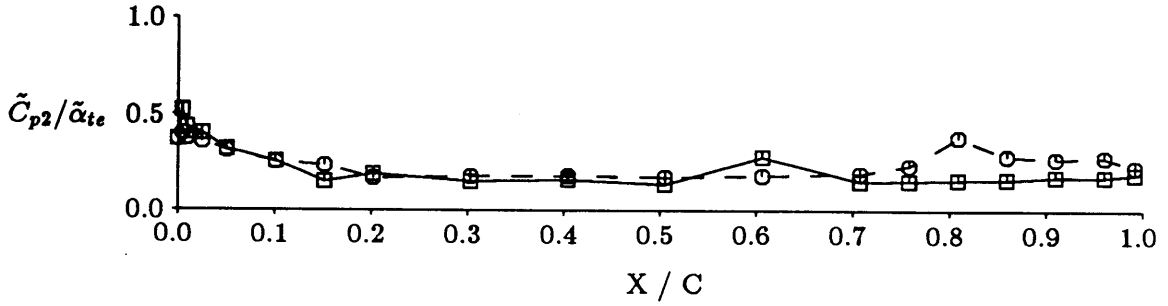


Figure E.57: Amplitude of C_p at 2^{nd} harmonic (0012, LTWT, $Re = 400000$, $\alpha = 0°$, $k = 0.15$)

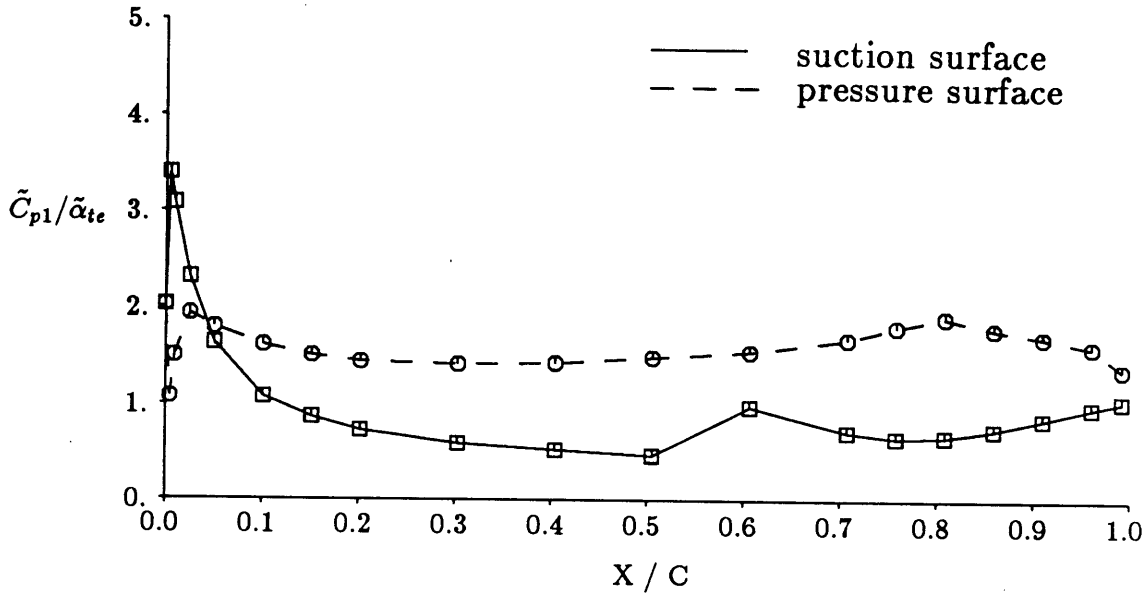


Figure E.58: Amplitude of C_p at fundamental frequency (0012, LTWT, Re = 400000, $\alpha = 0^o$, $k = 0.5$)

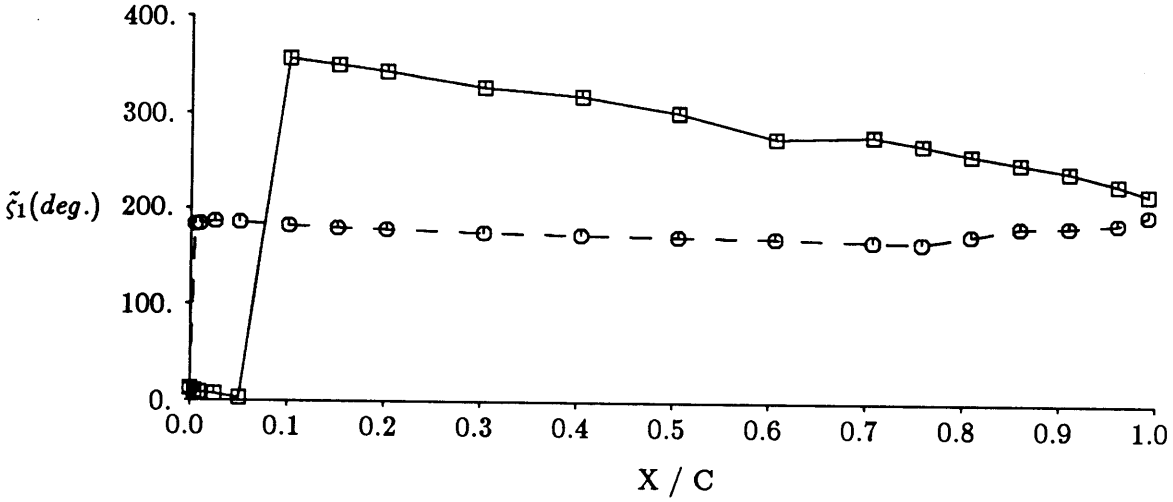


Figure E.59: Phase of C_p at fundamental frequency (0012, LTWT, Re = 400000, $\alpha = 0^o$, $k = 0.5$)

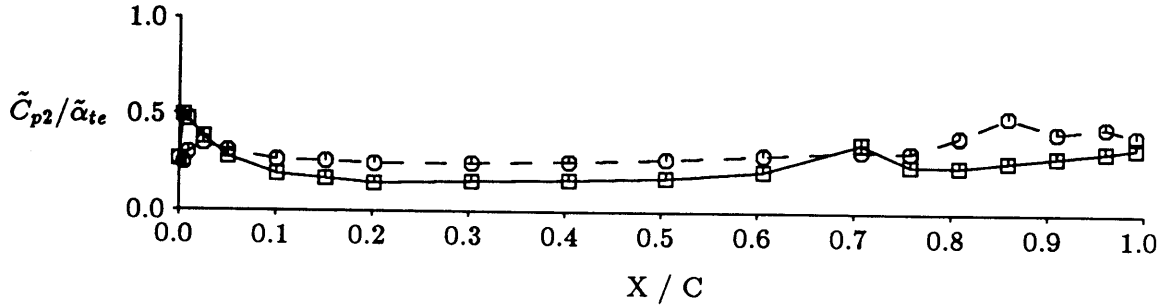


Figure E.60: Amplitude of C_p at 2^{nd} harmonic (0012, LTWT, Re = 400000, $\alpha = 0^o$, $k = 0.5$)

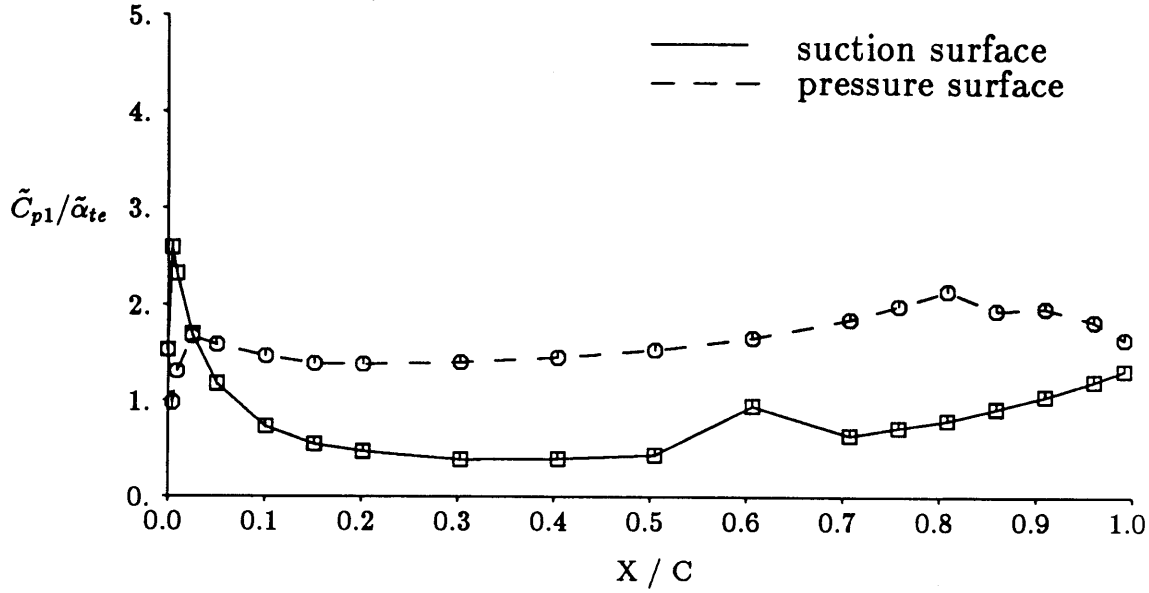


Figure E.61: Amplitude of C_p at fundamental frequency (0012, LTWT, Re = 400000, $\alpha = 0^o$, $k = 0.75$)

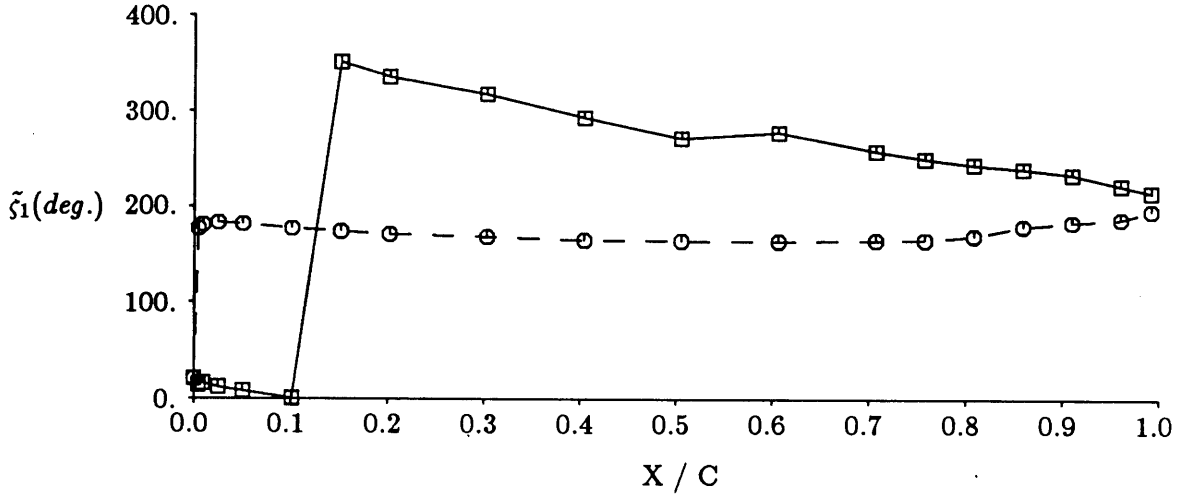


Figure E.62: Phase of C_p at fundamental frequency (0012, LTWT, Re = 400000, $\alpha = 0^o$, $k = 0.75$)

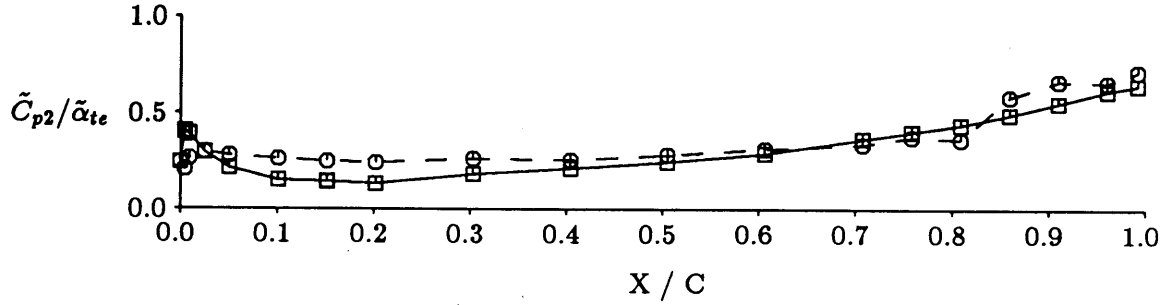


Figure E.63: Amplitude of C_p at 2^{nd} harmonic (0012, LTWT, Re = 400000, $\alpha = 0^o$, $k = 0.75$)

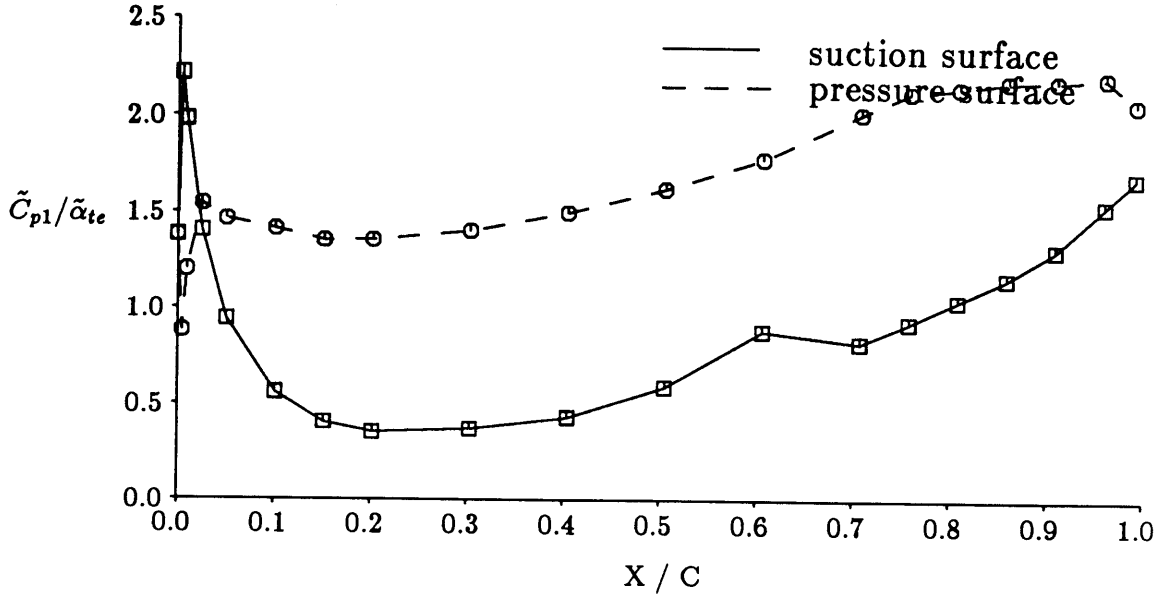


Figure E.64: Amplitude of C_p at fundamental frequency (0012, LTWT, Re = 400000, $\alpha = 0^o$, $k = 1.0$)

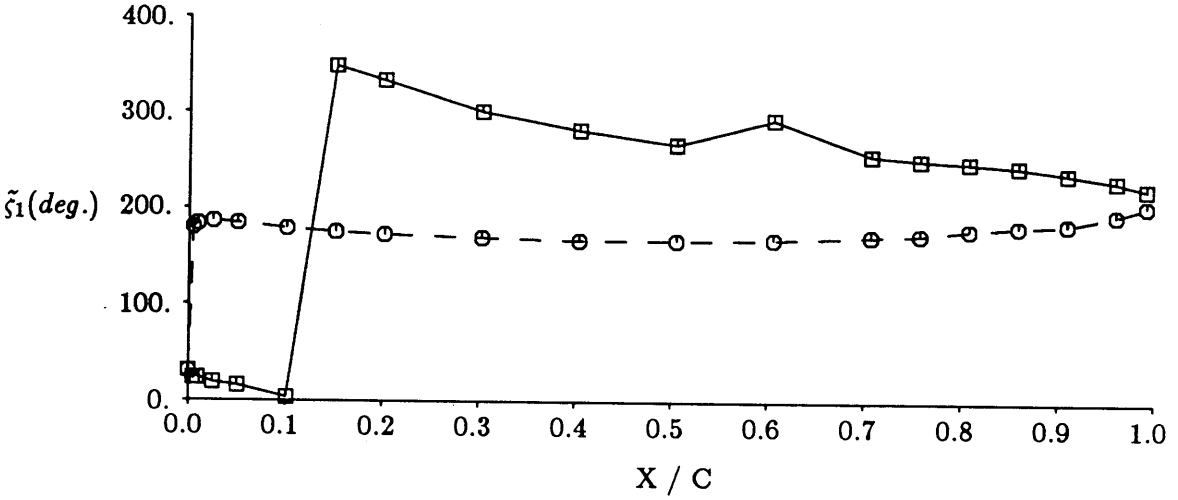


Figure E.65: Phase of C_p at fundamental frequency (0012, LTWT, Re = 400000, $\alpha = 0^o$, $k = 1.0$)

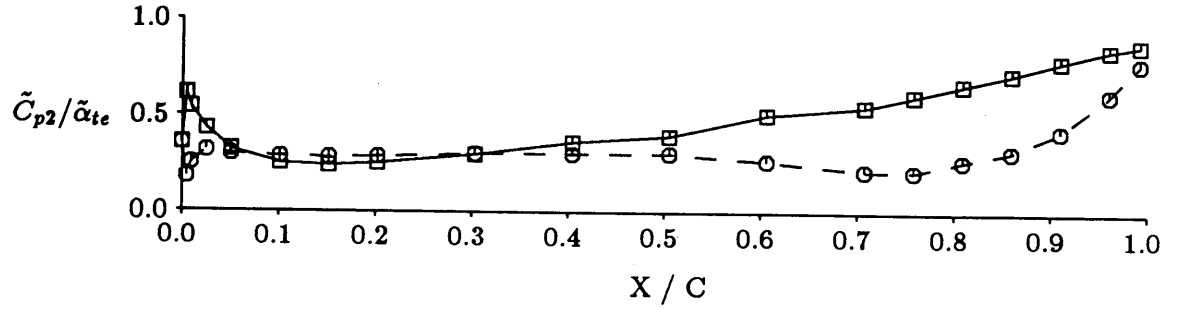


Figure E.66: Amplitude of C_p at 2^{nd} harmonic (0012, LTWT, $Re = 400000$, $\alpha = 0^o$, $k = 1.0$)

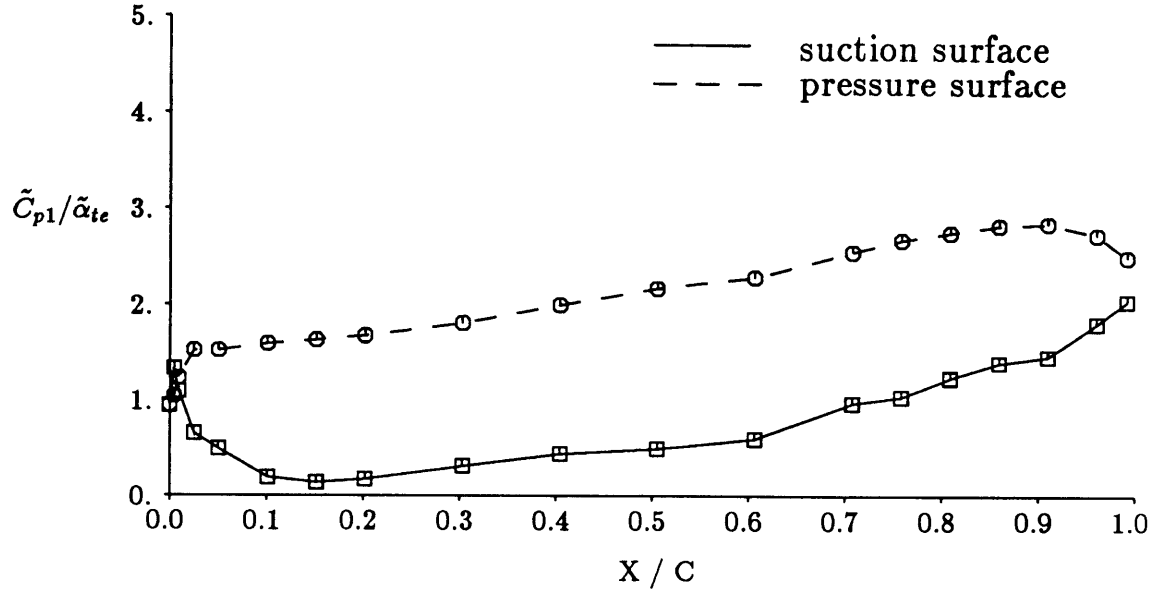


Figure E.67: Amplitude of C_p at fundamental frequency (0012, LTWT, Re = 400000, $\alpha = 0^o$, $k = 2.0$)

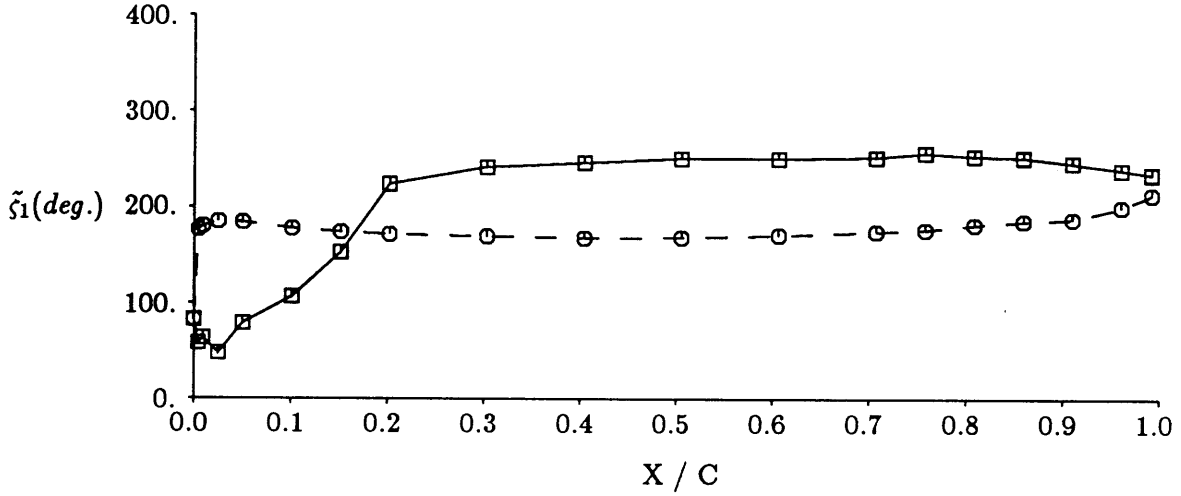


Figure E.68: Phase of C_p at fundamental frequency (0012, LTWT, Re = 400000, $\alpha = 0^o$, $k = 2.0$)

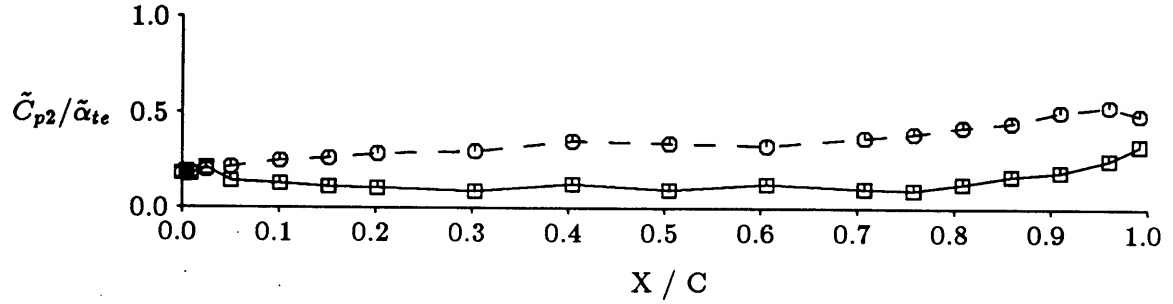


Figure E.69: Amplitude of C_p at 2^{nd} harmonic (0012, LTWT, $Re = 400000$, $\alpha = 0^o$, $k = 2.0$)

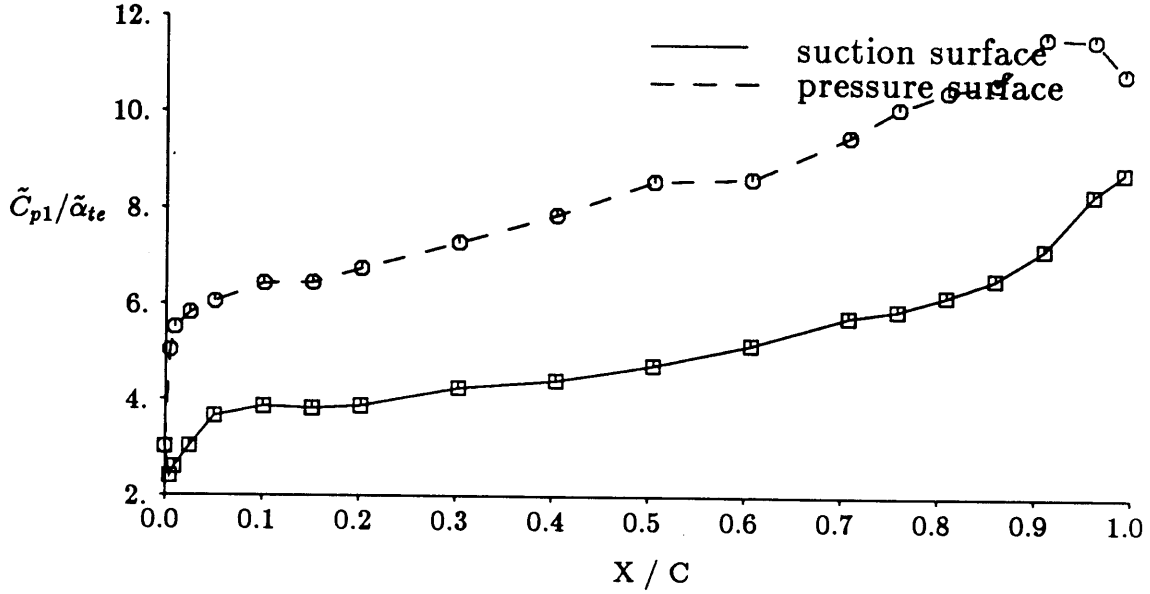


Figure E.70: Amplitude of C_p at fundamental frequency (0012, LTWT, Re = 400000, $\alpha = 0^o$, $k = 6.4$)

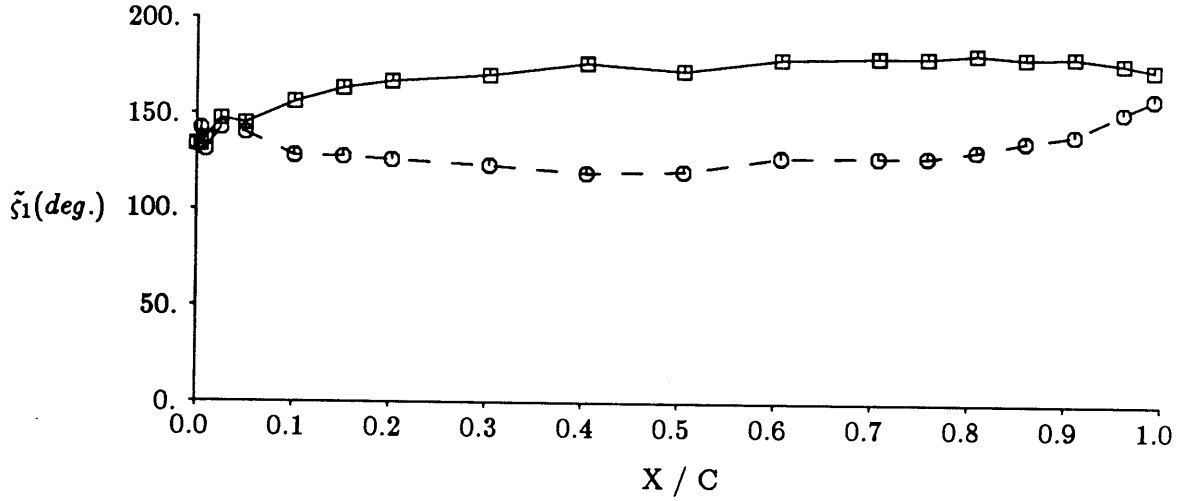


Figure E.71: Phase of C_p at fundamental frequency (0012, LTWT, Re = 400000, $\alpha = 0^o$, $k = 6.4$)

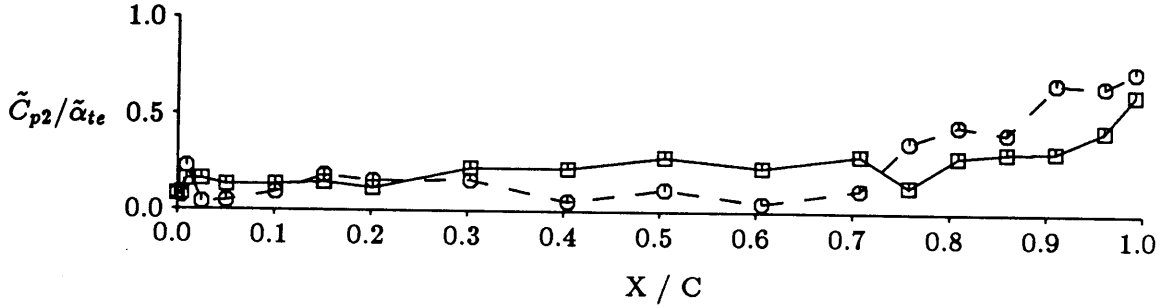


Figure E.72: Amplitude of C_p at 2^{nd} harmonic (0012, LTWT, Re = 400000, $\alpha = 0^o$, $k = 6.4$)